NASA Technical Memorandum 83250

Effects of Installation of F101 DFE Exhaust Nozzles on the Afterbody-Nozzle Characteristics of the F-14 Airplane

David E. Reubush and John R. Carlson

MARCH 1982

NASA

Effects of Installation of F101 DFE Exhaust Nozzles on the Afterbody-Nozzle Characteristics of the F-14 Airplane

David E. Reubush and John R. Carlson
Langley Research Center
Hampton, Virginia

SUMMARY

A wind-tunnel investigation was conducted to determine the effects of F101 DFE (derivative fighter engine) nozzle axial positioning on the afterbody-nozzle longitudinal aerodynamic characteristics of the F-14 airplane. The model was tested in the Langley 16-Foot Transonic Tunnel at Mach numbers from 0.7 to 1.25 and angles of attack from about -2° to 6°. Compressed air was used to simulate nozzle exhaust flow at jet total-pressure ratios from 1 (jet off) to about 8.

The results of this investigation show that variations in jet total-pressure ratio (once the jet has been turned on) have only small effects on afterbody-nozzle drag characteristics at subsonic speeds, whereas at supersonic speeds increasing jet total-pressure ratio resulted in reduced drag. At subsonic speeds the intermediate cruise nozzle position of the three positions tested resulted in the lowest drag, whereas at supersonic speeds for positive lift coefficients the aft nozzle position resulted in the lowest drag. Speed-brake deployment resulted in the expected increase in drag without significantly affecting lift or pitching moment.

INTRODUCTION

The Grumman F-14A is the current front-line, fleet, air-defense airplane for the U.S. Navy. It is powered by two Pratt & Whitney TF30-P-414 engines. A program is currently underway to investigate the feasibility of reengining this airplane with General Electric F101 DFE (derivative fighter engine) engines to increase its performance. The F101 DFE is a version of the F101 engine first developed to power the B-1 bomber.

As a part of the reengining program an investigation was conducted to determine the aerodynamic effects of integrating the F101 DFE engines and exhaust nozzles into the F-14 airframe. Since the F101 engine is somewhat shorter than the TF30 engine, there exists the possibility that the airplane afterbody can be shortened when the F101 engines are installed, thus resulting in a lighter configuration. However, it was feared that the drag for this configuration would be unacceptably high because of steep boattail angles where the F101 exhaust nozzles would be integrated into the afterbody. As a result, the investigation included afterbody-nozzle configurations (cruise power nozzles) representative of the shortest possible configuration, an intermediate nozzle location, and an aft nozzle configuration (which was the same as the formerly proposed F-14B configuration with Pratt & Whitney F401-PW-400 engines). (See refs. 1 to 3.) The intermediate and aft nozzle configurations would require extensions to be added to the F101 afterburner duct in order to place the nozzles at the desired location and would, therefore, be heavier than the short configuration.

This investigation was conducted in the Langley 16-Foot Transonic Tunnel at Mach numbers from 0.7 to 1.25. Angle of attack was varied from about -2° to 6°. The jet total-pressure ratio was varied from 1 (jet off) to about 8, depending on Mach number.

All force and moment coefficients are referenced to the stability-axis system and are based on the geometry of the model having a wing leading-edge sweep of 20°. The origin of this axis system is at fuselage station 0.9127 m and water line 0.3175 m. All reference dimensions are given in meters; model dimensions are shown in centimeters.

b wing span, 1.6289 m

$C_{D,a}$ afterbody drag coefficient, $\dfrac{\text{Afterbody drag}}{q_\infty S}$

$C_{D,n}$ nozzle drag coefficient obtained from integration of nozzle pressures and calculated skin friction, $\dfrac{\text{Drag of two nozzles}}{q_\infty S}$

$C_{D,t}$ total afterbody-nozzle drag coefficient, $\dfrac{(\text{Afterbody drag}) + (\text{Nozzle drag})}{q_\infty S}$

$C_{L,a}$ afterbody lift coefficient, $\dfrac{\text{Afterbody lift}}{q_\infty S}$

$C_{L,n}$ nozzle lift coefficient obtained from integration of nozzle pressures, $\dfrac{\text{Lift of two nozzles}}{q_\infty S}$

$C_{L,t}$ total afterbody-nozzle lift coefficient, $\dfrac{(\text{Afterbody lift}) + (\text{Nozzle lift})}{q_\infty S}$

$C_{m,a}$ afterbody pitching-moment coefficient, $\dfrac{\text{Afterbody pitching moment}}{q_\infty S \bar{c}}$

$C_{m,n}$ nozzle pitching-moment coefficient obtained from integration of nozzle pressures, $\dfrac{\text{Pitching moment of two nozzles}}{q_\infty S \bar{c}}$

$C_{m,t}$ total afterbody-nozzle pitching-moment coefficient, $\dfrac{(\text{Afterbody pitching moment}) + (\text{Nozzle pitching moment})}{q_\infty S \bar{c}}$

$\bar{c}$ mean aerodynamic chord of wing, 0.2490 m

M free-stream Mach number

$p_{t,j}$ jet total pressure, Pa

p_∞ free-stream static pressure, Pa

q_∞ free-stream dynamic pressure, Pa

S   wing reference area, 0.3645 m^2

α angle of attack, deg

δ_h horizontal-tail deflection, deg

δ_s speed-brake deflection, deg

Λ wing sweep angle, deg

Abbreviations:

A/B   afterburning

BL   buttock line

FS   fuselage station

NPR   nozzle pressure ratio, $p_{t,j}/p_\infty$

WL   water line

APPARATUS AND PROCEDURE

Wind Tunnel

This investigation was conducted in the Langley 16-Foot Transonic Tunnel, which is a single-return, continuous-flow, exchange-air-cooled, atmospheric wind tunnel. The test section is a regular octagon in cross section with slots at the corners of the octagon. The tunnel speed is continuously variable for a Mach number range from 0.20 to 1.30. Further description of the Langley 16-Foot Transonic Tunnel can be found in reference 4.

Model

Photographs of the model mounted in the Langley 16-Foot Transonic Tunnel are shown in figure 1. A sketch showing the principal dimensions of the model is shown in figure 2(a). The model was supported in the 16-foot tunnel by a thin sweptback strut attached to the bottom of the fuselage just aft of the nose, as shown in figure 2(b). The strut blended into a sting which had a constant cross section beginning at the intersection with the strut trailing edge and extending downstream to a station well aft of the model. Model details and dimensions are presented in figure 3.

The model was tested with two wing-sweep positions: 22° for subsonic speeds (M ≤ 0.9) with extendible glove vanes retracted, and 68° for transonic and supersonic speeds (M ≥ 0.9) with glove vanes extended. The inlets, located on each side of the fuselage, maintained true geometric lines but were closed to flow passage a short distance inside the inlet lip. The model consisted of three parts: the

3

forebody and wings, the aft fuselage and empennage (hereinafter referred to as the afterbody), and the engine exhaust nozzles. The forebody and wings were rigidly attached to the support system and were not metric. The afterbody was the metric portion of the model and started at the model metric break (station 1.1261 m, FS 112.607); it included the horizontal and vertical tails, ventral fins, speed brake, aft fuselage, and interfairing between the engines. The metric break is indicated in the sketches of figure 2 and can be seen in the photographs shown in figure 1. A flexible Teflon[1] strip, inserted into slots machined into the metric and nonmetric portions of the model, was used as a seal at the metric-break station to prevent flow through the gap between the afterbody and the forebody.

Four different pairs of exhaust nozzles representing cruise and afterburning power settings for the F101 DFE engines were tested. Three pairs represented cruise power-setting nozzles installed at three different axial stations (forward, intermediate, and aft as shown in figs. 1 and 4). (It must be noted that the aft-position nozzles were the same as those tested in refs. 1, 2, and 3 as configuration 9. It was deemed that they were sufficiently similar to the F101 DFE nozzles that, in the interest of economy, new nozzles did not need to be constructed.) The fourth pair of nozzles represented after-burning power-setting nozzles at the forward position. (See figs. 1 and 4.) The nozzle exhaust flow was simulated by use of a high-pressure compressed-air system.

Instrumentation

External static-pressure orifices were located on the exhaust nozzles, and the pressure coefficients were integrated to obtain nozzle force characteristics. In addition, internal static-pressure orifices were located in the afterbody cavity and at the seal station in the gap between the forebody and afterbody. The jet total pressures and temperatures were measured in each tailpipe by use of a total-pressure probe and a thermocouple. Forces and moments on the metric portion (afterbody) of the model were obtained by use of a six-component strain-gage balance.

Tests

Data were obtained for Mach numbers from 0.7 to 1.25 at angles of attack from about -2° to 6°. The average Reynolds number per meter varied from 1.12×10^7 at $M = 0.7$ to 1.26×10^7 at $M = 1.25$ in the 16-foot tunnel. The jet total-pressure ratio was varied from 1 (jet off) to about 8, depending on Mach number.

Transition was fixed on the model by means of 3.2-mm-wide strips of No. 120 carborundum grains. The transition strips were located on the ventral fins and on the horizontal- and vertical-tail surfaces at a distance of 5.08 mm measured normal to the leading edge. The transition strips on the wing were located as shown in figure 5. A 3.2-mm-wide ring of transition-strip grit was also located 13.5 mm aft of the nose of the fuselage.

In addition to the various exhaust nozzles, other variables investigated included the effect of wing sweep, speed-brake deflection, and horizontal-tail deflection.

---

[1]Teflon: Trademark of E. I. du Pont de Nemours & Co., Inc.

Data Reduction

Model data recorded on magnetic tape were used to compute standard force and pressure coefficients. All force and moment data in this paper are referenced to the stability axes through the airplane center of gravity. Model angle of attack was corrected for support deflection due to loads and for tunnel upflow. No correction was made for strut interference since data from references 5 and 6 indicate that the effect is small for a similar type of support system.

The afterbody axial force was obtained from the reading for balance axial force corrected for pressure-area terms which consisted of internal-cavity and seal-cavity forces. The forces and moments on the exhaust nozzles were obtained from pressure measurements by assigning an incremental projected area to each nozzle pressure orifice and summing the incremental forces. Skin friction on the nozzles was calculated by using the Frankl and Voishel method (ref. 7) for compressible, turbulent flow on a flat plate.

RESULTS AND DISCUSSION

Data for this model have been previously reported in references 1, 2, and 3. However, the data in these references were obtained with various nozzle interfairings which were different from that on the current configuration, although the current interfairing is a derivative of interfairing 6 of reference 3. As a result, no comparisons with the previous data will be made in this report.

Presentation of Results

The following table lists the figures through which the results of this investigation are presented. When more than one figure is indicated for a given condition, such as 6(a), (b), and (c), the first (6(a)) presents the afterbody-nozzle characteristics, the second (6(b)) presents the afterbody characteristics, and the third (6(c)) presents the nozzle characteristics.

Basic Force and Moment Data

Basic afterbody and nozzle force and moment coefficient data for the four nozzle configurations investigated are presented in figures 6 to 9. These figures present the afterbody and total afterbody-nozzle forces and moments as a function of afterbody or afterbody-nozzle lift coefficient and the nozzle forces and moments as a function of angle of attack at the various nozzle pressure ratios investigated. (Nozzle characteristics are shown as a function of angle of attack and not lift since nozzle lift remains essentially zero for all conditions tested.) It should be noted that these aerodynamic forces and moments represent only those measured on the aft portion of the model (afterbody-nozzle combination was approximately one-third of the model length) and do not include forces and moments on the wings or forward portion of the fuselage. Nozzle pressure ratio had virtually no effect on the lift or pitching moment of the afterbody or nozzles for all four configurations at all conditions tested. At subsonic speeds, turning on the jet exhaust generally reduced both afterbody and nozzle drag (except at $M = 0.7$ shown in fig. 6(a)), whereas increases in nozzle pressure ratio above the initial jet-on point generally resulted in either a small further reduction in afterbody or nozzle drag or no effect at all. (For example, see figs. 6(a) to 6(l).) At supersonic speeds turning on the jet exhaust

Configuration	Figures showing results of this investigation for -					
	Λ = 22°			Λ = 68°		
	M = 0.7	M = 0.8	M = 0.9	M = 0.9	M = 1.15	M = 1.25
Effect of nozzle pressure ratio						
Cruise-nozzle position:						
Aft	6(a), (b), (c)	6(d), (e), (f)	6(g), (h), (i)	6(j), (k), (l)	6(m), (n), (o)	6(p), (q), (r)
Intermediate	7(a), (b), (c)	7(d), (e), (f)	7(g), (h), (i)	7(j), (k), (l)	7(m), (n), (o)	7(p), (q), (r)
Forward	8(a), (b), (c)	8(d), (e), (f)	8(g), (h), (i)	8(j), (k), (l)	8(m), (n), (o)	8(p), (q), (r)
A/B nozzles, forward position	9(a), (b), (c)	9(d), (e), (f)	9(g), (h), (i)	9(j), (k), (l)	9(m), (n), (o)	9(p), (q), (r)
Effect of cruise-nozzle position ...	10(a), (b), (c)	10(d), (e), (f)	10(g), (h), (i)	10(j), (k), (l)	10(m), (n), (o)	10(p), (q), (r)
Effect of power setting	11(a), (b), (c)	11(d), (e), (f)	11(g), (h), (i)	11(j), (k), (l)	11(m), (n), (o)	11(p), (q), (r)
Effect of wing sweep (M = 0.9 only)						
Cruise-nozzle position:						
Aft			12(a)	12(a)		
Intermediate			12(b)	12(b)		
Forward			12(c)	12(c)		
A/B nozzles, forward position			12(d)	12(d)		
Effect of 20° speed brake						
Cruise-nozzle position:						
Intermediate				13(a), (b), (c)	13(d), (e), (f)	13(g), (h), (i)
Forward				14(a), (b), (c)	14(d), (e), (f)	14(g), (h), (i)
Effect of horizontal-tail deflection						
Forward position:						
Cruise nozzles				15(a)		
A/B nozzles				15(b)		

generally resulted in a decrease in afterbody and nozzle drag which was further enhanced by increases in nozzle pressure ratio. (For example, see figs. 6(m) to 6(r).) Since nozzle pressure ratio generally had virtually no effect on afterbody and nozzle lift and on pitching-moment coefficients and since the effect on drag was generally consistent, further data comparisons will be made at only one nozzle pressure ratio for each Mach number tested.

Effect of Nozzle Position

The primary purpose of this investigation was to determine the nozzle axial position for lowest drag. Comparisons of the aerodynamic data for the three cruise-nozzle axial positions are shown in figure 10. At subsonic speeds for both wing sweeps, the changes in afterbody and nozzle lift and pitching moment with nozzle position were virtually negligible. At supersonic speeds the nozzle lift and pitching moment were about the same for all three axial positions, whereas the afterbody lift and pitching moment were the same for the intermediate and aft nozzle positions. The forward nozzle position resulted in a somewhat lower afterbody lift and pitching moment than that of the other two positions at supersonic speeds. Since the subsonic lift and pitching-moment characteristics do not change with nozzle position, direct comparisons of the drag characteristics of the three nozzle positions can be made without adjustment of the data for possible changes due to trim. At supersonic speeds, with the comparisons made at a constant lift coefficient, in order to get a totally accurate comparison between configurations the differences in pitching-moment characteristics should be taken into account. However, since the pitching-moment differences between configurations are generally small and the supersonic comparison is not realistic (because the airplane will never operate at supersonic speeds with the nozzles at the cruise power setting except in the event of a flameout, and then not for long), the comparison will be made without adjusting for the pitching-moment difference between configurations.

At subsonic speeds with a wing sweep of 22°, the intermediate cruise-nozzle position had the lowest total afterbody-nozzle drag, the aft nozzle position had a somewhat higher drag, and the forward nozzle position had the highest drag. The data show that the difference in total afterbody-nozzle drag between the aft and forward nozzle positions is almost entirely the result of the difference in nozzle drag between the two configurations. This is due to the higher boattail angles on the forward configuration since the nozzle closure must occur in a much shorter distance. The intermediate nozzle position has both lower afterbody drag and lower nozzle drag than either of the other two configurations. As expected, the nozzle drag of the intermediate configuration was lower than that of the forward configuration, again because of a shallower boattail angle. The fact that the intermediate configuration had a lower nozzle drag than that of the aft configuration may be explained because the aft nozzle was not exactly of the same design (being a cost-saving holdover from previous tests with a different external contour and a slightly higher closure than the other two cruise nozzles). However, without data from diagnostic pressure taps on the afterbody, the advantage that the intermediate-nozzle configuration holds in afterbody drag over the aft configuration is not explainable at the present time. It might be possible that the exits of the intermediate nozzles were in such a position that the jet exhaust provided a favorable interference on the adjacent portions of the interfairing. However, when the data for the jet-off condition were examined (not shown), the intermediate-nozzle position also exhibited the lower afterbody drag. Therefore, the characteristic is not a plume effect and may be due to details of the integration of the nozzles with the afterbody.

7

At $M = 0.9$ with a wing sweep of 68°, the intermediate- and aft-nozzle configurations have approximately the same afterbody-nozzle drag level $C_{D,t}$, whereas the forward-nozzle configuration has significantly higher drag. The aft-nozzle position yields slightly lower afterbody drag $C_{D,a}$ than that of the intermediate position, whereas the intermediate position yields slightly lower nozzle drag $C_{D,n}$. Thus, the total afterbody-nozzle drags for the two configurations are about the same.

At supersonic speeds the relative positions of the total afterbody-nozzle drag and the afterbody drag for the three configurations vary with lift coefficient. However, for positive values of lift coefficient, the aft configuration has the lowest drag, the intermediate configuration has a slightly higher drag, and the forward configuration has the highest drag. This is as expected at supersonic speeds because of area-rule considerations and is reflected in only the afterbody drag (as expected). The three cruise nozzles have about the same drag at supersonic speeds because their boattail angles almost ensure that all three are highly separated at these supersonic speeds.

Effect of Nozzle Power Setting

Figure 11 presents a comparison of the cruise- and afterburning-nozzle data (forward position) for the various Mach numbers investigated. The only unexpected result shown by this figure is that the cruise power-setting nozzles resulted in slightly lower afterbody lift and, hence, total afterbody-nozzle lift than did the afterburning-nozzle configuration at both subsonic and supersonic speeds. It was expected that the lift would be the same for both configurations as was the pitching moment. As expected, the A/B configuration exhibited lower nozzle and resulting total drag than that of the cruise-nozzle configurations as a result of the much shallower boattail angles of the A/B configuration.

Effect of Wing Sweep

At $M = 0.9$, tests were conducted with the wings swept at both 22° and 68°. The comparison of results for the two wing sweeps is presented in figure 12. The results shown are not unexpected since, at 68°, the wings are in much closer proximity to the afterbody and horizontal tails than at 22° and, therefore, would be expected to cause a higher level of interference. Generally, the 68° wing sweep resulted in slightly higher afterbody lift and, hence, total lift than that of the 22° wing sweep. Also, in all cases, the 68° wing sweep resulted in increased drag (nozzle, afterbody, and total) over the 22° wing sweep. Pitching moment was not significantly affected by wing sweep.

Effects of Speed-Brake Deployment

The effects of 20° speed-brake deployment for the intermediate and forward cruise-nozzle configurations are shown in figures 13 and 14, respectively. As expected and desired, the afterbody and total drag coefficients were significantly increased at all conditions with the speed brakes deployed. At subsonic speeds the nozzle drag was also increased. However, at supersonic speeds the nozzle drag was reduced when the speed brakes were deployed. This phenomenon was a result of the flow aft of the speed brakes (especially at supersonic speeds) having a greatly reduced velocity; hence, the nozzles were at least in part in a reduced Mach number flow field and, therefore, the drag was reduced. Also, generally the afterbody and,

hence, total lift were reduced slightly with speed-brake deployment, whereas the pitching moment remained essentially constant with constant lift.

Effect of Horizontal-Tail Deflection

The effects of -2° horizontal-tail deflection for the forward cruise-nozzle configuration in combination with 20° speed-brake deflection are shown in figure 14 and with the basic afterbody in figure 15. The effects of the -2° tail deflection on the afterburning-nozzle configuration are also shown in figure 15. The drag results for -2° tail deflection are mixed, with some conditions resulting in higher drag than the 0° tail deflection, some with the same, and some with lower. The effects of the -2° tail deflection on lift, however, are consistent. It was expected that the -2° tail deflection would result in a reduction in afterbody lift, and this was the case for both the cruise and afterburning-nozzle configurations with the basic afterbody. However, with the speed brakes deflected, the flow interference from the speed brakes was such that the -2° of tail deflection resulted in an increase in lift rather than a decrease. In addition, for all conditions and configurations, when compared at a constant lift coefficient, the afterbody, nozzle, and total pitching-moment coefficients remained the same at both tail settings. This would indicate that, at a constant angle of attack, the pitching-moment change due to the change in tail deflection was being offset by a change in lift; thus, when compared at a constant lift-coefficient, the pitching moments were essentially identical.

CONCLUSIONS

A wind-tunnel investigation of the axial positioning of the F101 DFE (derivative fighter engine) exhaust nozzles and other configuration variables on the afterbody-nozzle longitudinal aerodynamic characteristics of the F-14 airplane has indicated the following conclusions:

1. At all conditions investigated jet total-pressure ratio had virtually no effect on either the afterbody, nozzle, or total lift or on pitching-moment coefficients for all four nozzle configurations investigated.

2. At subsonic speeds increases in jet total-pressure ratio, once the jet had been turned on, had only small effects on afterbody and nozzle drag characteristics for the four nozzle configurations investigated.

3. At supersonic speeds increases in jet total-pressure ratio resulted in reduced drag for all four nozzle configurations investigated.

4. The intermediate cruise-nozzle position of the three positions investigated resulted in the lowest afterbody-nozzle drag for subsonic Mach numbers. At supersonic Mach numbers and positive values of lift coefficient, the aft cruise-nozzle position resulted in the lowest drag.

5. Speed-brake deployment resulted in higher drag with only small changes in afterbody-nozzle lift and with essentially none in pitching moment.

Langley Research Center
National Aeronautics and Space Administration
Hampton, VA 23665
January 14, 1982

9

REFERENCES

1. Mercer, Charles E.; and Reubush, David E.: Sting and Jet Interference Effects on Longitudinal Aerodynamic Characteristics of a Twin-Jet, Variable-Wing-Sweep Fighter Model at Mach Numbers to 2.2. NASA TM X-2825, 1973.

2. Reubush, David E.; and Mercer, Charles E.: Exhaust-Nozzle Characteristics for a Twin-Jet Variable-Wing-Sweep Fighter Airplane Model at Mach Numbers to 2.2. NASA TM X-2947, 1974.

3. Reubush, David E.; and Mercer, Charles E.: Effects of Nozzle Interfairing Modifications on Longitudinal Aerodynamic Characteristics of a Twin-Jet, Variable-Wing-Sweep Fighter Model. NASA TN D-7817, 1975.

4. Corson, Blake W., Jr.; Runckel, Jack F.; and Igoe, William B.: Calibration of the Langley 16-Foot Transonic Tunnel With Test Section Air Removal. NASA TR R-423, 1974.

5. Re, Richard J.; Wilmoth, Richard G.; and Runckel, Jack F.: Investigation of Effects of Afterbody Closure and Jet Interference on the Drag of a Twin-Engine Tactical Fighter. NASA TM X-1382, 1967.

6. Runckel, Jack F.; Lee, Edwin E., Jr.; and Simonson, Albert J.: Sting and Jet Interference Effects on the Afterbody Drag of a Twin-Engine Variable-Sweep Fighter Model at Transonic Speeds. NASA TM X-755, 1963.

7. Frankl, F.; and Voishel, V.: Turbulent Friction in the Boundary Layer of a Flat Plate in a Two-Dimensional Compressible Flow at High Speeds. NACA TM 1053, 1943.
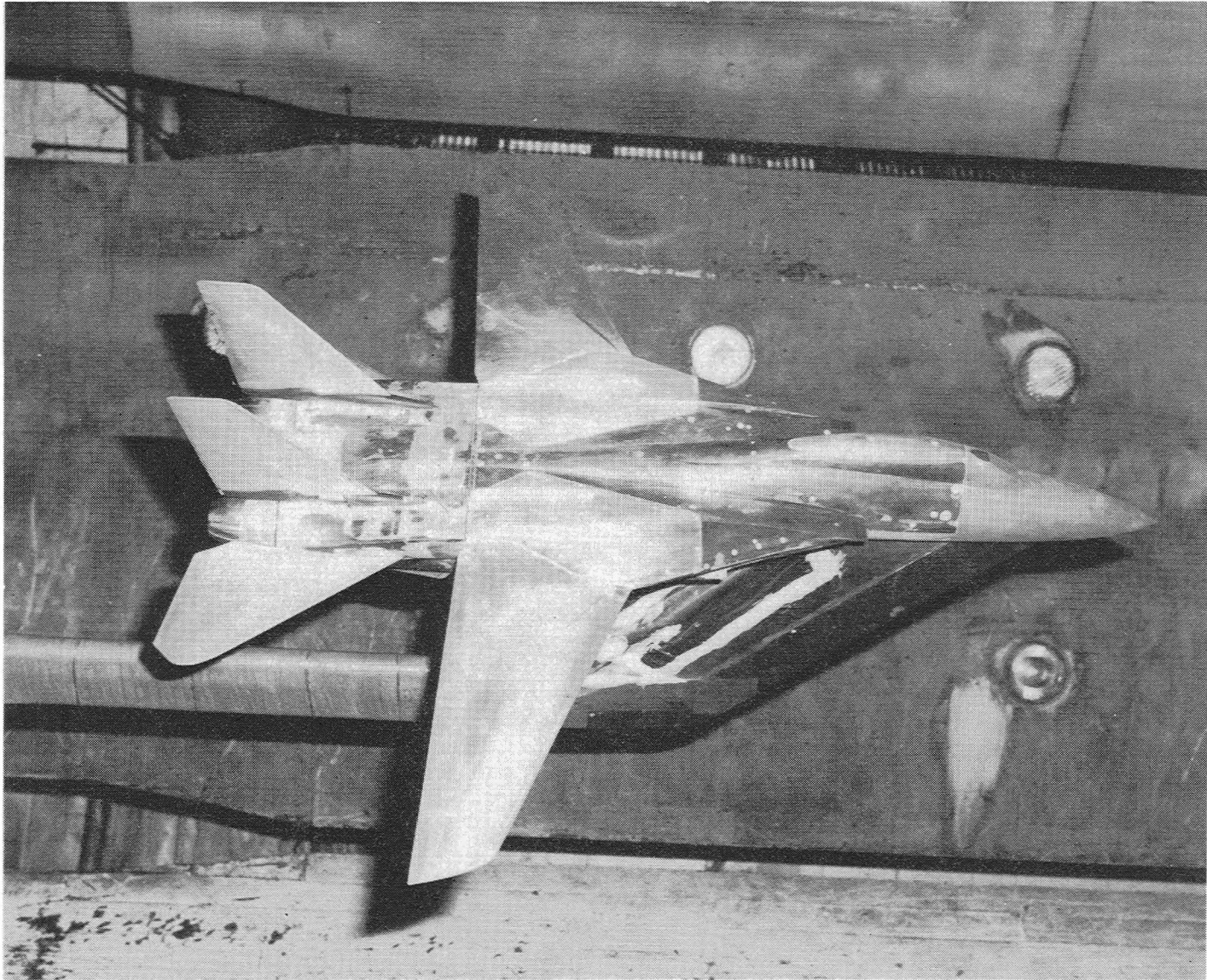
L-80-5146

(a) Side view with aft-position cruise power nozzles installed.

Figure 1.- Model installed in the Langley 16-Foot Transonic Tunnel.
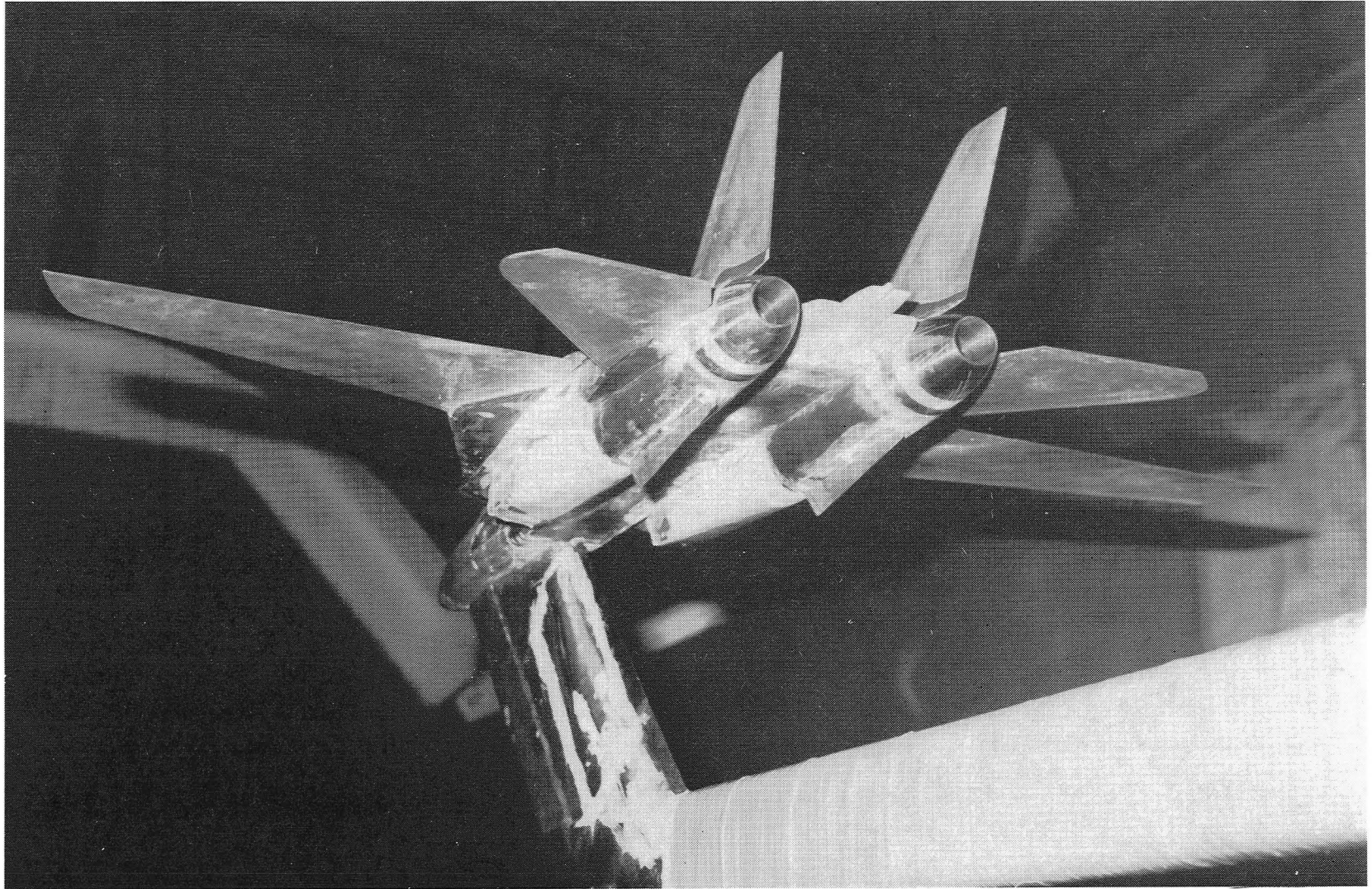
L-80-5150

(b) Rear view with intermediate-position cruise power nozzles installed.

Figure 1.- Continued.
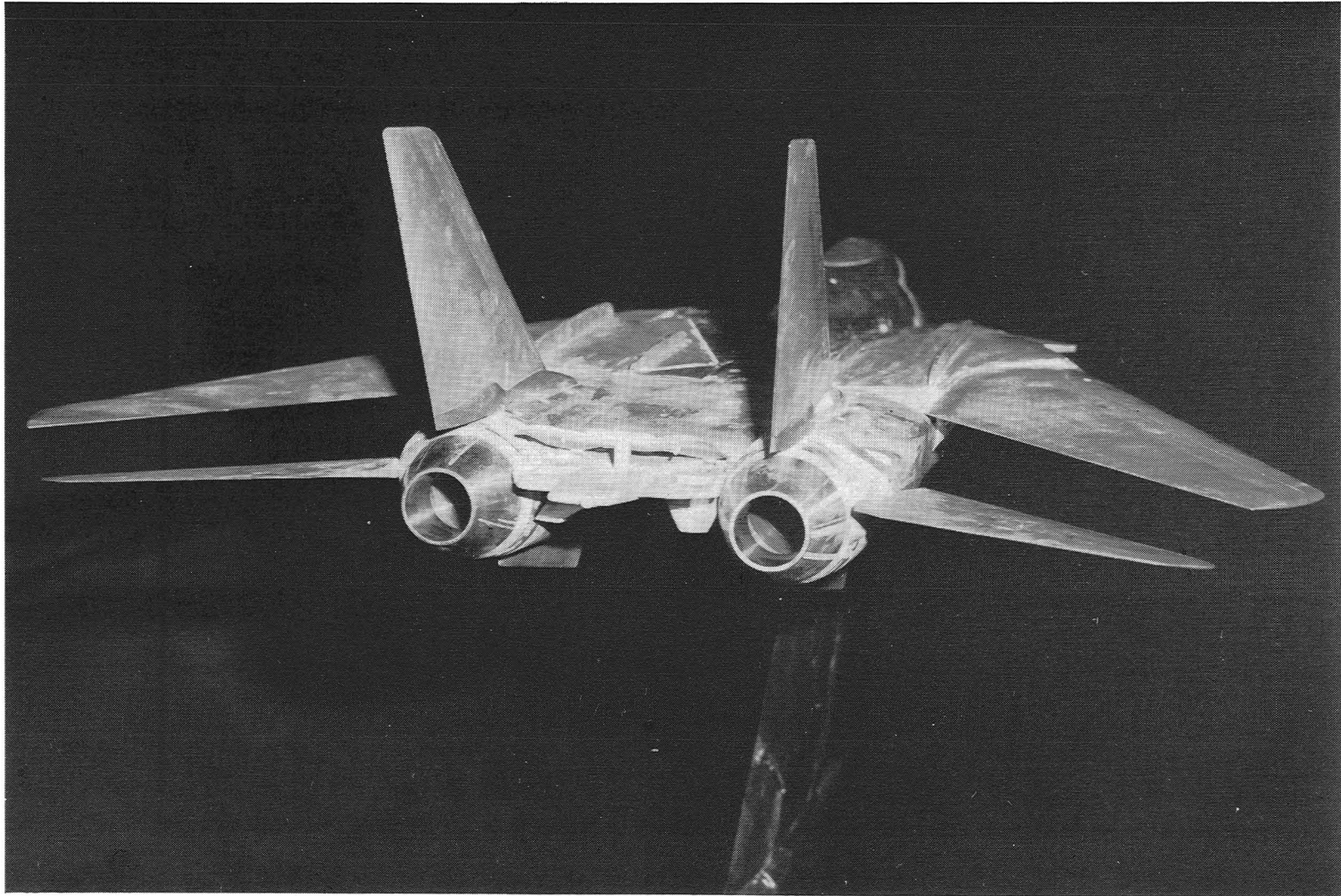
L-80-5565

(c) Rear view with forward-position cruise power nozzles installed and speed brakes deflected 20°.

Figure 1.- Continued.
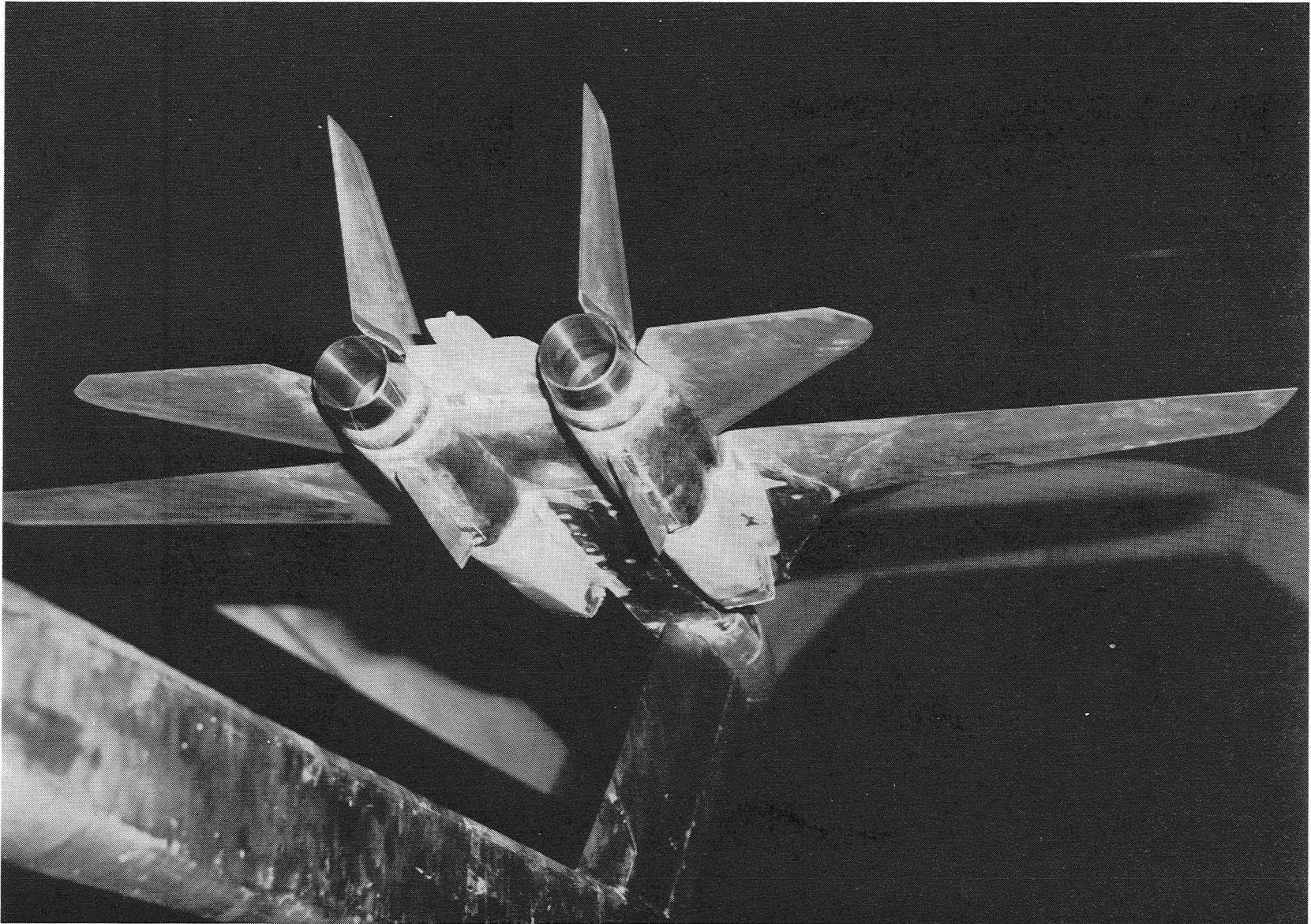
L-80-5606

(d) Rear view with forward-position A/B power nozzles installed.

Figure 1.- Concluded.

FS 91.271

20°

Wing pivot

Metric Break

Glove vane

FS 49.741
BL 22.648

83.079

Interfairing

FS 0

Bottom view

97.028

13.547

162.885

Top view

48°

Inlet bleed
Wing fences
BL 32.407

$\bar{c} = 24.896$

68°

FS 88.897

156.808

WL 56.304

Moment reference center at WL 31.749

FS 92.933

Wing fence

WL 27.767

Gun pods

8.110

149.528

156.845
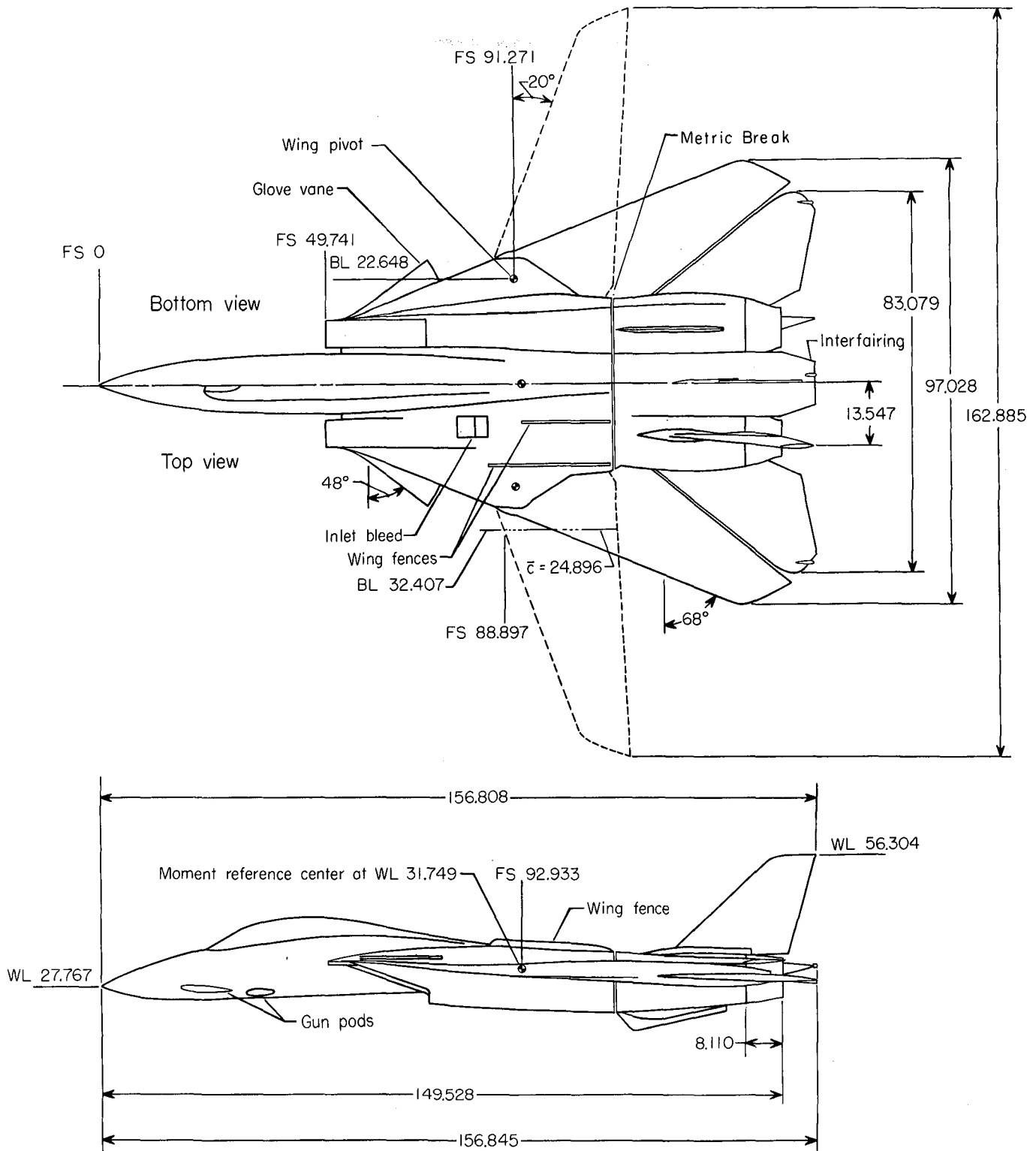
(a) Model with maximum-afterburning, power-setting nozzles of type A installed.

Figure 2.- Sketch of model with geometric details of model support. All
dimensions are in centimeters unless otherwise specified.

15

FS 112.607   FS 141.499

FS 0

48.514

5.080

Angle-of-attack reference

Metric Break

156.808

WL 27.767

35.941

51.029

2.54

5.08

15.24
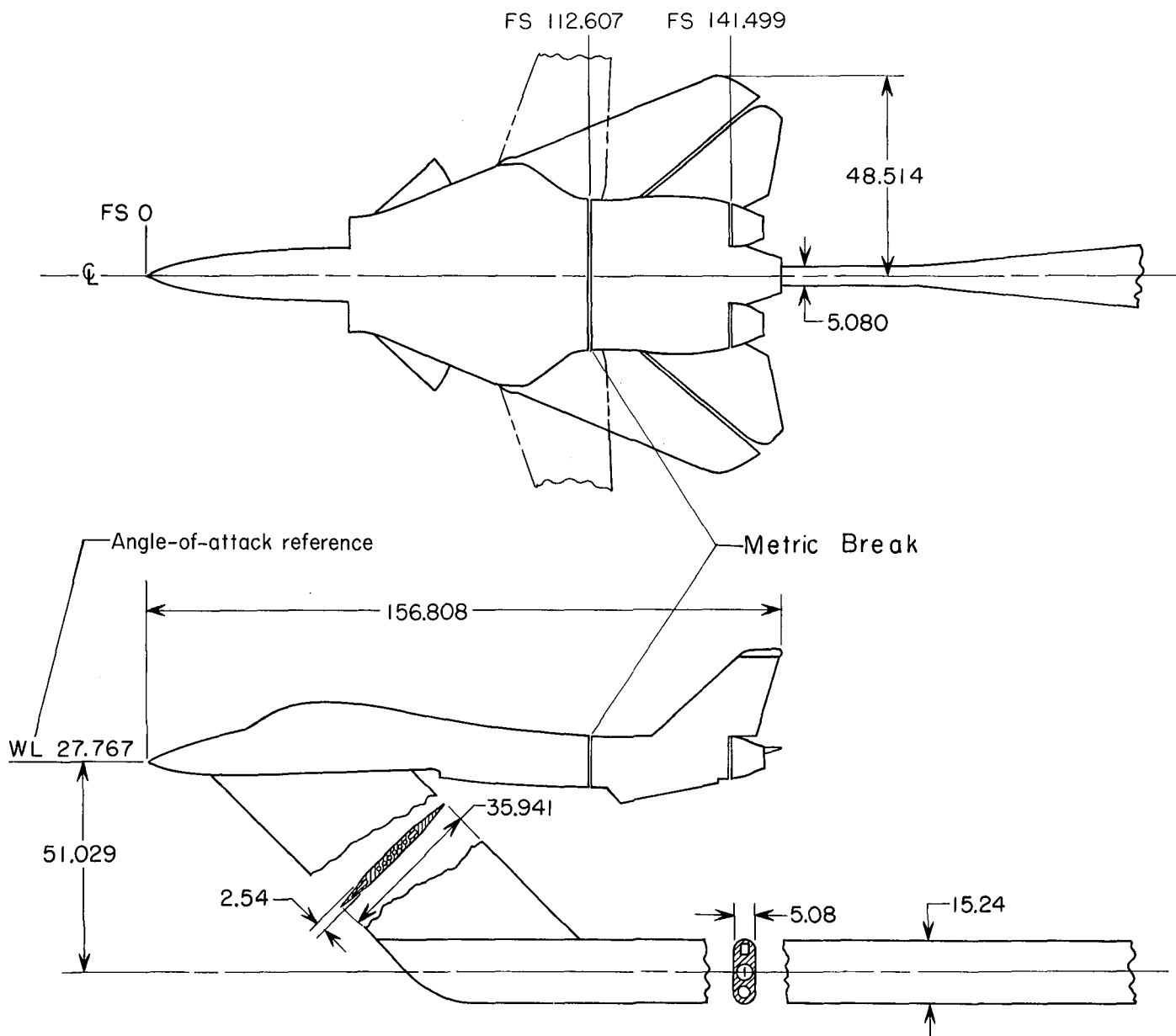
(b) Geometric details of model support.

Figure 2.- Concluded.
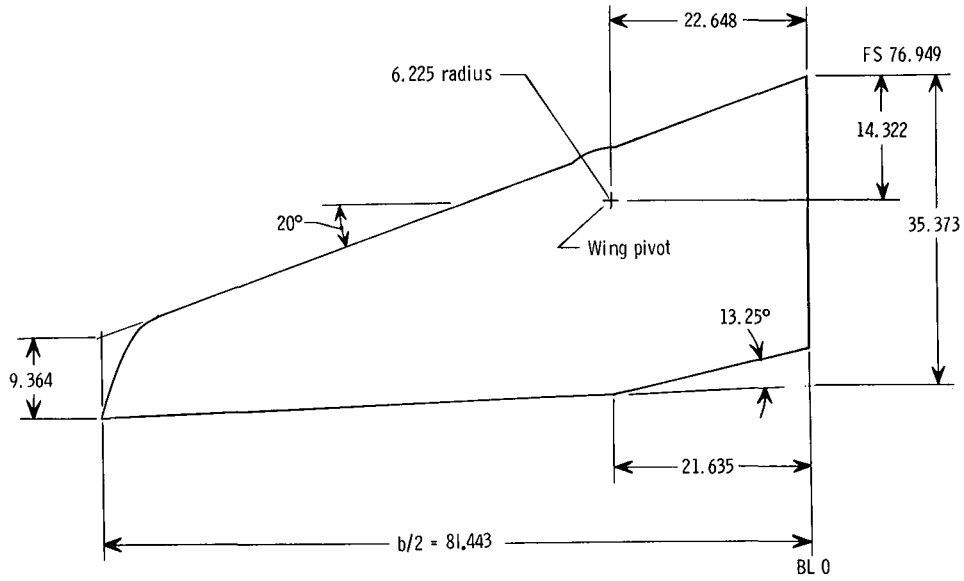
(a) Wing.
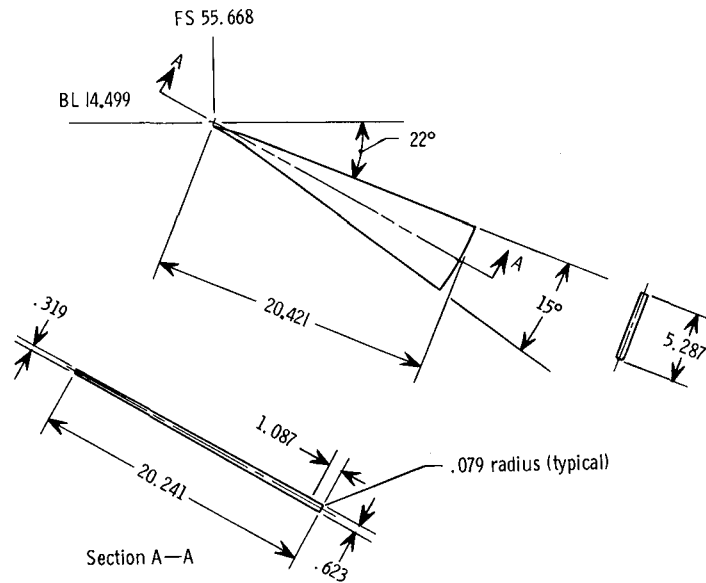
(b) Glove vane.

Figure 3.- Details of model. All dimensions are in centimeters
unless otherwise specified.
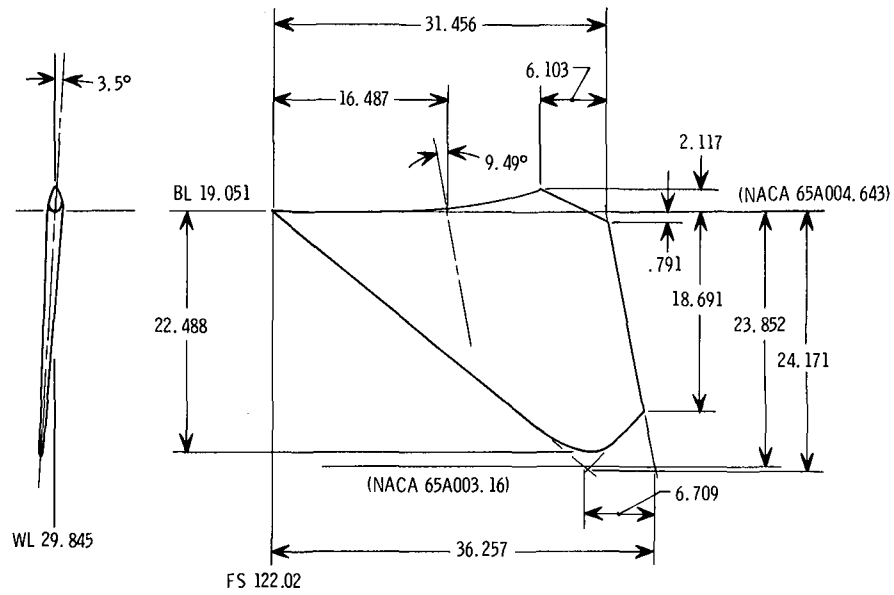
(c) Horizontal tail.
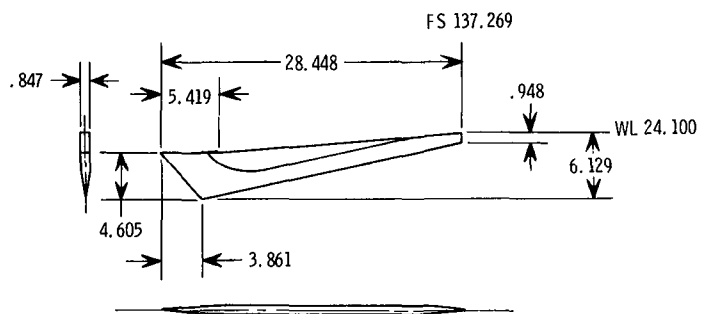
(d) Ventral fin.
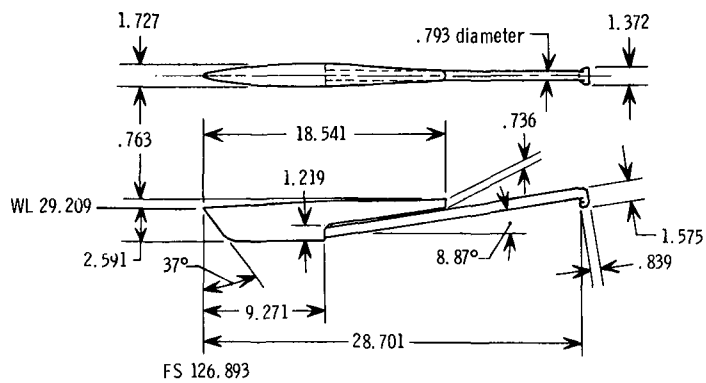
(e) Tail hook and fairing.

Figure 3.- Continued.

18

FS 156.808

32.387

9.312

(NACA 65A004.5)

WL 56.304

21.591

5°

21.671

26.033

BL 11.644
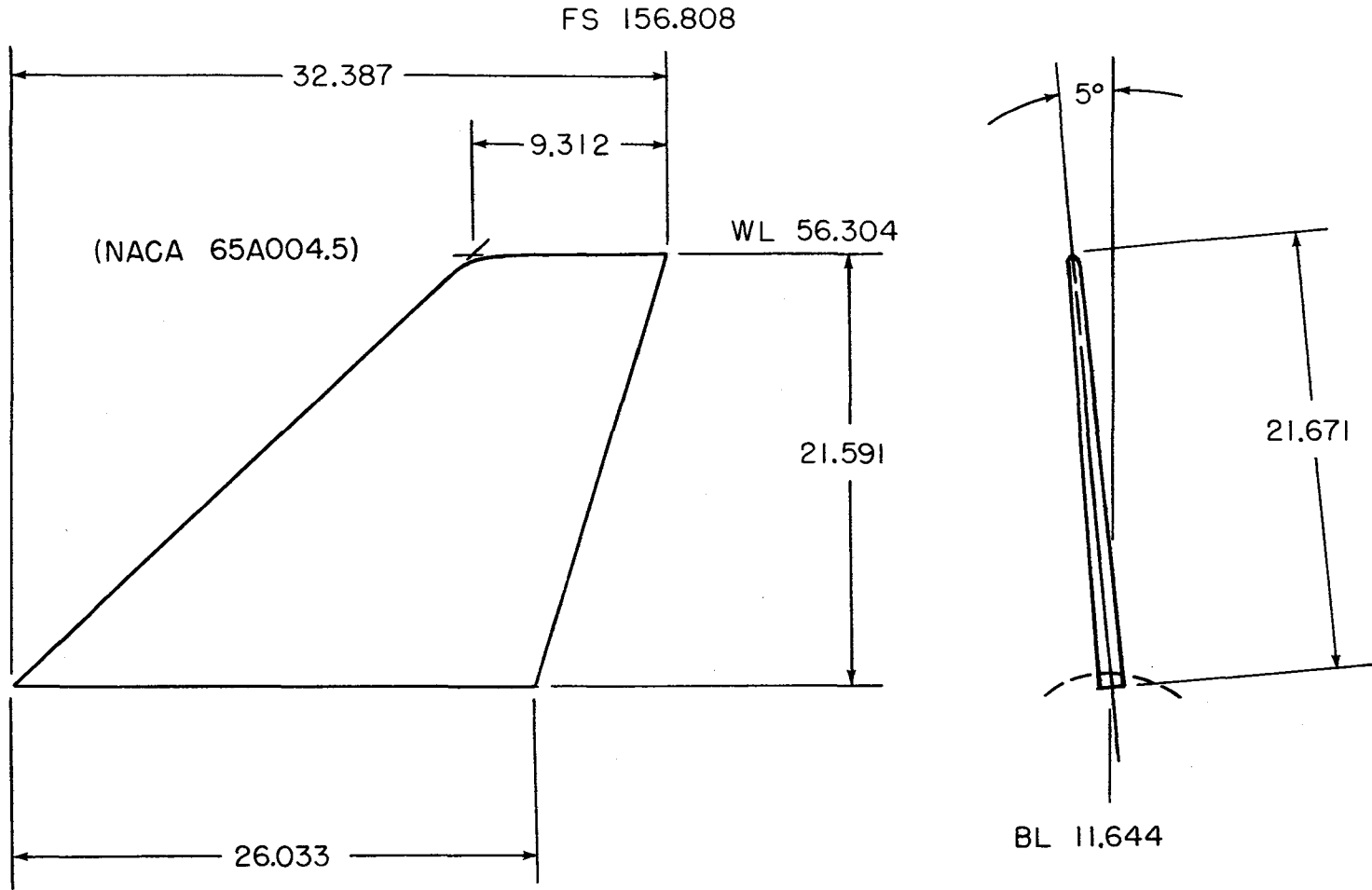
(f) Vertical tails. Left tail shown.

Figure 3.- Continued.

19

FS 149.648

FS 150.495

FS 150.707

FS 151.765

FS 152.823

FS 154.940

FS 155.575

13.653

6.414

A

A

BL 0

4.445

18.519

FS 137.050

WL 31.750
WL 31.221
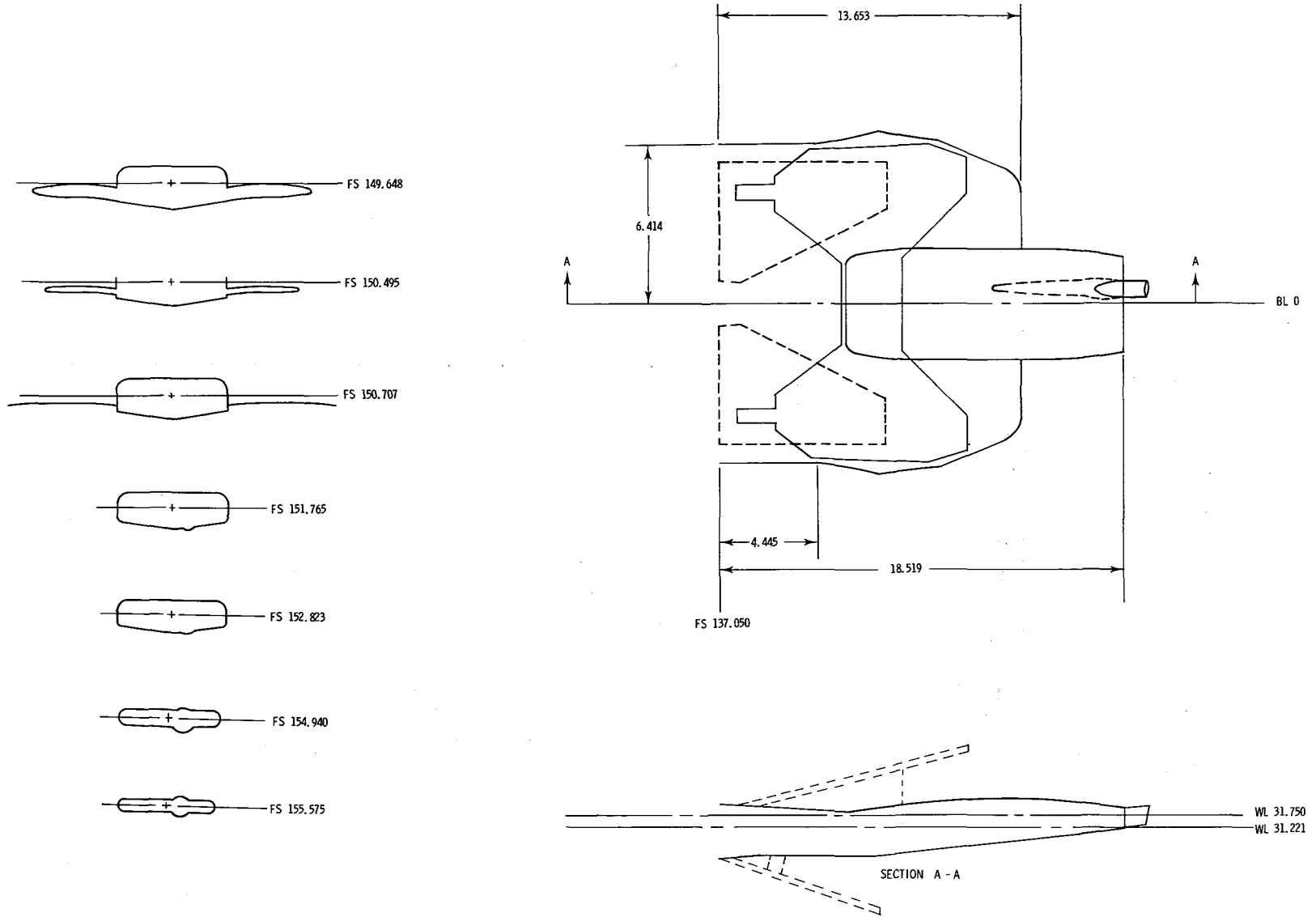
SECTION A - A

(g) Interfairing with cross sections and position of speed brakes.

Figure 3.- Concluded.
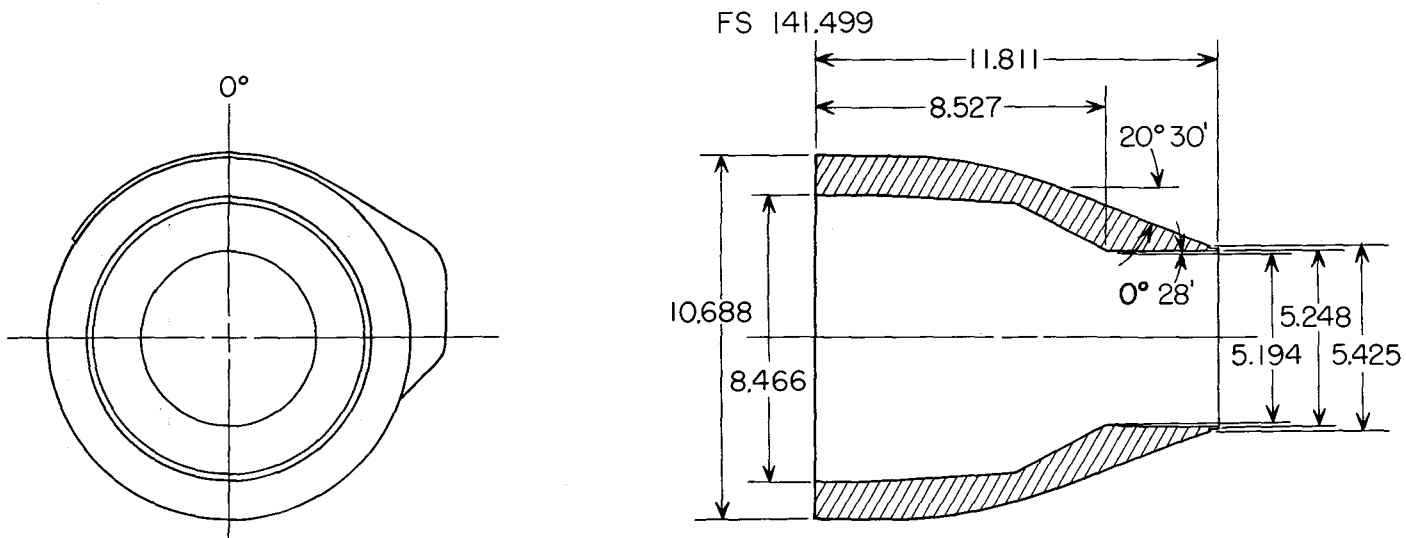
(a) Cruise power-setting nozzles installed at aft position.

Figure 4.- Sketches of nozzle configurations. All linear dimensions are given in centimeters.
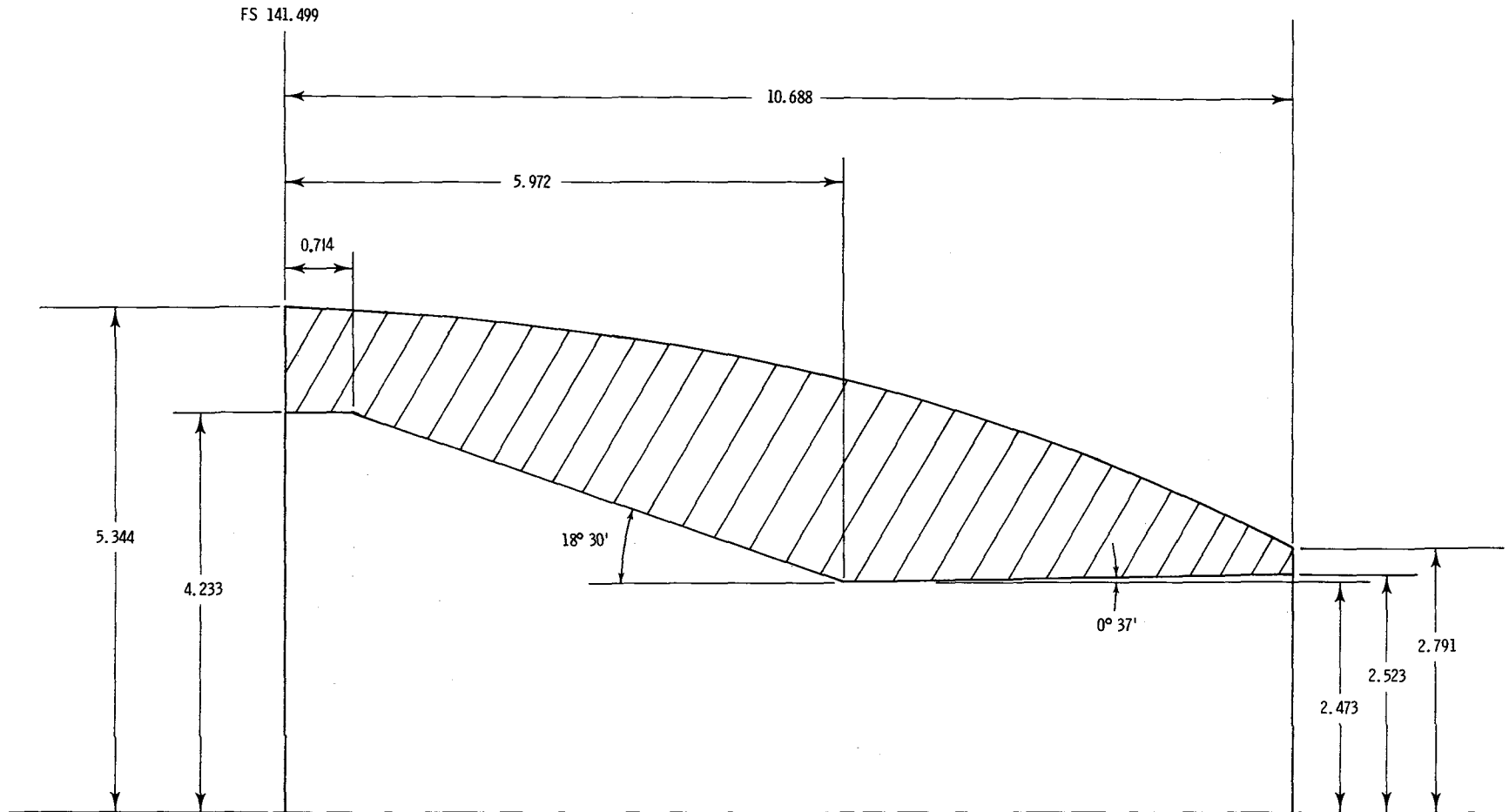
(b) Cruise power-setting nozzles installed at intermediate position.

Figure 4.- Continued.
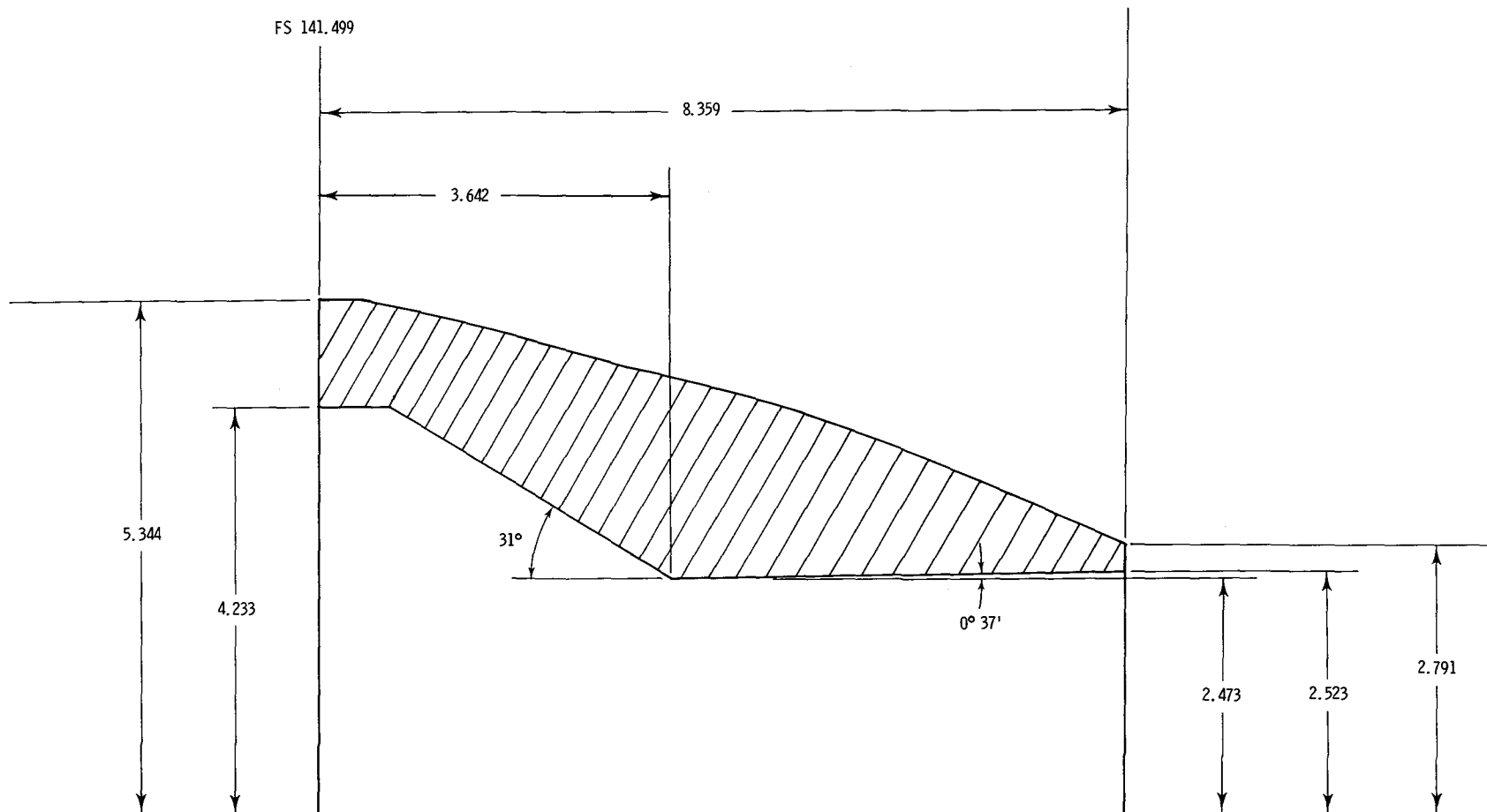
(c) Cruise power-setting nozzles installed at forward position.

Figure 4.- Continued.
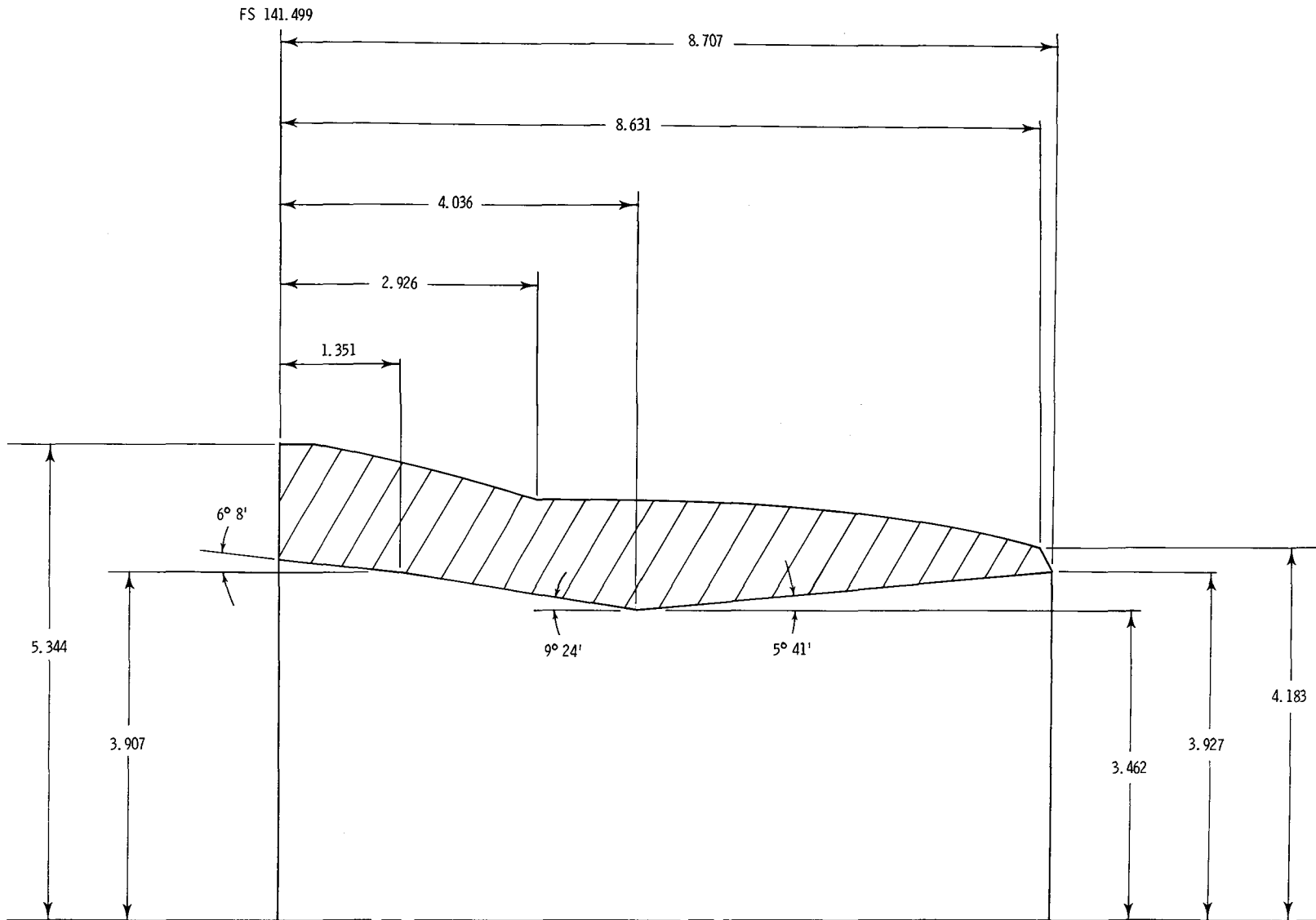
(d) A/B power-setting nozzles installed at forward position.

Figure 4.- Concluded.
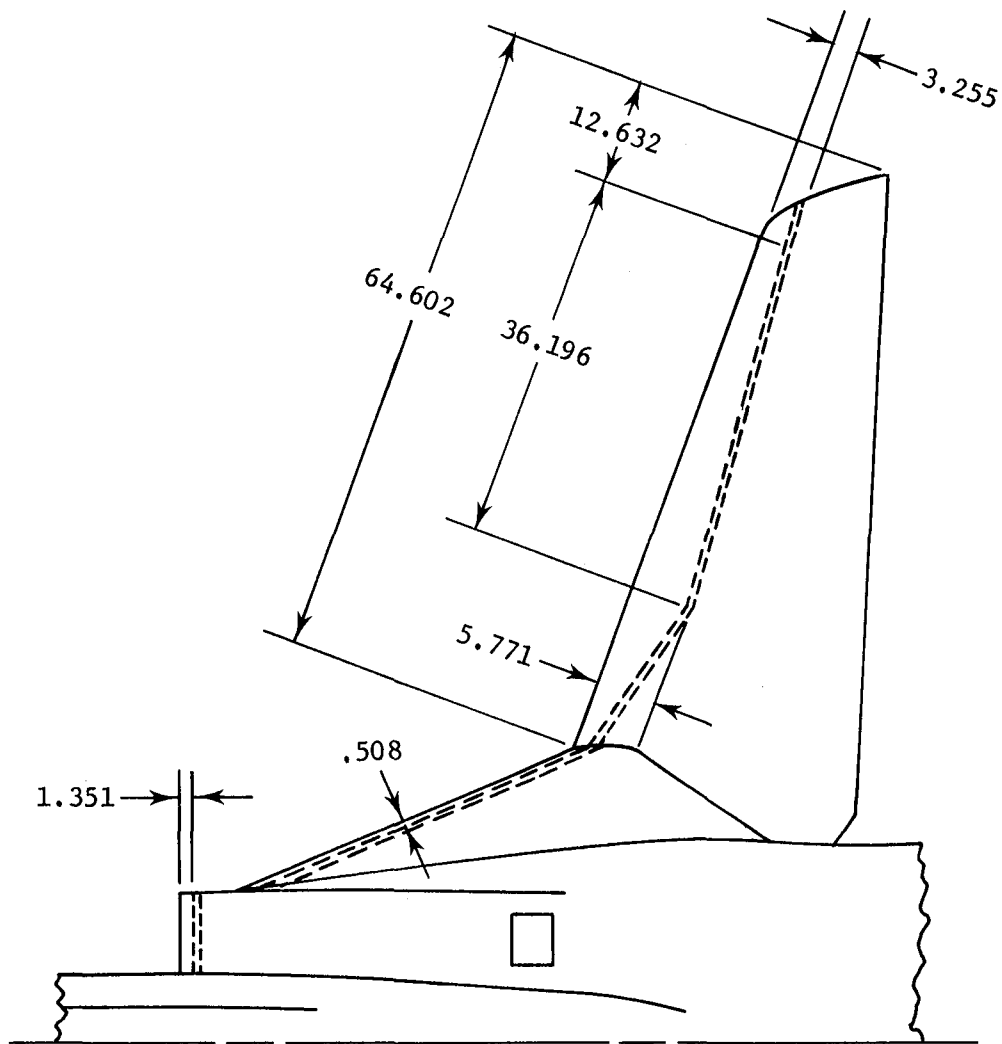
Figure 5.- Sketch showing transition-strip location on upper wing
surface for configurations with $\Lambda = 22°$. All dimensions are
in centimeters.
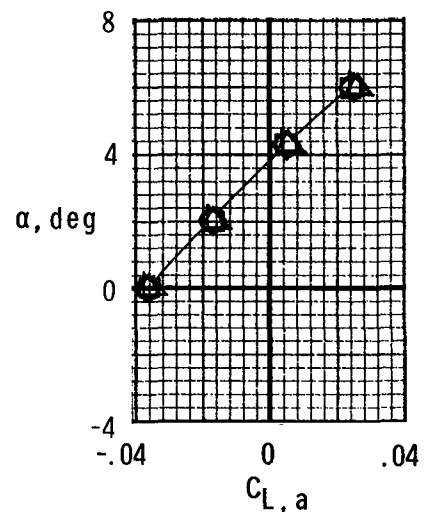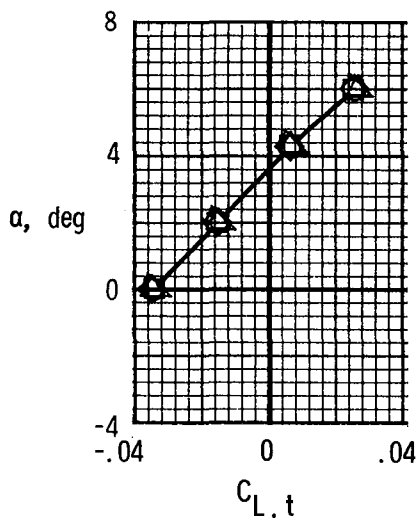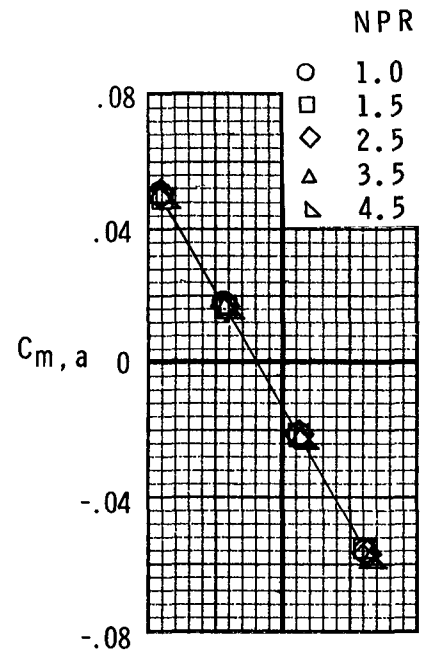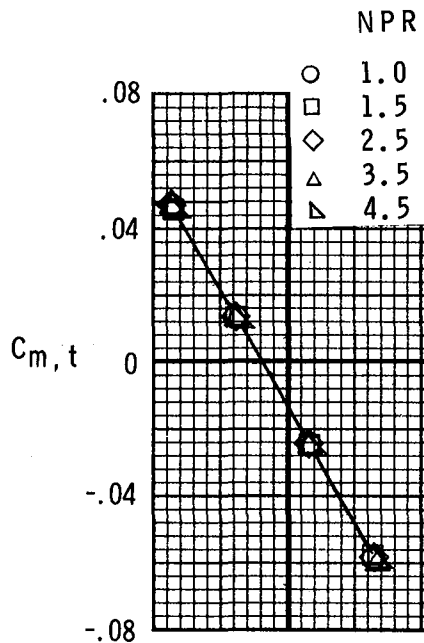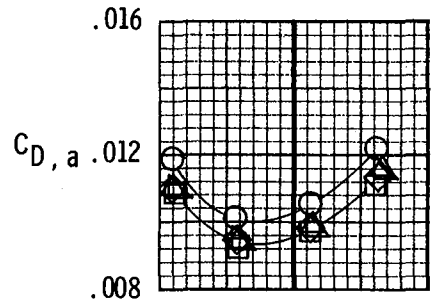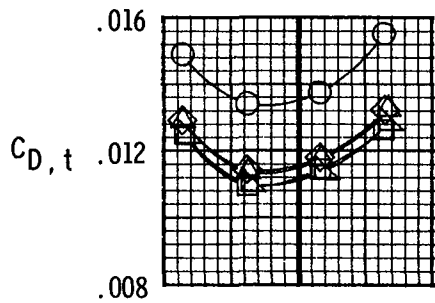
(a) Afterbody-nozzle characteristics.
M = 0.7; Λ = 22°.

(b) Afterbody characteristics.
M = 0.7; Λ = 22°.

Figure 6.- Effect of nozzle pressure ratio (NPR) on afterbody-nozzle aerodynamic characteristics for configuration with cruise nozzles in aft position.
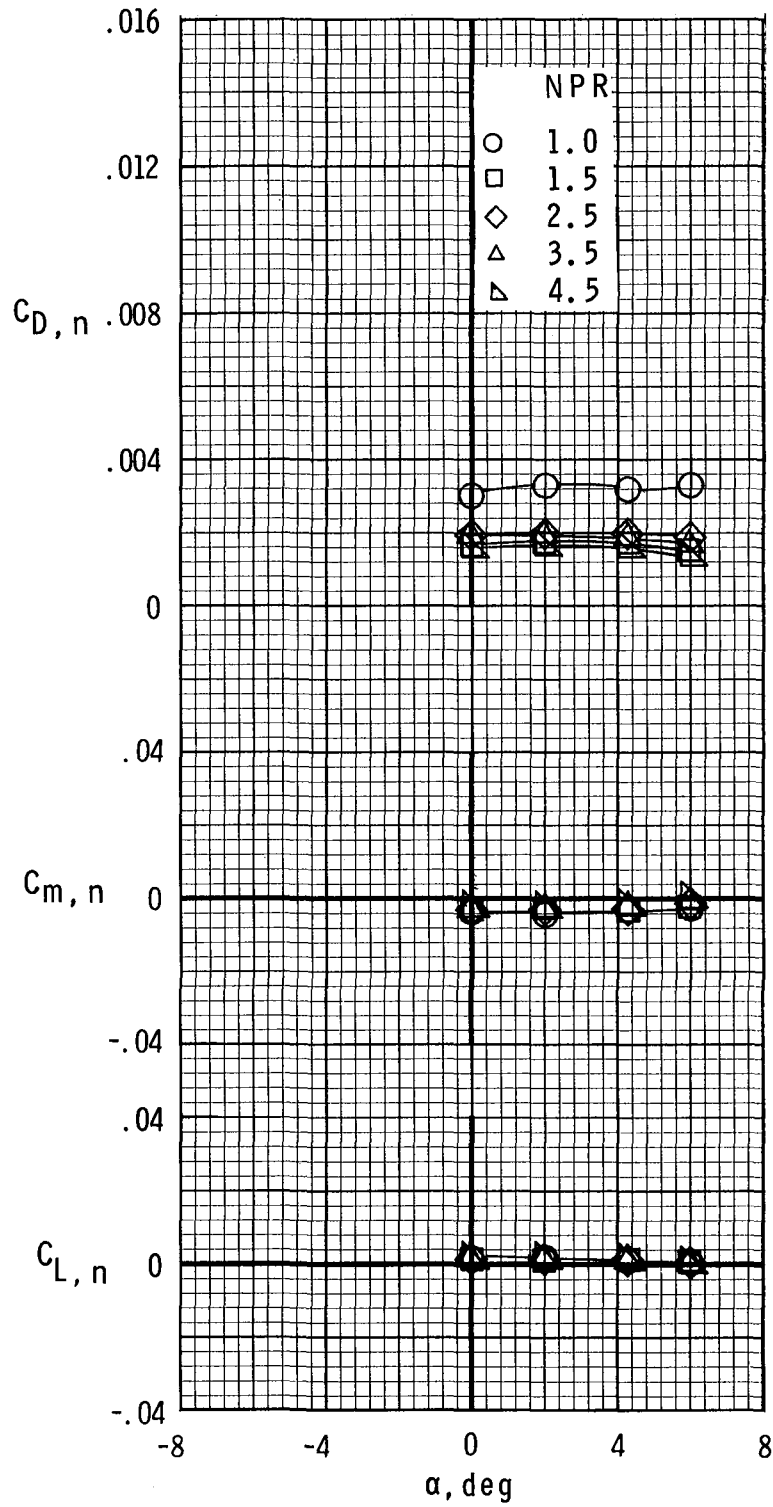
(c) Nozzle characteristics.
M = 0.7; Λ = 22°.
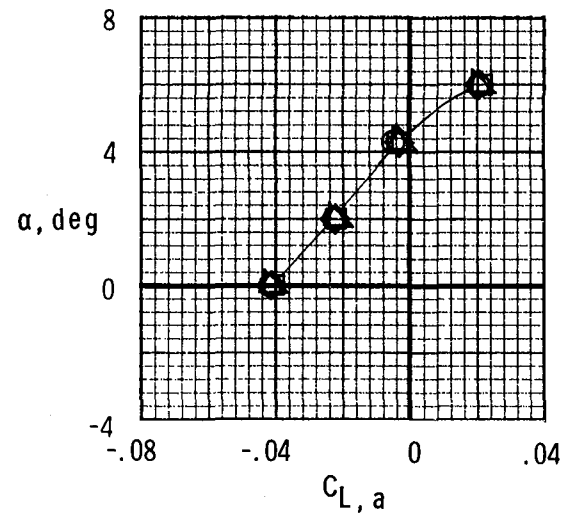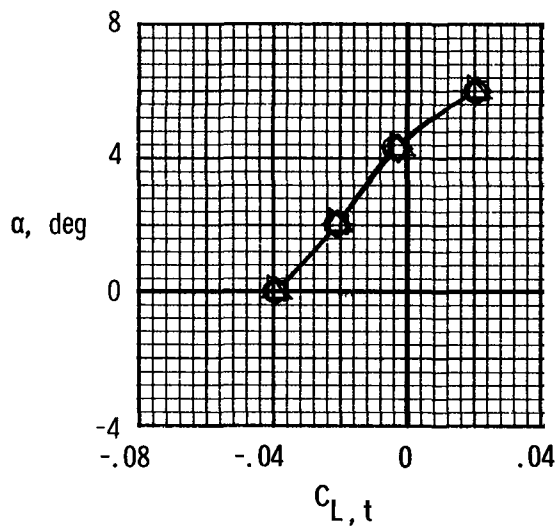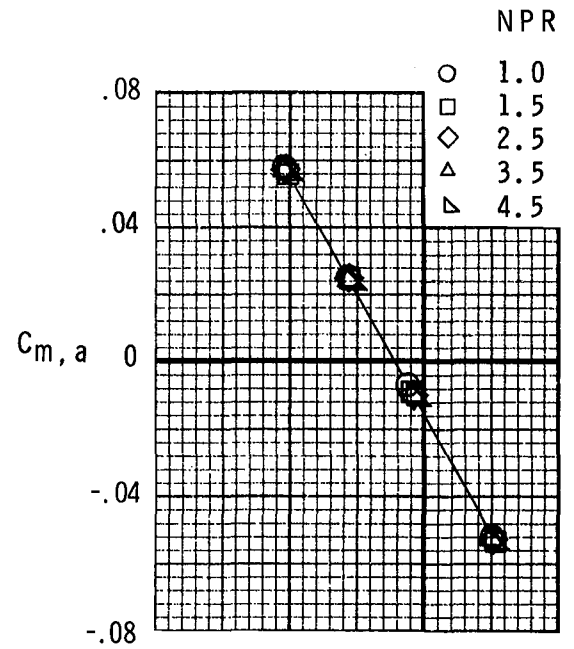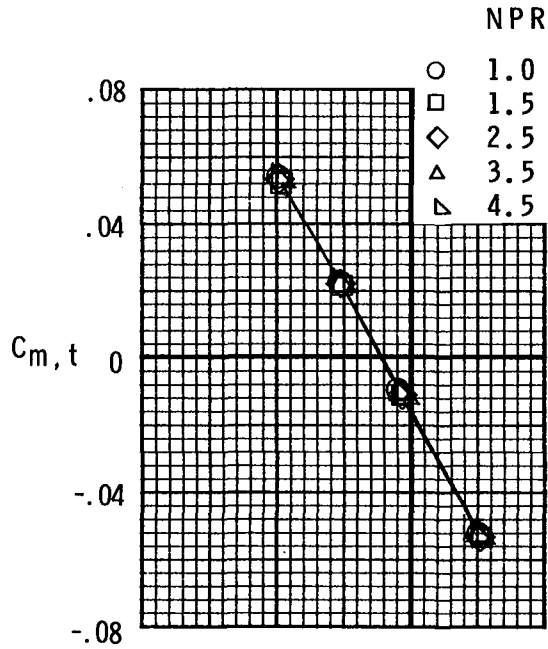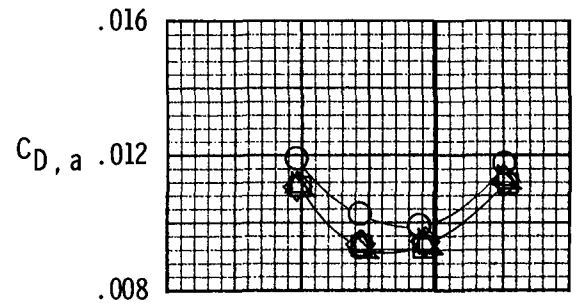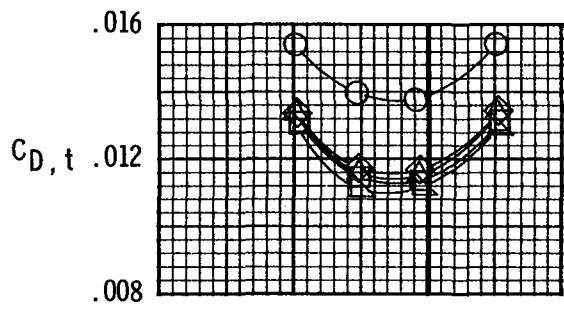
Figure 6.- Continued.

(d) Afterbody-nozzle characteristics.
M = 0.8; Λ = 22°.

(e) Afterbody characteristics.
M = 0.8; Λ = 22°.

Figure 6.- Continued.
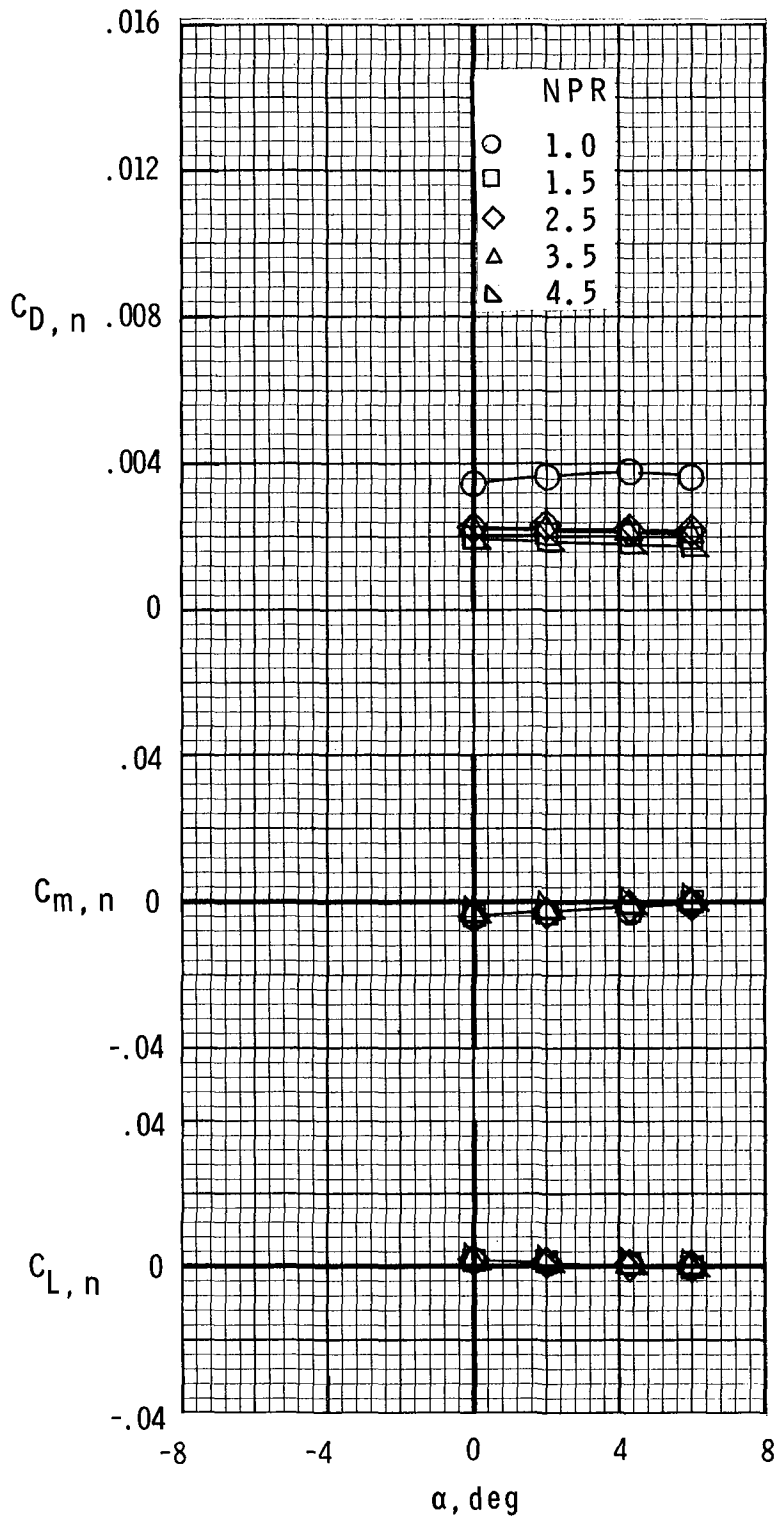
(f) Nozzle characteristics.
M = 0.8;   Λ = 22°.
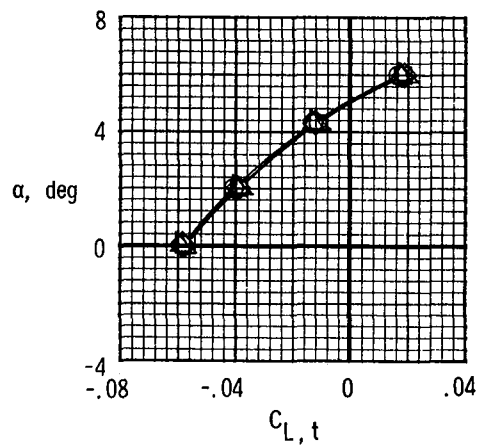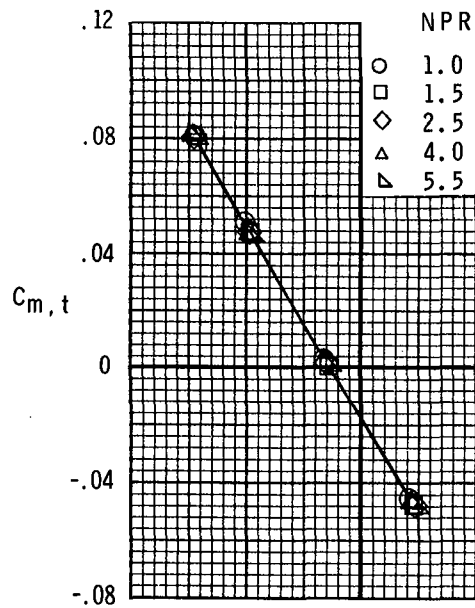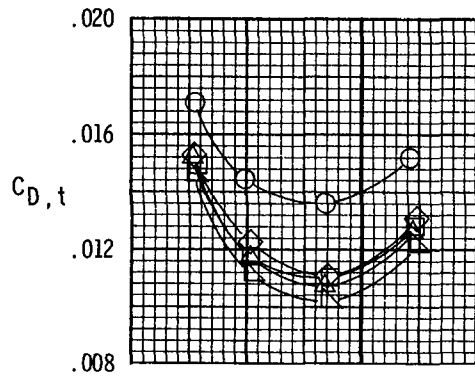
Figure 6.- Continued.

(g) Afterbody-nozzle characteristics.
M = 0.9; Λ = 22°.
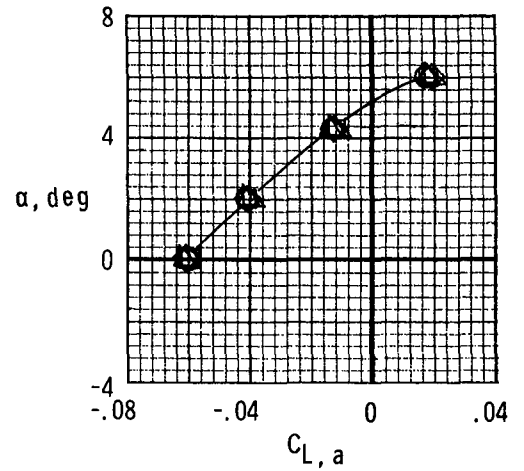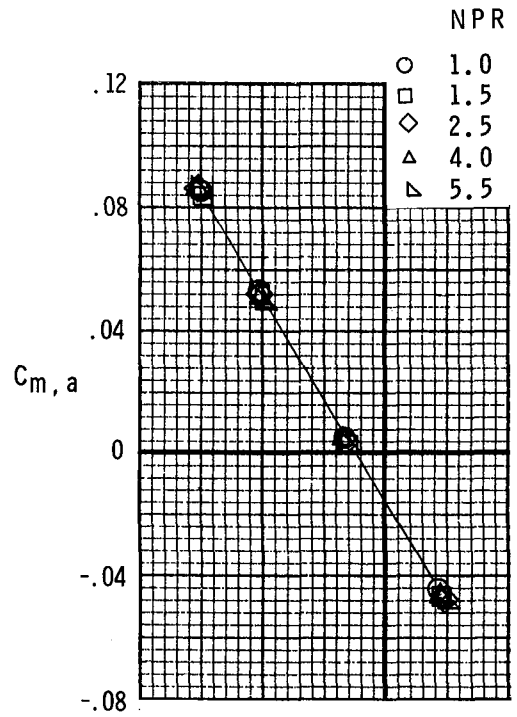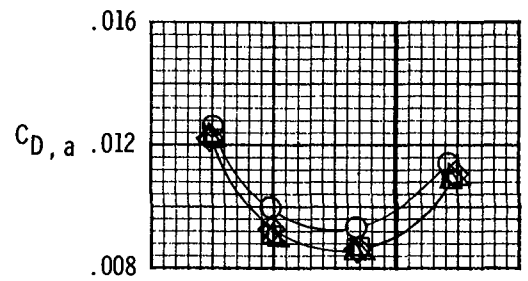
(h) Afterbody characteristics.
M = 0.9; Λ = 22°.

Figure 6.- Continued.
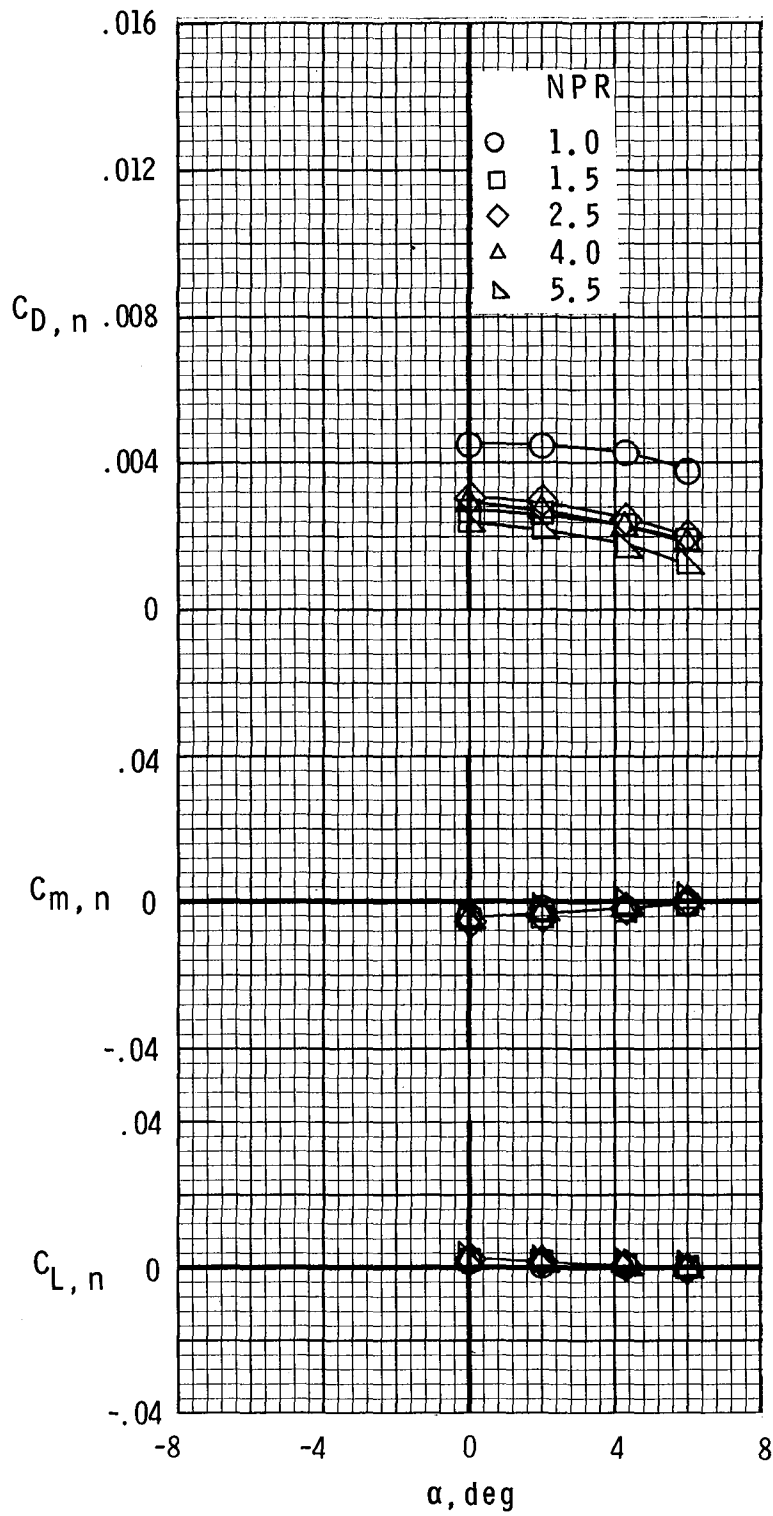
(i) Nozzle characteristics.
M = 0.9;   Λ = 22°.
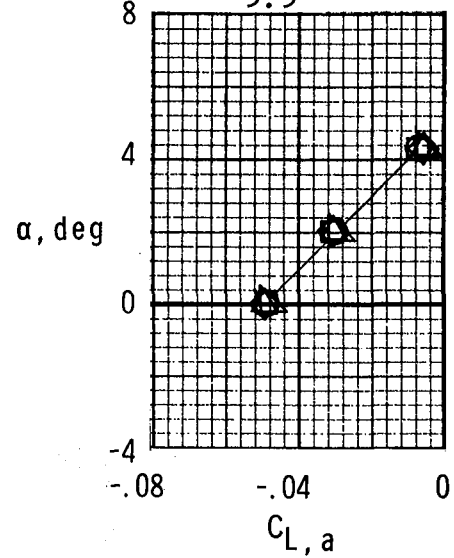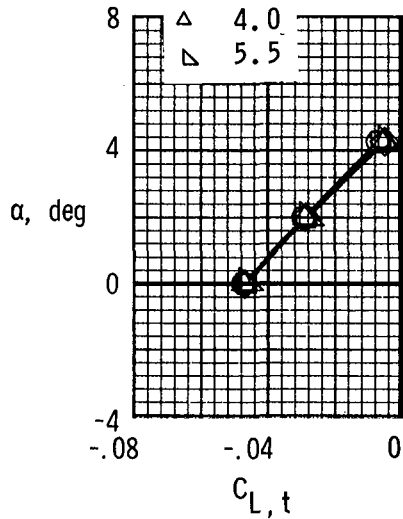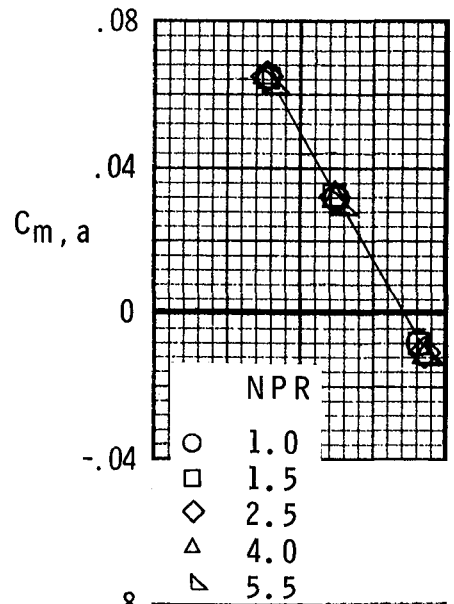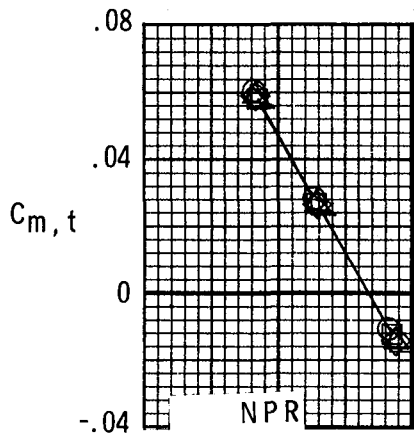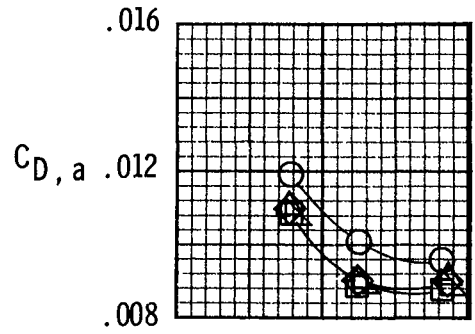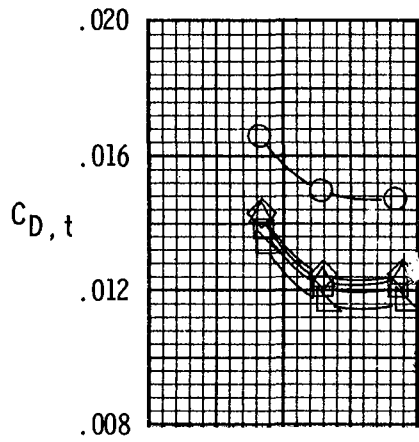
Figure 6.- Continued.

(j) Afterbody-nozzle characteristics.
M = 0.9;   Λ = 68°.

(k) Afterbody characteristics.
M = 0.9;   Λ = 68°.

Figure 6.- Continued.
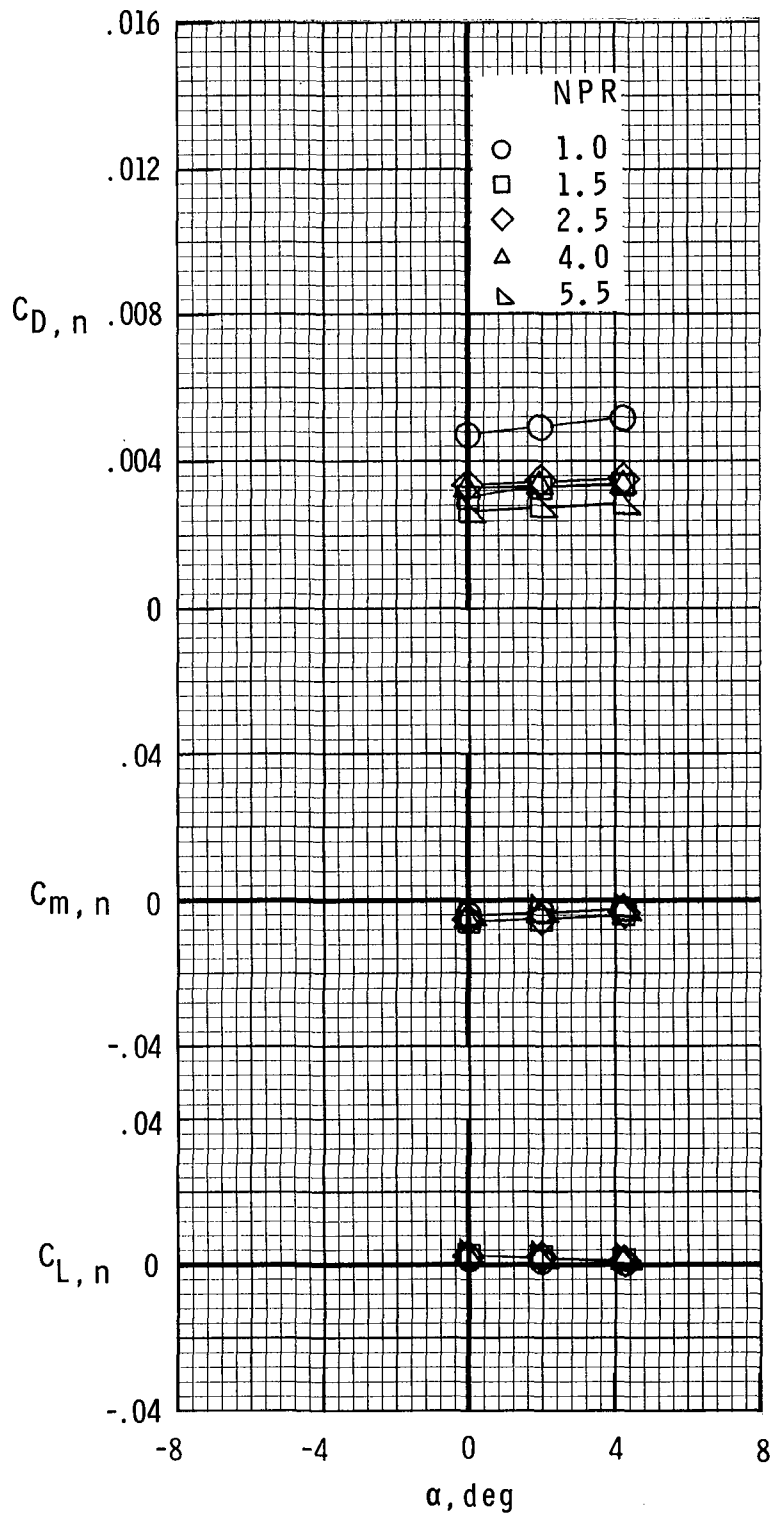
(1) Nozzle characteristics.
M = 0.9;   Λ = 68°.

Figure 6.- Continued.
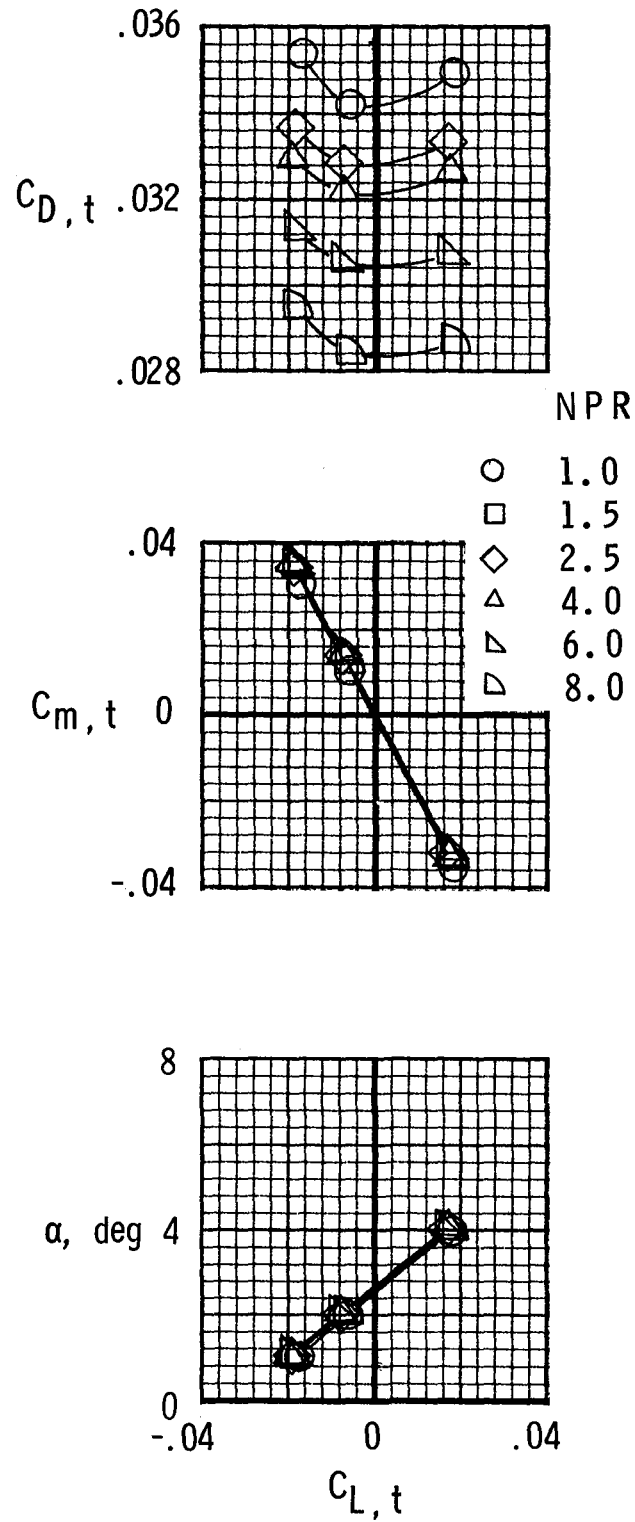
(m) Afterbody-nozzle characteristics.
M = 1.15;   Λ = 68°.
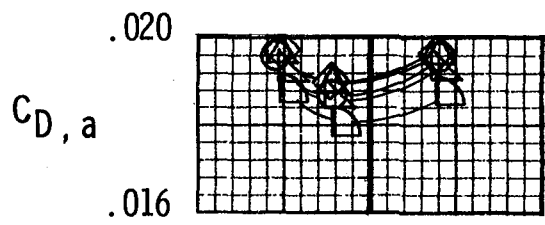
Figure 6.- Continued.
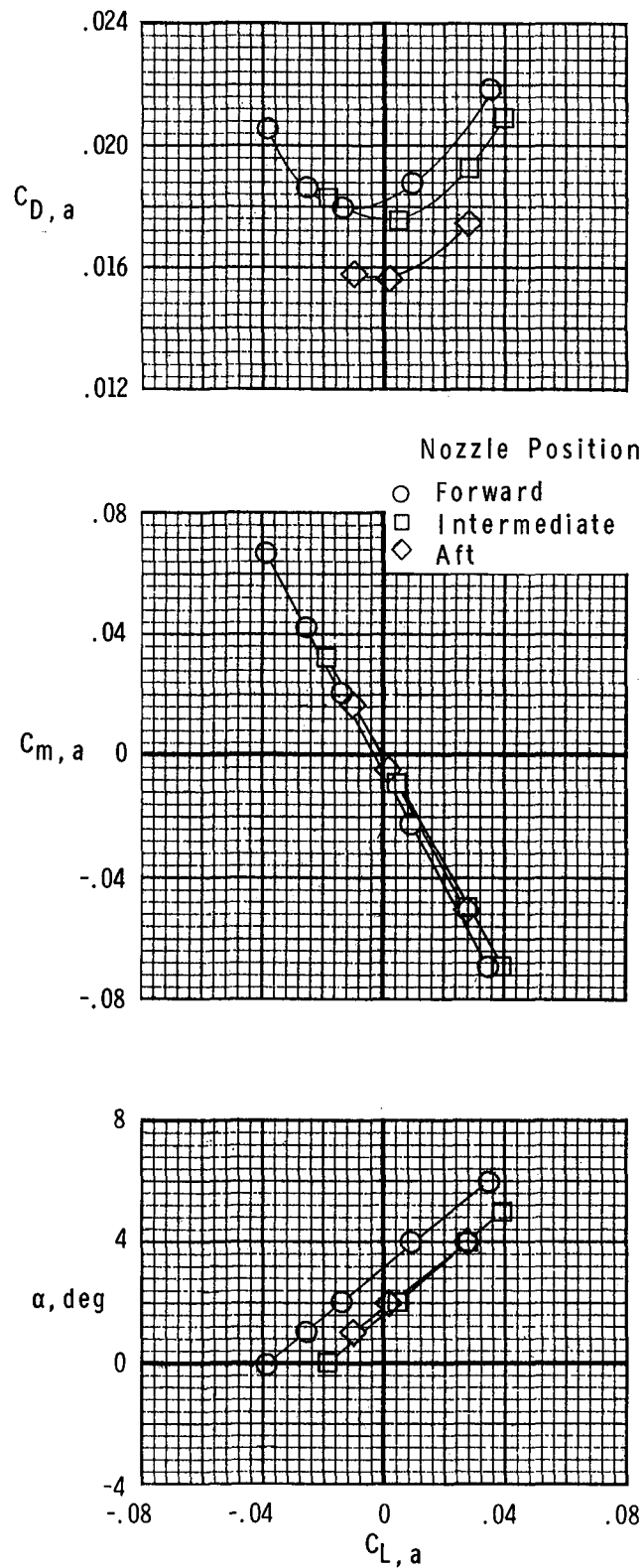
(n) Afterbody characteristics.
M = 1.15;   Λ = 68°.
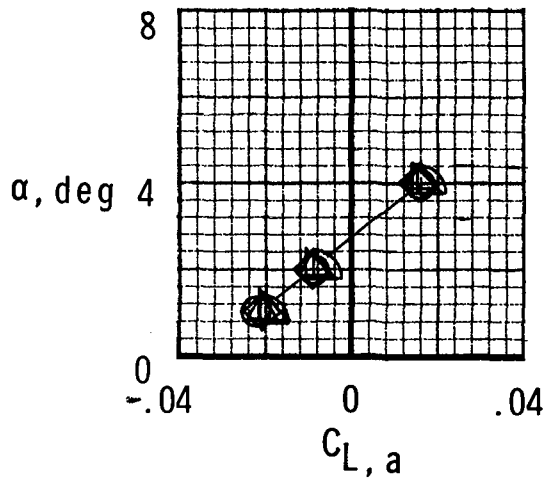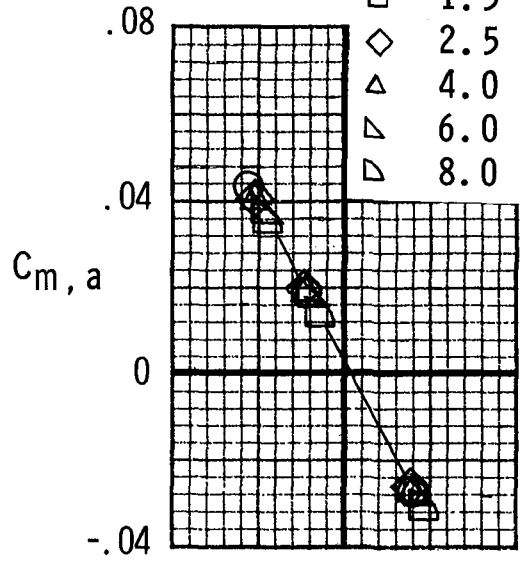
Figure 6.- Continued.
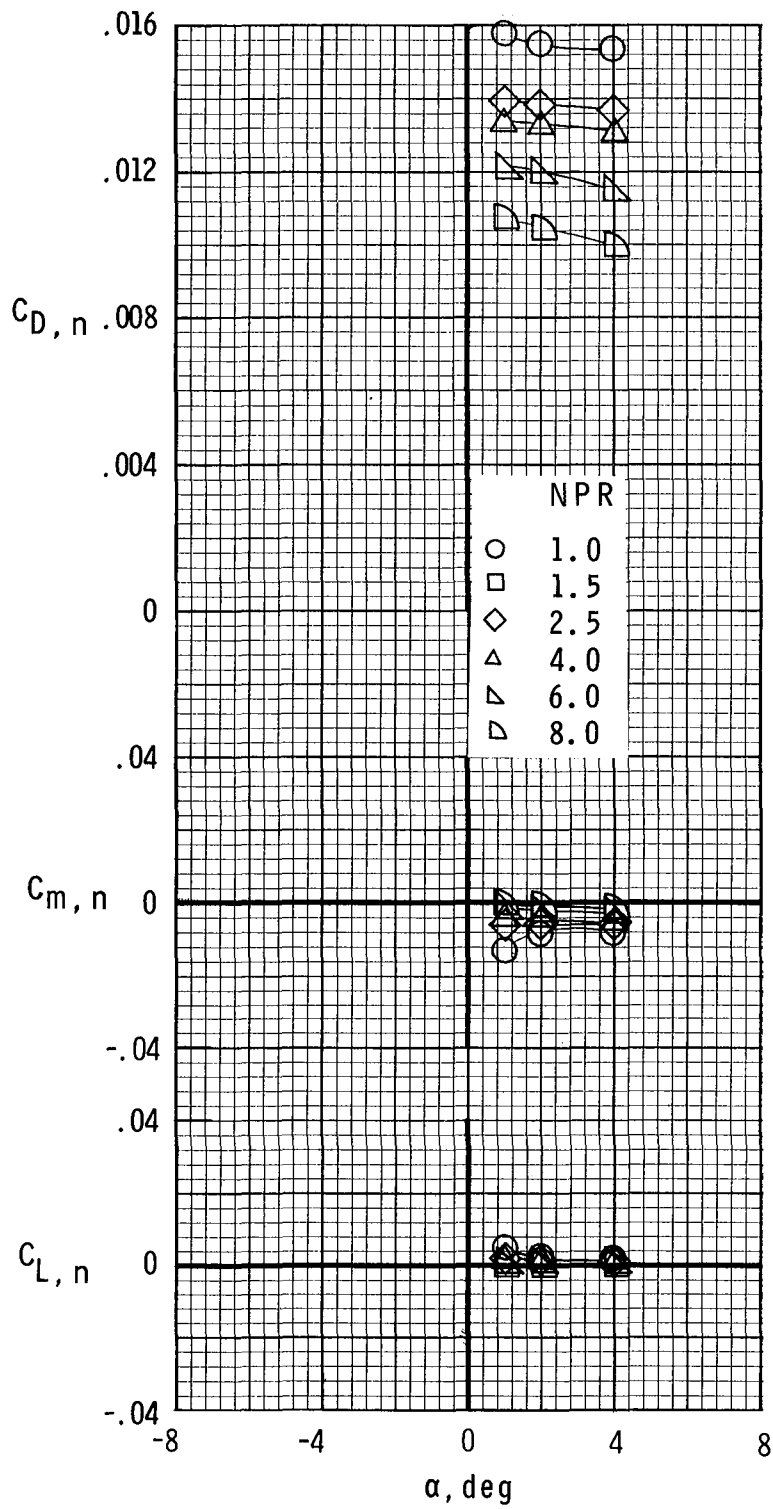
(o) Nozzle characteristics.
M = 1.15; Λ = 68°.
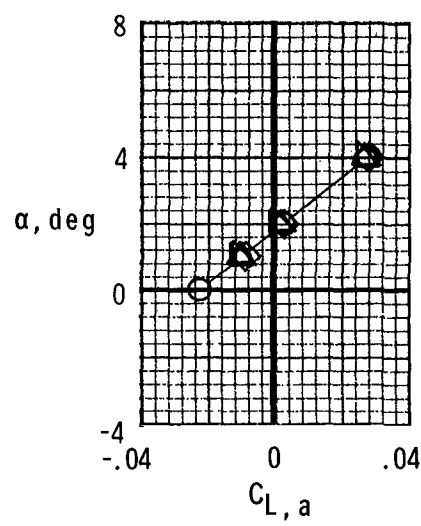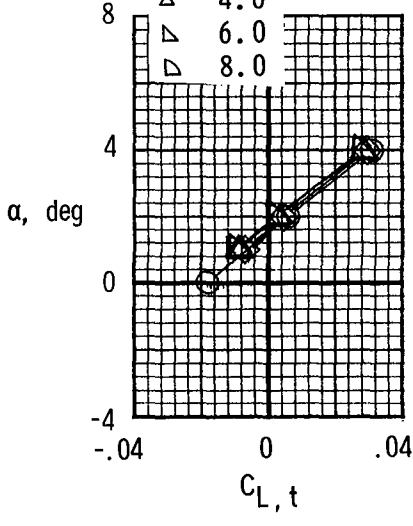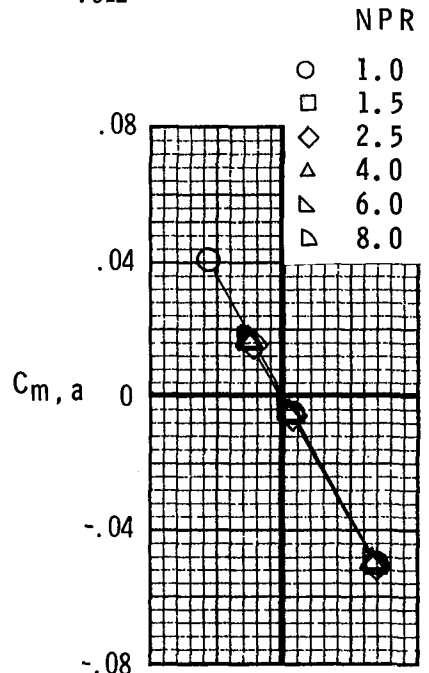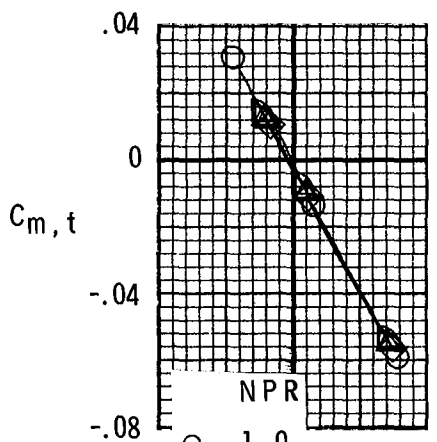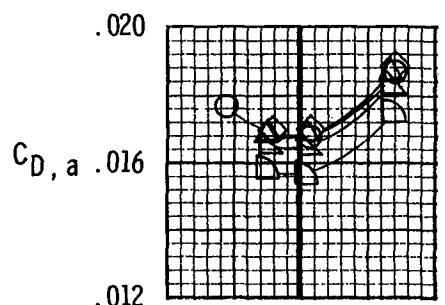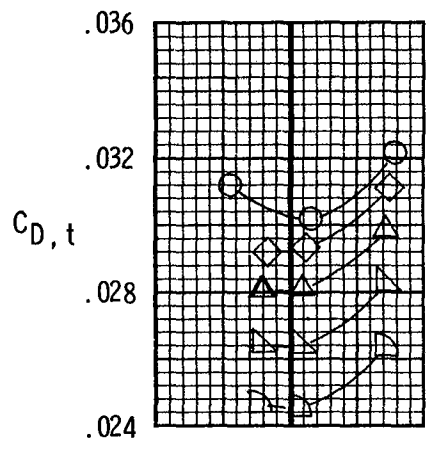
Figure 6.- Continued.

(p) Afterbody-nozzle characteristics.
M = 1.25; Λ = 68°.

(q) Afterbody characteristics.
M = 1.25; Λ = 68°.

Figure 6.- Continued.
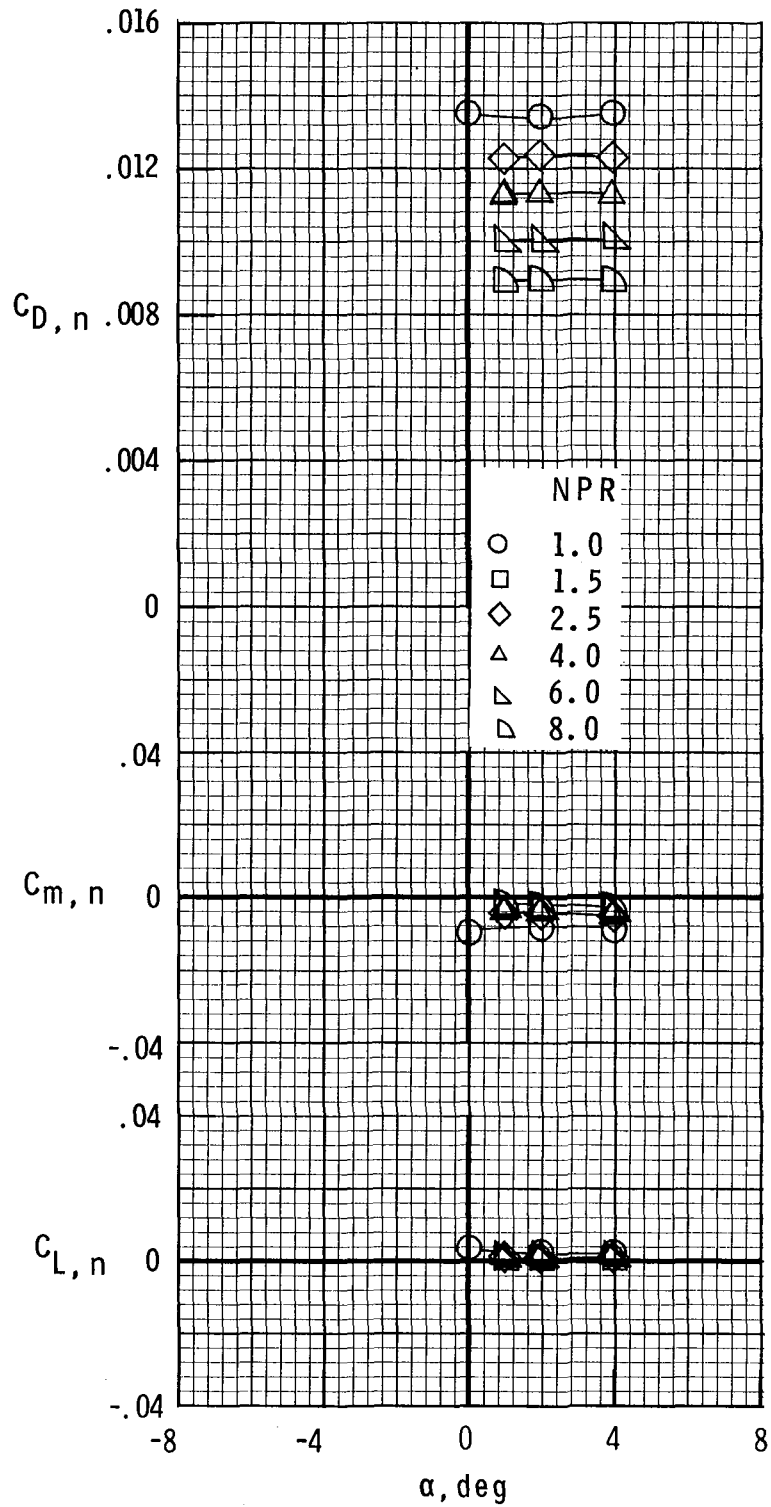
(r) Nozzle characteristics.
M = 1.25;   Λ = 68°.

Figure 6.- Concluded.
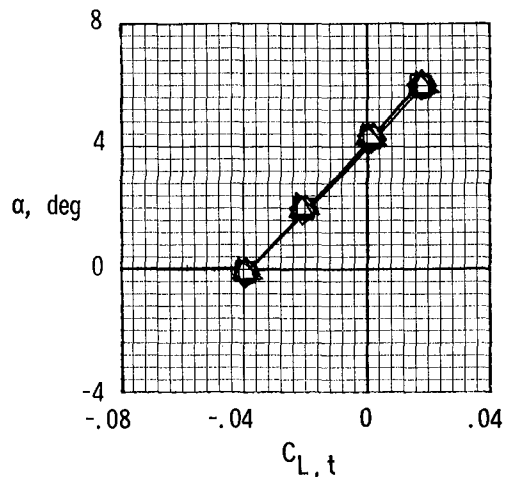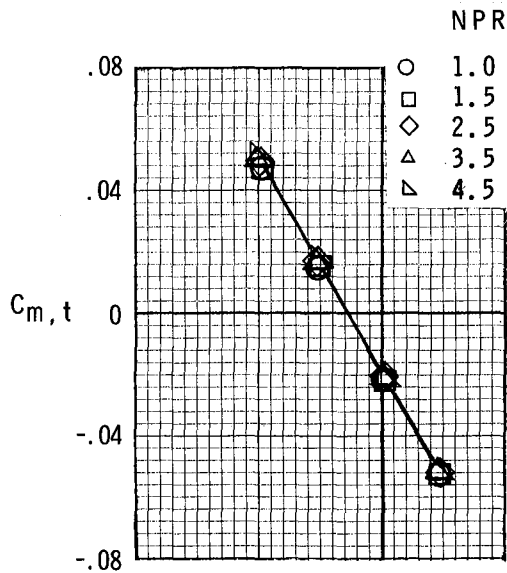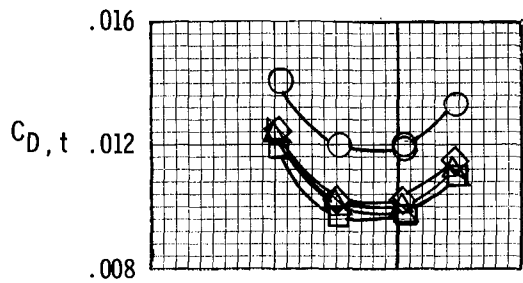
(a) Afterbody-nozzle characteristics.
M = 0.7; Λ = 22°.
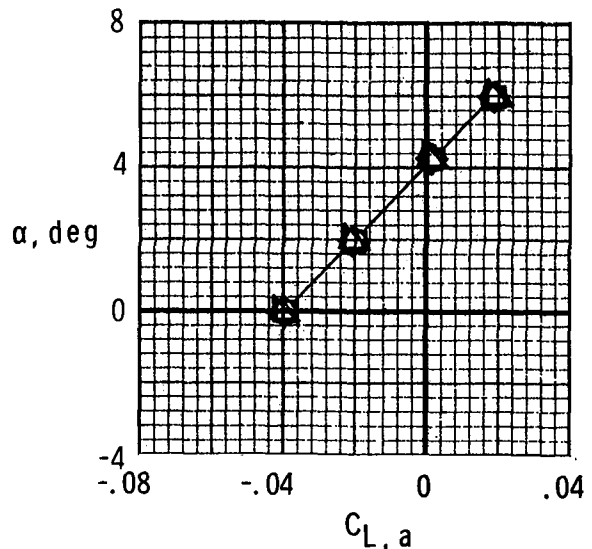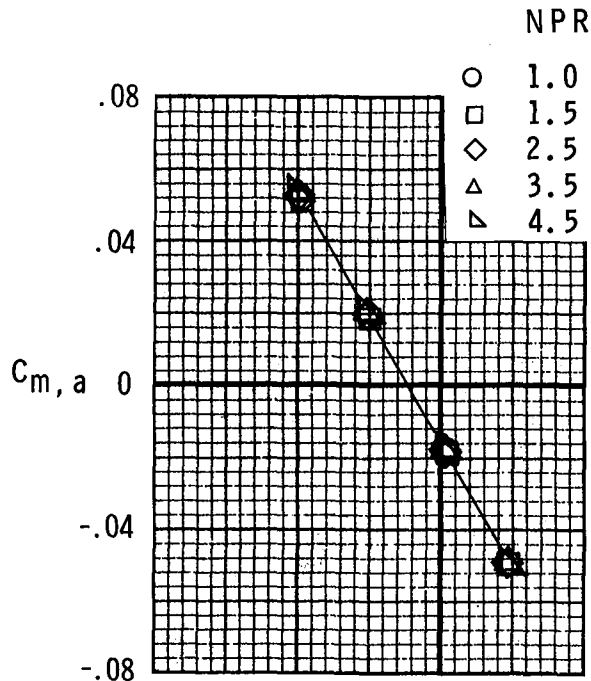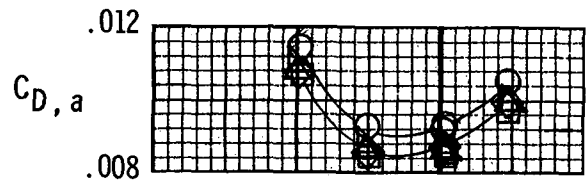
(b) Afterbody characteristics.
M = 0.7; Λ = 22°.

Figure 7.- Effect of nozzle pressure ratio (NPR) on afterbody-nozzle aerodynamic characteristics for configuration with cruise nozzles in intermediate position.
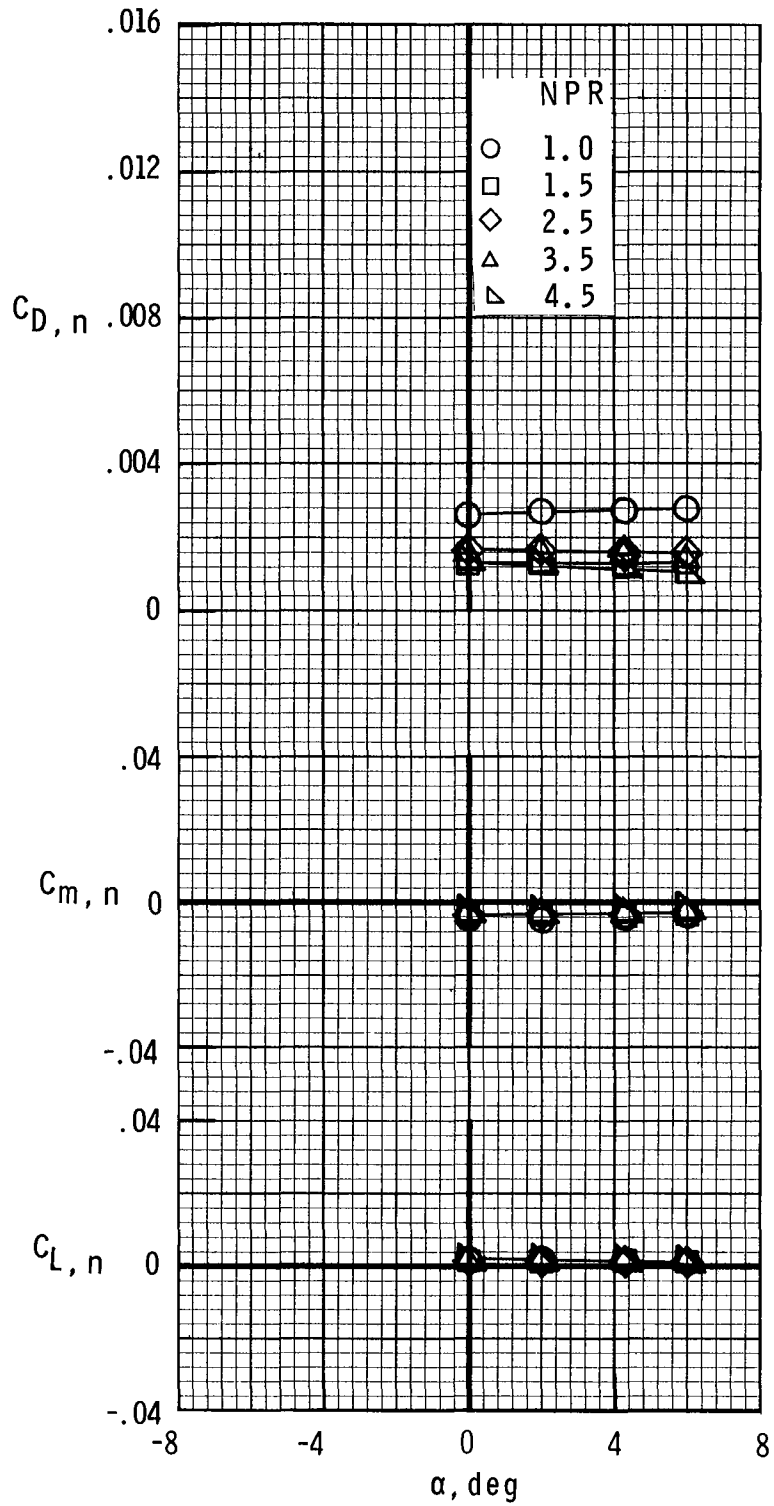
(c) Nozzle characteristics.
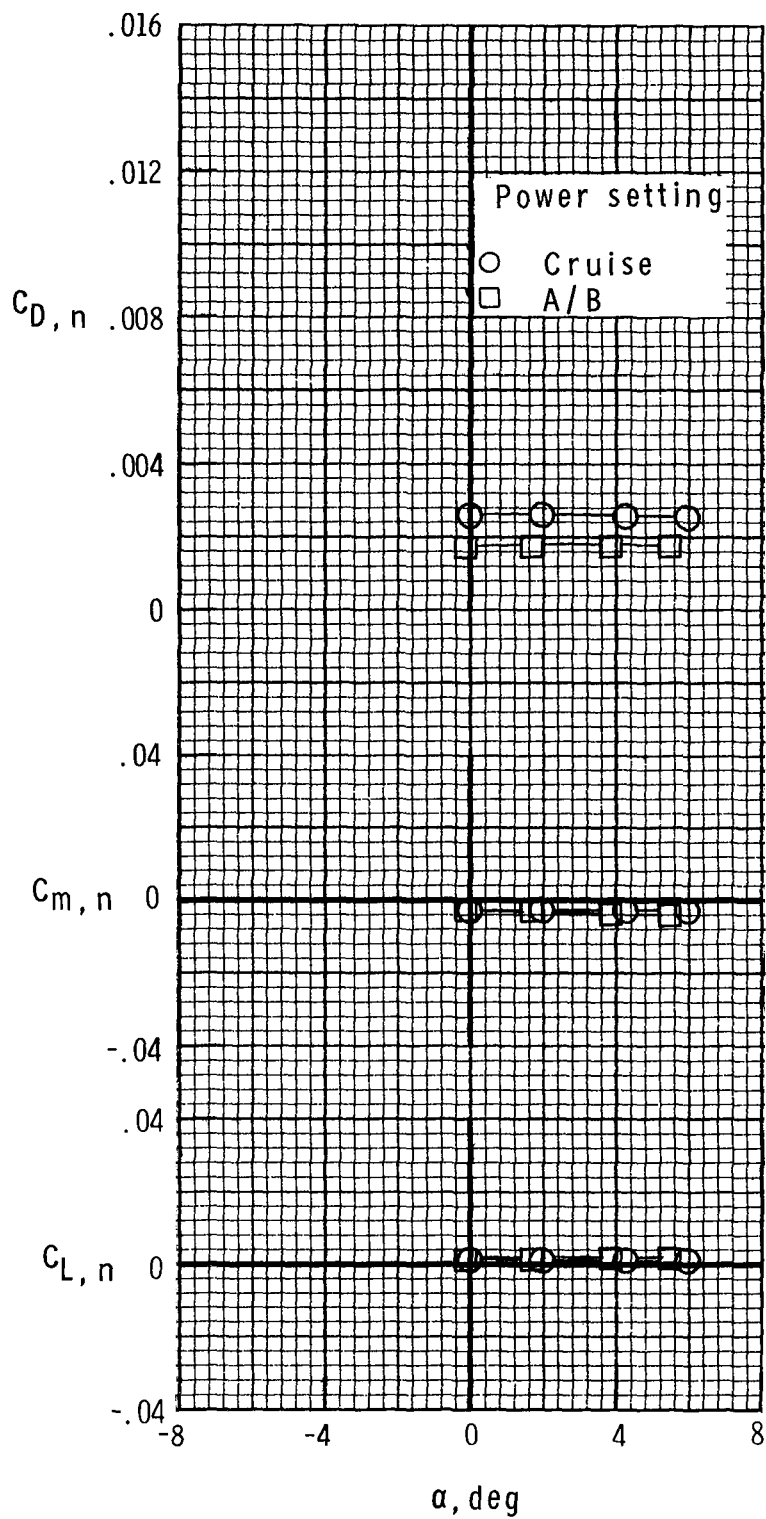M = 0.7; Λ = 22°.
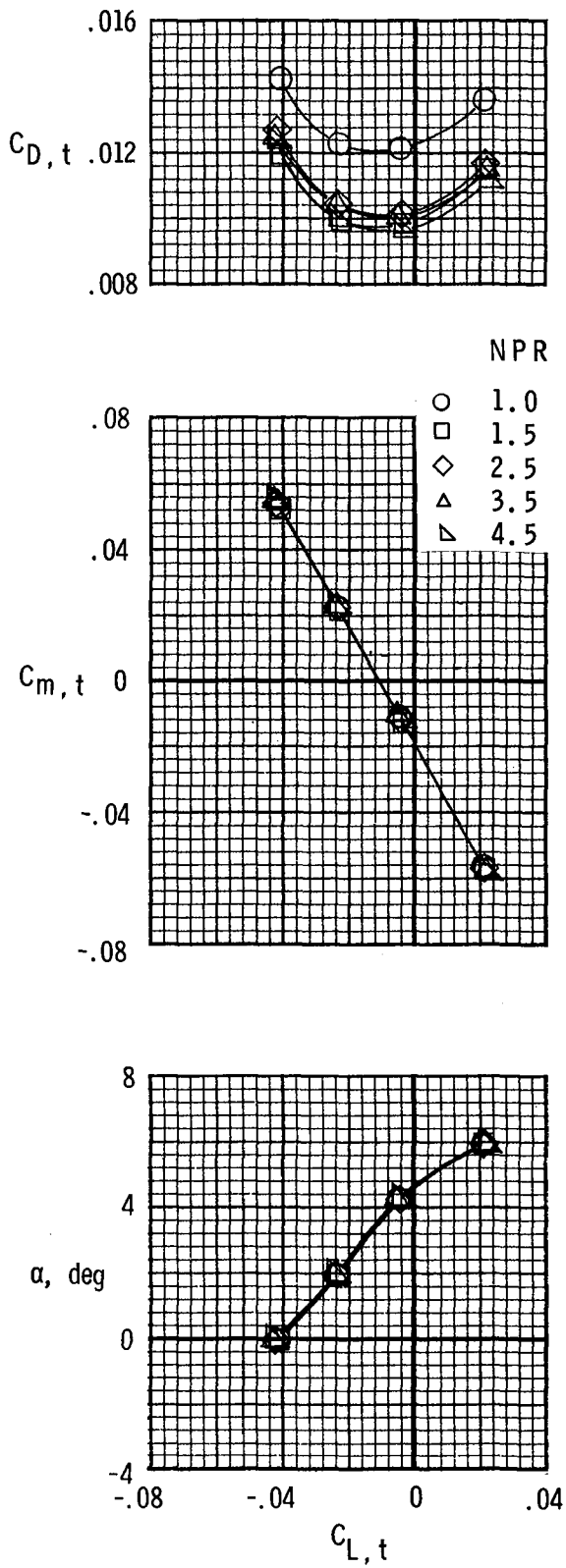
Figure 7.- Continued.

(d) Afterbody-nozzle characteristics.
M = 0.8; Λ = 22°.
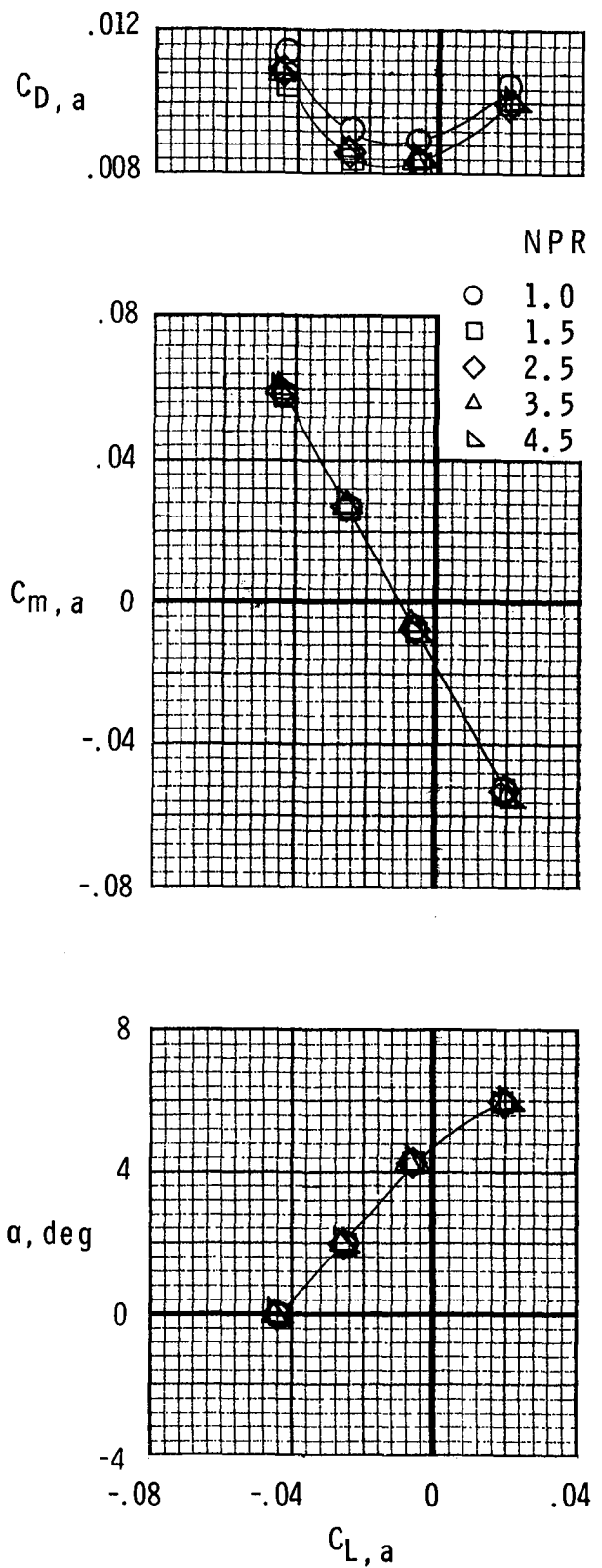
(e) Afterbody characteristics.
M = 0.8; Λ = 22°.

Figure 7.- Continued.

41
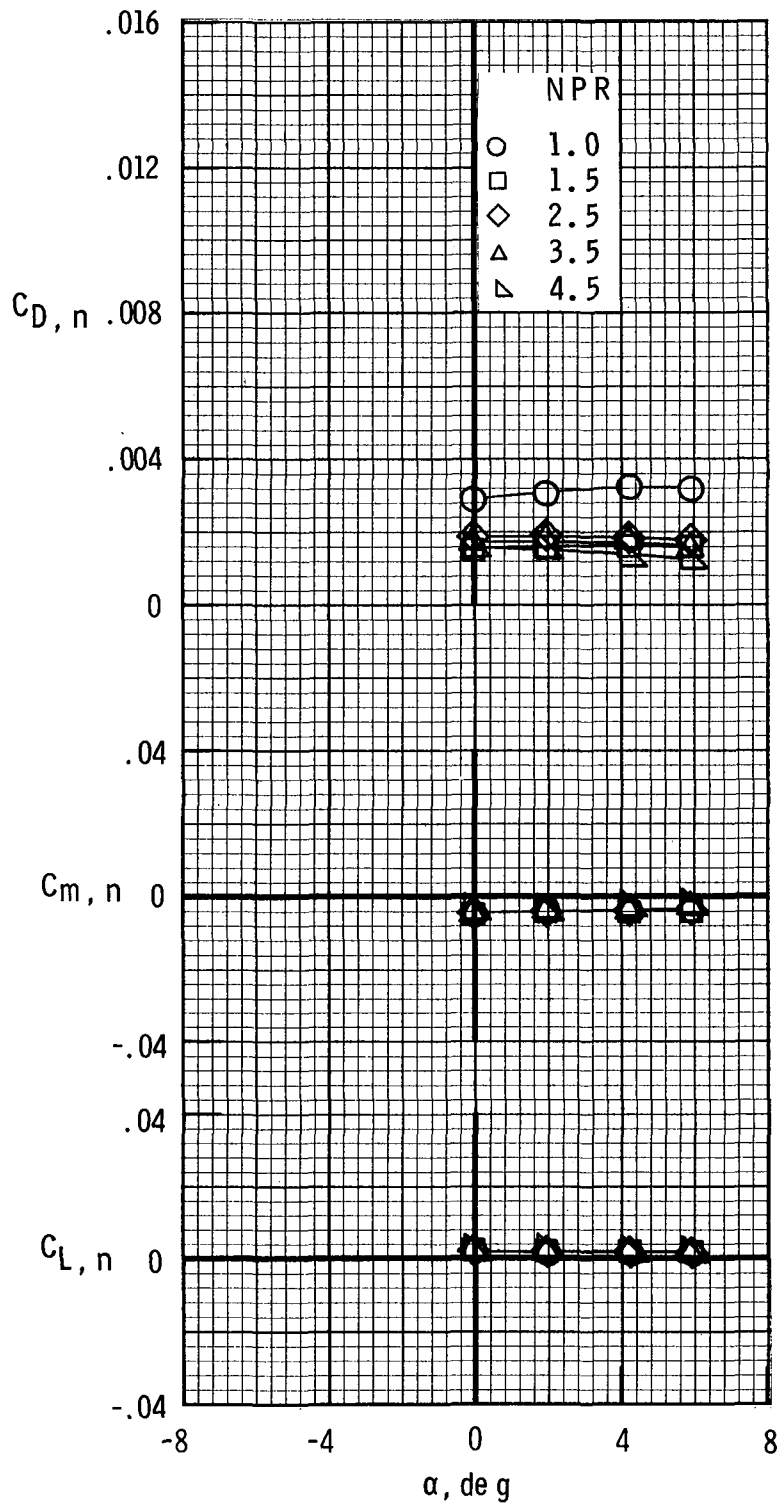
(f) Nozzle characteristics.
M = 0.8; Λ = 22°.

Figure 7.- Continued.
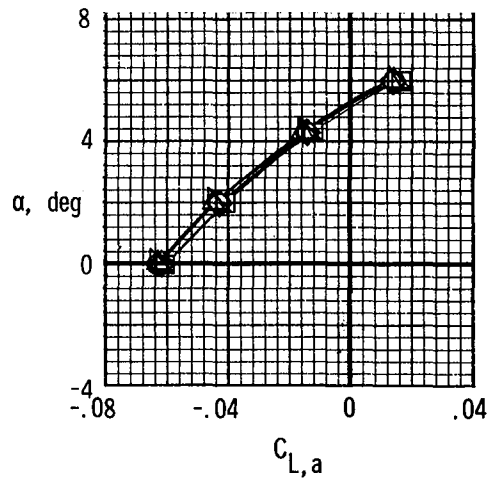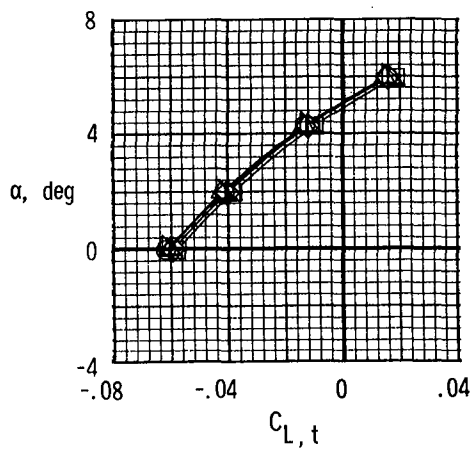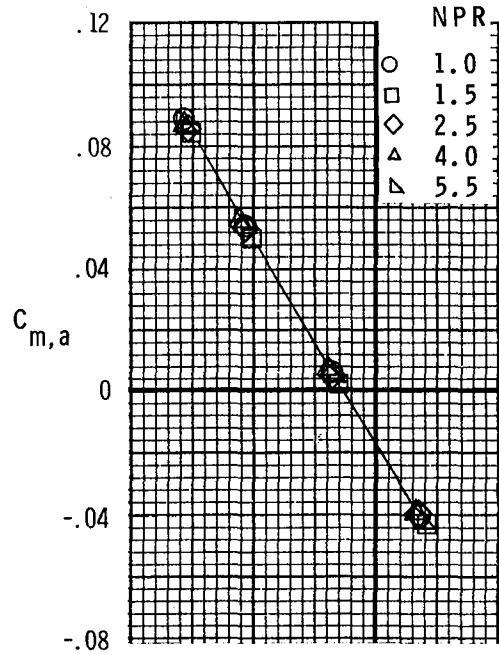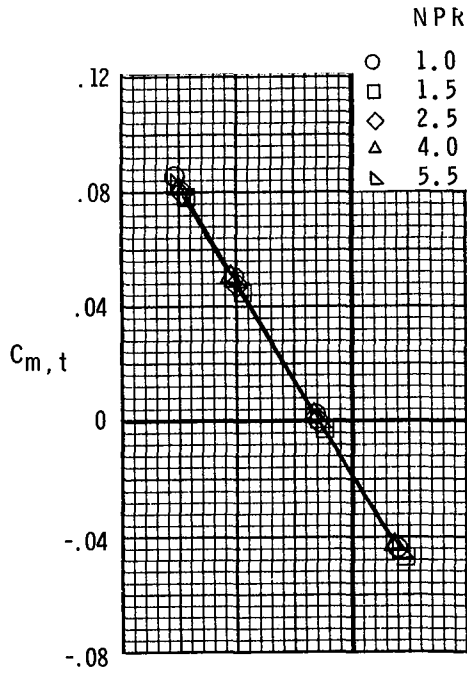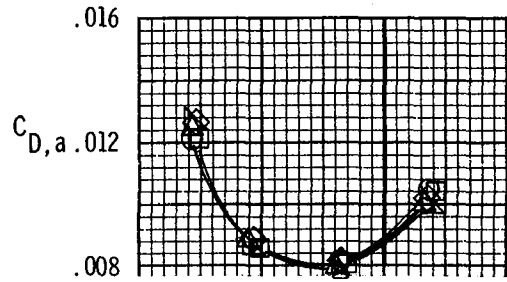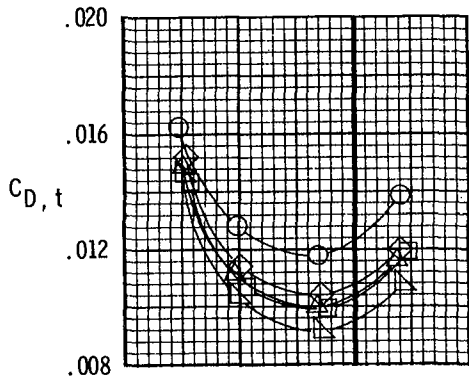
(g) Afterbody-nozzle characteristics.
M = 0.9; Λ = 22°.

(h) Afterbody characteristics.
M = 0.9; Λ = 22°.

Figure 7.- Continued.
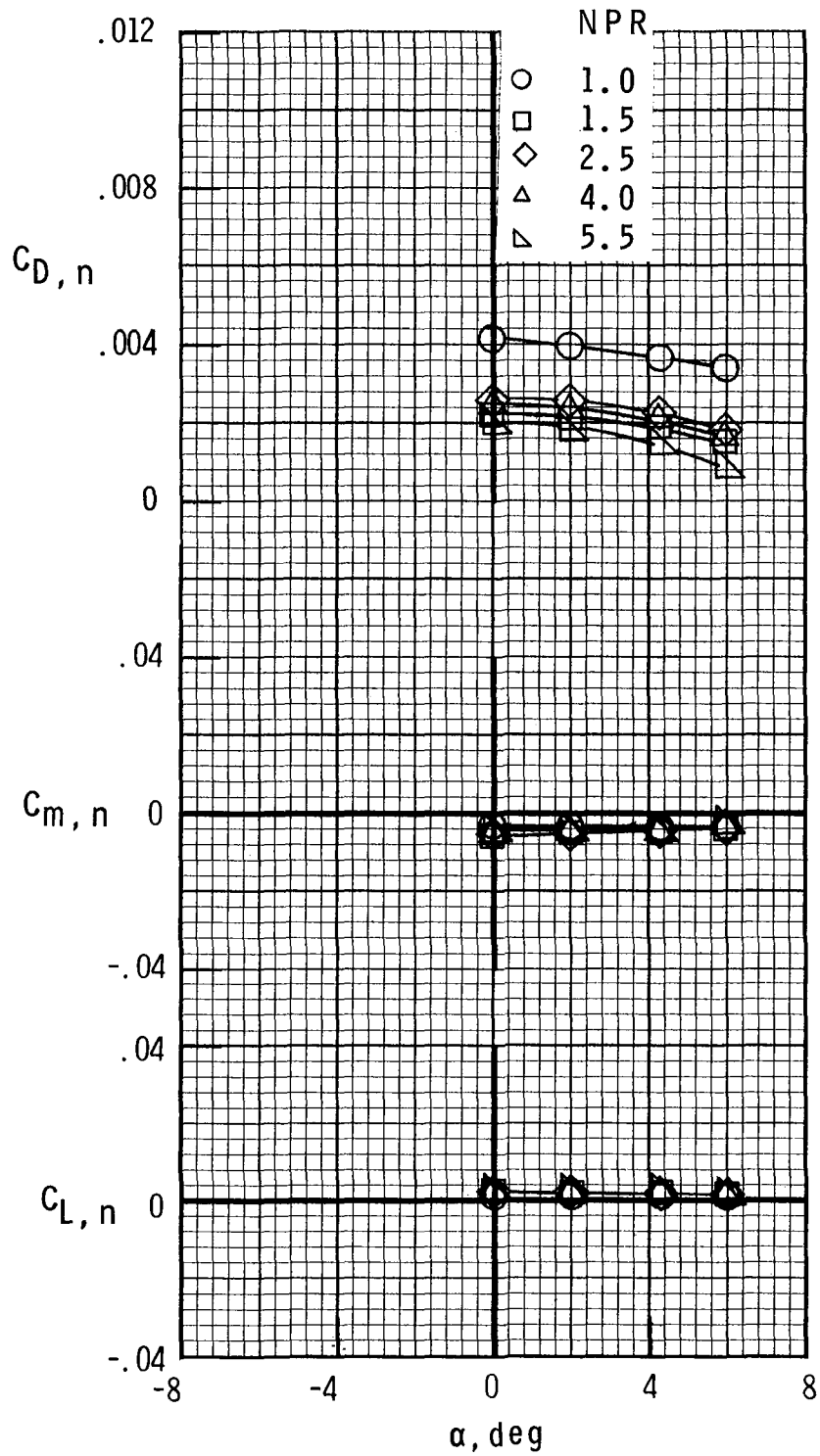
(i) Nozzle characteristics.
M = 0.9; Λ = 22°.
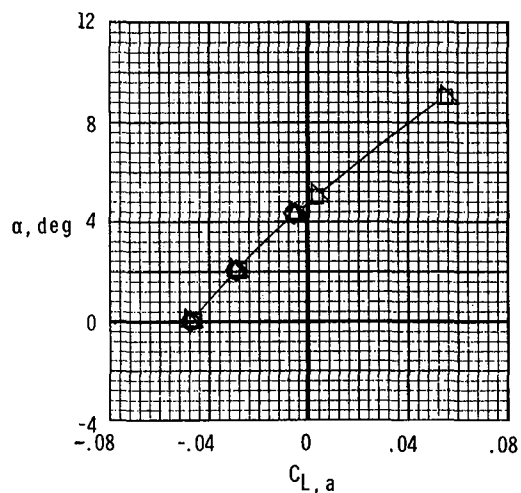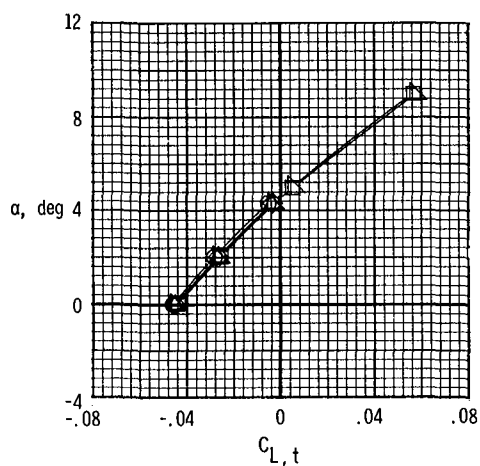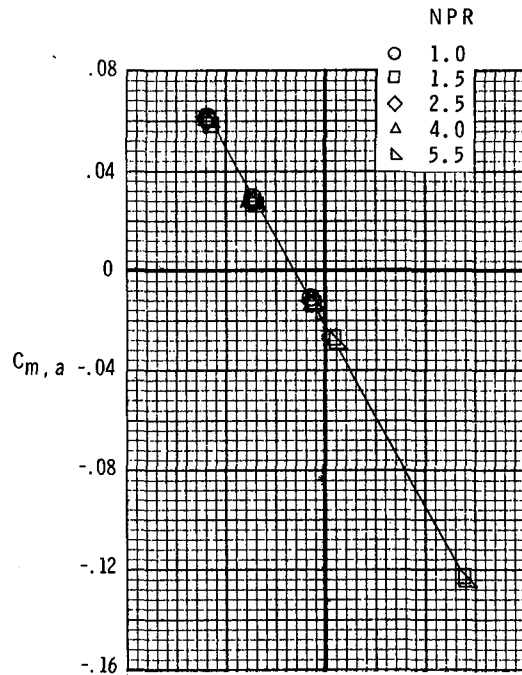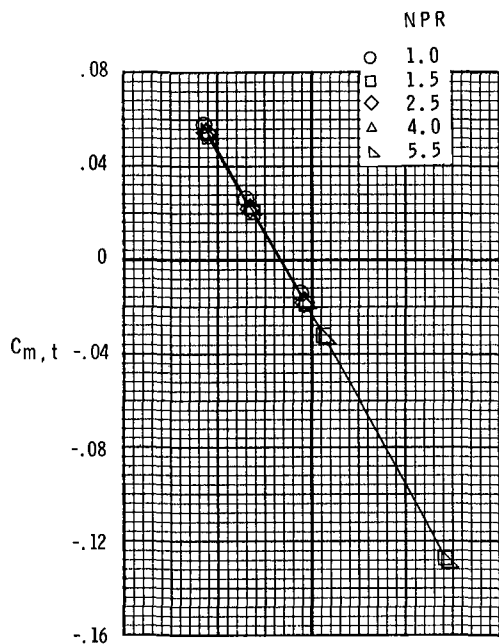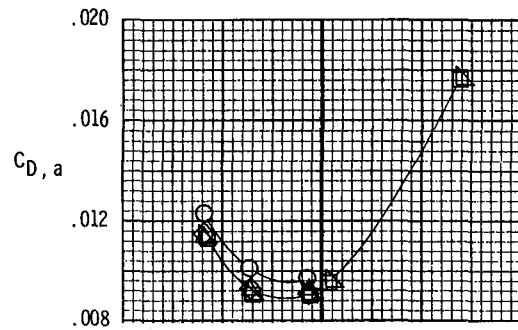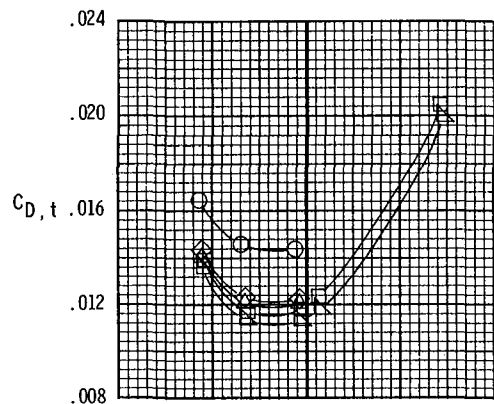
Figure 7.- Continued.

(j) Afterbody-nozzle characteristics.
M = 0.9; Λ = 68°.

(k) Afterbody characteristics.
M = 0.9; Λ = 68°.

Figure 7.- Continued.
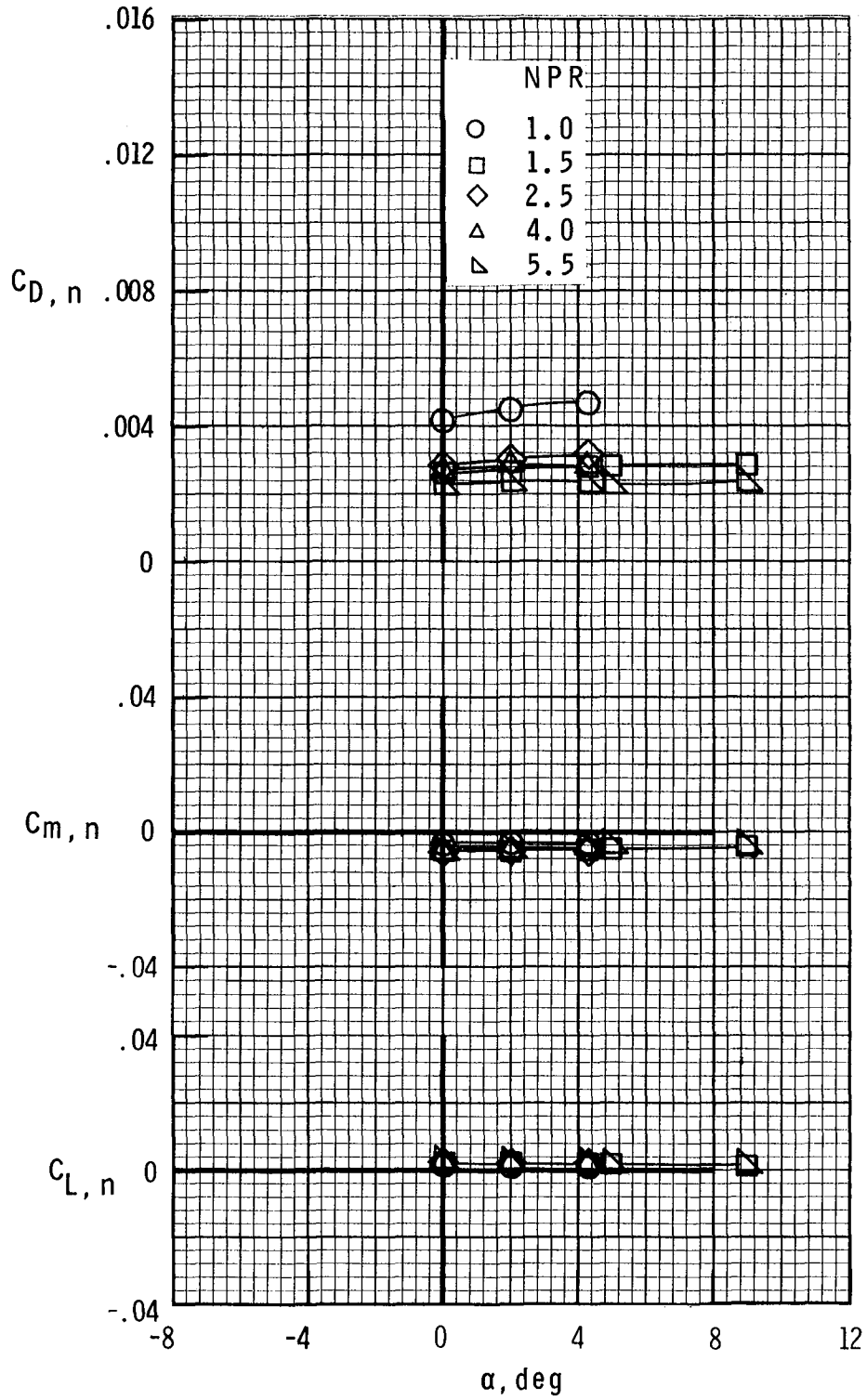
(1) Nozzle characteristics.
M = 0.9; Λ = 68°.
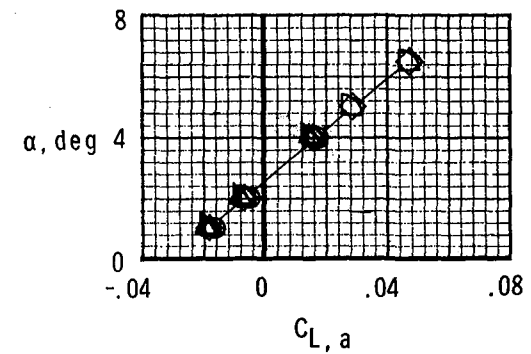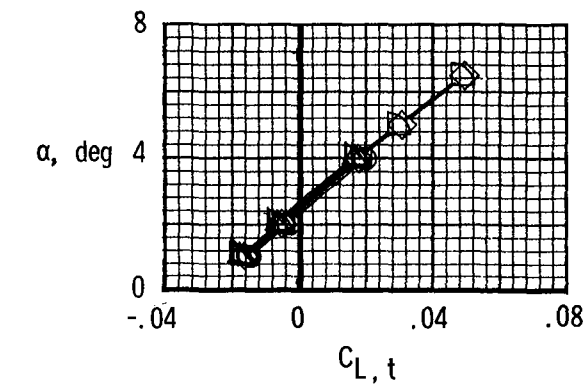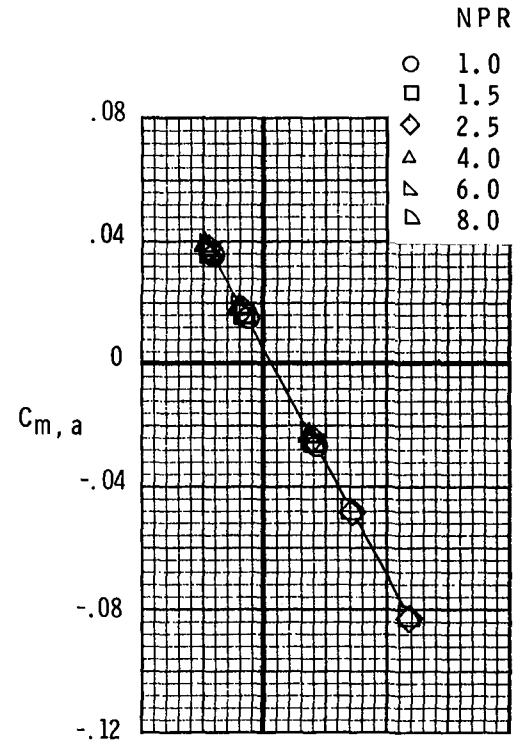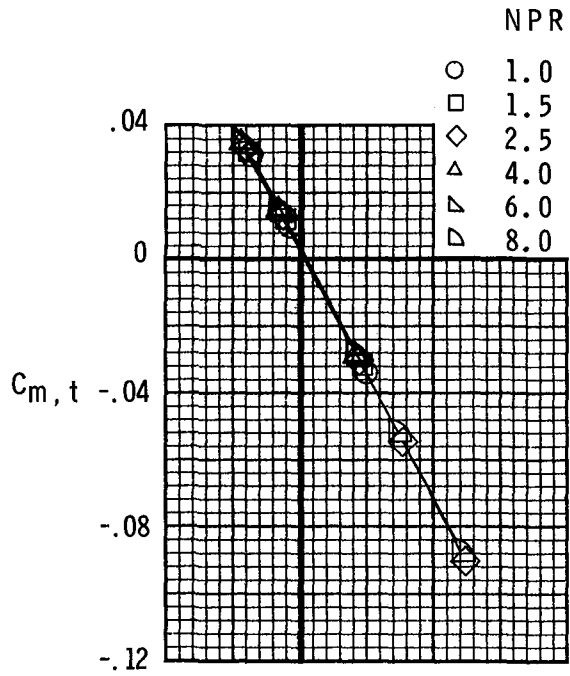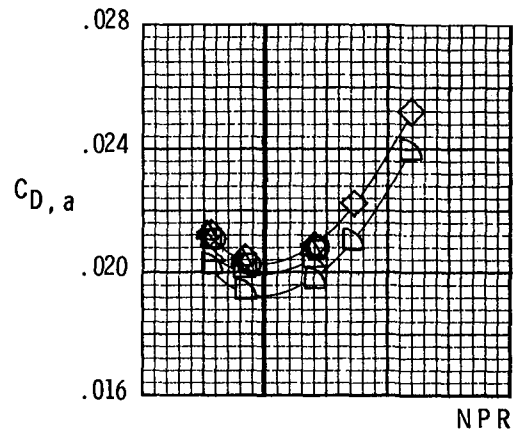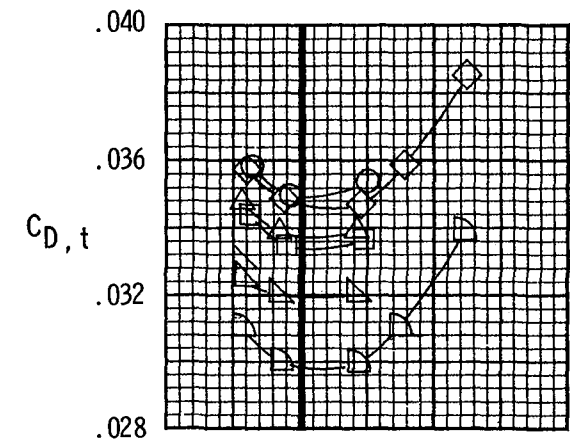
Figure 7.- Continued.

(m) Afterbody-nozzle characteristics.
M = 1.15; Λ = 68°.

(n) Afterbody characteristics.
M = 1.15; Λ = 68°.

Figure 7.- Continued.

47
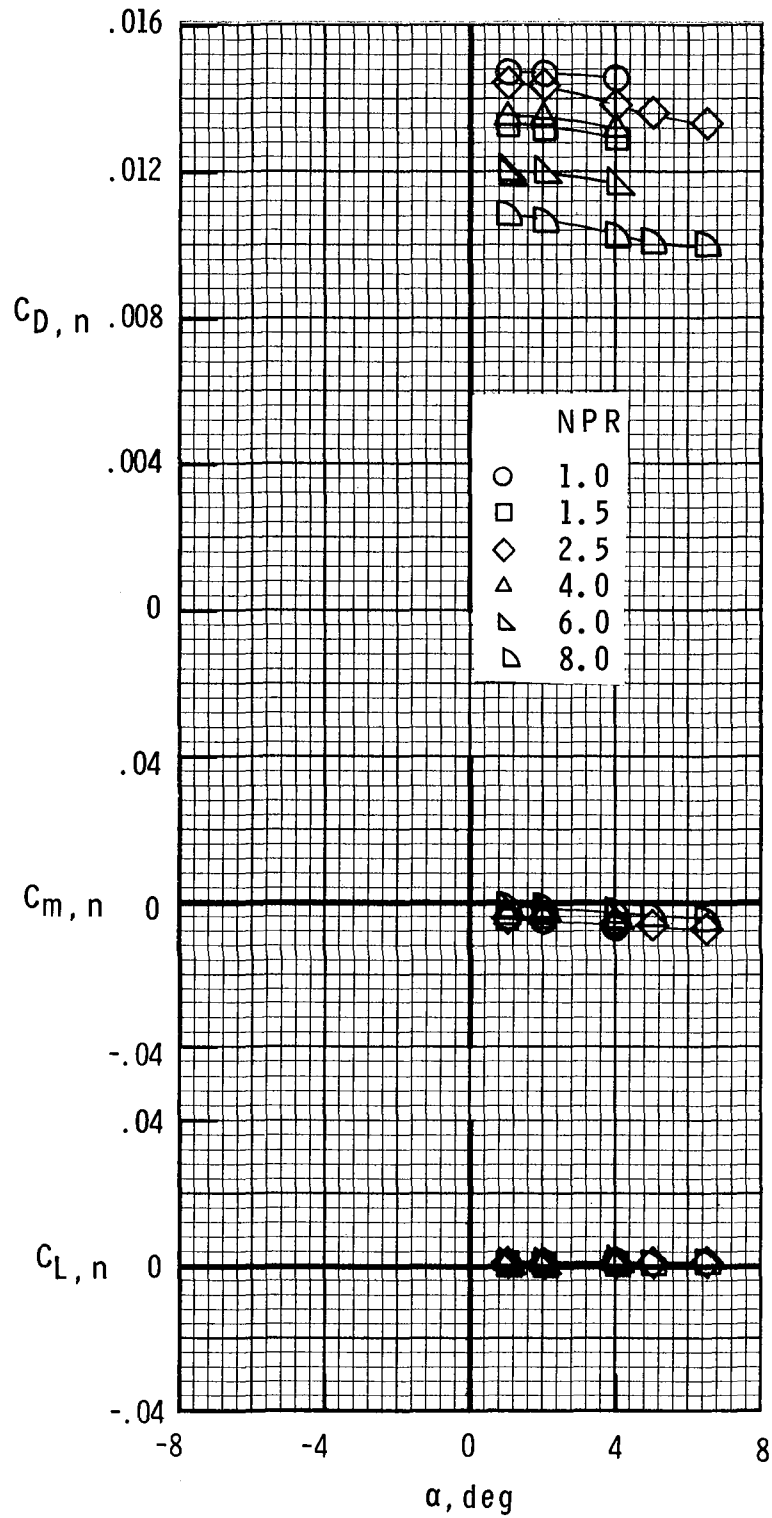
(o) Nozzle characteristics.
M = 1.15; Λ = 68°.

Figure 7.- Continued.
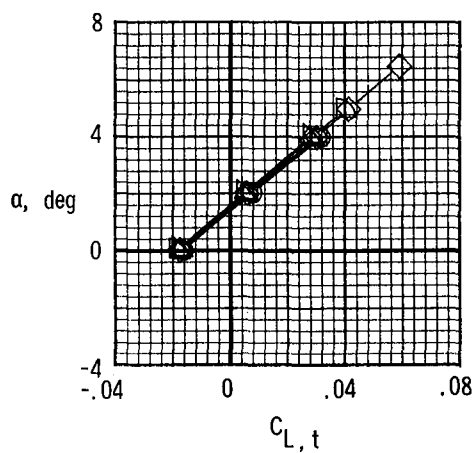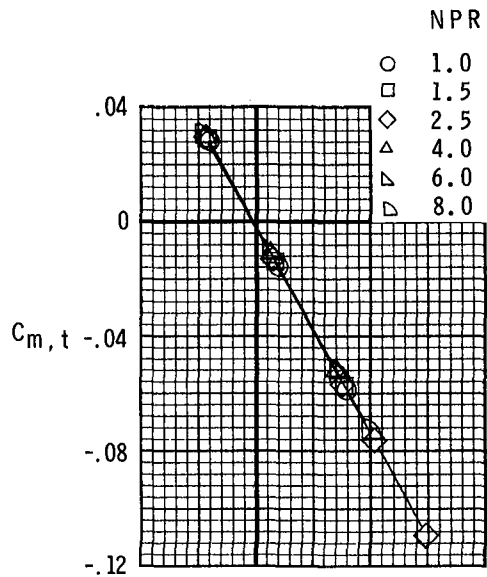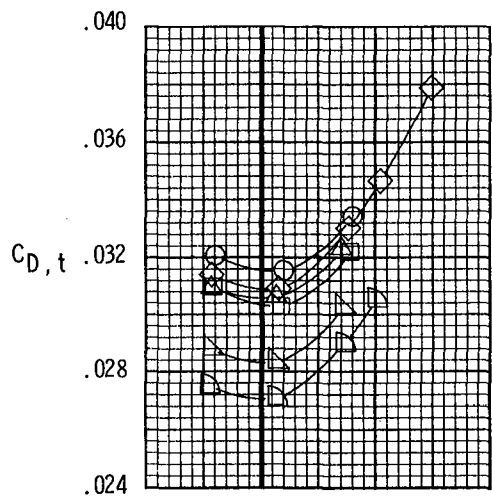
(p) Afterbody-nozzle characteristics.
M = 1.25; Λ = 68°.
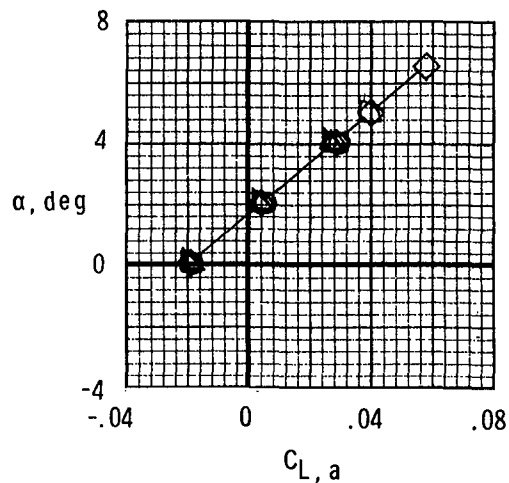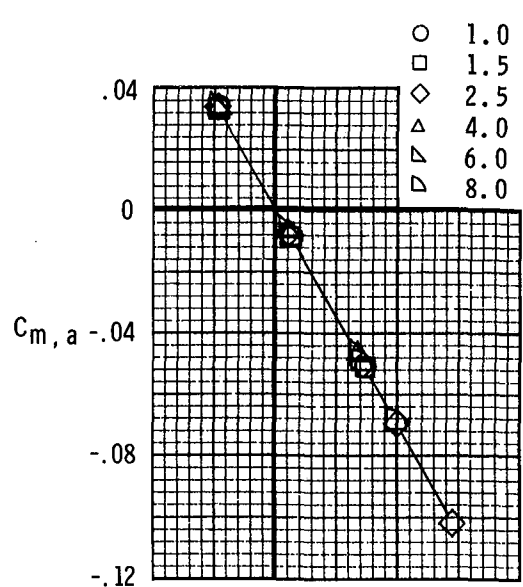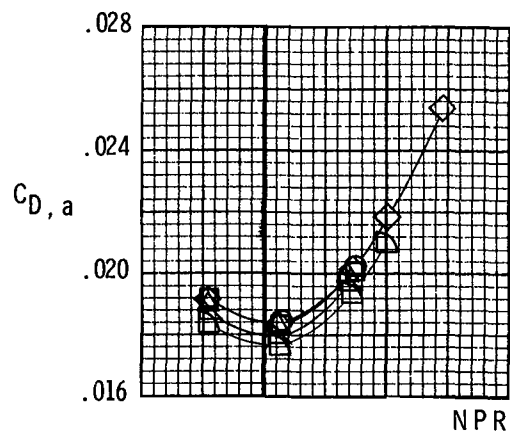
(q) Afterbody characteristics.
M = 1.25; Λ = 68°.

Figure 7.- Continued.
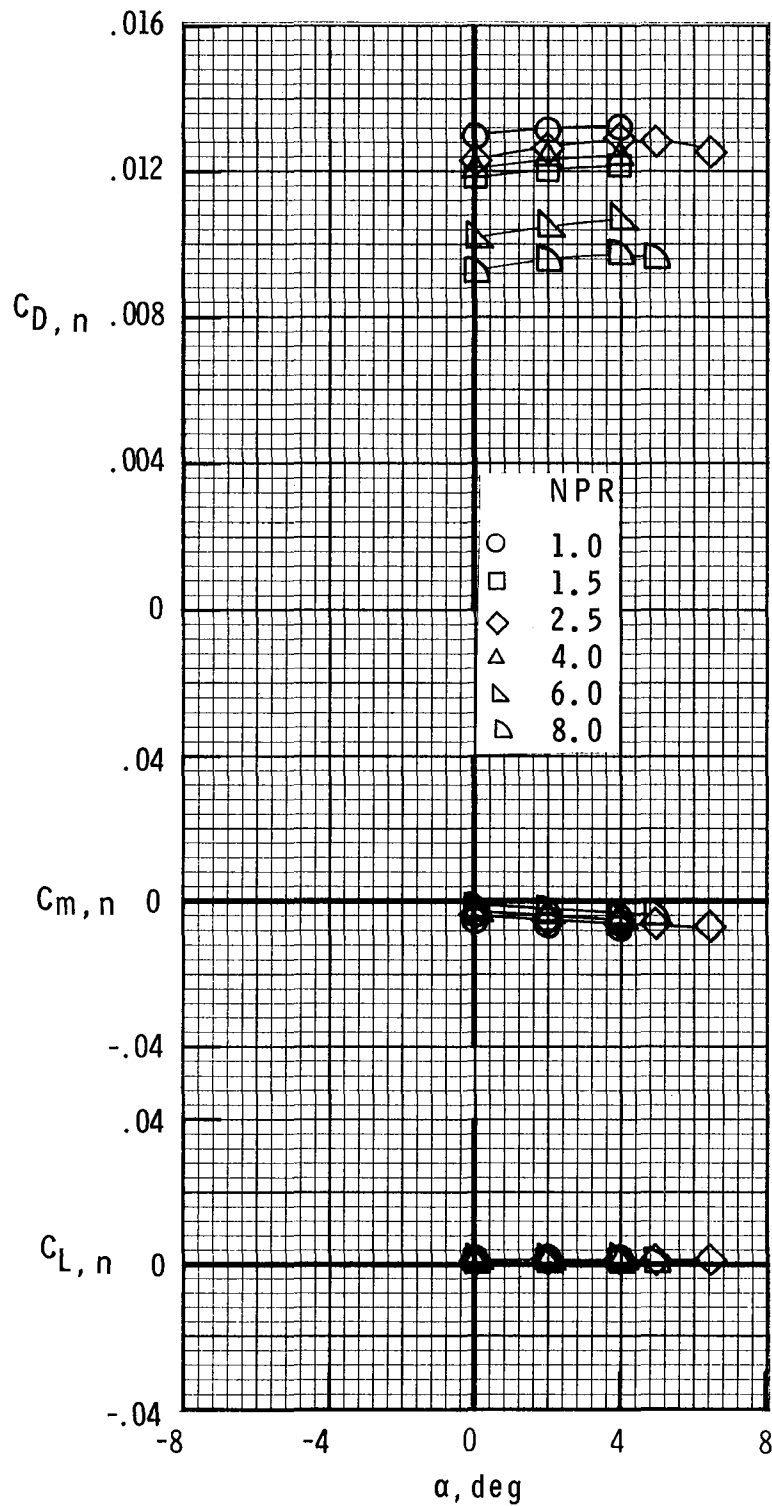
(r) Nozzle characteristics.
M = 1.25; Λ = 68°.

Figure 7.- Concluded.
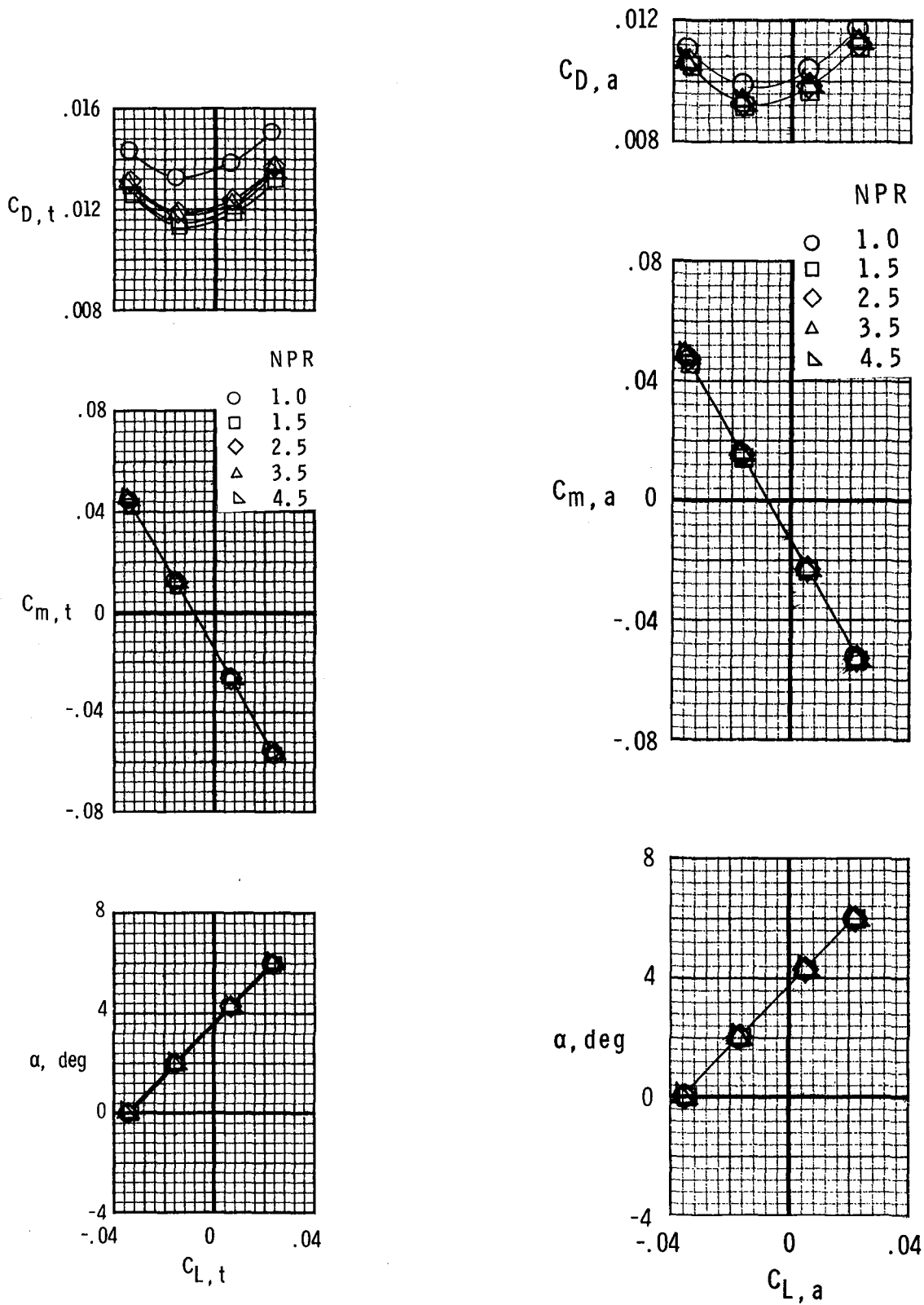
(a) Afterbody-nozzle characteristics.
M = 0.7;   Λ = 22°.

(b) Afterbody characteristics.
M = 0.7;   Λ = 22°.

Figure 8.- Effect of nozzle pressure ratio (NPR) on afterbody-nozzle aerodynamic characteristics for configuration with cruise nozzles in forward position.
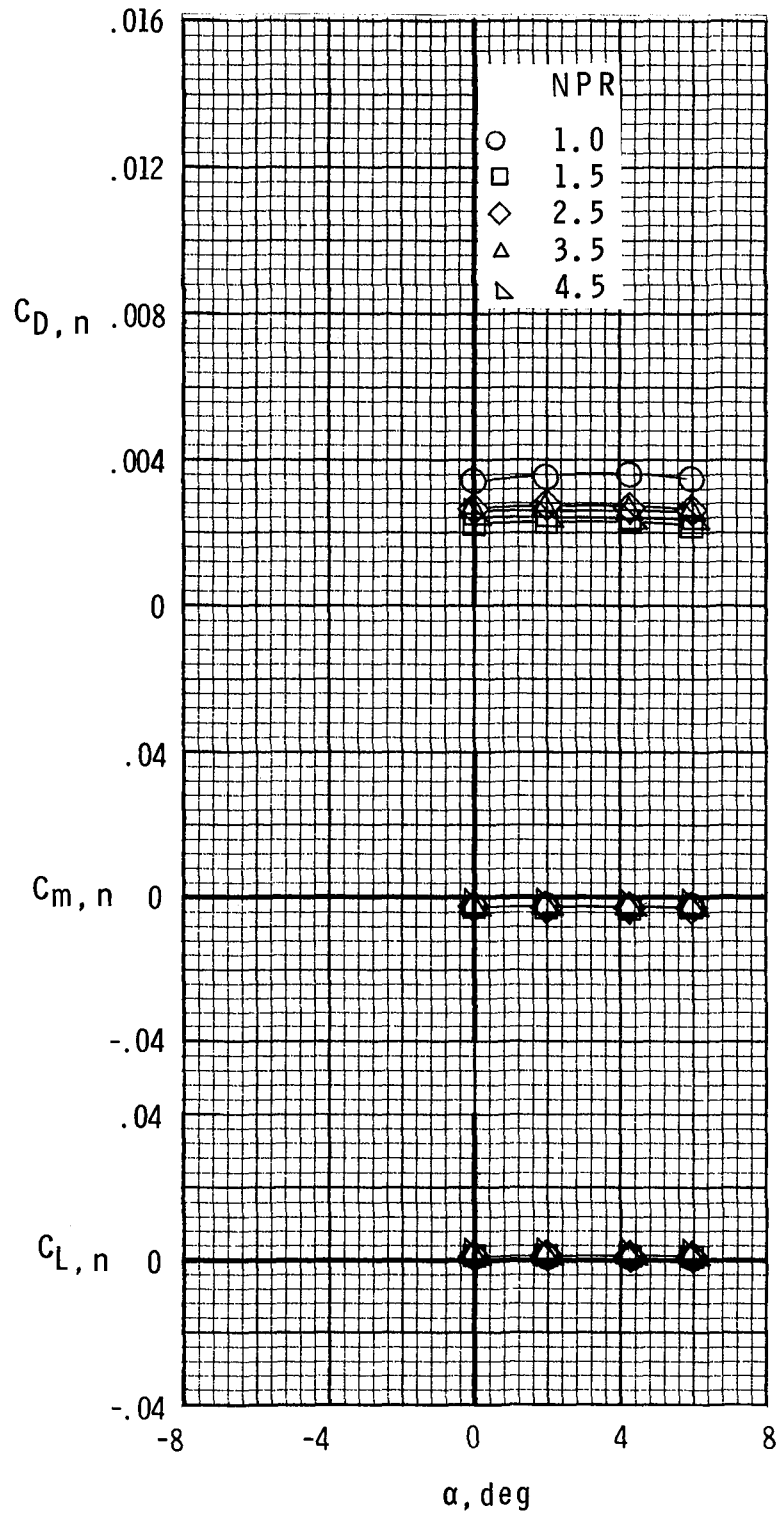
(c) Nozzle characteristics.
M = 0.7; Λ = 22°.

Figure 8.- Continued.
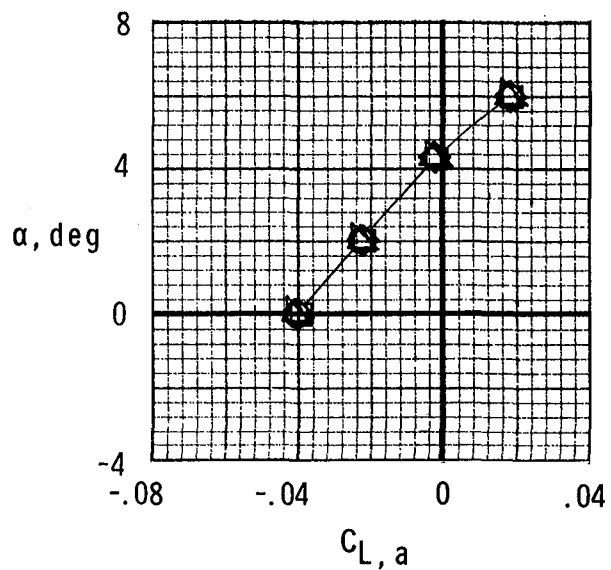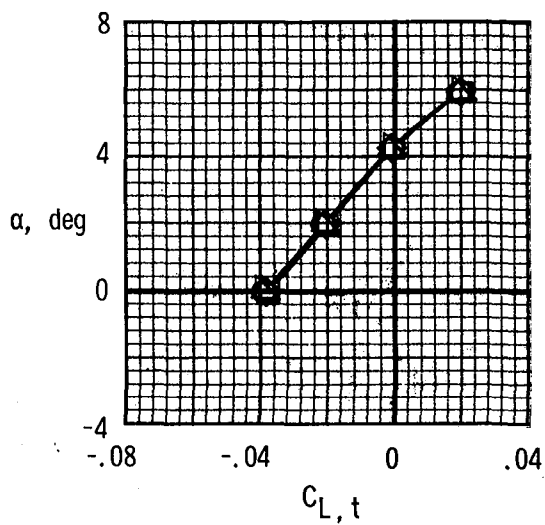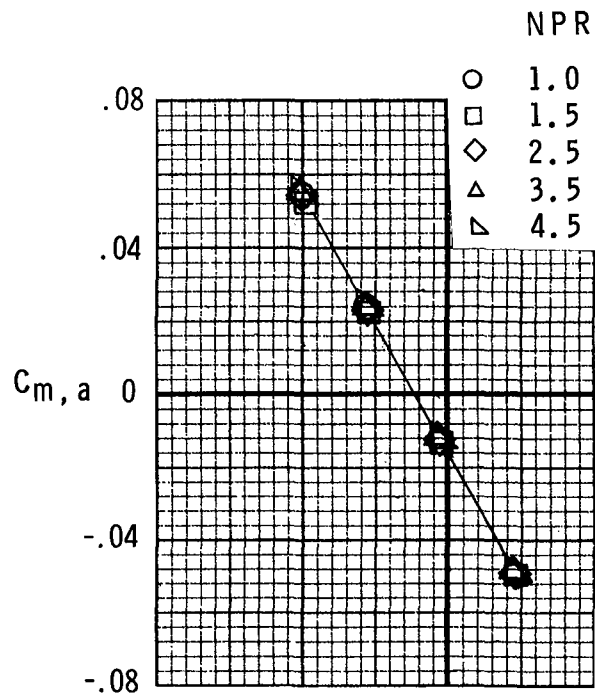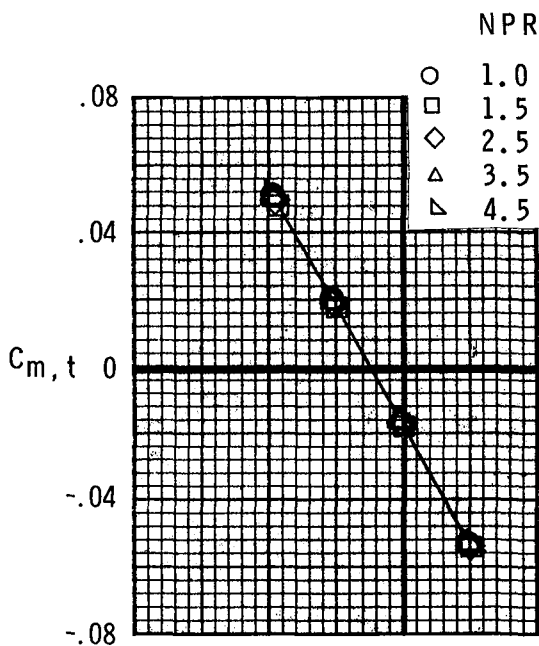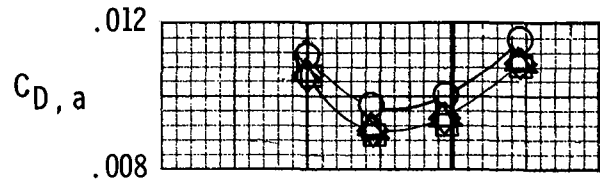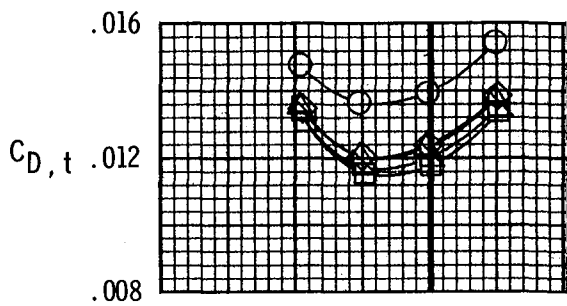
(d) Afterbody-nozzle characteristics.
M = 0.8;   Λ = 22°.

(e) Afterbody characteristics.
M = 0.8;   Λ = 22°.

Figure 8.- Continued.
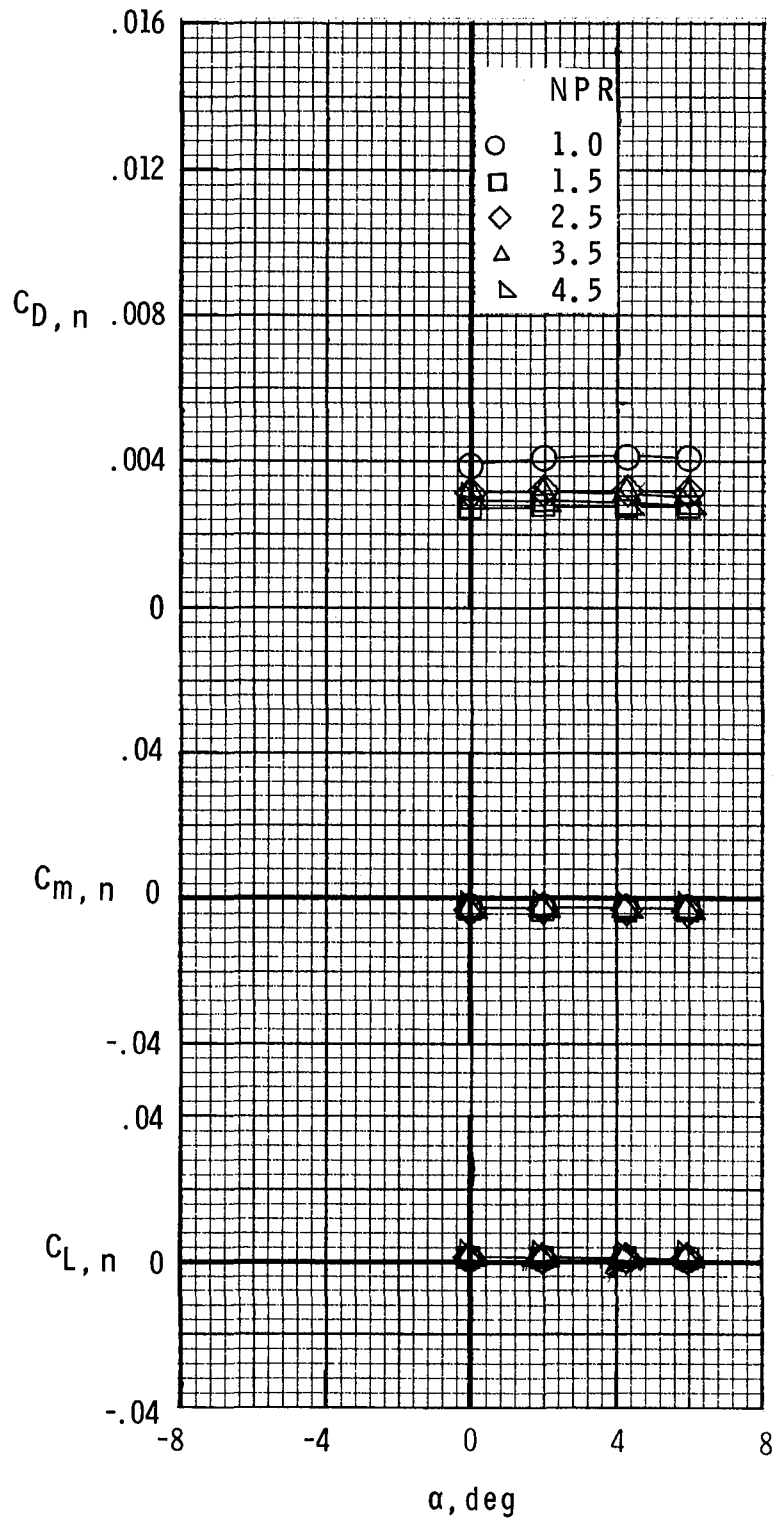
(f) Nozzle characteristics.
M = 0.8; Λ = 22°.

Figure 8.- Continued.

(g) Afterbody-nozzle characteristics.
M = 0.9; Λ = 22°.

(h) Afterbody characteristics.
M = 0.9; Λ = 22°.

Figure 8.- Continued.

(i) Nozzle characteristics.
M = 0.9; Λ = 22°.

Figure 8.- Continued.

(j) Afterbody-nozzle characteristics.
M = 0.9; Λ = 68°.

(k) Afterbody characteristics.
M = 0.9; Λ = 68°.

Figure 8.- Continued.
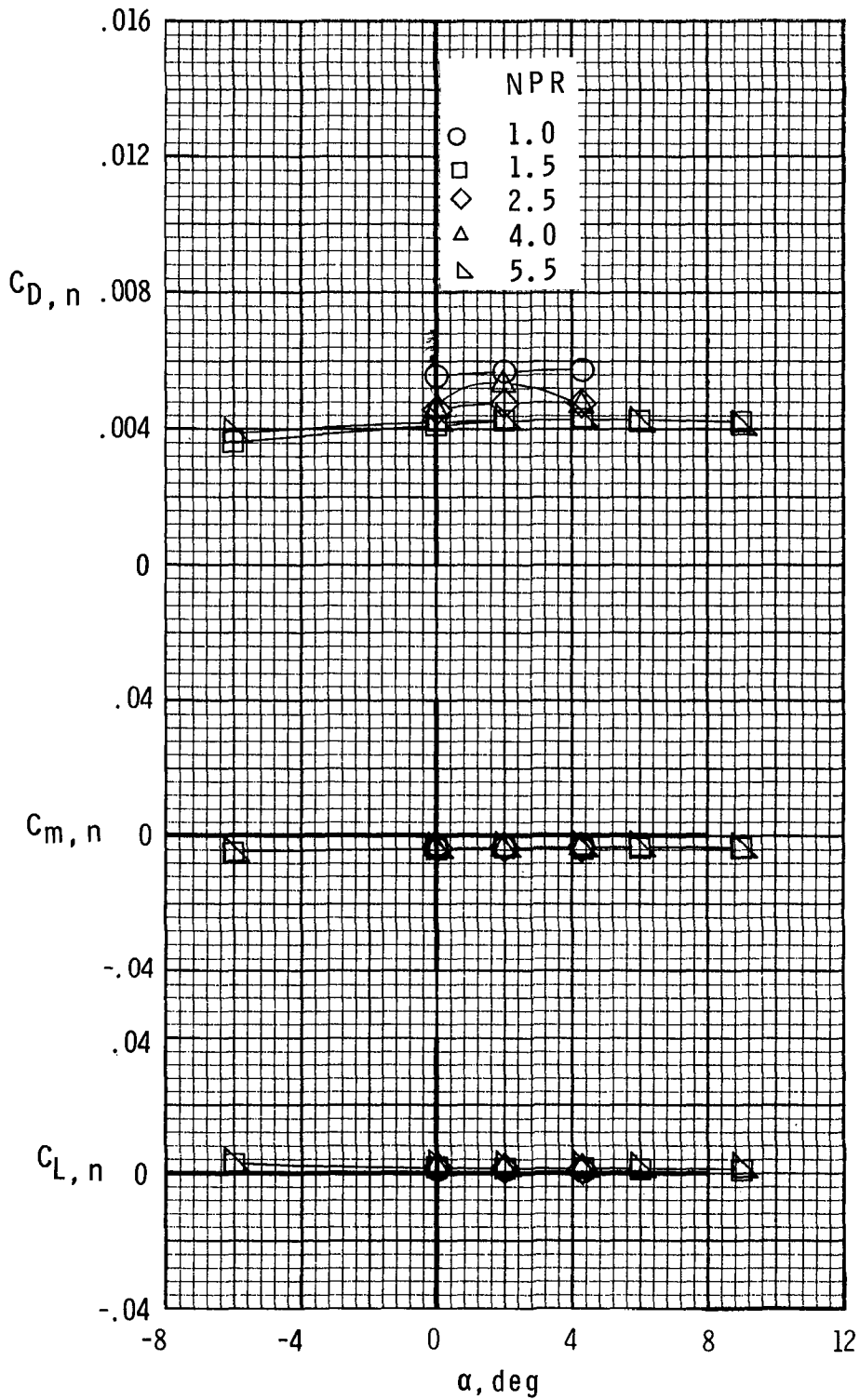
(l) Nozzle characteristics.
M = 0.9; Λ = 68°.

Figure 8.- Continued.
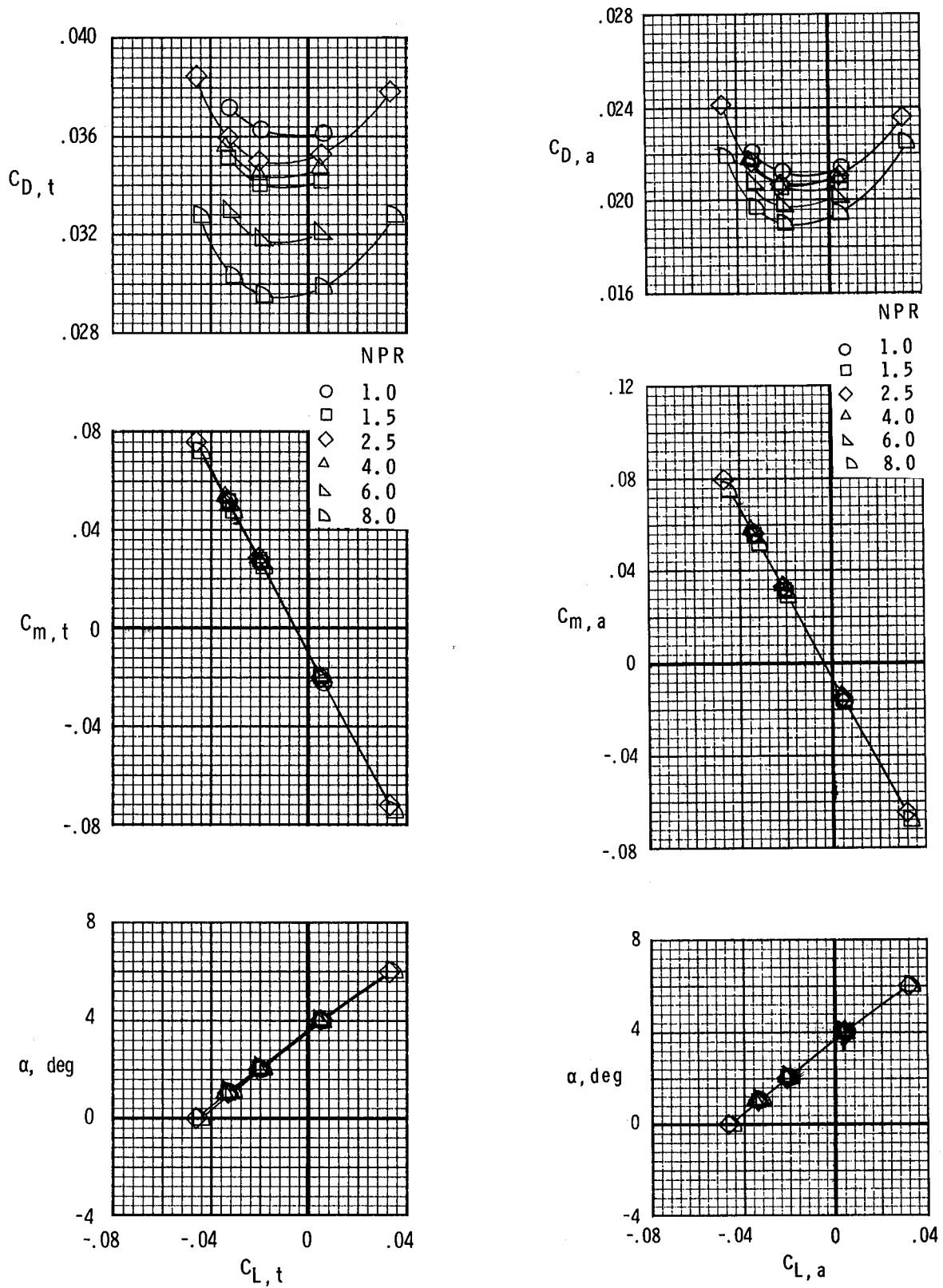
(m) Afterbody-nozzle characteristics.
M = 1.15; Λ = 68°.

(n) Afterbody characteristics.
M = 1.15; Λ = 68°.

Figure 8.- Continued.
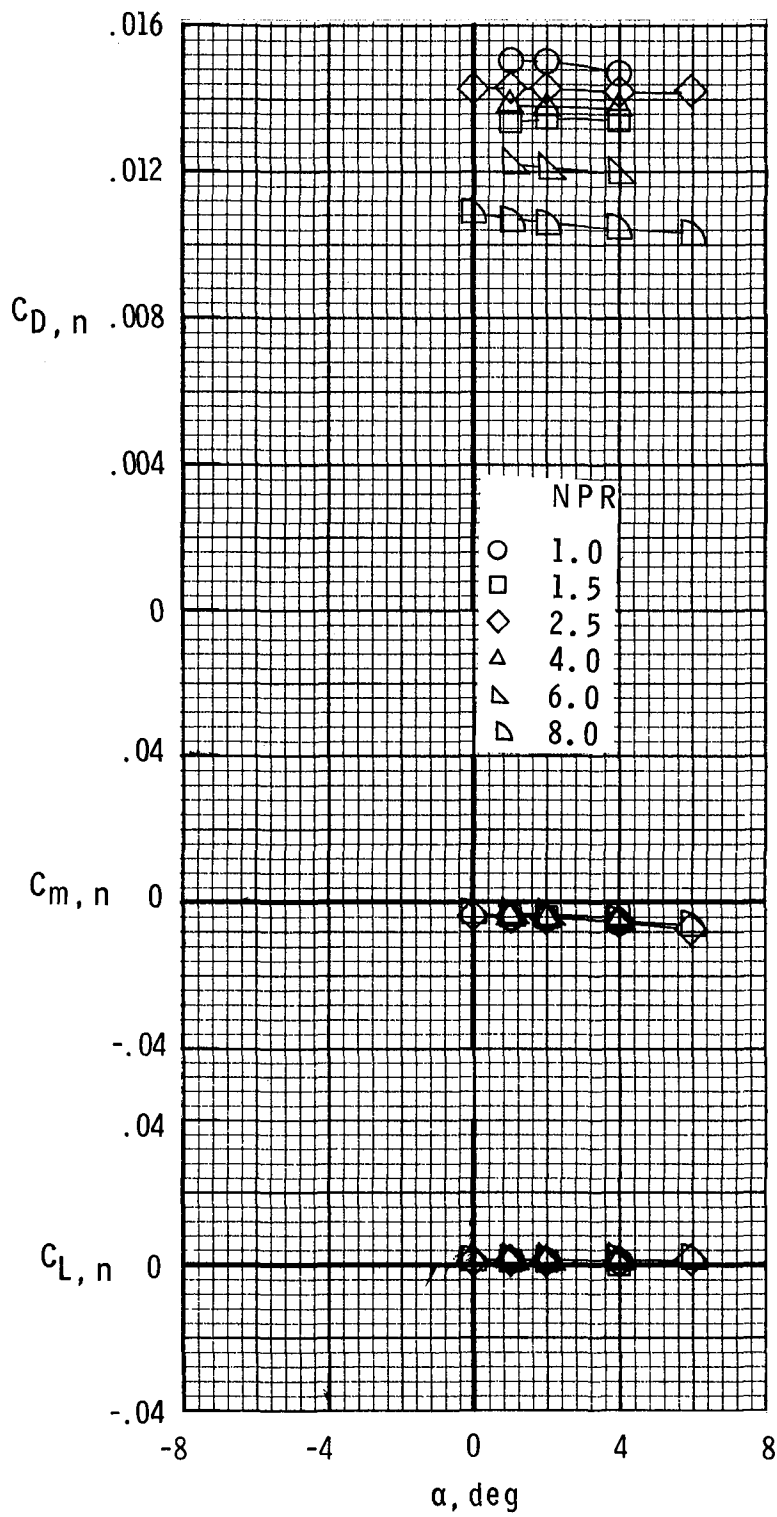
(o) Nozzle characteristics.
M = 1.15; Λ = 68°.
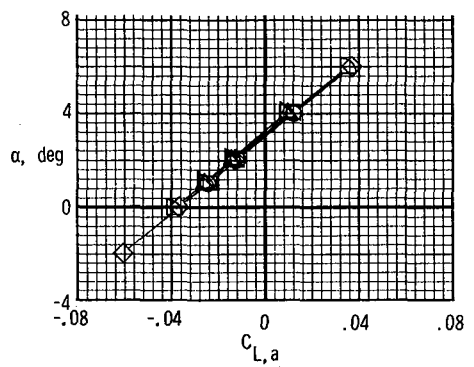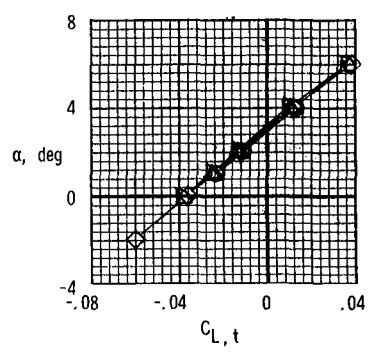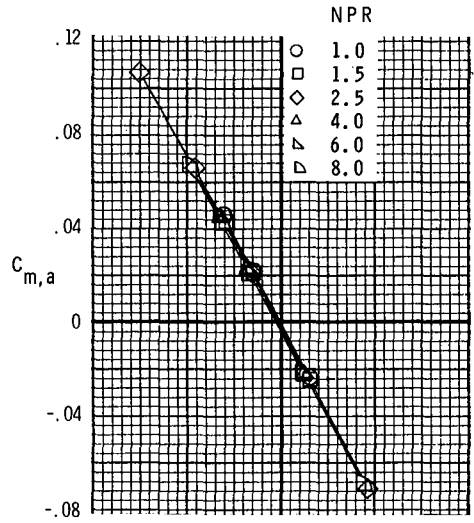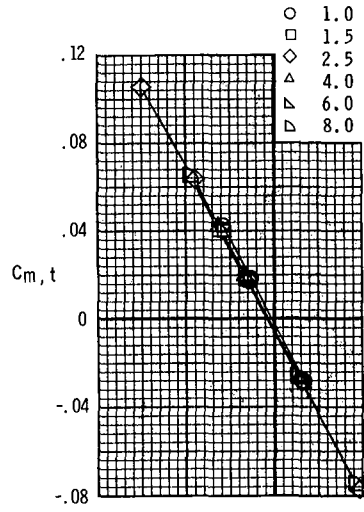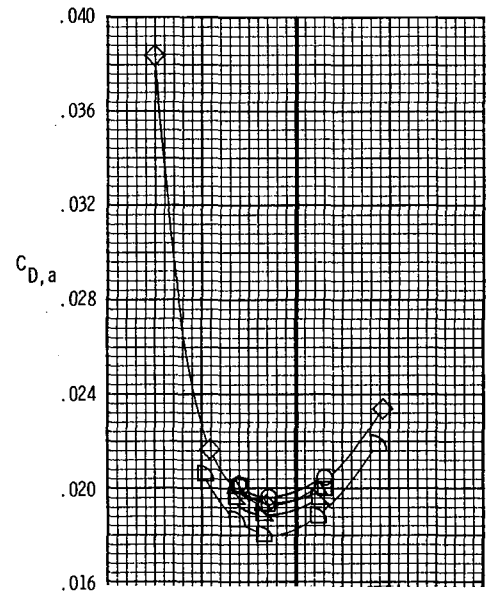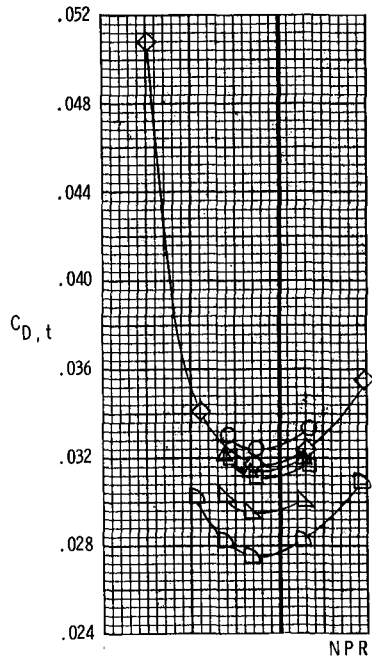
Figure 8.- Continued.

(p) Afterbody-nozzle characteristics.
M = 1.25; Λ = 68°.

(q) Afterbody characteristics.
M = 1.25; Λ = 68°.

Figure 8.- Continued.
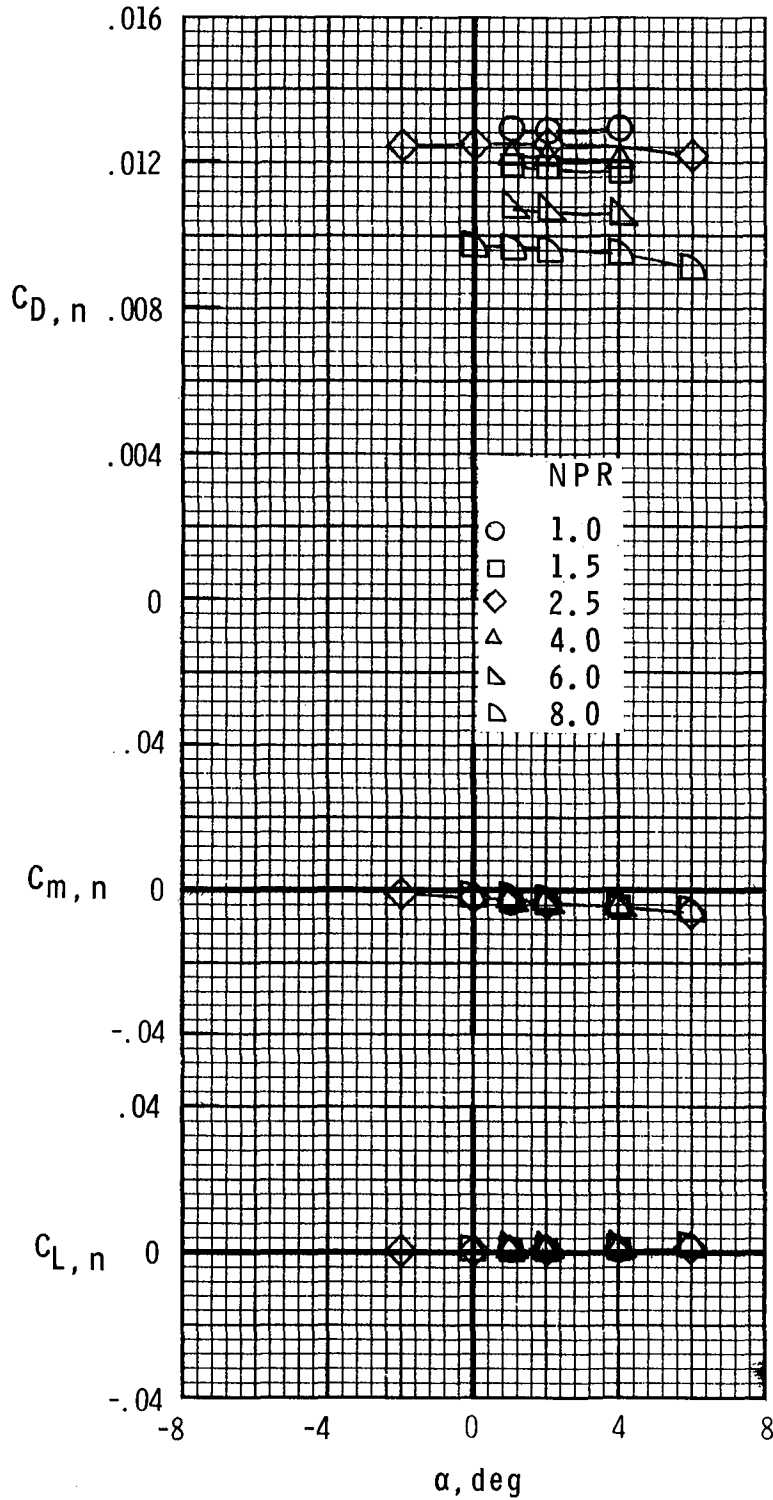
(r) Nozzle characteristics.
M = 1.25; Λ = 68°.

Figure 8.- Concluded.
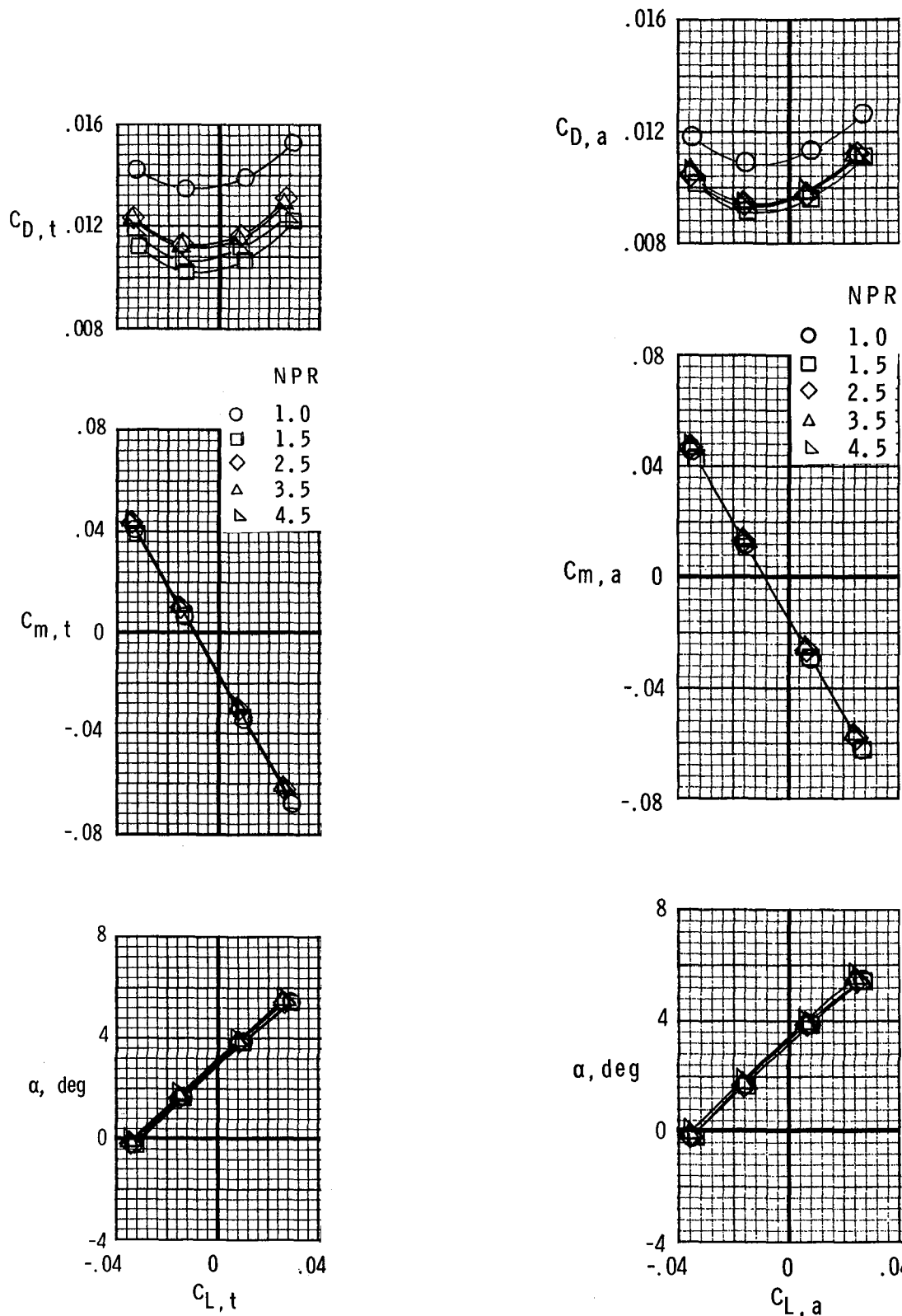
(a) Afterbody-nozzle characteristics.
M = 0.7; Λ = 22°.

(b) Afterbody characteristics.
M = 0.7; Λ = 22°.

Figure 9.- Effect of nozzle pressure ratio (NPR) afterbody-nozzle aerodynamic characteristics for configuration with afterburning nozzles in forward position.
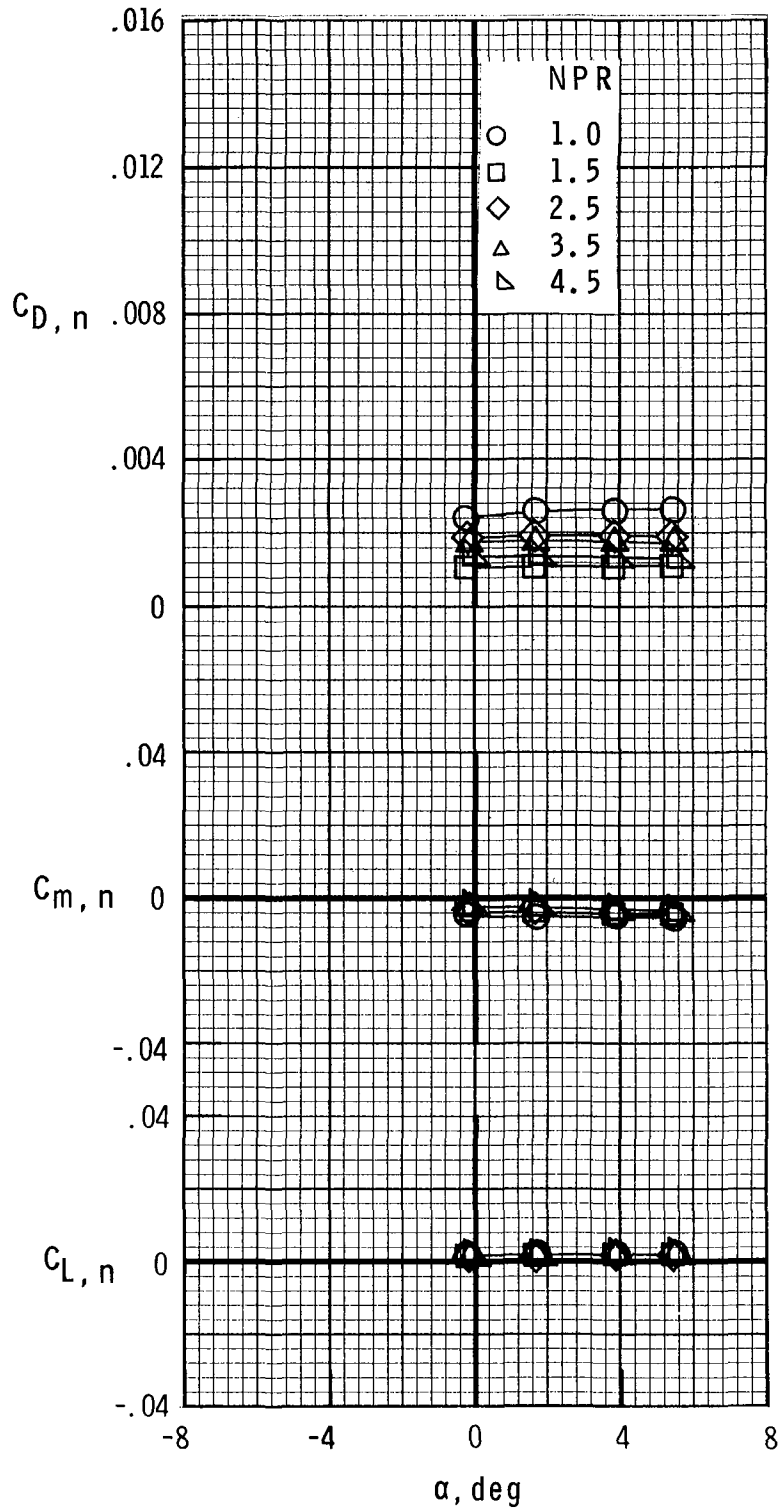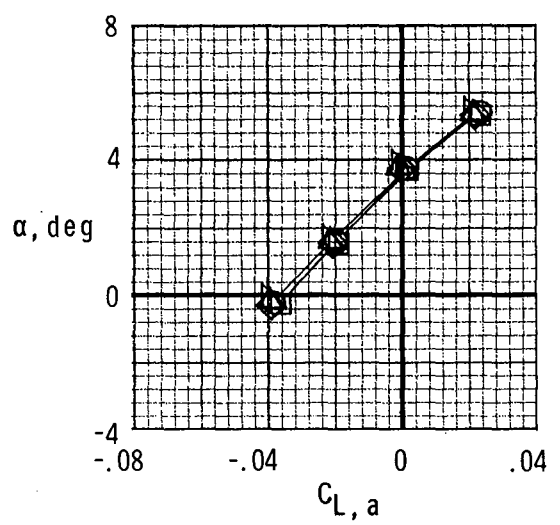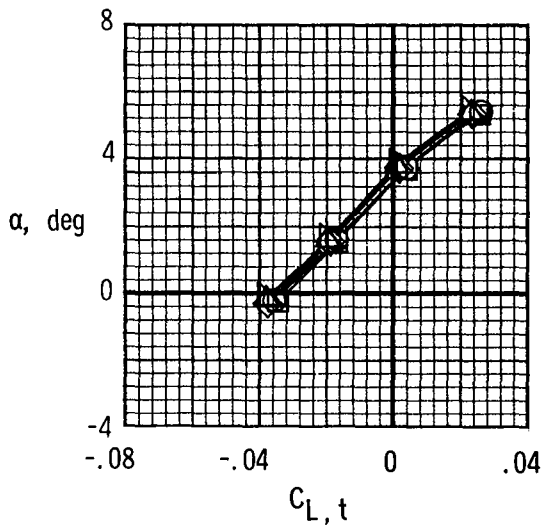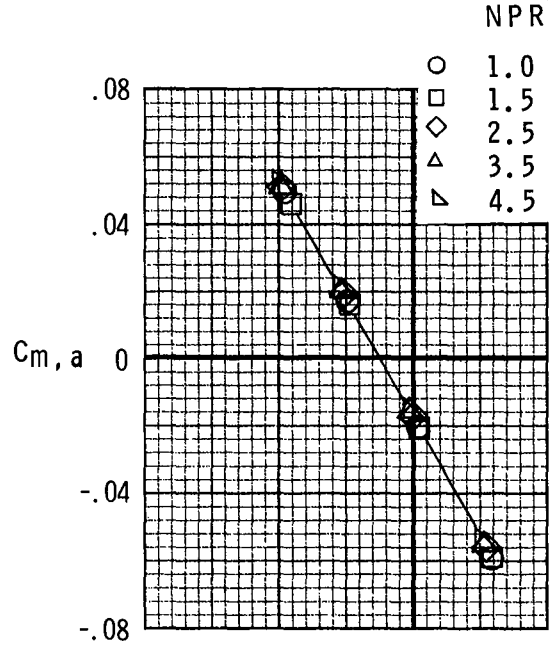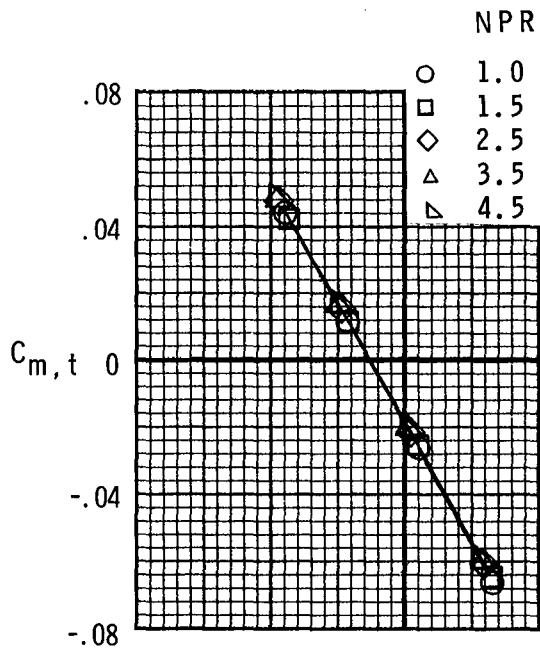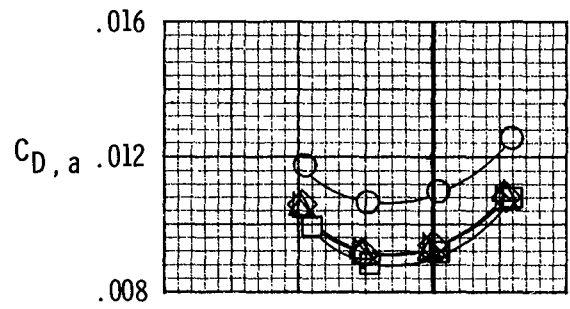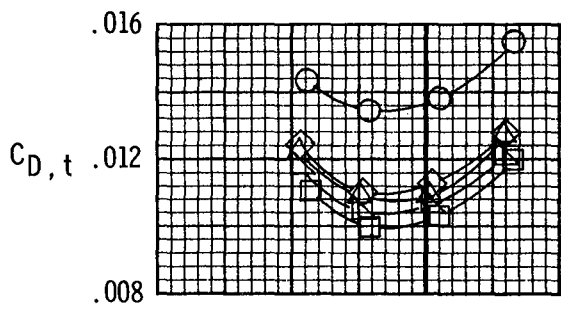
(c) Nozzle characteristics.
M = 0.7; Λ = 22°.

Figure 9.- Continued.

(d) Afterbody-nozzle characteristics.
M = 0.8; Λ = 22°.

(e) Afterbody characteristics.
M = 0.8; Λ = 22°.

Figure 9.- Continued.
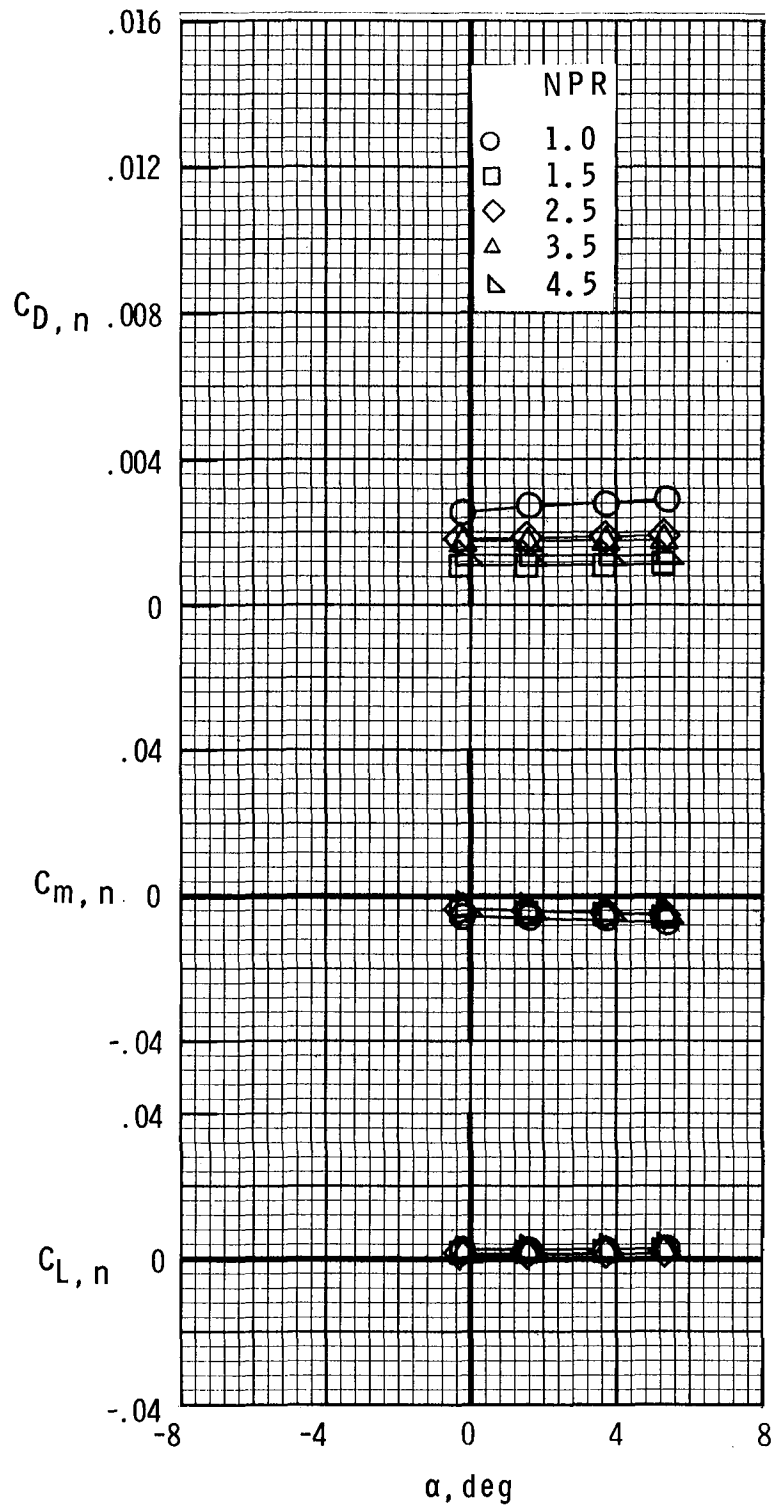
(f) Nozzle characteristics.
M = 0.8; Λ = 22°.
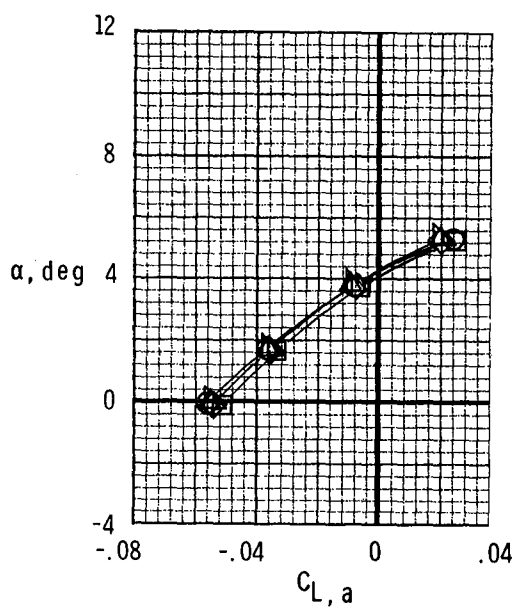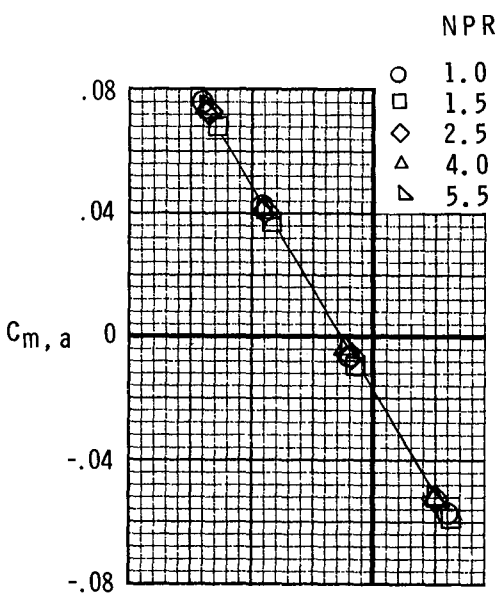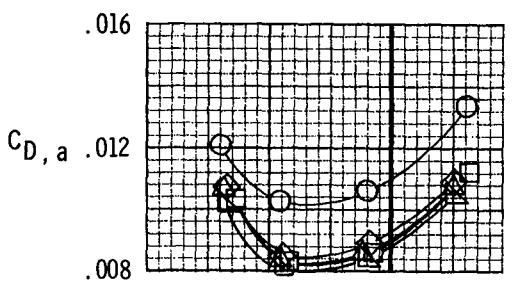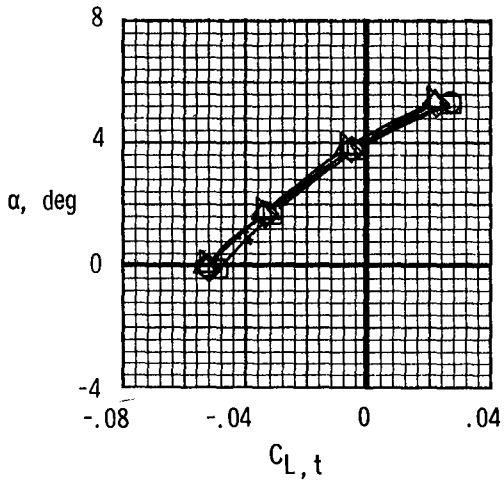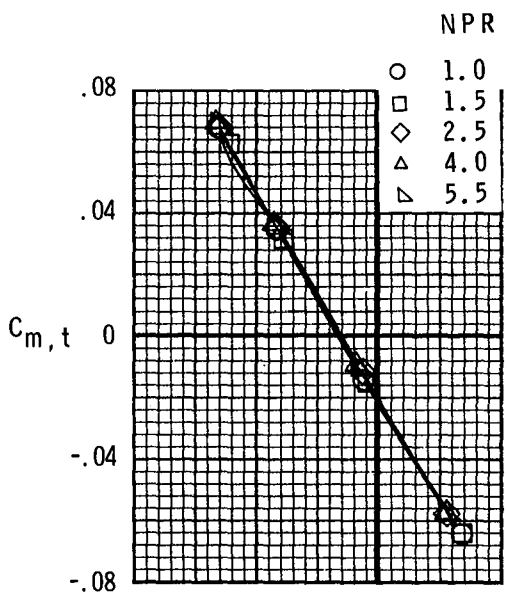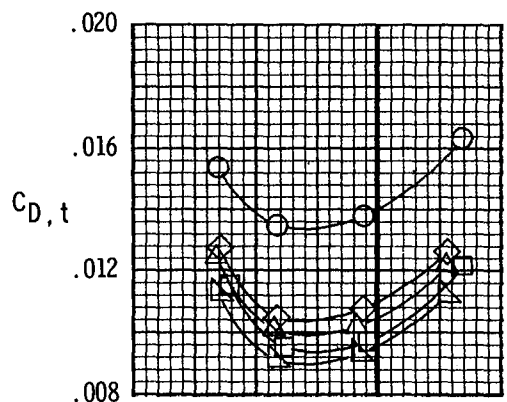
Figure 9.- Continued.

(g) Afterbody-nozzle characteristics.
$M = 0.9;$ $\Lambda = 22°.$

(h) Afterbody characteristics.
$M = 0.9;$ $\Lambda = 22°.$

Figure 9.- Continued.
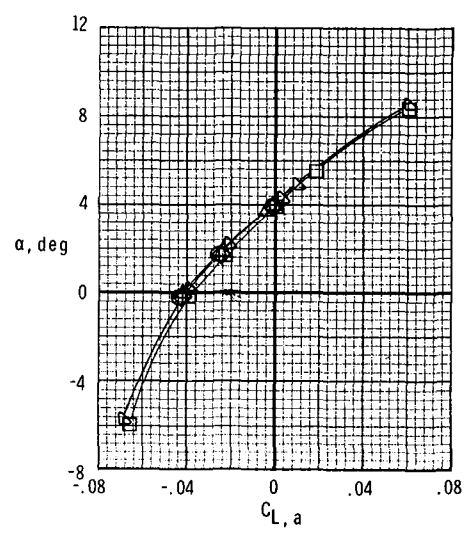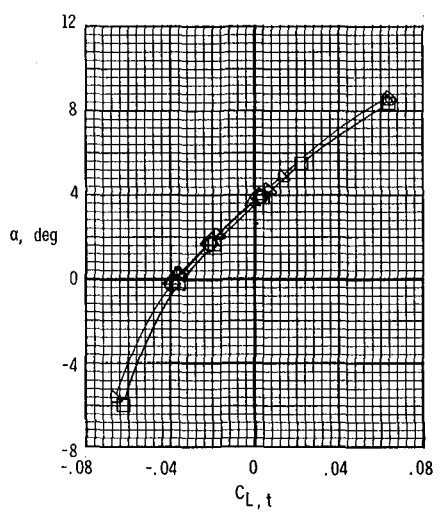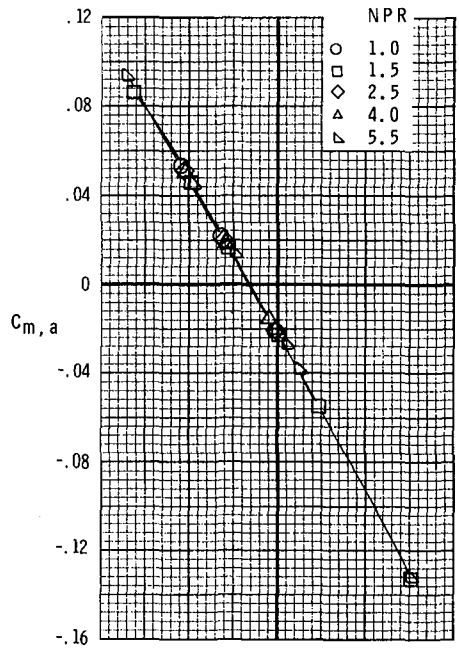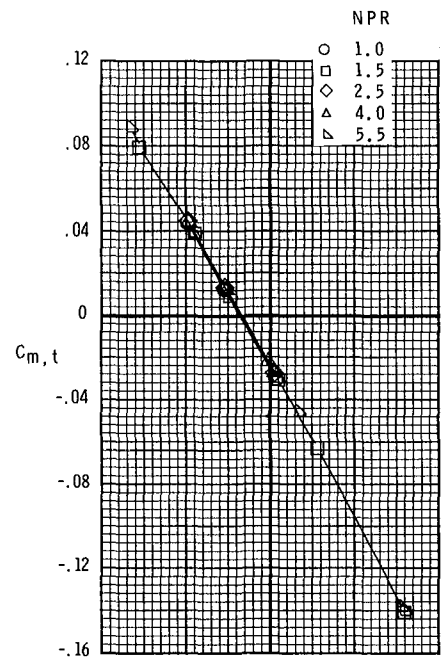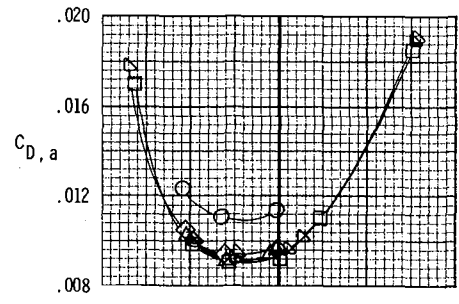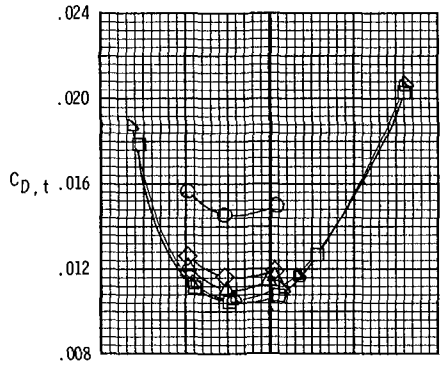
(i) Nozzle characteristics.
M = 0.9; Λ = 22°.

Figure 9.- Continued.

(j) Afterbody-nozzle characteristics.
M = 0.9; Λ = 68°.

(k) Afterbody characteristics.
M = 0.9; Λ = 68°.

Figure 9.- Continued.
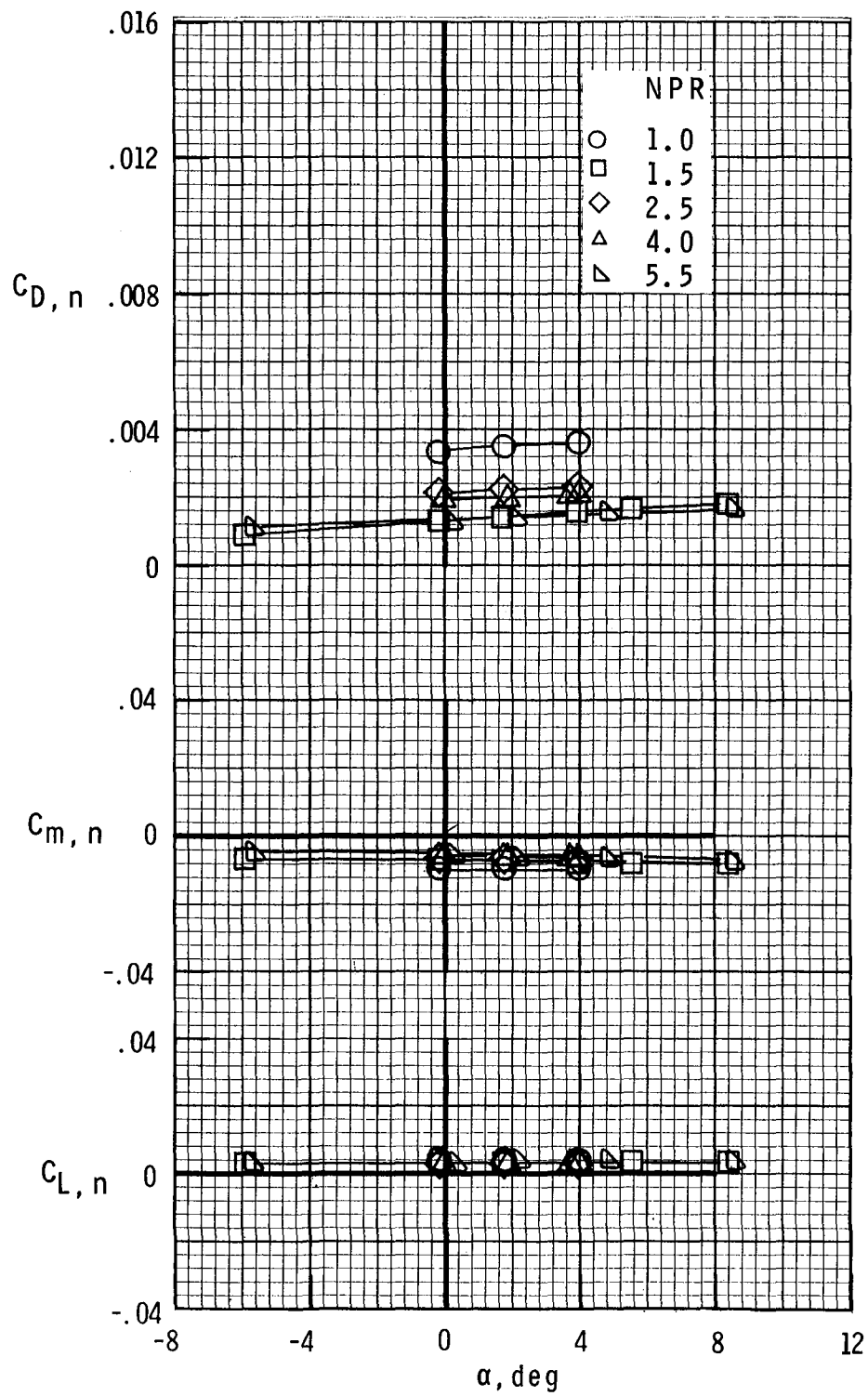
(l) Nozzle characteristics.
M = 0.9; Λ = 68°.

Figure 9.- Continued.
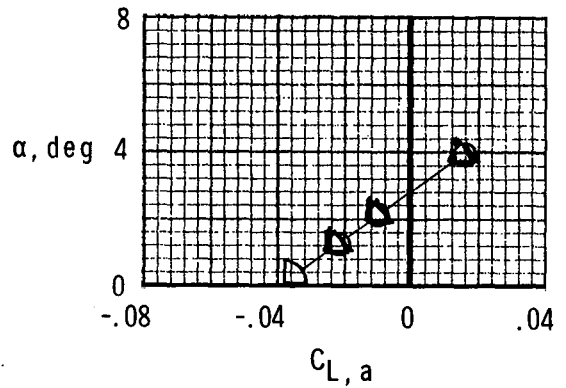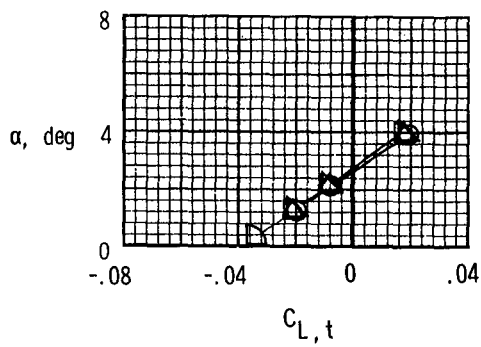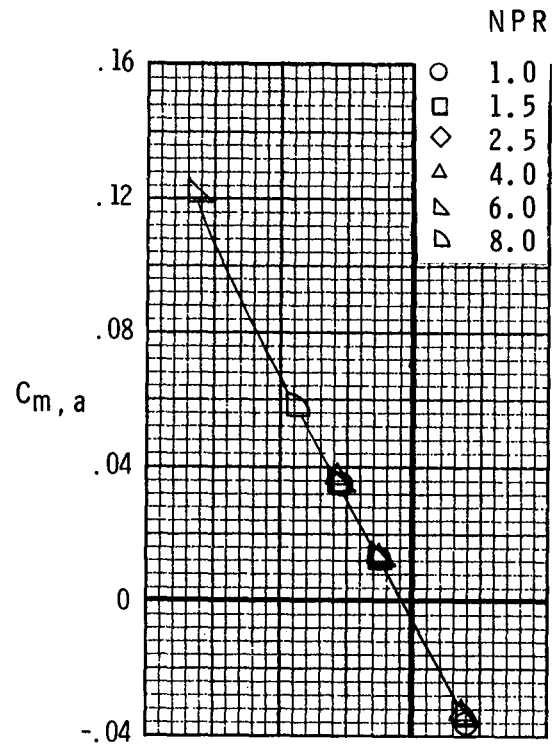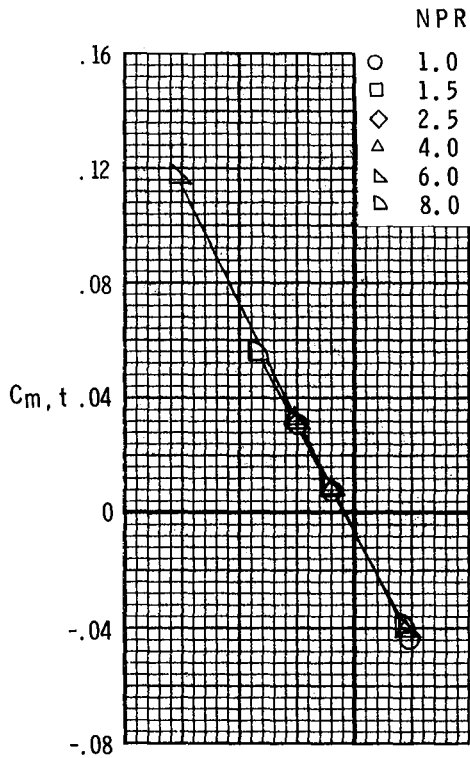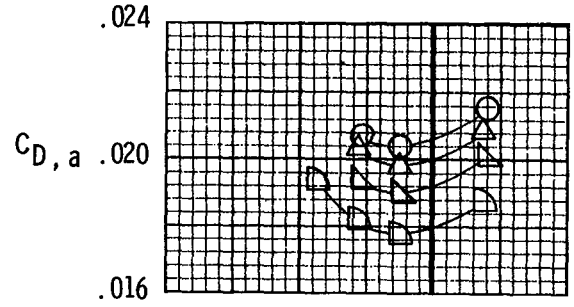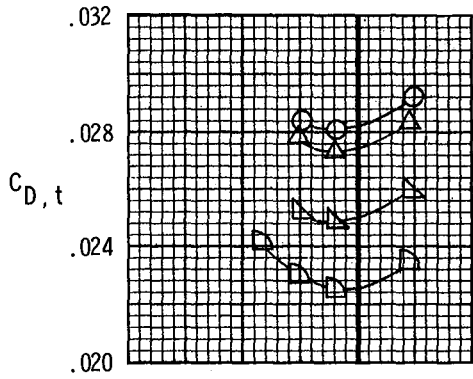
(m) Afterbody-nozzle characteristics.
M = 1.15;   Λ = 68°.

(n) Afterbody characteristics.
M = 1.15;   Λ = 68°.

Figure 9.- Continued.
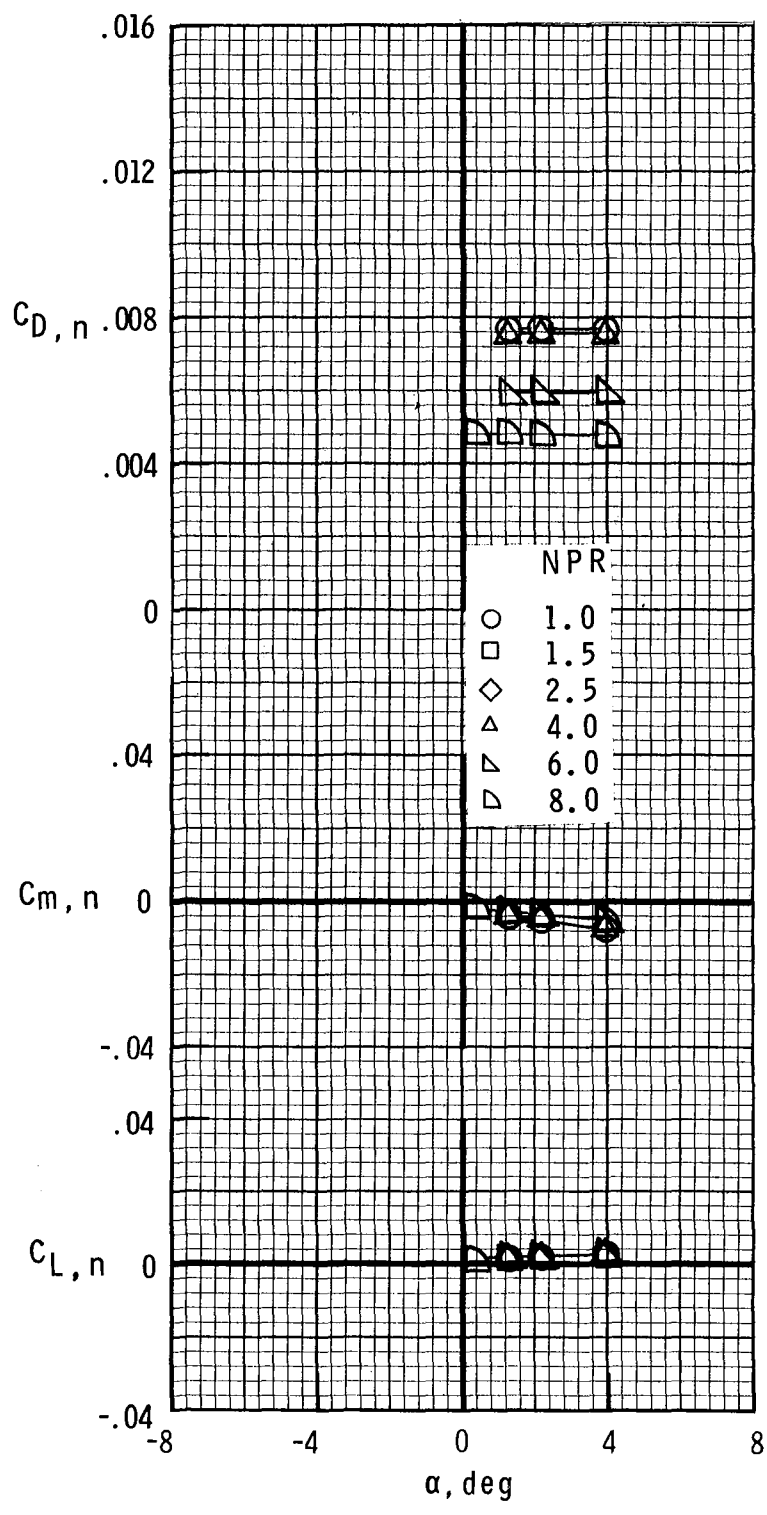
(o) Nozzle characteristics.
M = 1.15; Λ = 68°.
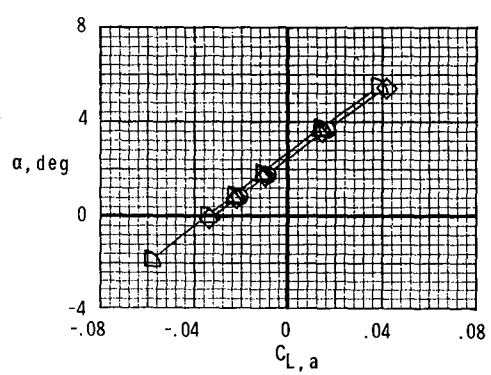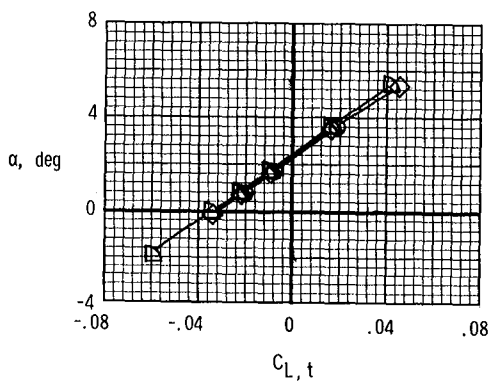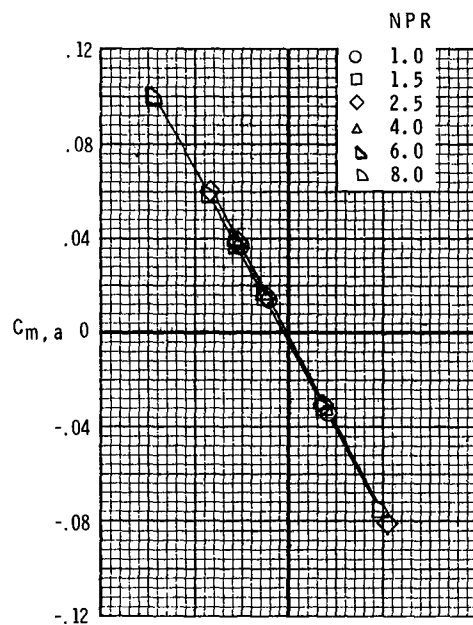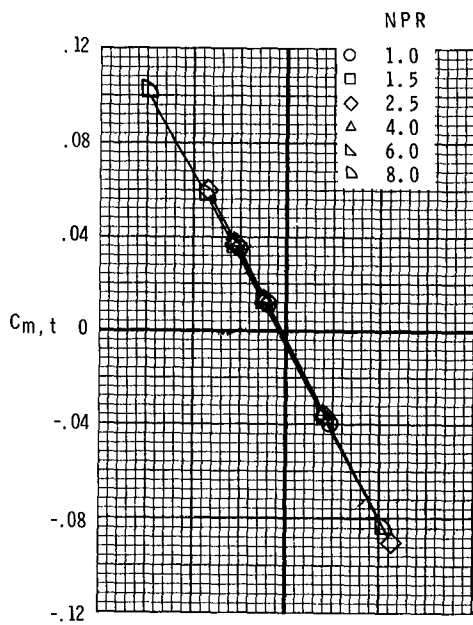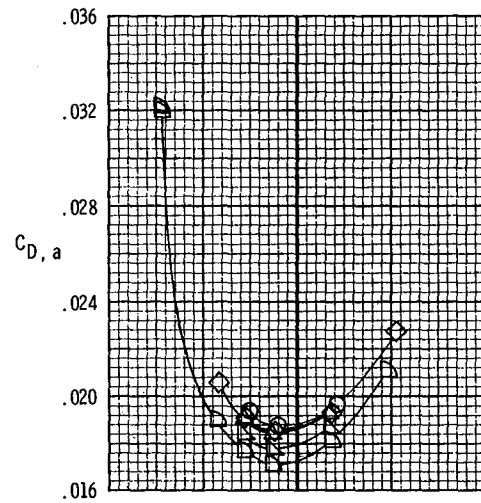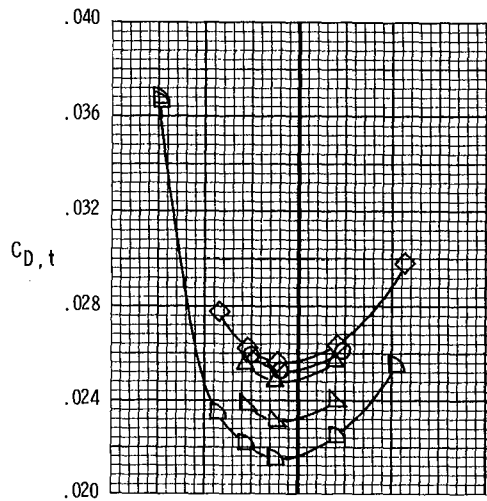
Figure 9.- Continued.

(p) Afterbody-nozzle characteristics.
M = 1.25; Λ = 68°.

(q) Afterbody characteristics.
M = 1.25; Λ = 68°.

Figure 9.- Continued.
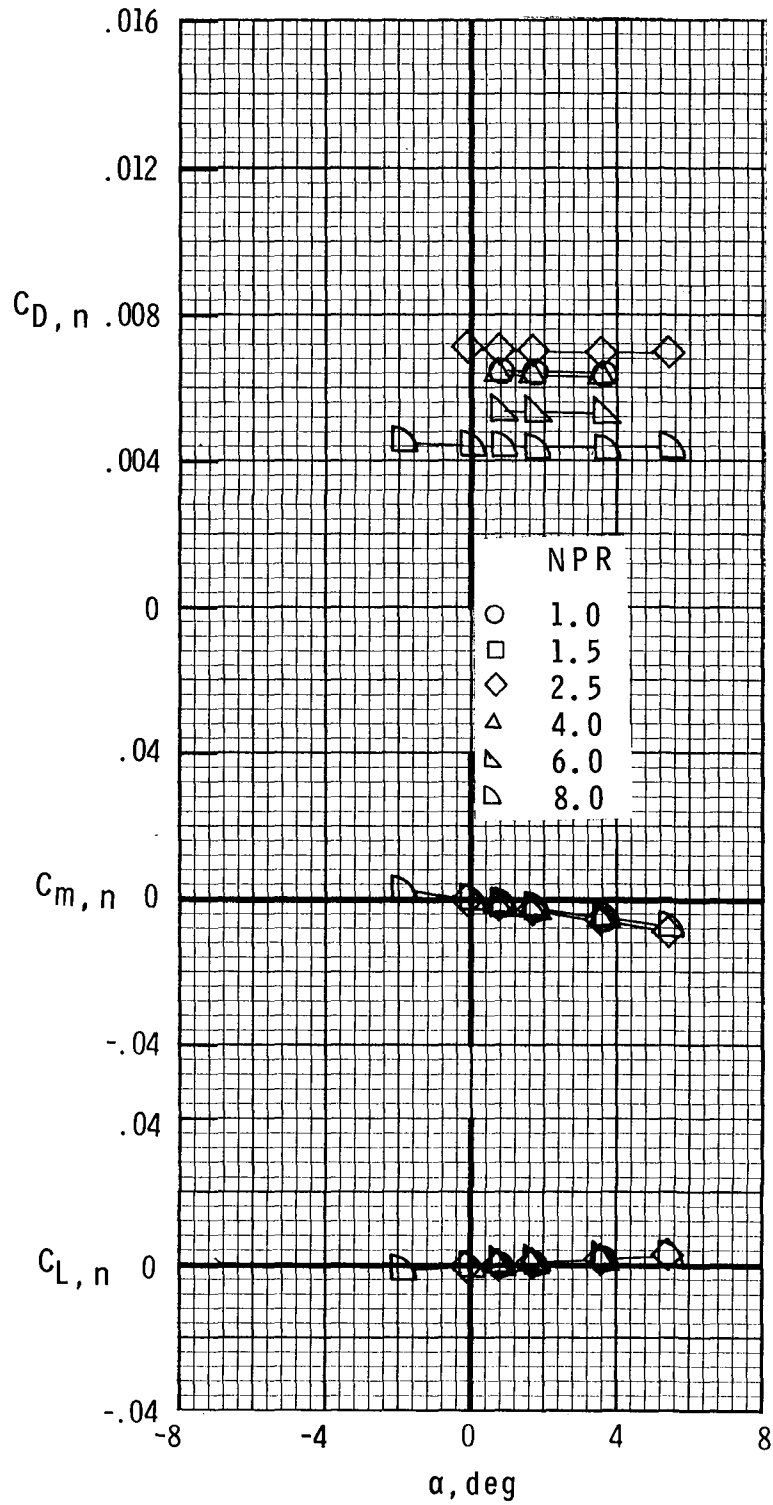
(r) Nozzle characteristics.
M = 1.25;   Λ = 68°.

Figure 9.- Concluded.
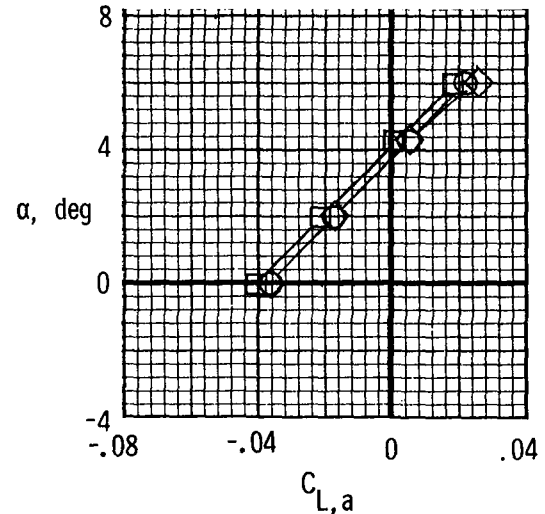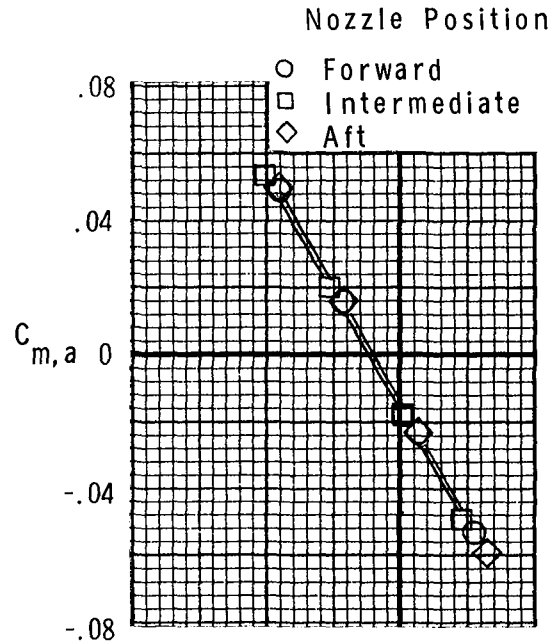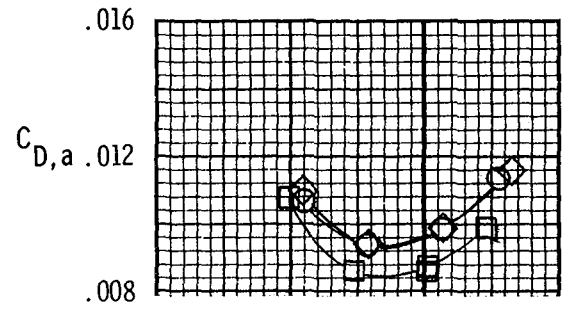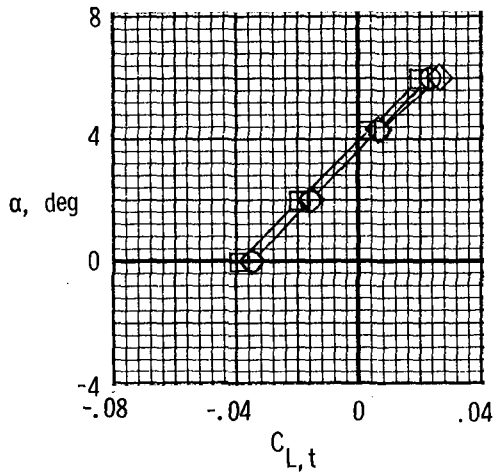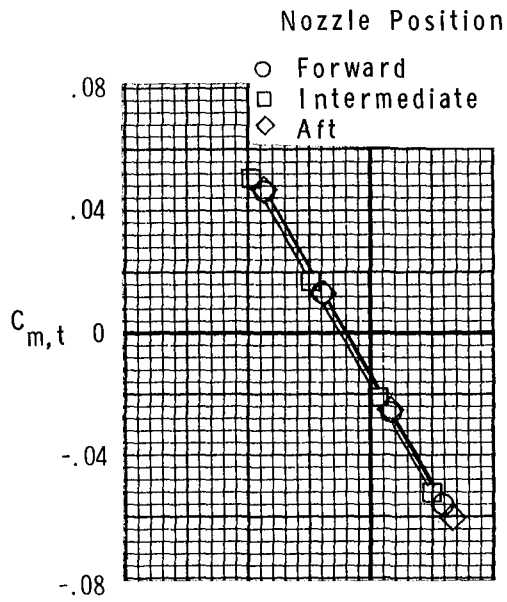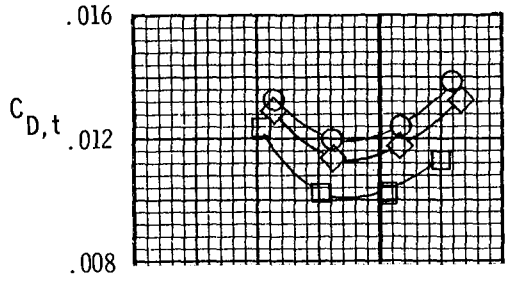
(a) Afterbody-nozzle characteristics. M = 0.7; NPR, 3.5; Λ = 22°.

(b) Afterbody characteristics. M = 0.7; NPR, 3.5; Λ = 22°.

Figure 10.- Effect of cruise-nozzle position on afterbody-nozzle aerodynamic characteristics.
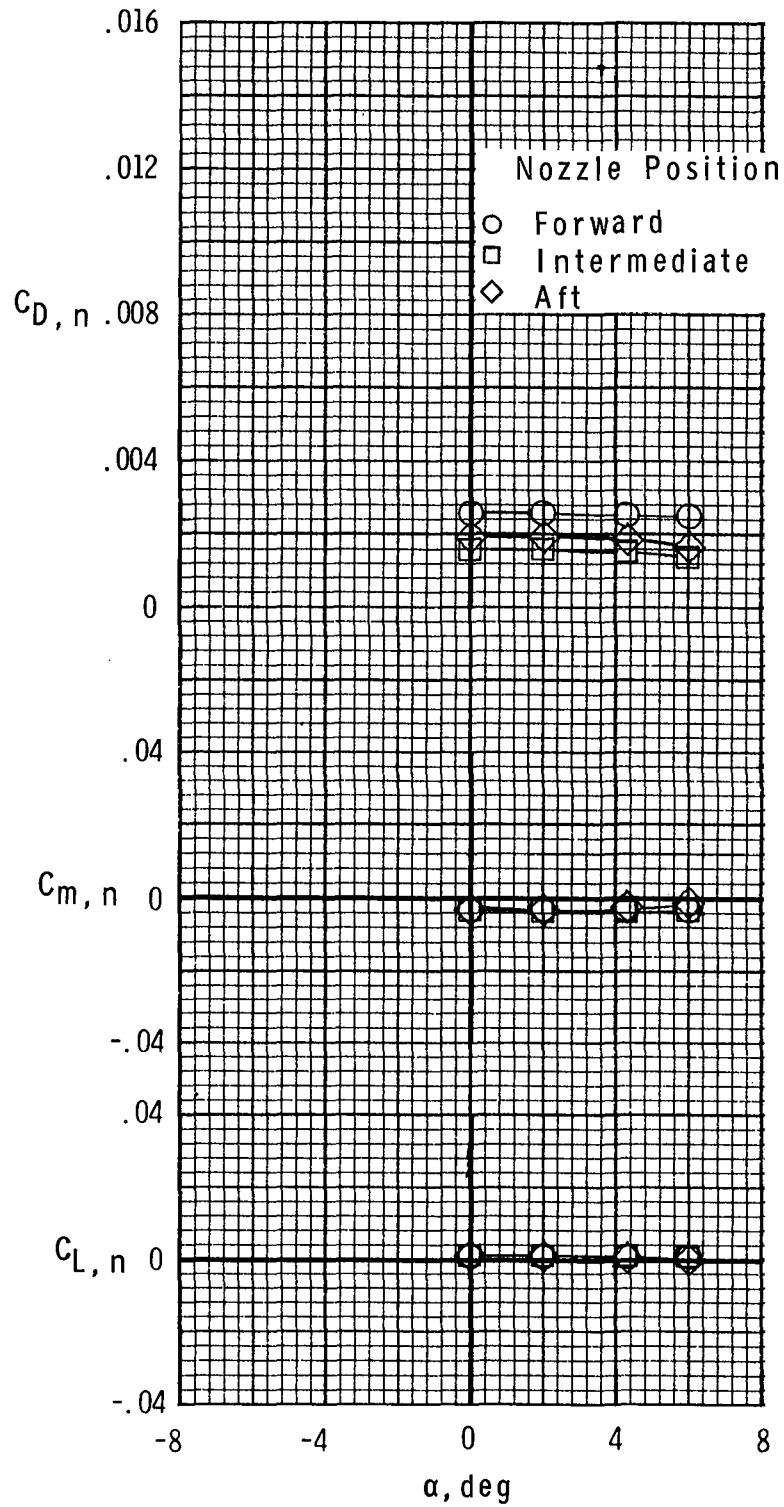
(c) Nozzle characteristics. M = 0.7;
NPR, 3.5; Λ = 22°.
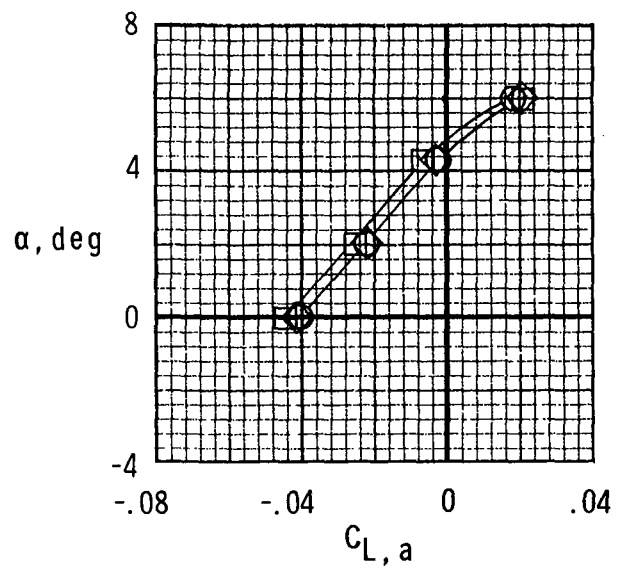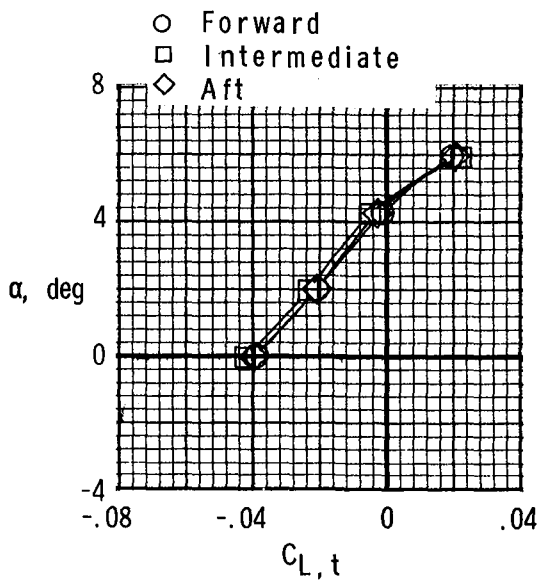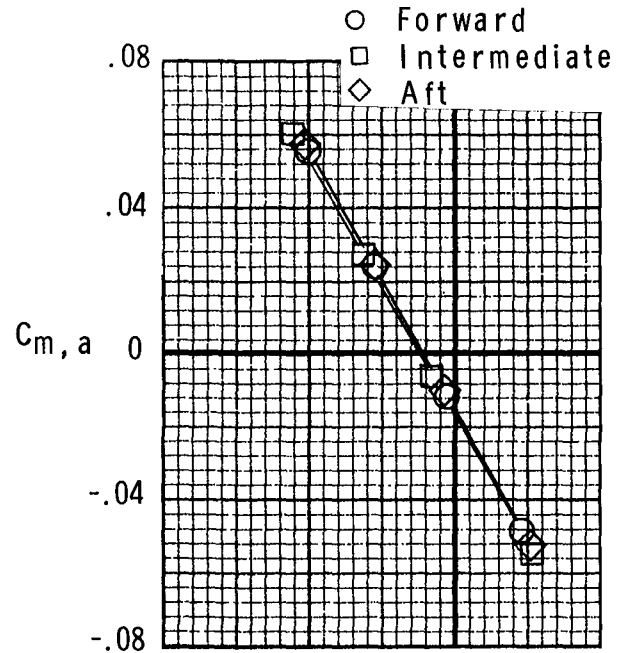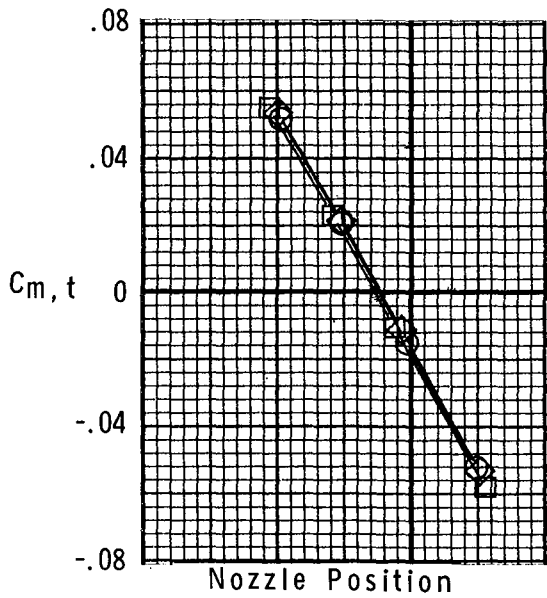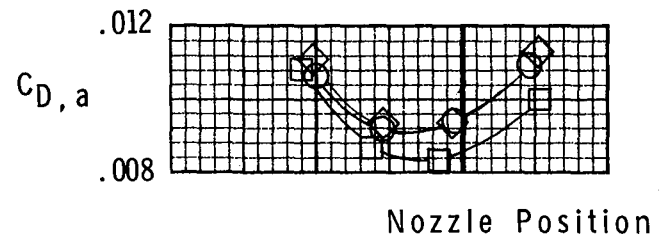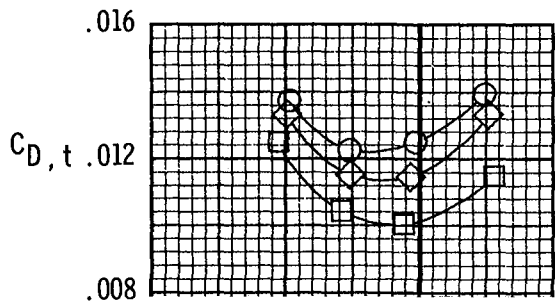
Figure 10.- Continued.

(d) Afterbody-nozzle characteristics.
M = 0.8; NPR, 3.5; Λ = 22°.

(e) Afterbody characteristics. M = 0.8;
NPR, 3.5; Λ = 22°.

Figure 10.- Continued.
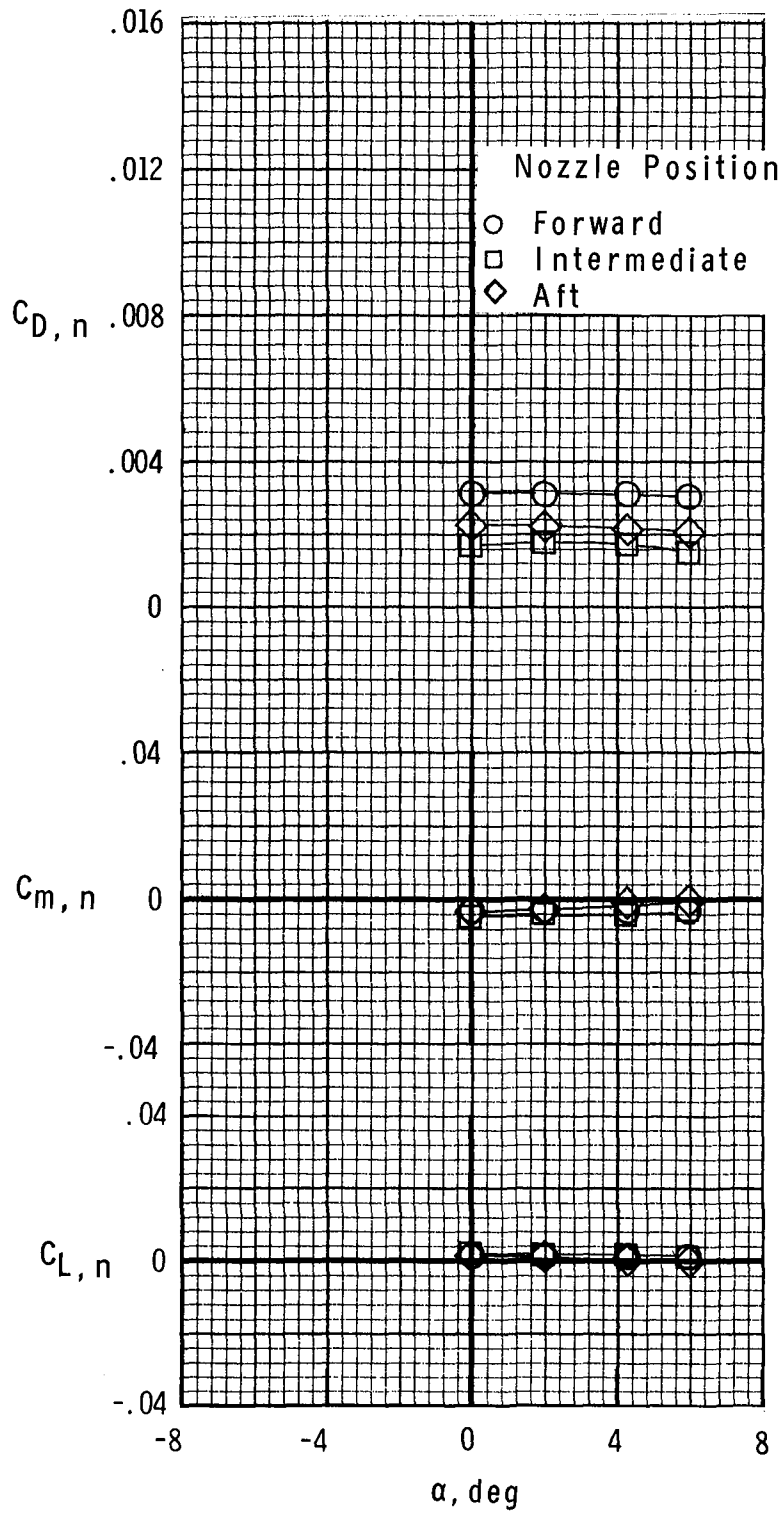
(f) Nozzle characteristics. M = 0.8;
NPR, 3.5; Λ = 22°.
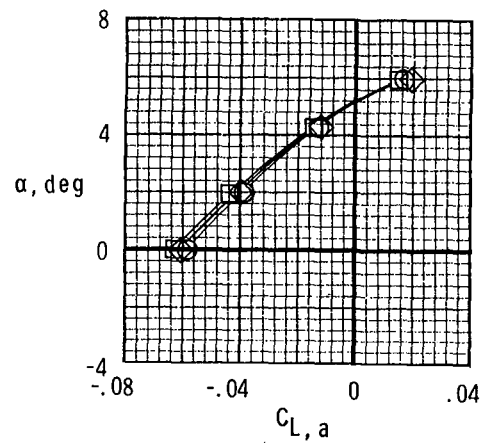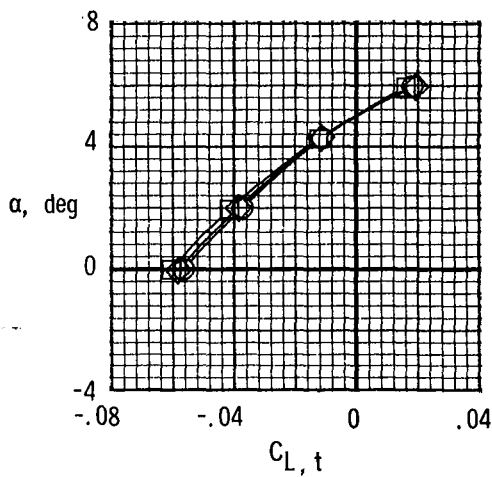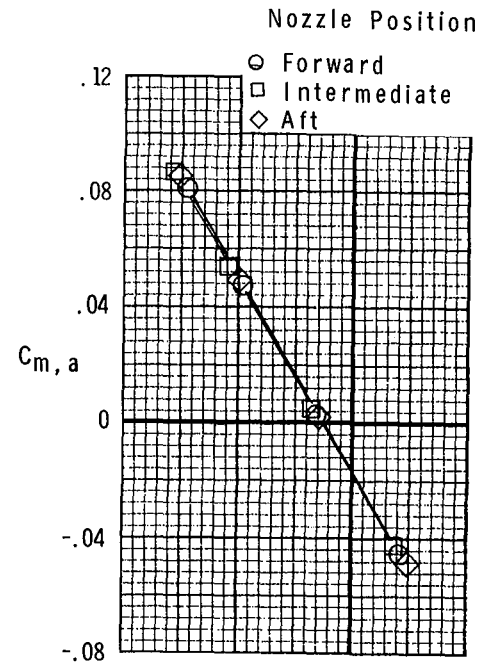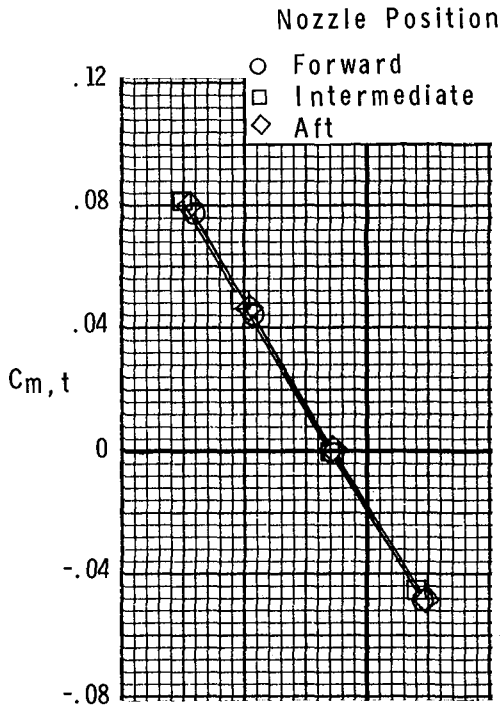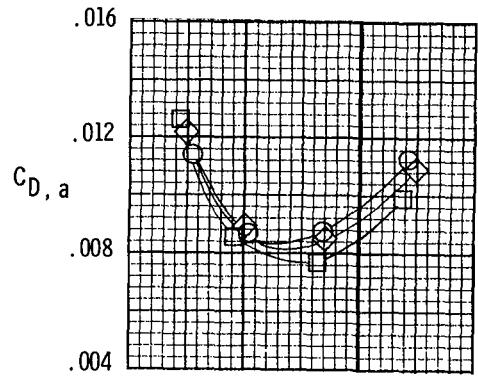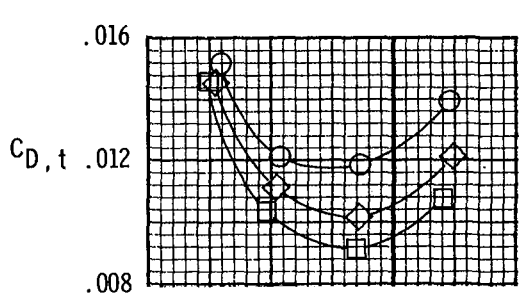
Figure 10.- Continued.

(g) Afterbody-nozzle characteristics.
M = 0.9; NPR, 5.5; Λ = 22°.

(h) Afterbody characteristics. M = 0.9;
NPR, 5.5; Λ = 22°.

Figure 10.- Continued.
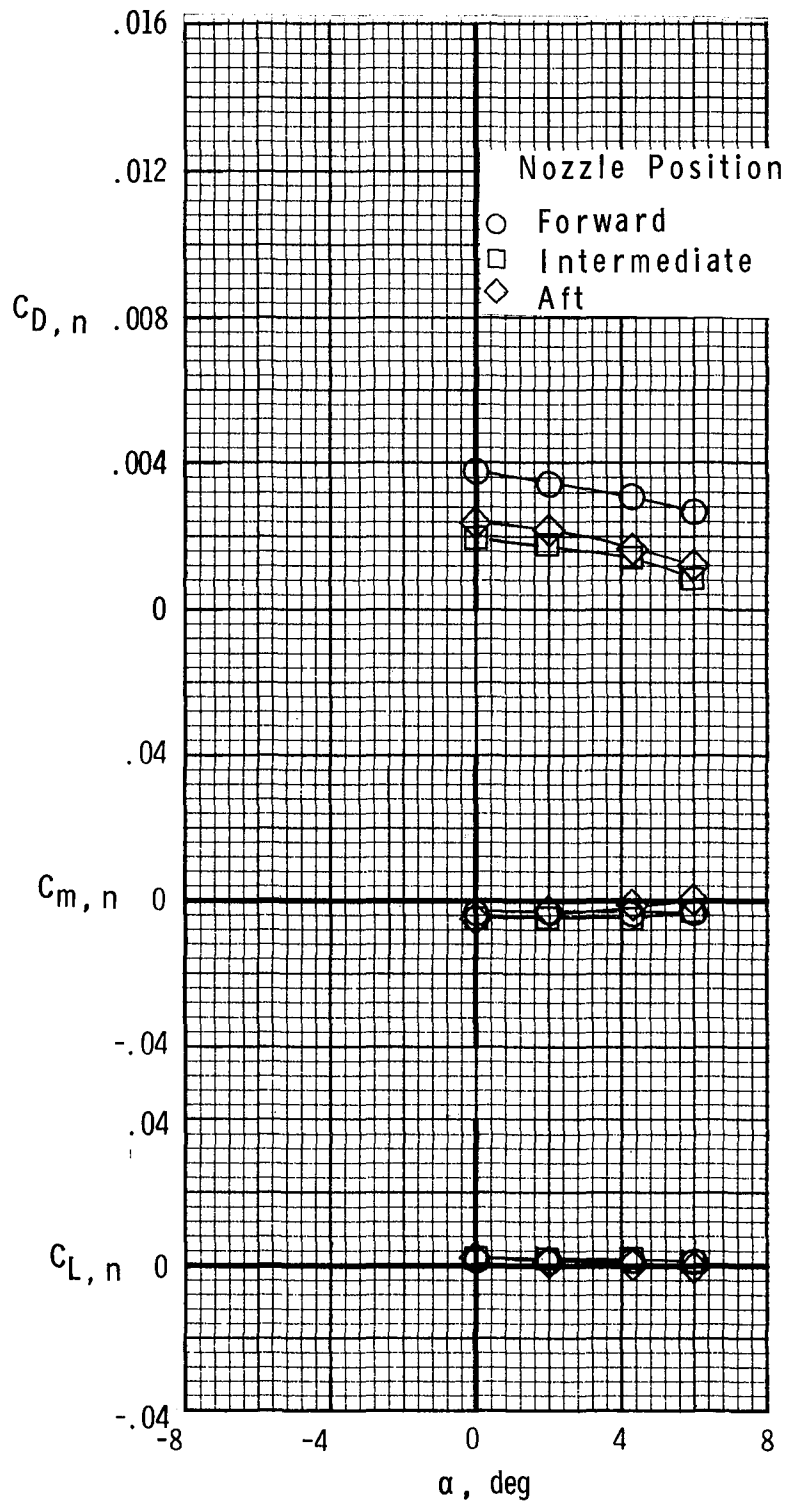
(i) Nozzle characteristics. M = 0.9;
NPR, 5.5; Λ = 22°.
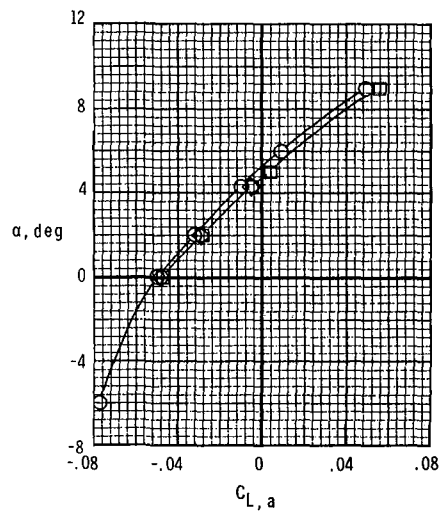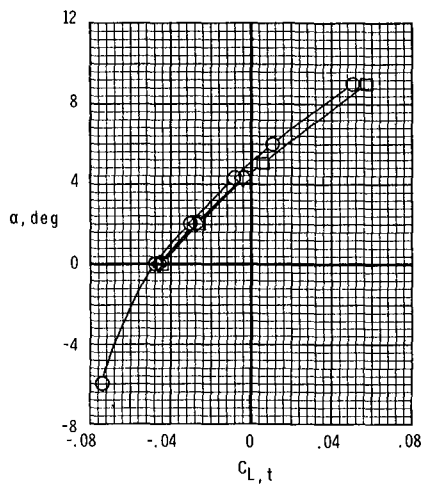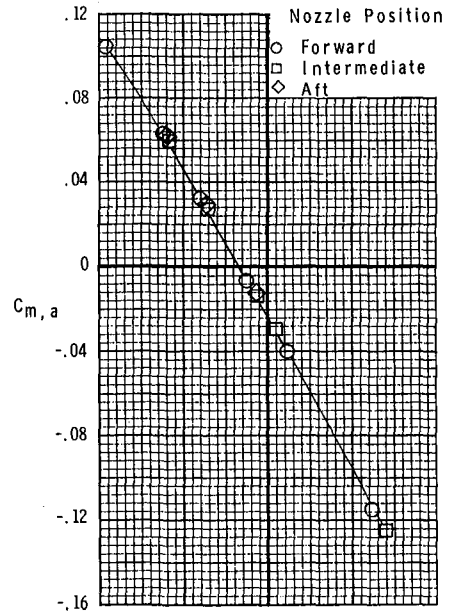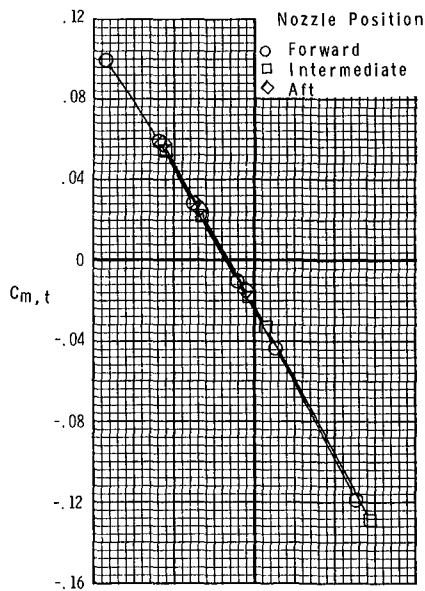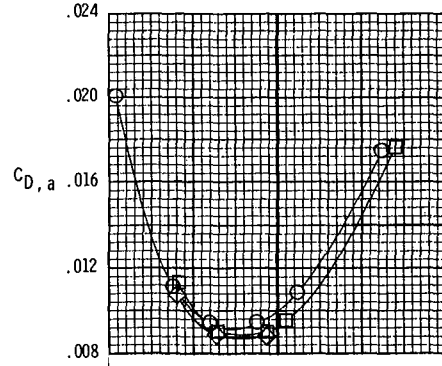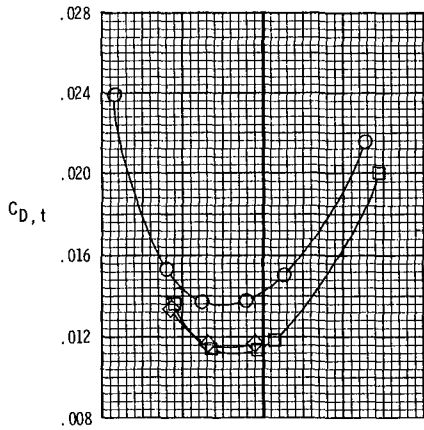
Figure 10.- Continued.

(j) Afterbody-nozzle characteristics.
M = 0.9; NPR, 5.5; Λ = 68°.

(k) Afterbody characteristics. M = 0.9;
NPR, 5.5; Λ = 68°.

Figure 10.- Continued.

81
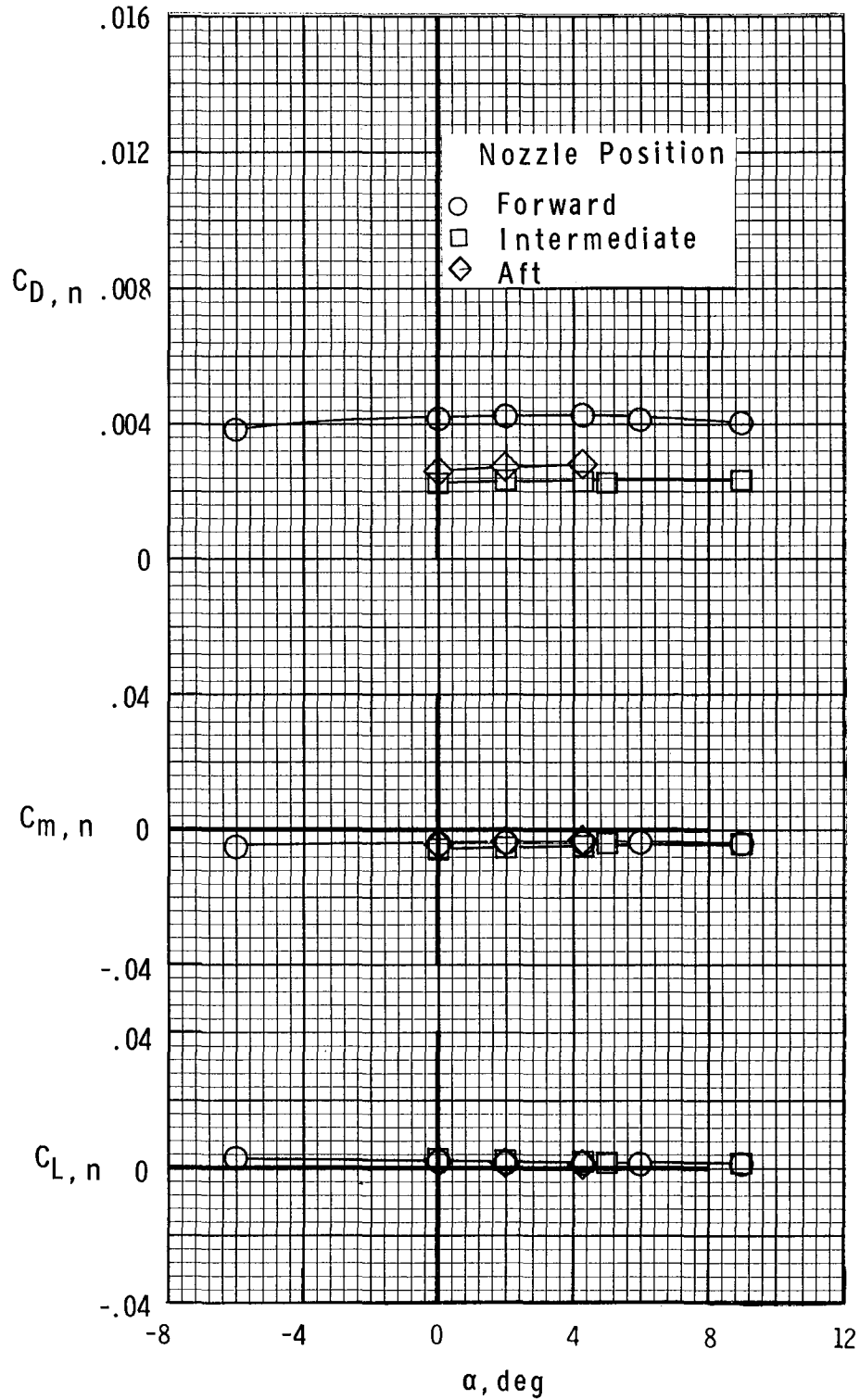
(1) Nozzle characteristics. M = 0.9;
NPR, 5.5; Λ = 68°.

Figure 10.- Continued.
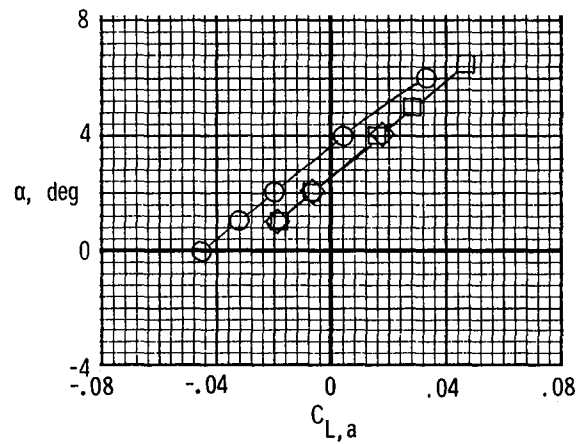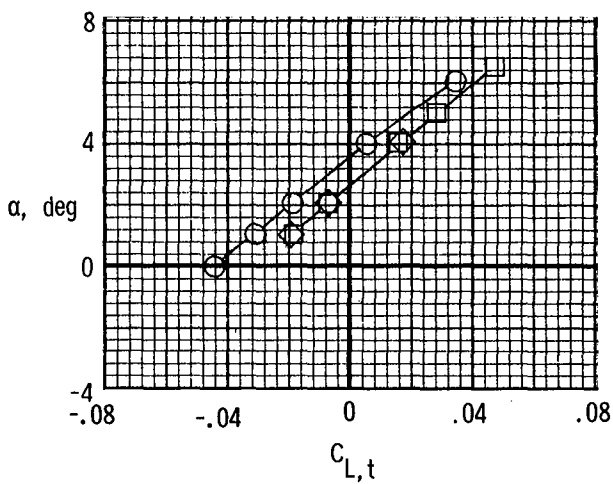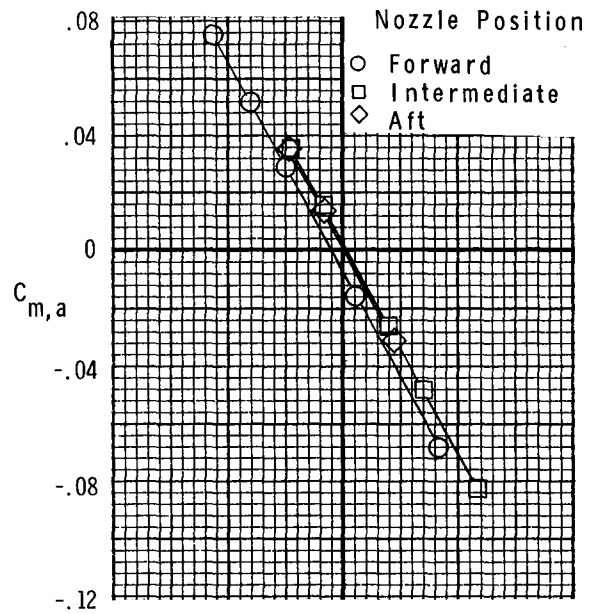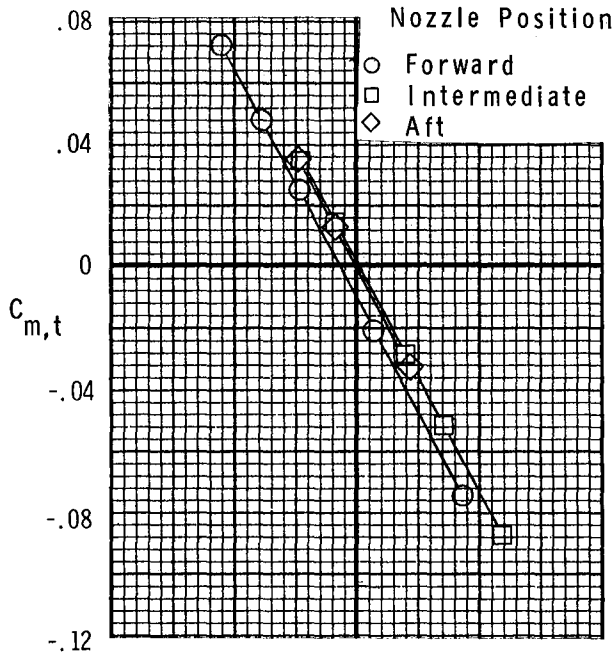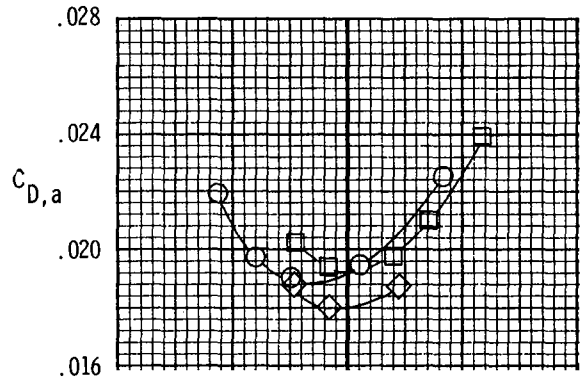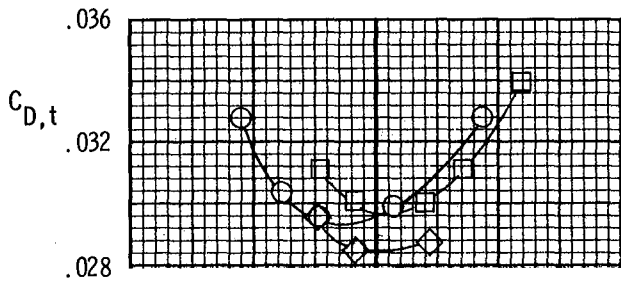
(m) Afterbody-nozzle characteristics.
M = 1.15; NPR, 8.0; Λ = 68°.

(n) Afterbody characteristics. M = 1.15;
NPR, 8.0; Λ = 68°.

Figure 10.- Continued.
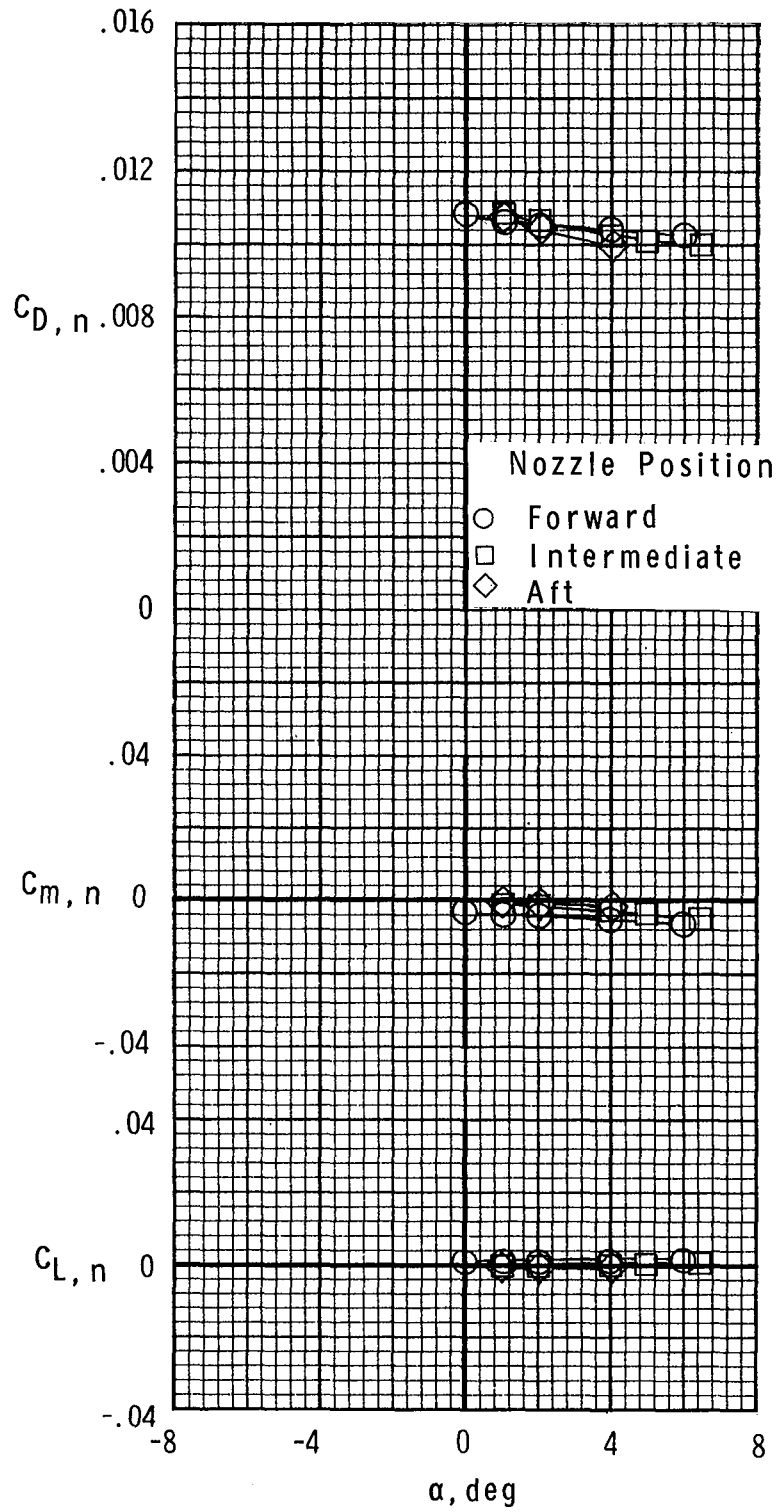
(o) Nozzle characteristics. M = 1.15;
NPR, 8.0; Λ = 68°.

Figure 10.- Continued.
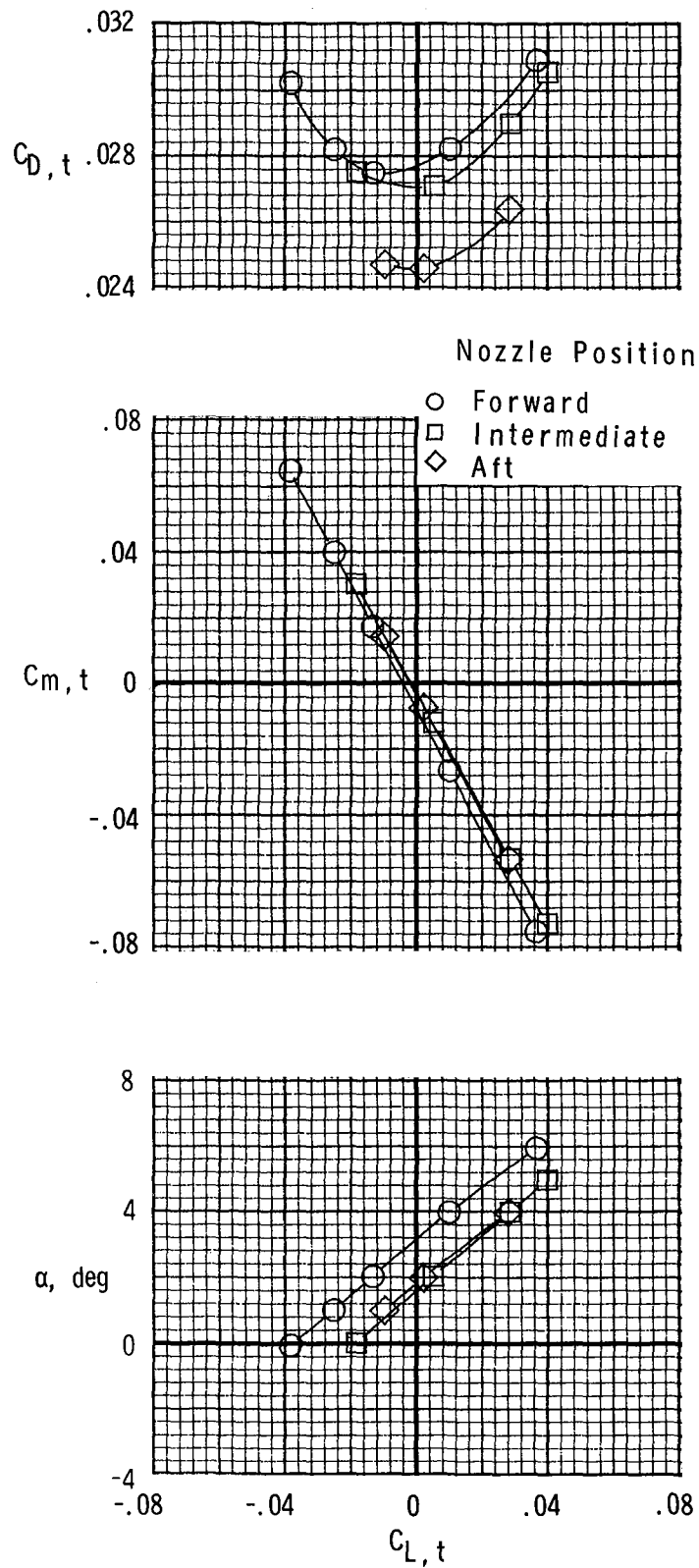
(p) Afterbody-nozzle characteristics.
M = 1.25; NPR, 8.0; Λ = 68°.

Figure 10.- Continued.

(q) Afterbody characteristics. M = 1.25;
NPR, 8.0; Λ = 68°.

Figure 10.- Continued.
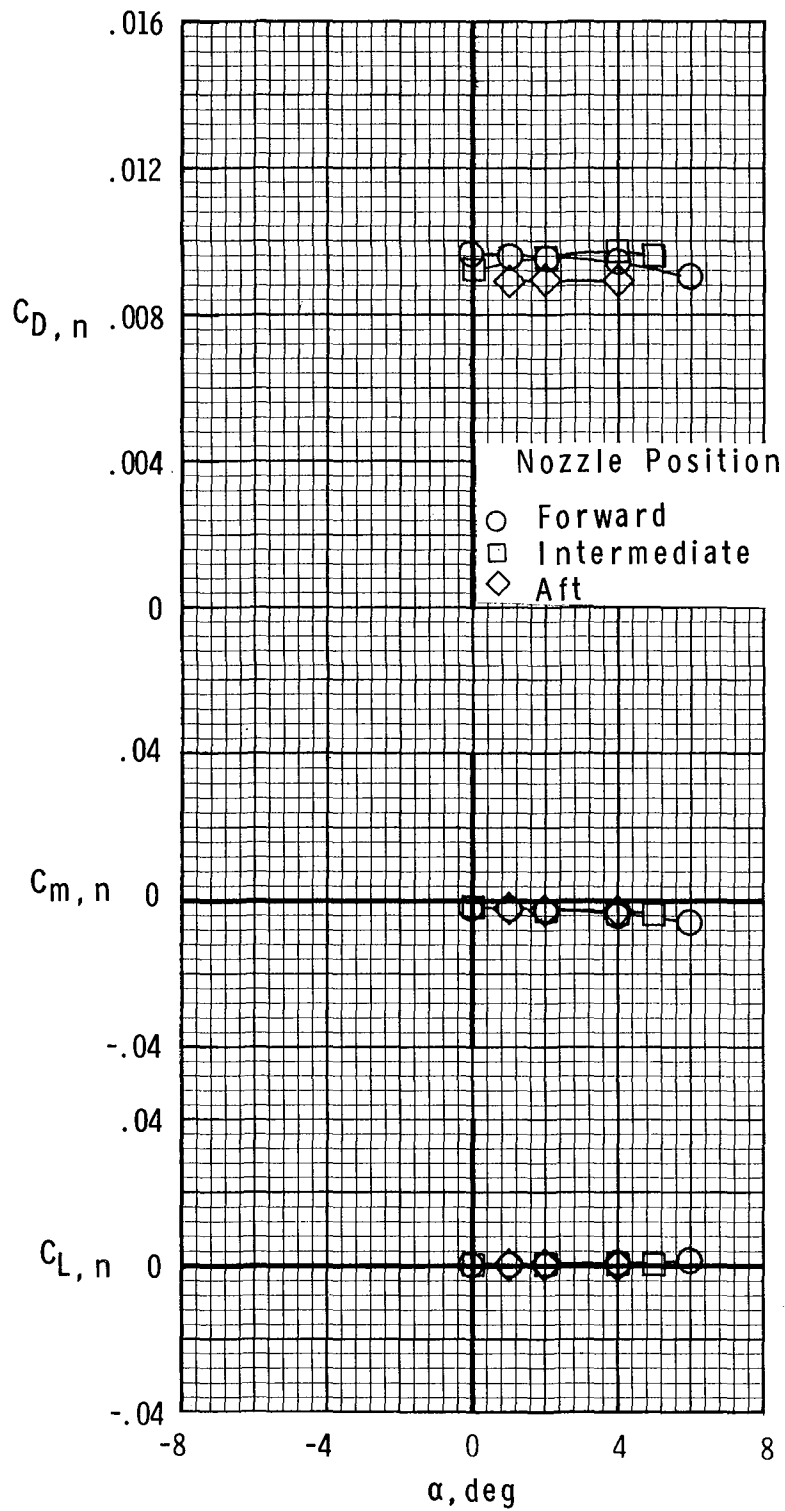
(r) Nozzle characteristics. M = 1.25;
NPR, 8.0; Λ = 68°.

Figure 10.- Concluded.
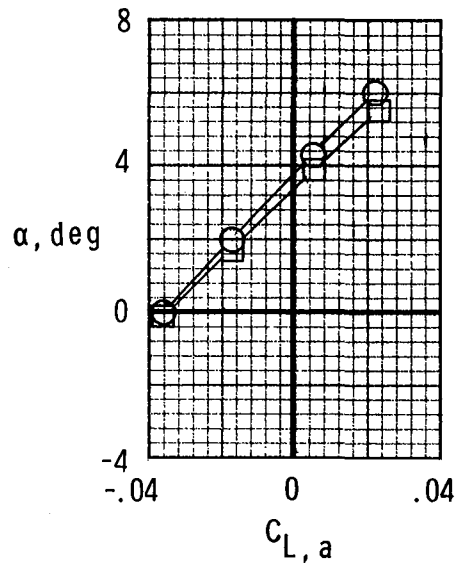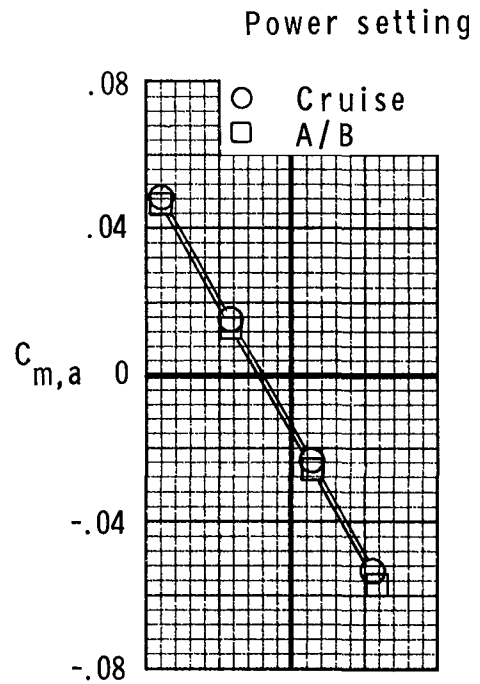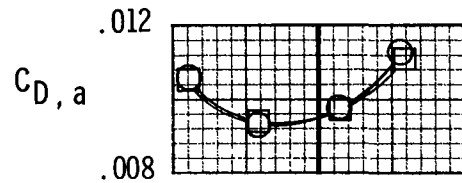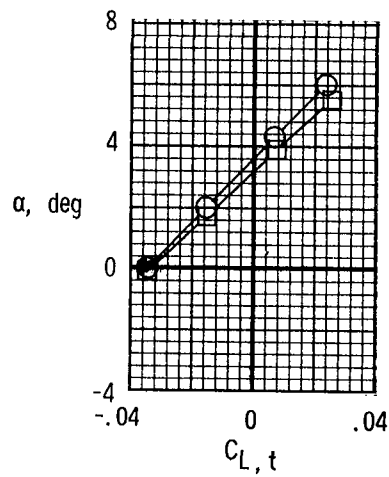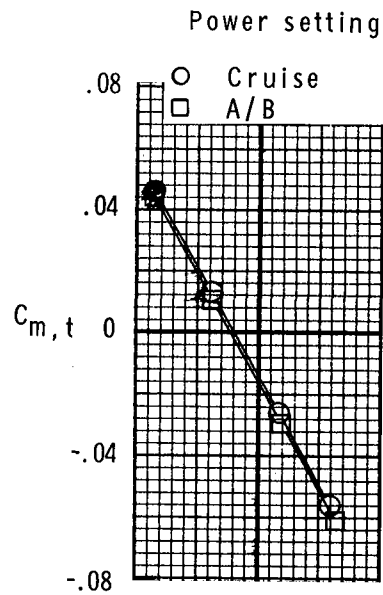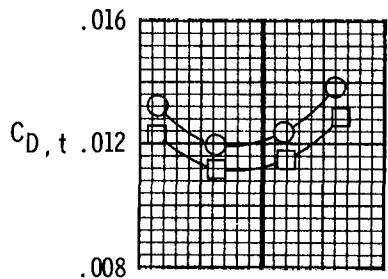
(a) Afterbody-nozzle characteristics.
M = 0.7; NPR, 3.5; Λ = 22°.

(b) Afterbody characteristics. M = 0.7;
NPR, 3.5; Λ = 22°.

Figure 11.- Effect of power setting on afterbody-nozzle characteristics
for configurations with nozzles in forward position.

88

(c) Nozzle characteristics. M = 0.7; NPR, 3.5; Λ = 22°.
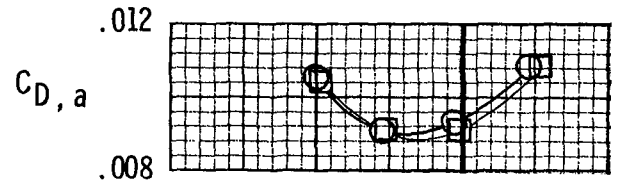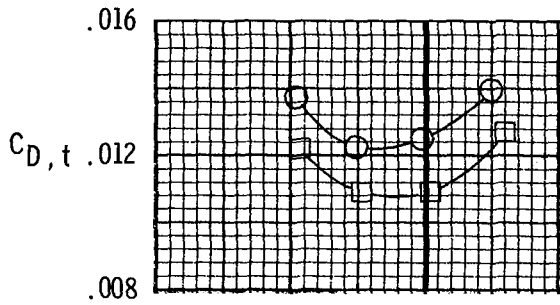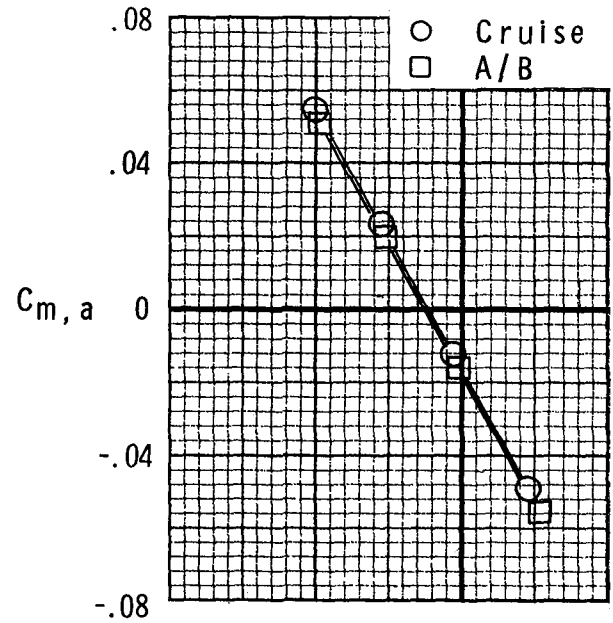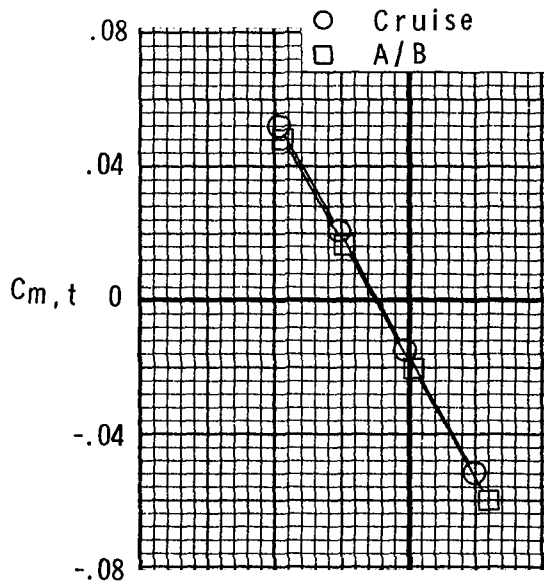
Figure 11.- Continued.
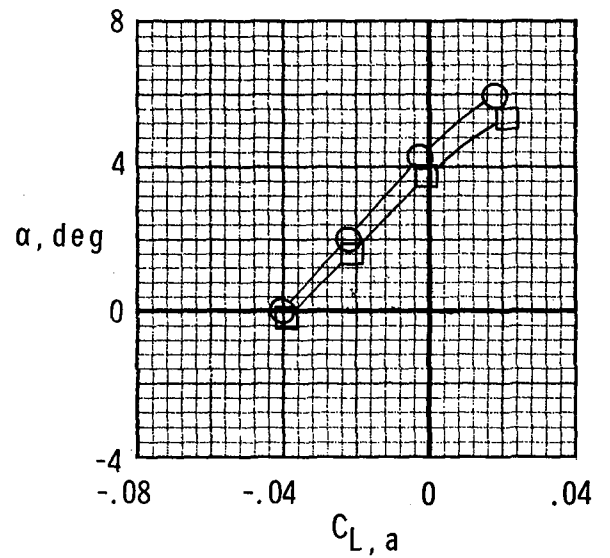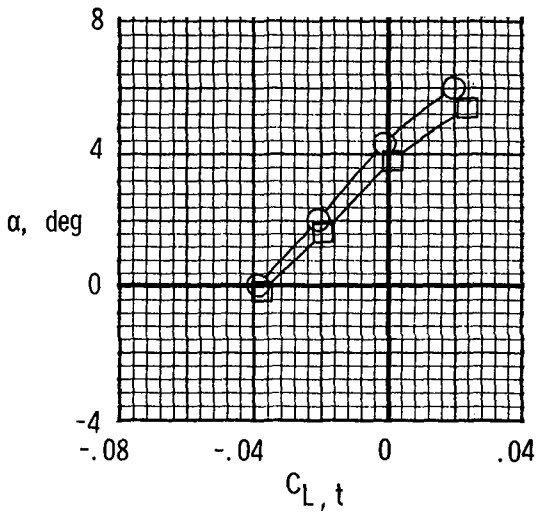
(d) Afterbody-nozzle characteristics.
M = 0.8; NPR, 3.5; Λ = 22°.

(e) Afterbody characteristics. M = 0.8;
NPR, 3.5; Λ = 22°.
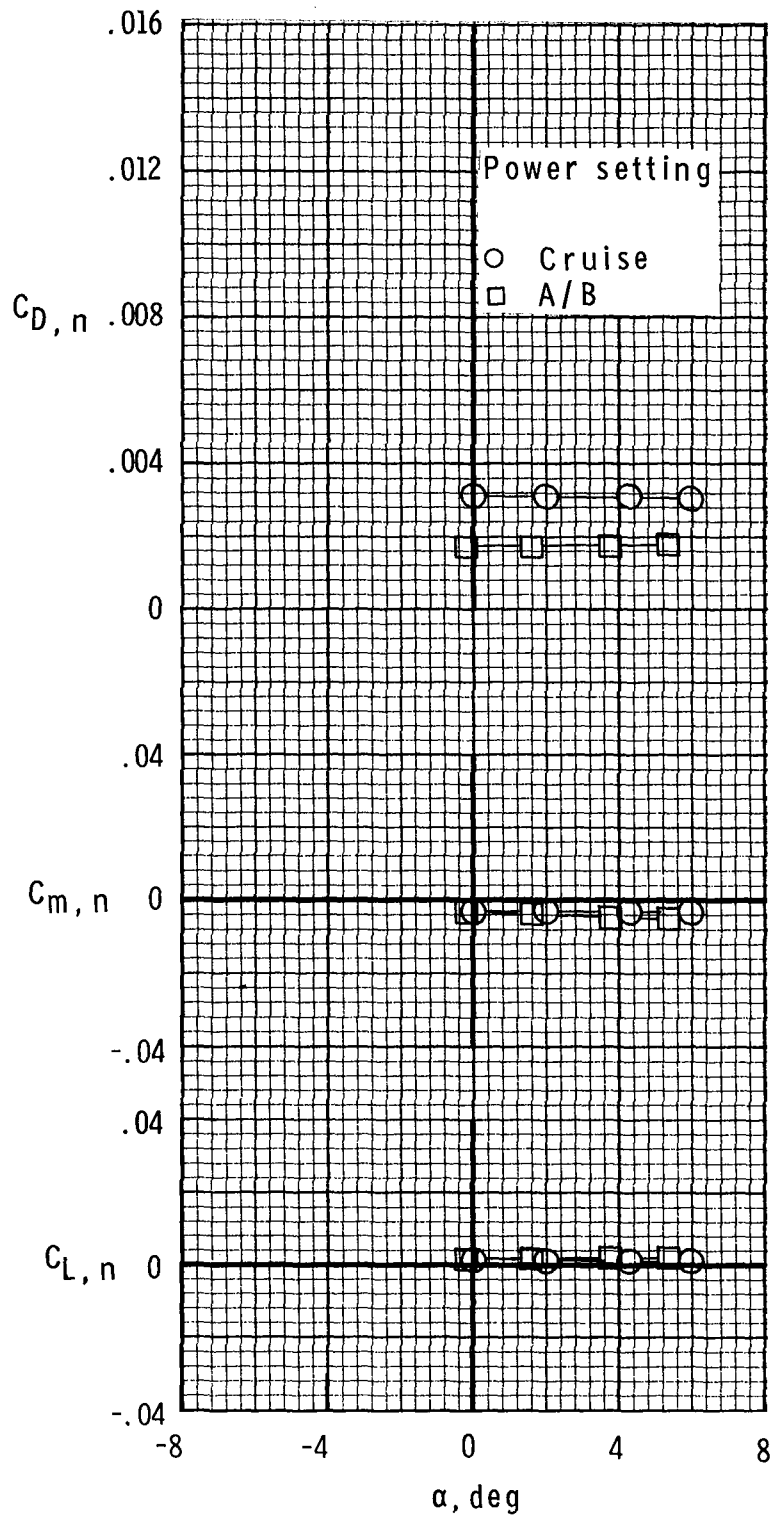
Figure 11.- Continued.

(f) Nozzle characteristics. M = 0.8;
NPR, 3.5; Λ = 22°.
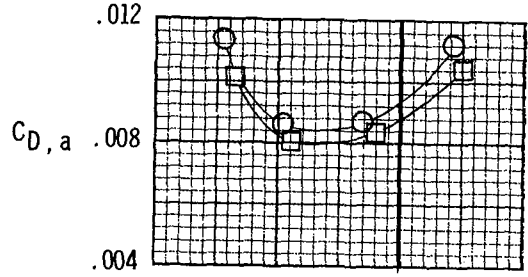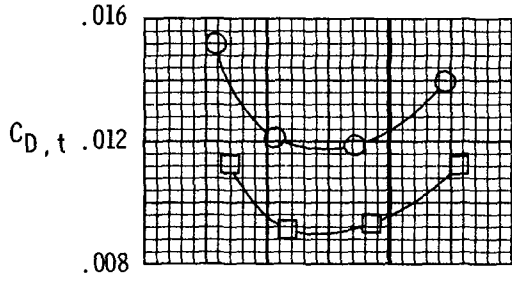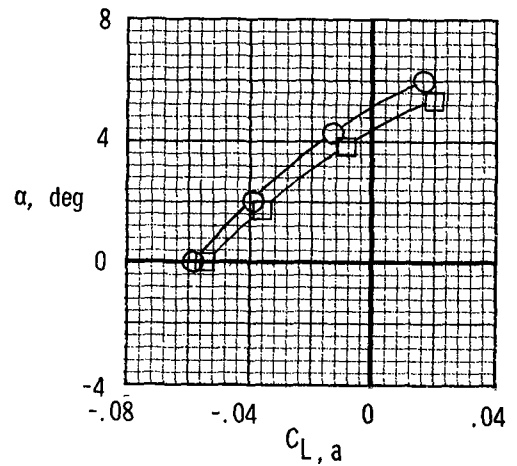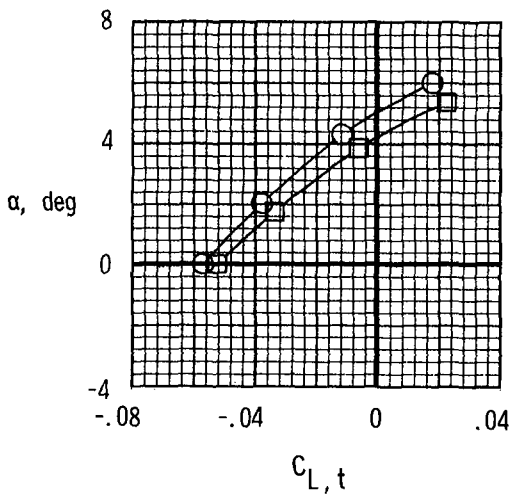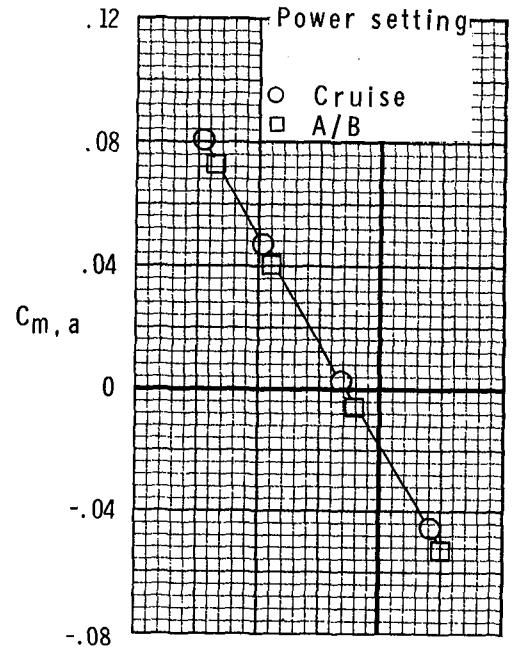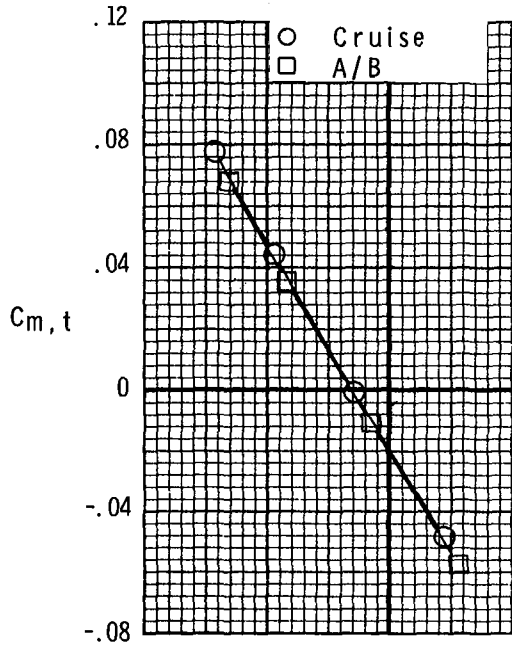
Figure 11.- Continued.

(g) Afterbody-nozzle characteristics.
M = 0.9; NPR, 5.5; Λ = 22°.

(h) Afterbody characteristics. M = 0.9;
NPR, 5.5; Λ = 22°.

Figure 11.- Continued.
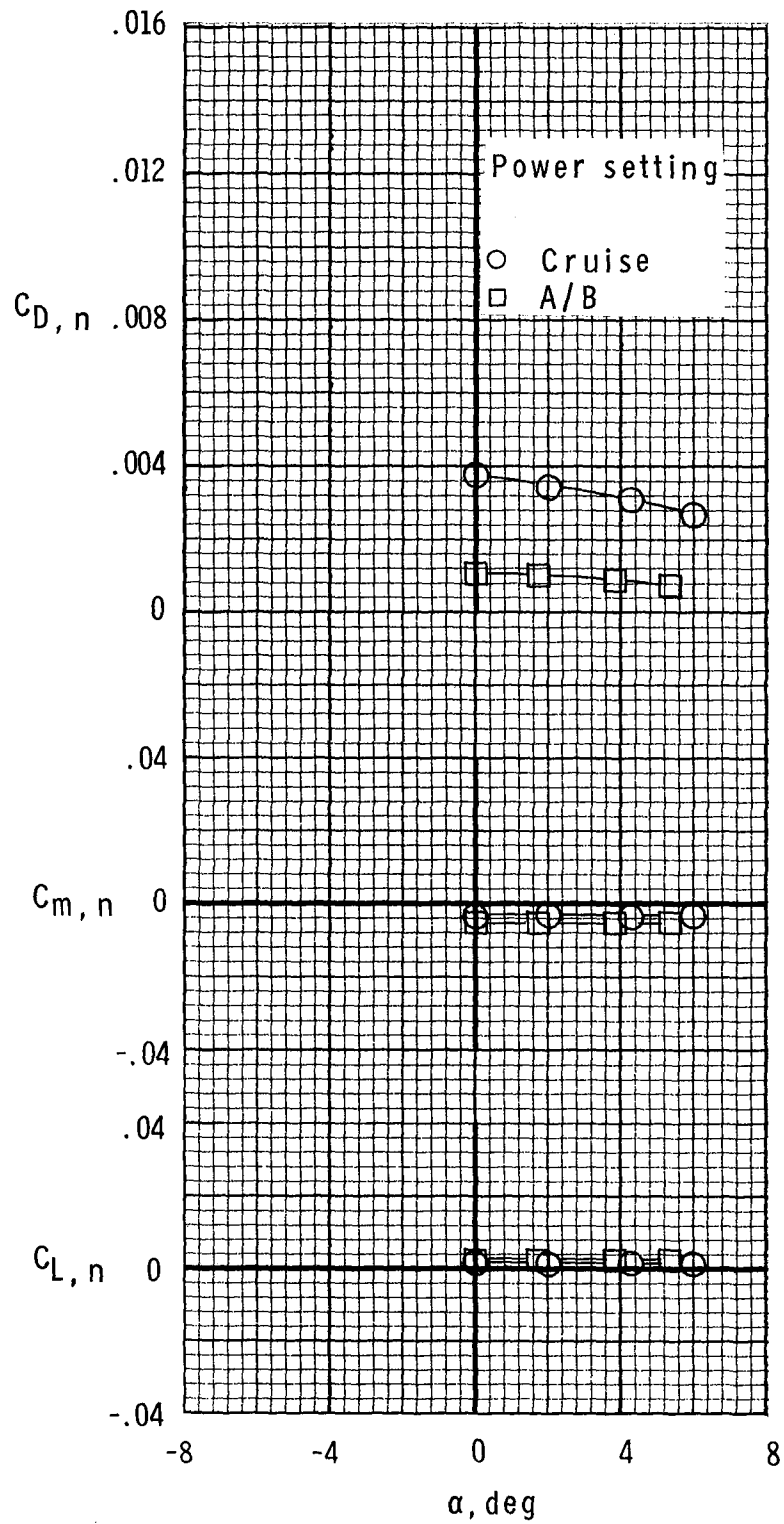
(i) Nozzle characteristics. M = 0.9;
NPR, 5.5; Λ = 22°.
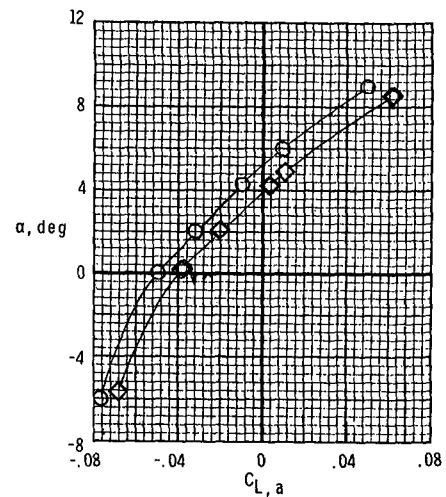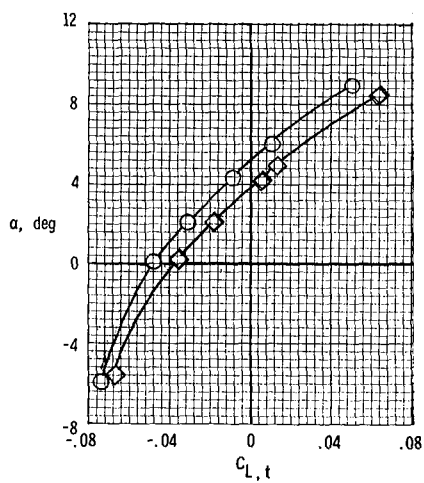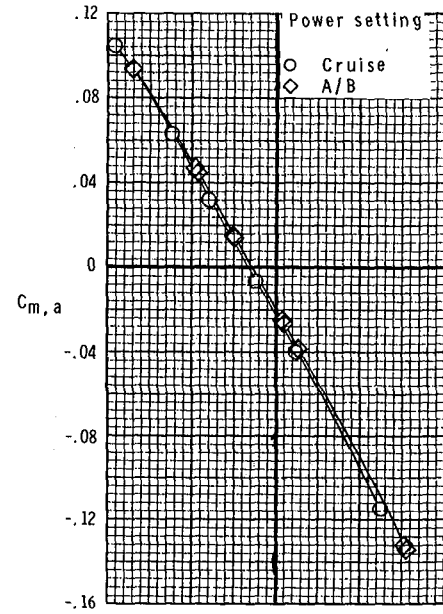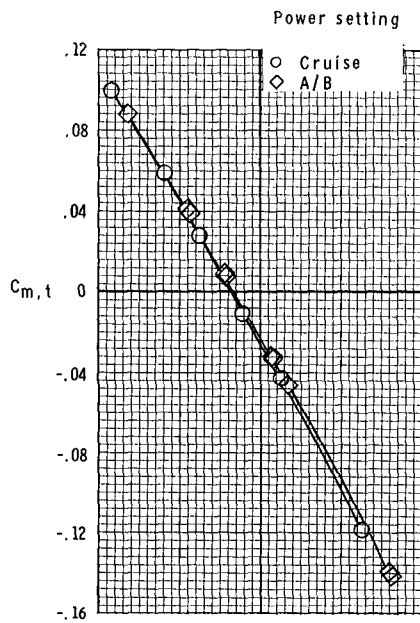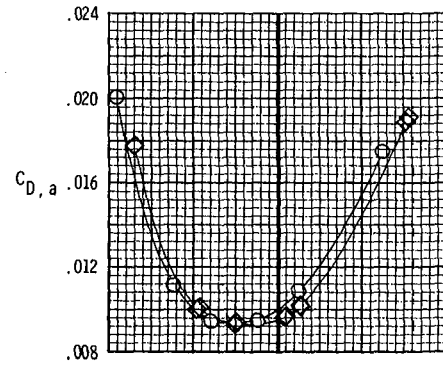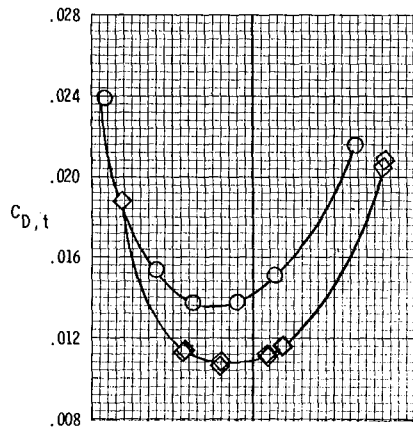
Figure 11.- Continued.

(j) Afterbody-nozzle characteristics.
M = 0.9;   NPR, 5.5;   Λ = 68°.

(k) Afterbody characteristics.   M = 0.9;
NPR, 5.5;   Λ = 68°.

Figure 11.- Continued.
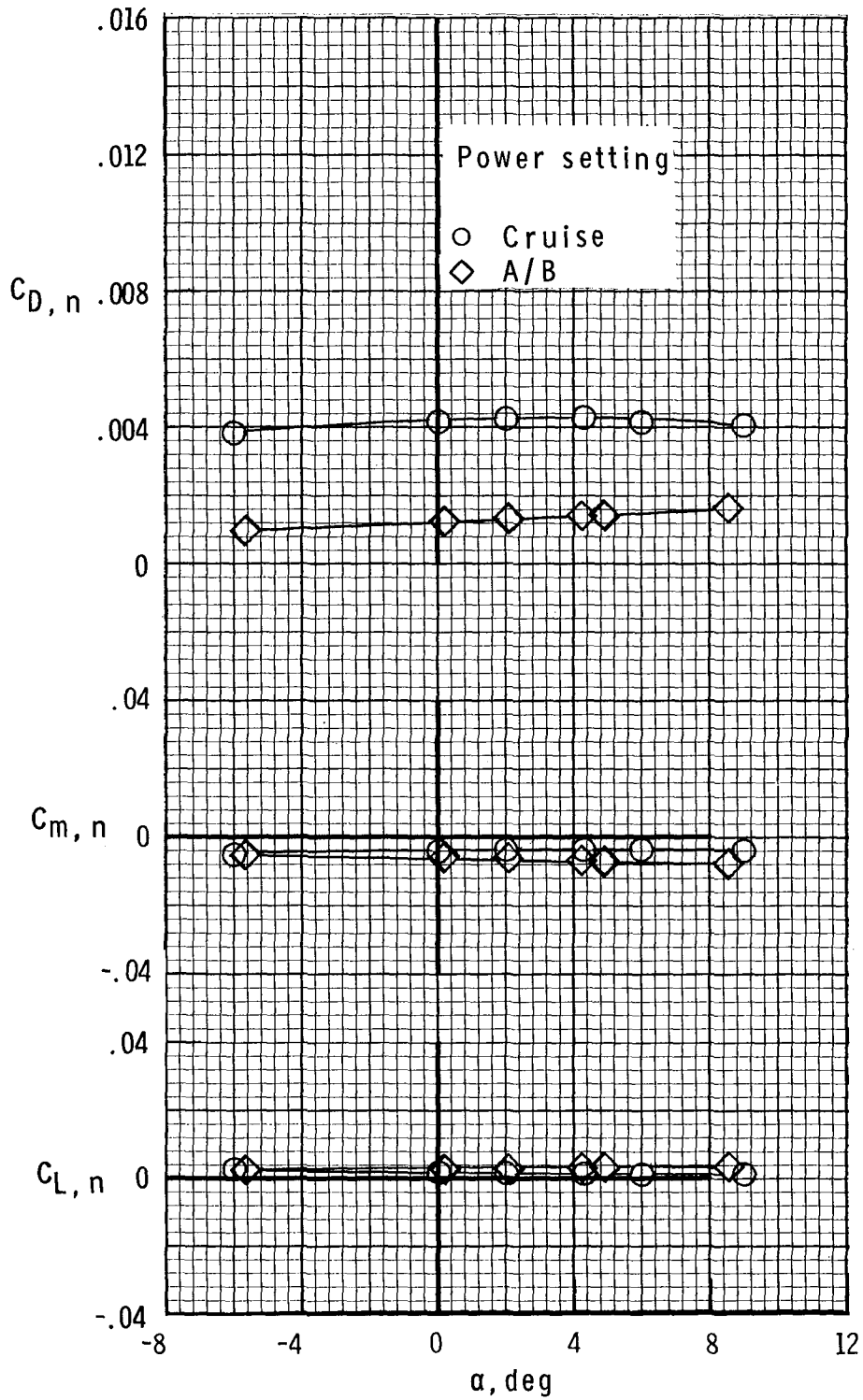
(1) Nozzle characteristics. M = 0.9;
NPR, 5.5; Λ = 68°.
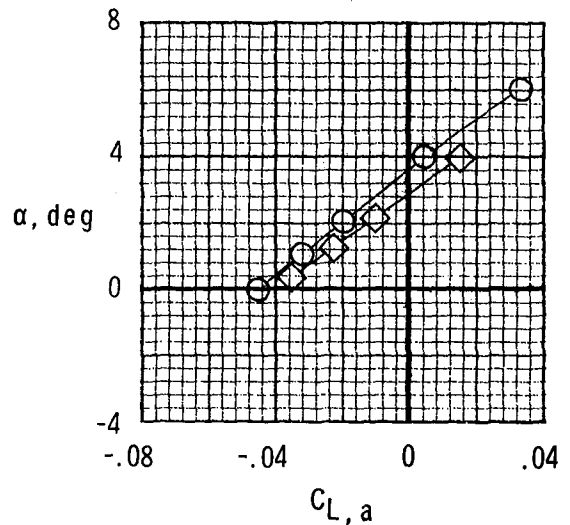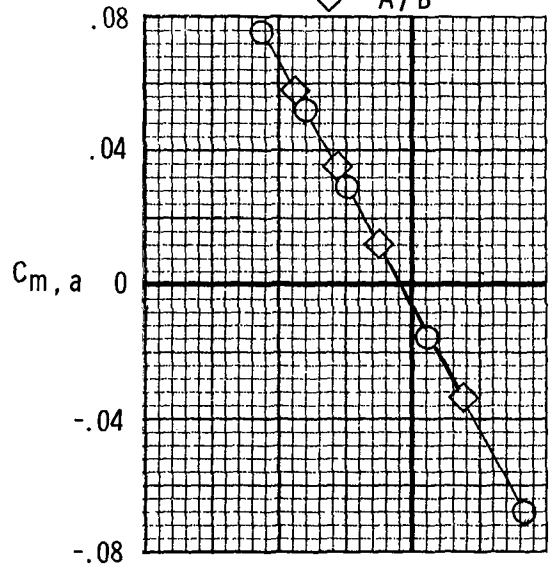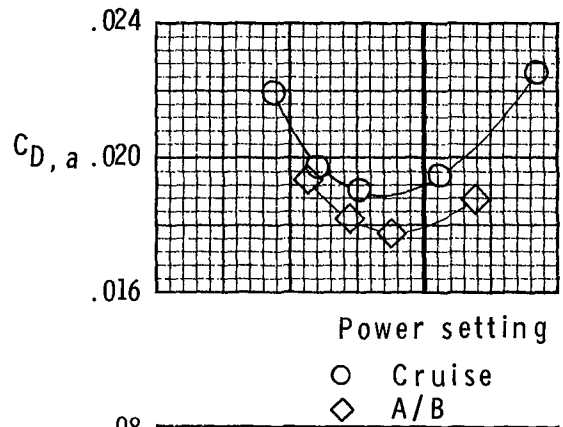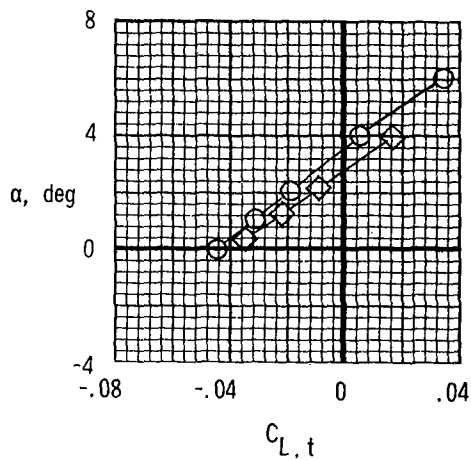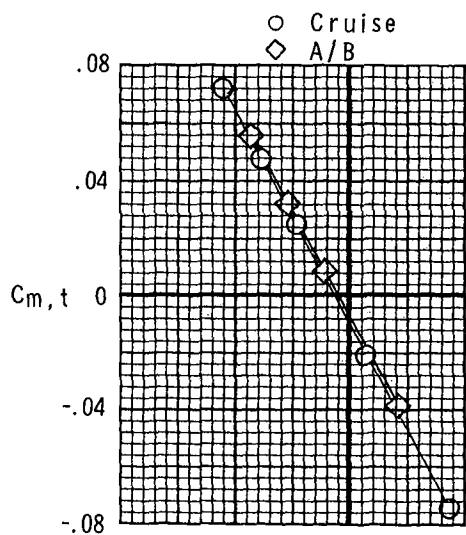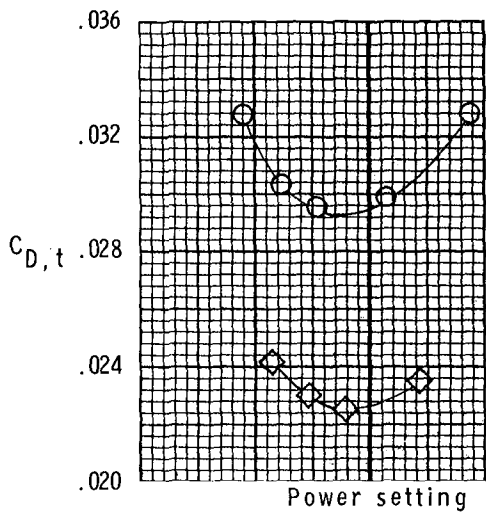
Figure 11.- Continued.

(m) Afterbody-nozzle characteristics.
M = 1.15;   NPR, 8.0;   Λ = 68°.

(n) Afterbody characteristics.   M = 1.15;
NPR, 8.0;   Λ = 68°.

Figure 11.- Continued.
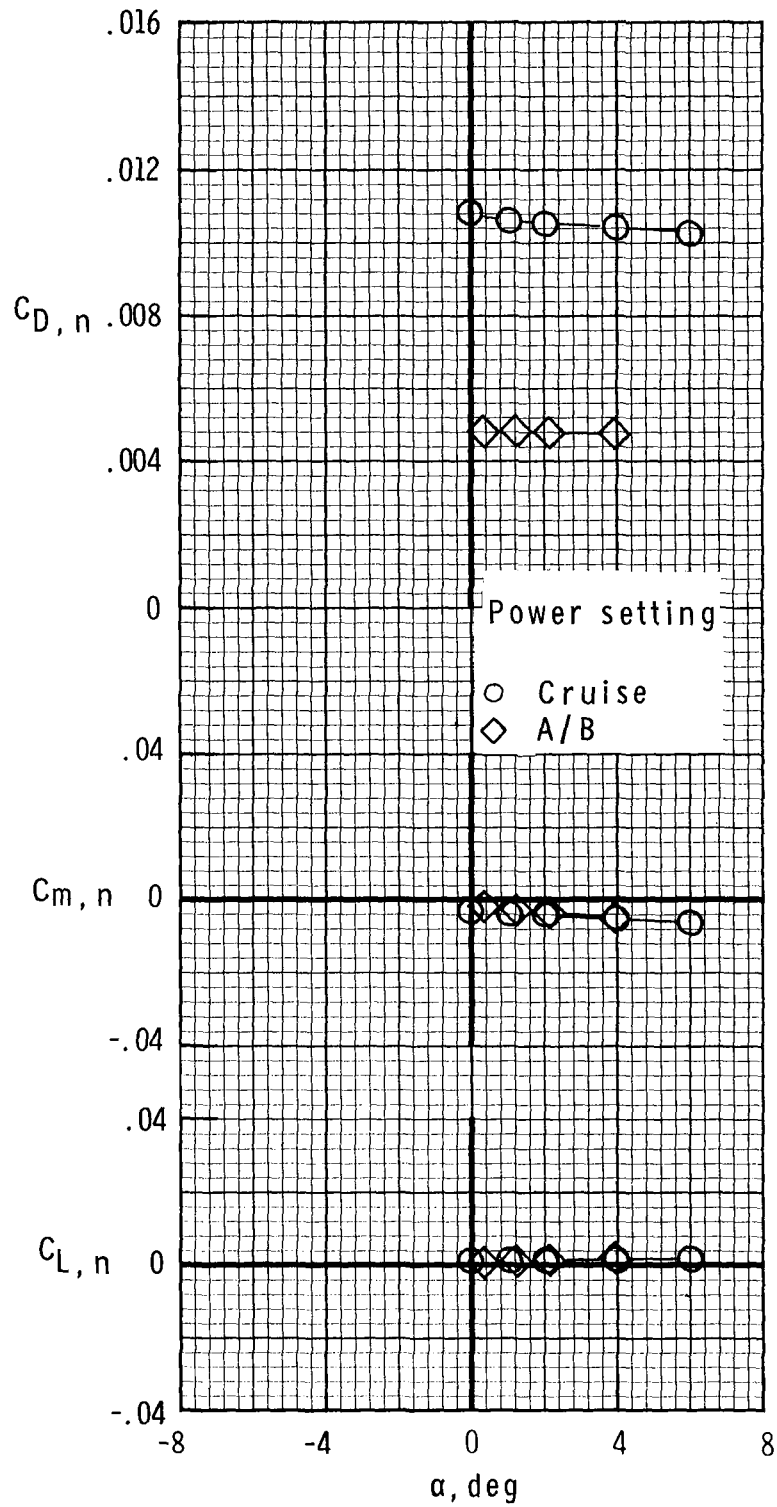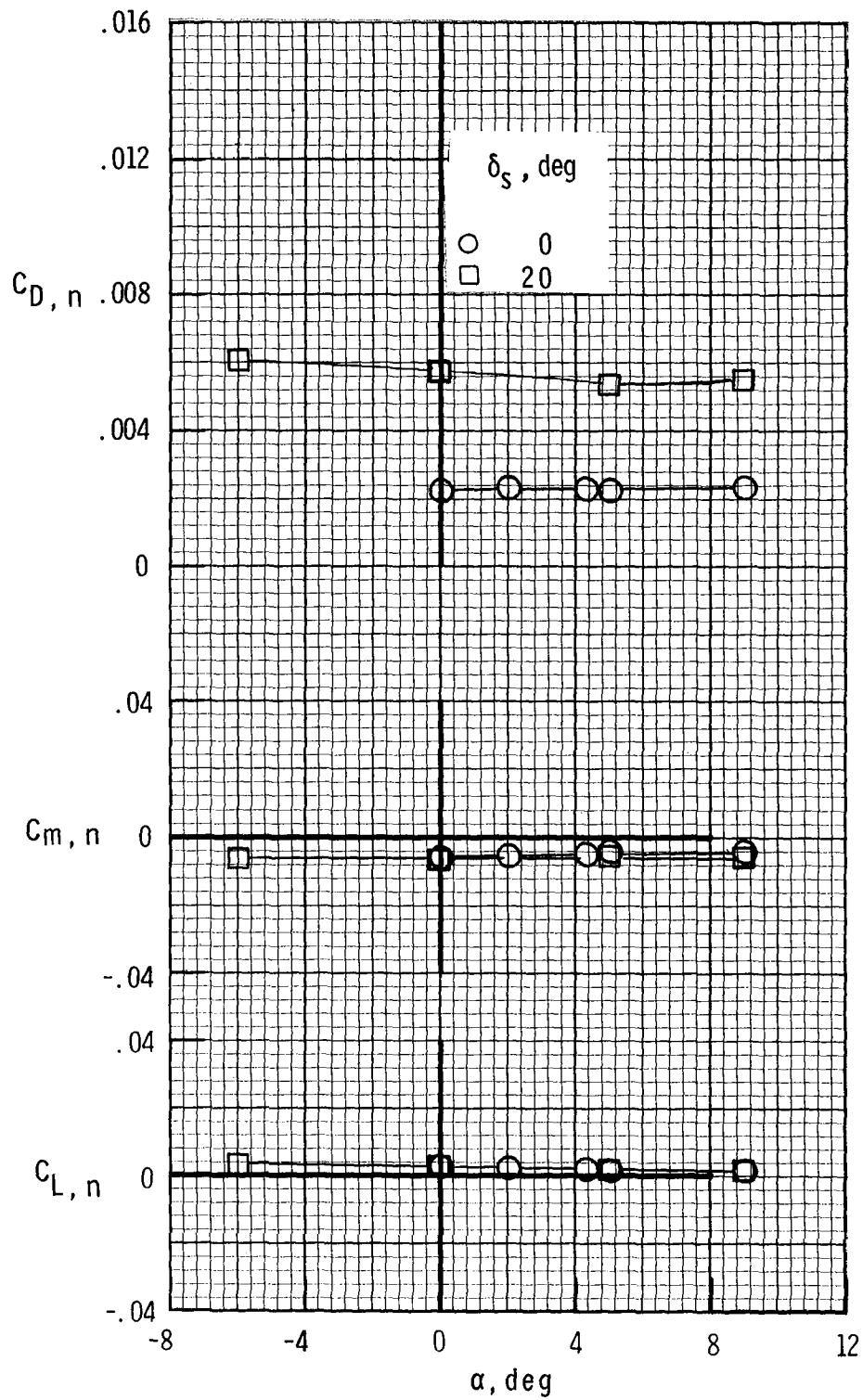
(o) Nozzle characteristics.   M = 1.15;
NPR, 8.0;   Λ = 68°.
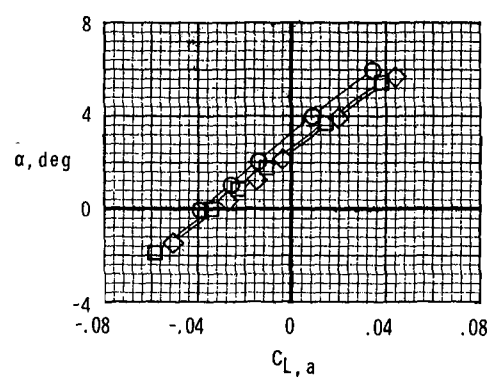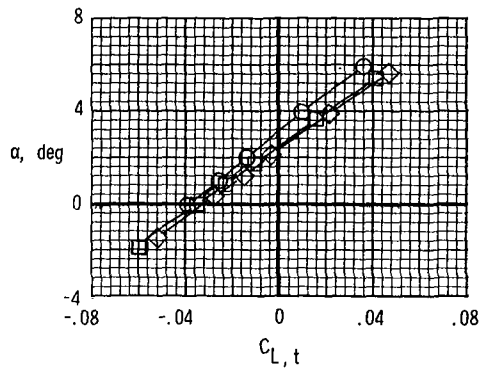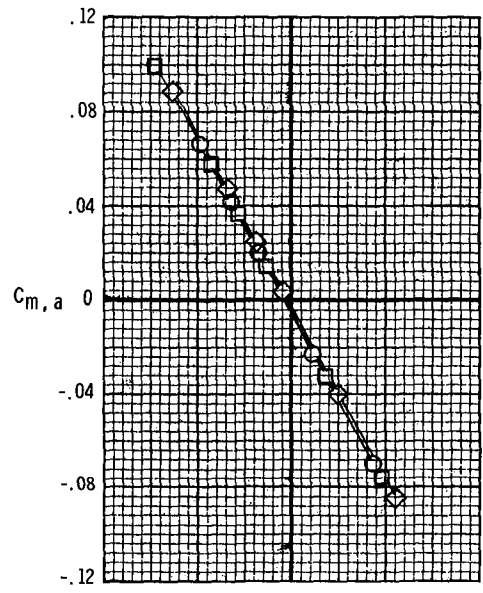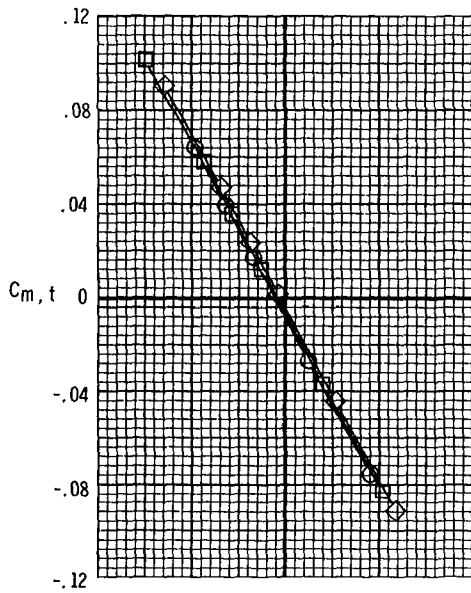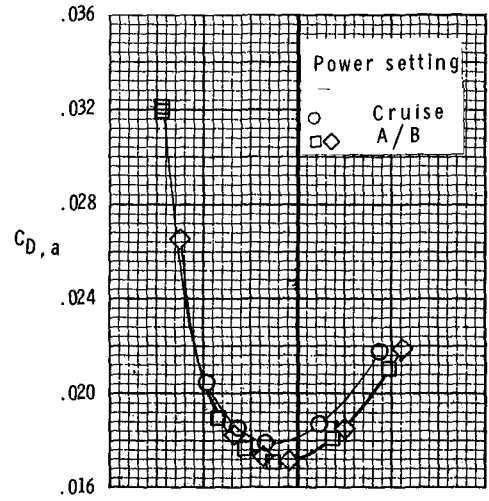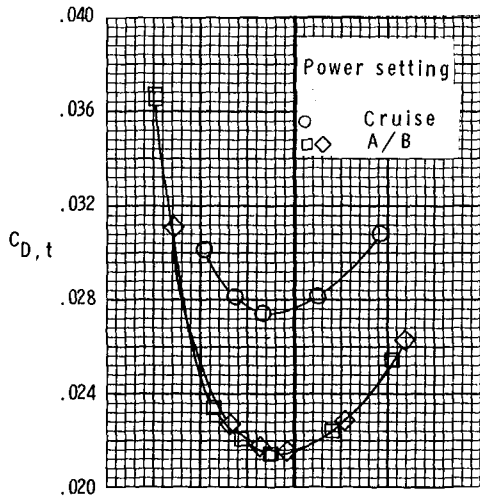
Figure 11.- Continued.

(p) Afterbody-nozzle characteristics.
M = 1.25; NPR, 8.0; Λ = 68°.

(q) Afterbody characteristics. M = 1.25;
NPR, 8.0; Λ = 68°.

Figure 11.- Continued.
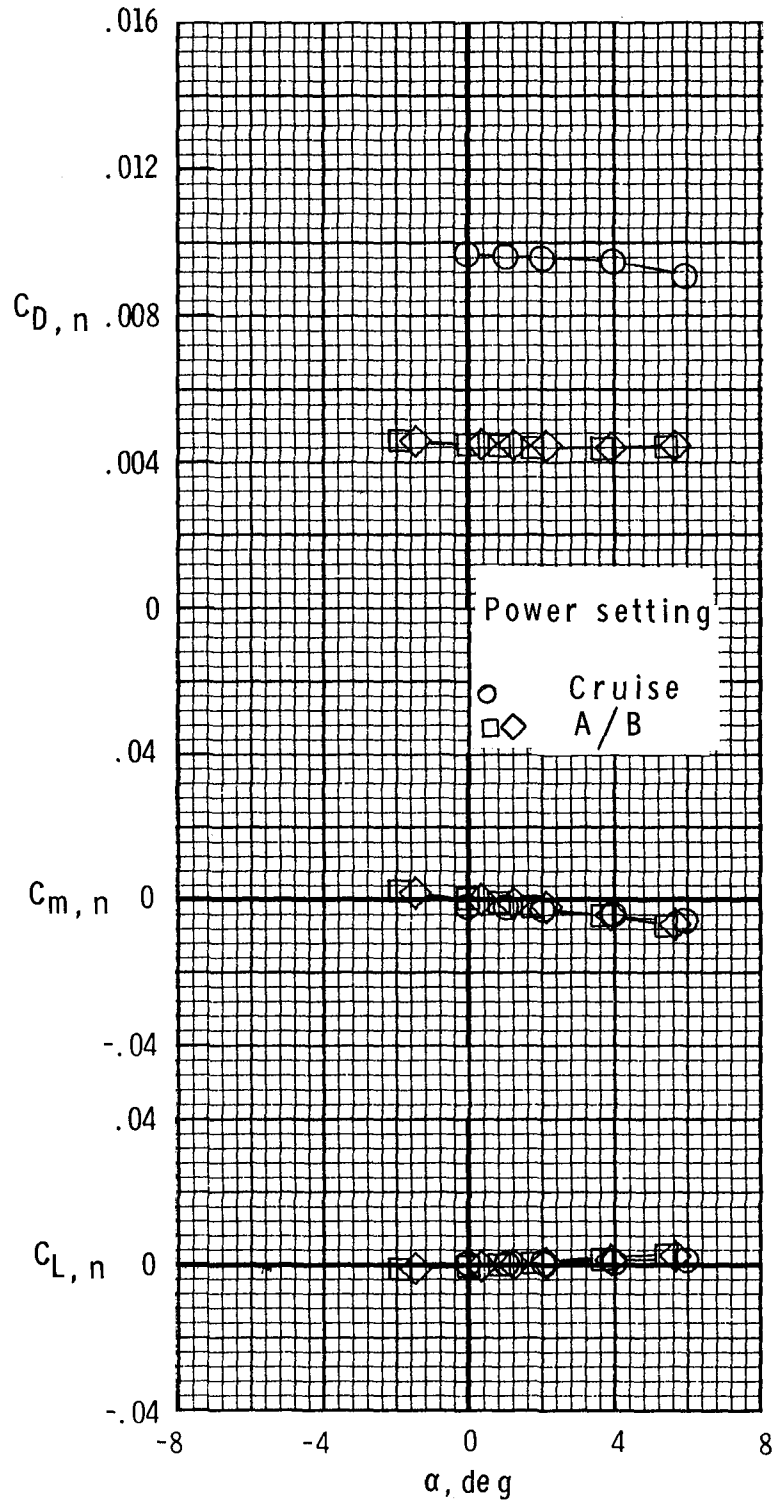
(r) Nozzle characteristics. M = 1.25;
NPR, 8.0; Λ = 68°.

Figure 11.- Concluded.
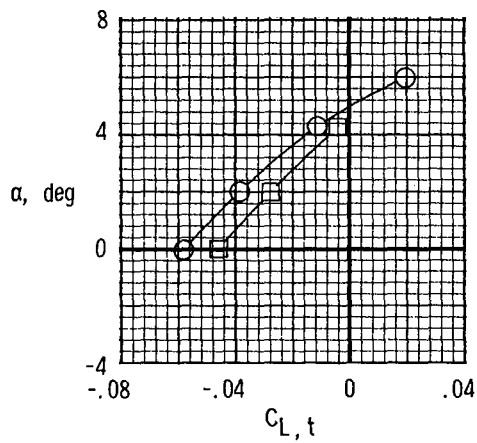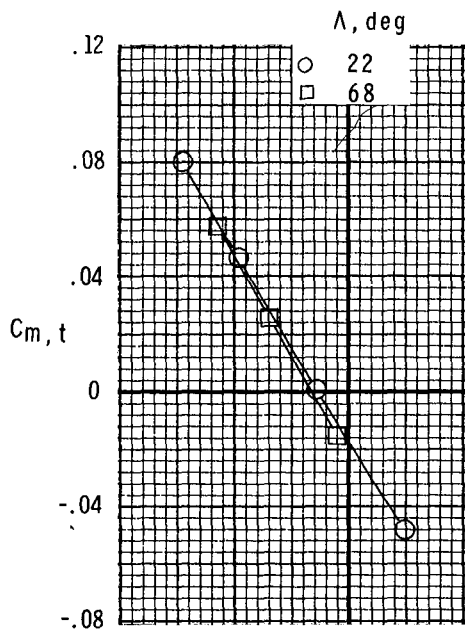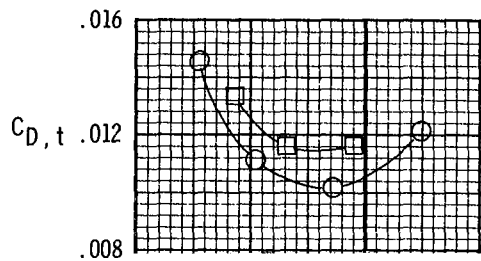
(a) Cruise nozzles in aft position. Afterbody-
nozzle characteristics.

Figure 12.- Typical effects of wing sweep on afterbody-nozzle
aerodynamic characteristics. M = 0.9; NPR, 5.5.
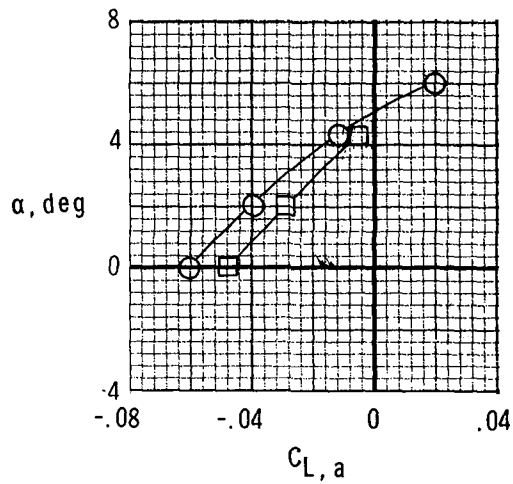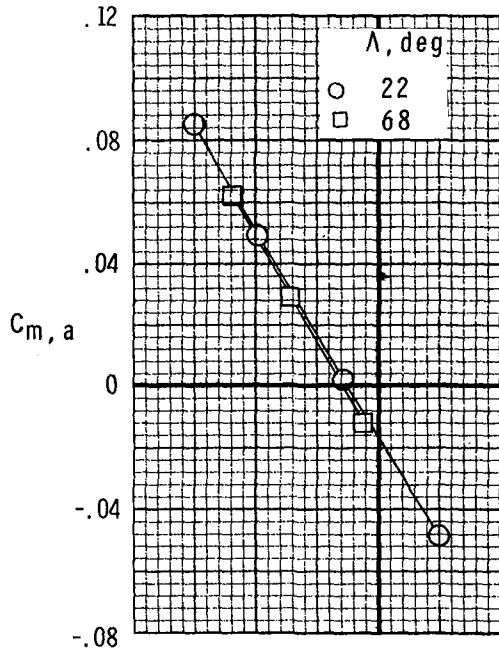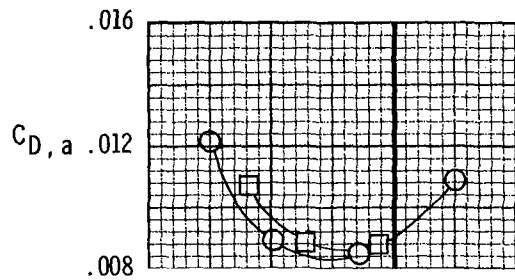
(a) Cruise nozzles in aft position - continued.
Afterbody characteristics.

Figure 12.- Continued.
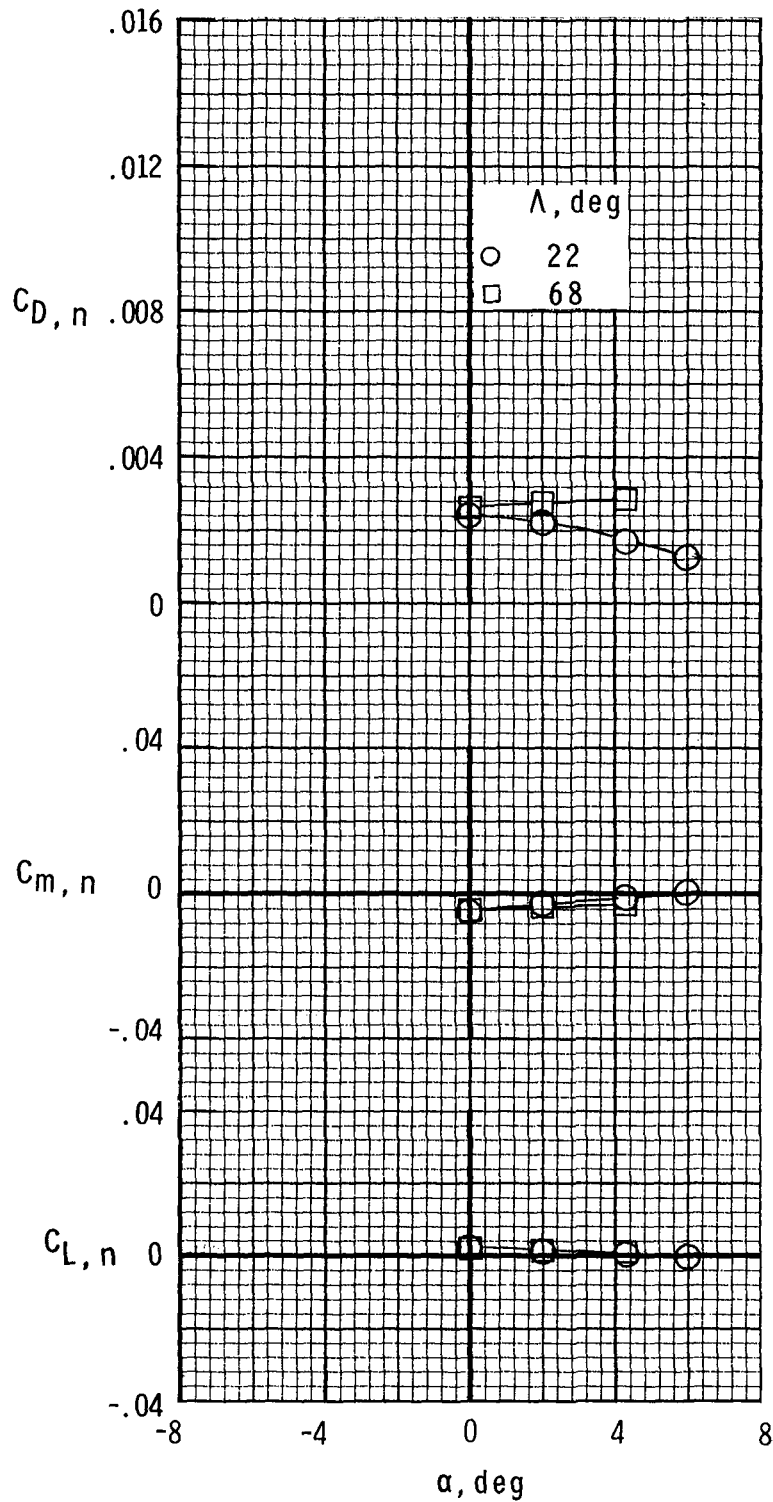
(a) Cruise nozzles in aft position - concluded.
Nozzle characteristics.

Figure 12.- Continued.
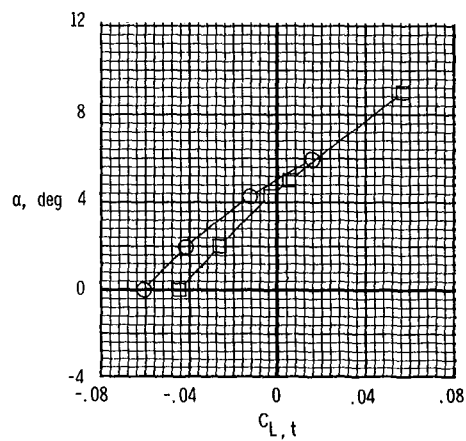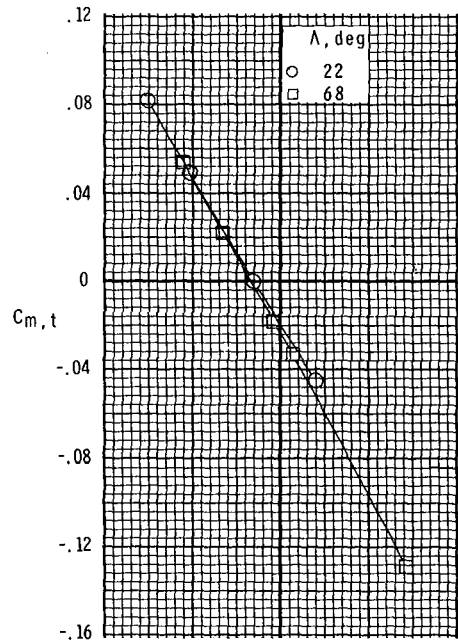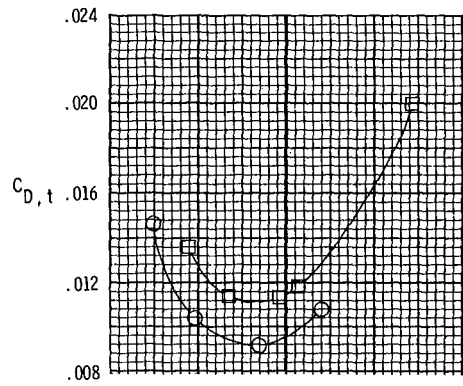
(b) Cruise nozzles in intermediate position.
Afterbody-nozzle characteristics.

Figure 12.- Continued.

(b) Cruise nozzles in intermediate position - continued.
Afterbody characteristics.

Figure 12.- Continued.

(b) Cruise nozzles in intermediate position - concluded.
Nozzle characteristics.

Figure 12.- Continued.

(c) Cruise nozzles in forward position. Afterbody-
nozzle characteristics.

Figure 12.- Continued.

(c) Cruise nozzles in forward position - continued.
Afterbody characteristics.

Figure 12.- Continued.
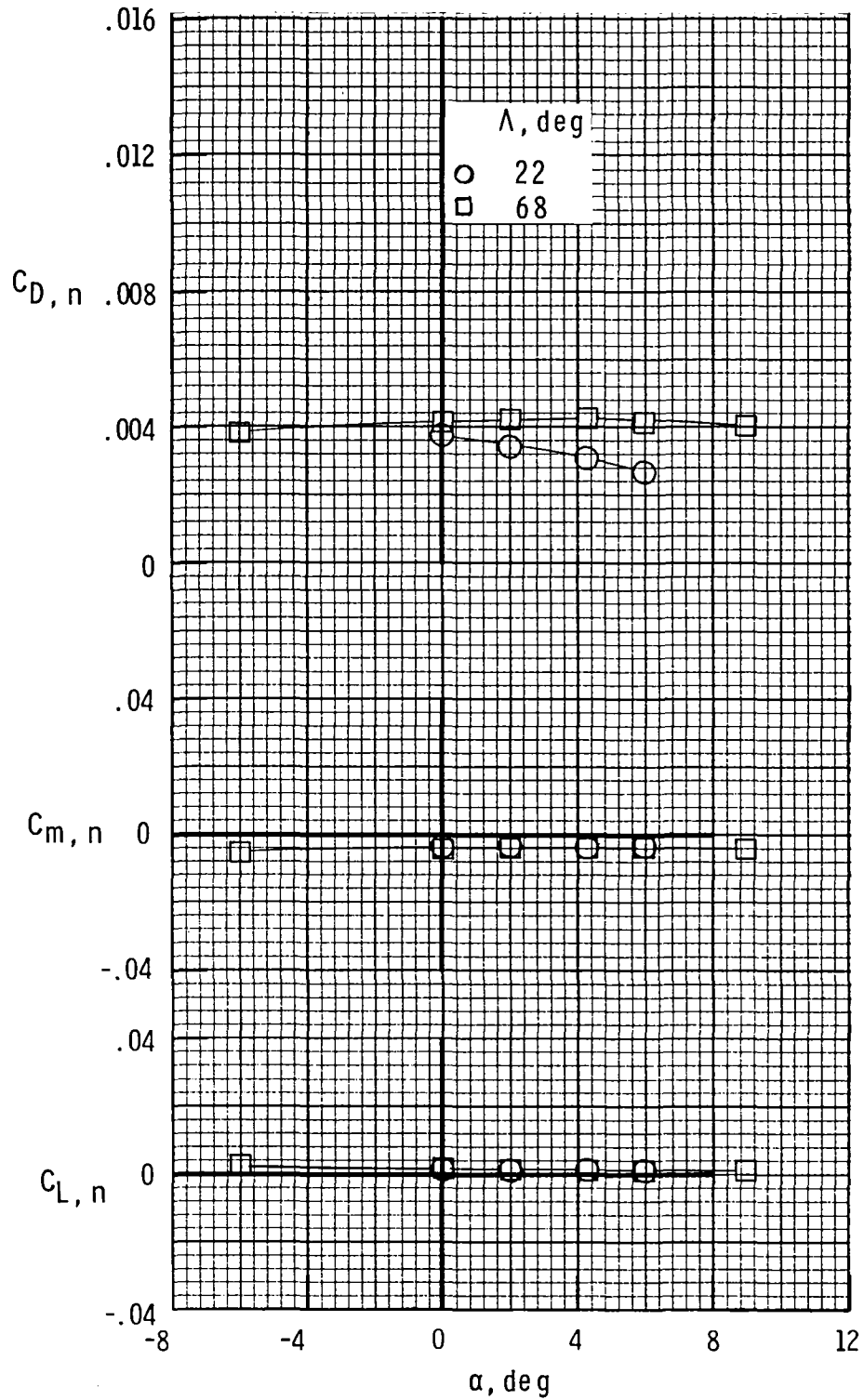
(c) Cruise nozzles in forward position - concluded.
Nozzle characteristics.

Figure 12.- Continued.

(d) A/B nozzles in forward position.
Afterbody-nozzle characteristics.

Figure 12.- Continued.

(d) A/B nozzles in forward position - continued.
Afterbody characteristics.

Figure 12.- Continued.

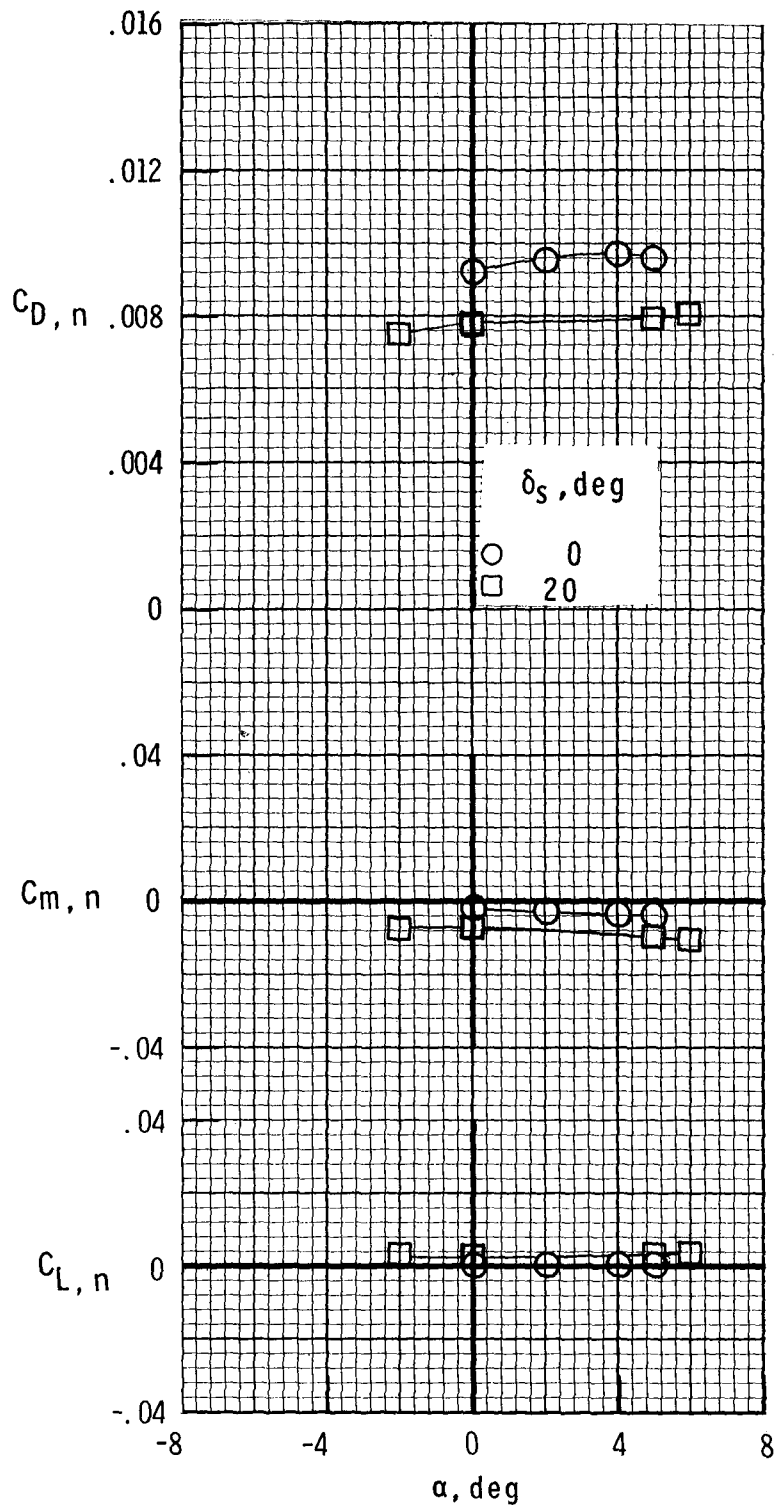(d) A/B nozzles in forward position - concluded.
Nozzle characteristics.

Figure 12.- Concluded.
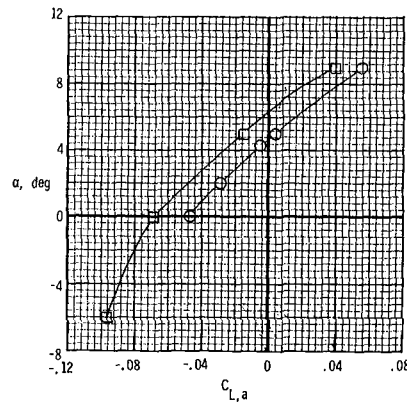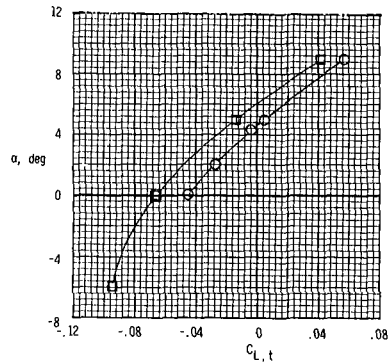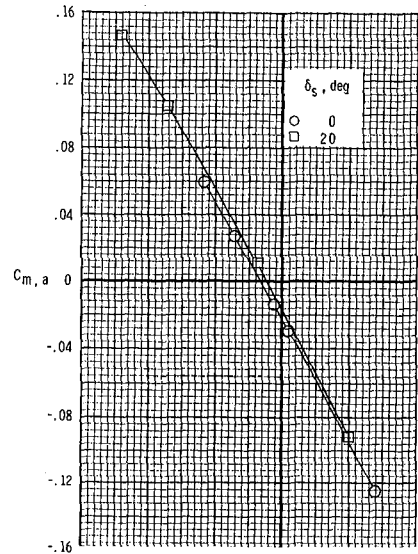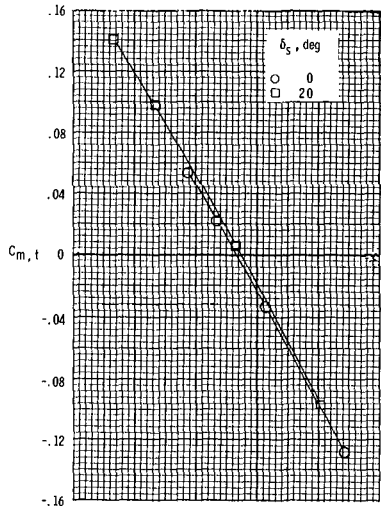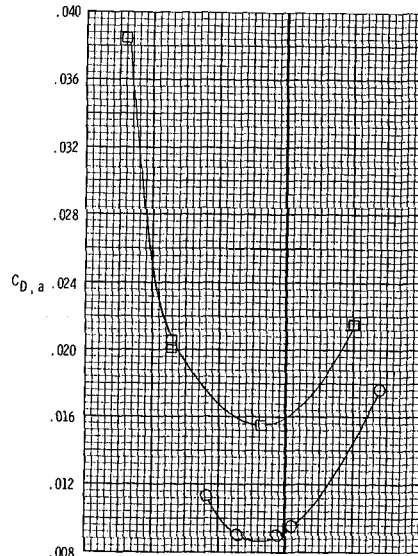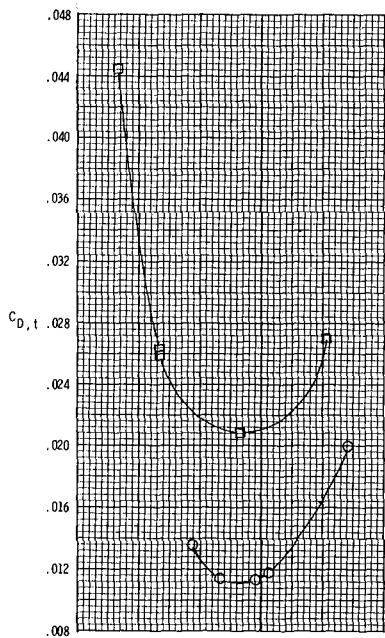
(a) Afterbody-nozzle characteristics.
M = 0.9; NPR, 5.5.

(b) Afterbody characteristics.
M = 0.9; NPR, 5.5.

Figure 13.- Typical effects of 20° speed-brake deployment on afterbody-nozzle aerodynamic characteristics for configuration with cruise nozzles in intermediate position. Λ = 68°.

(c) Nozzle characteristics.
M = 0.9; NPR, 5.5.

Figure 13.- Continued.
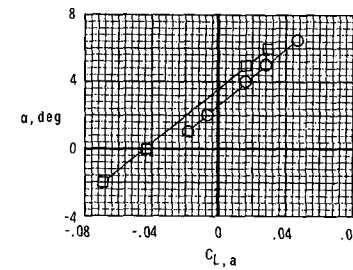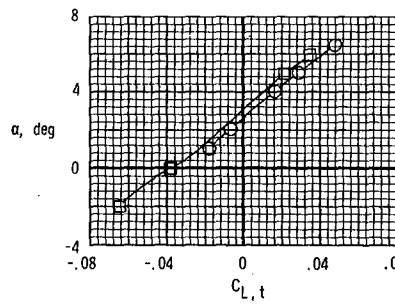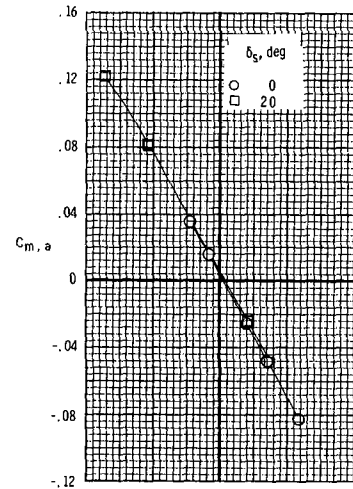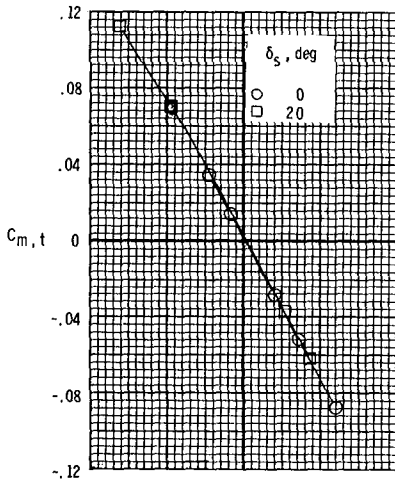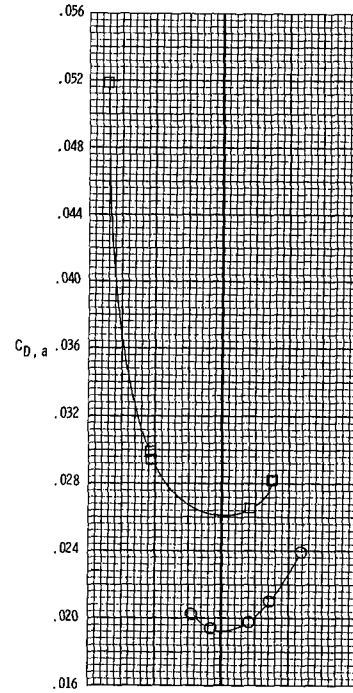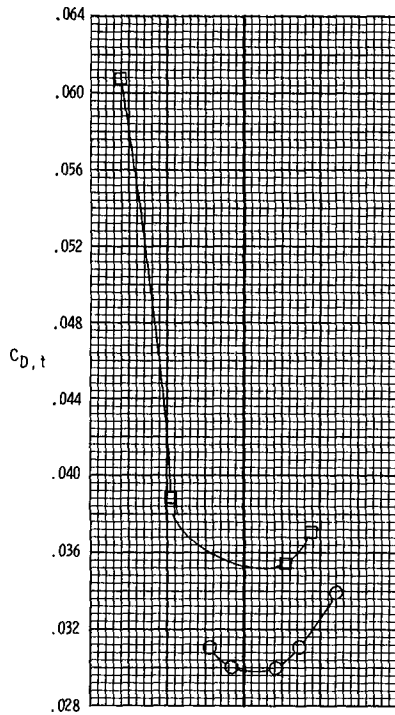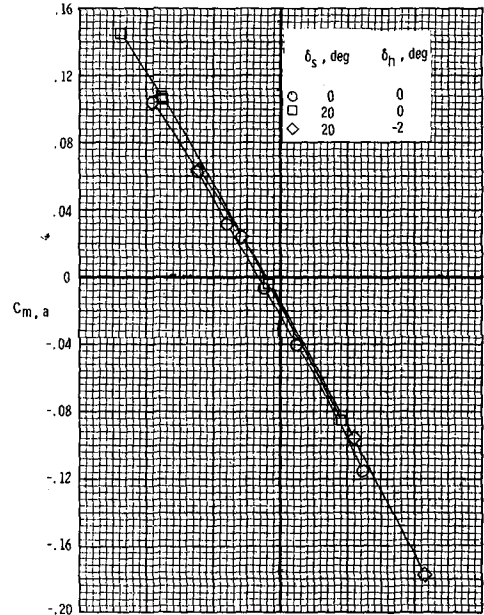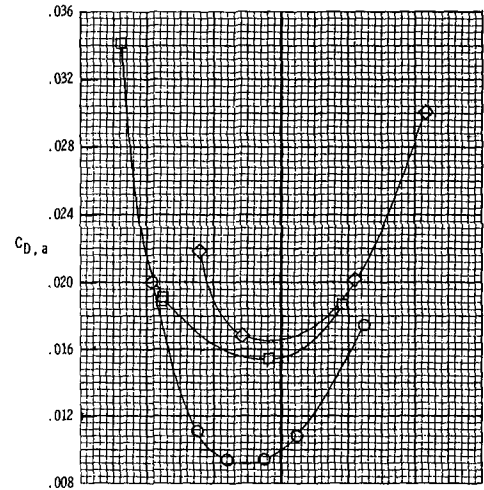
(d) Afterbody-nozzle characteristics.
M = 1.15; NPR, 8.0.

(e) Afterbody characteristics.
M = 1.15; NPR, 8.0.

Figure 13.- Continued.
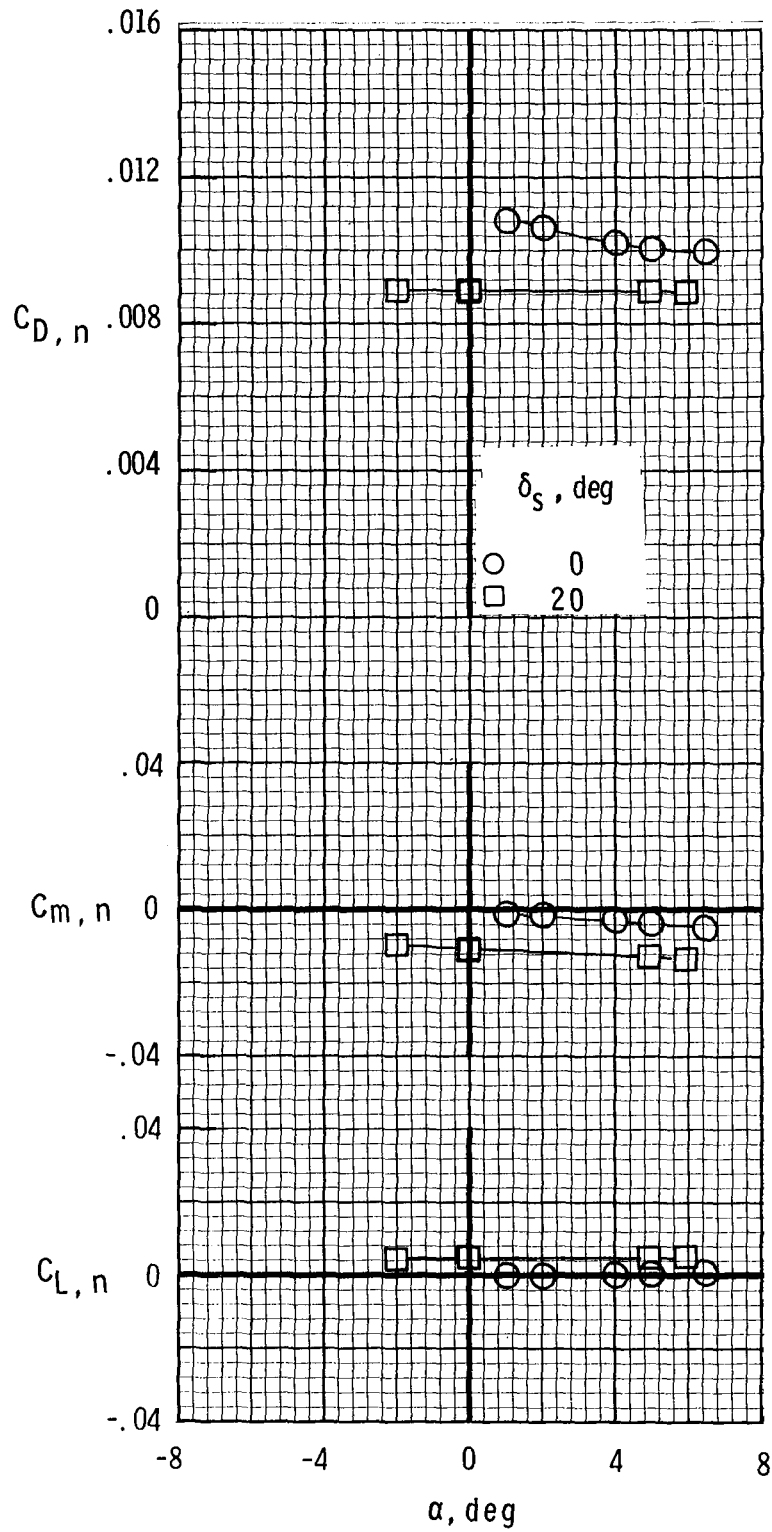
(f) Nozzle characteristics.
M = 1.15; NPR, 8.0.
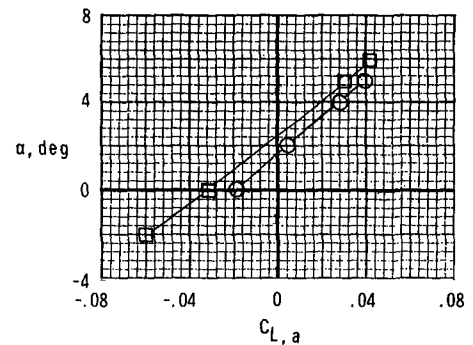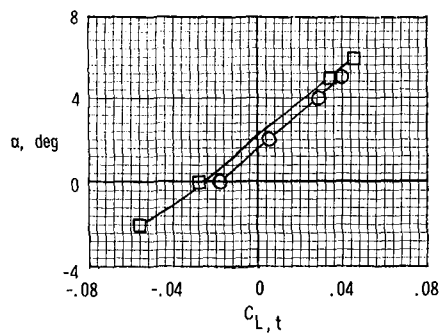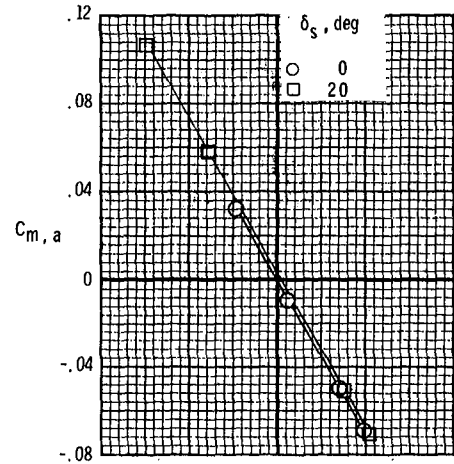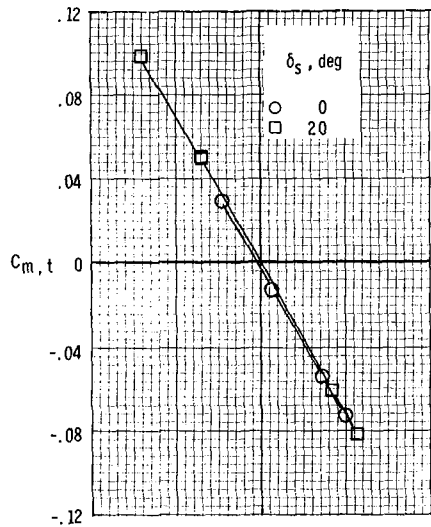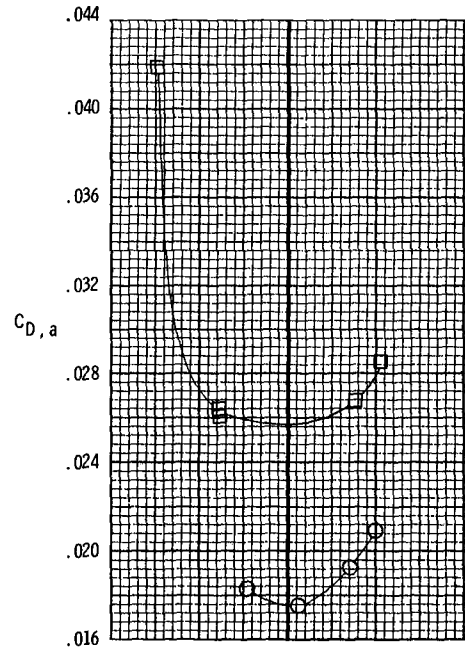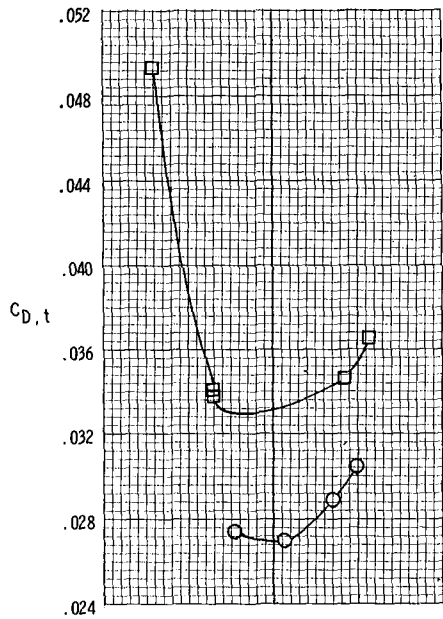
Figure 13.- Continued.
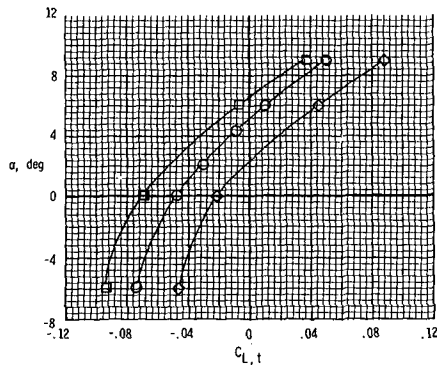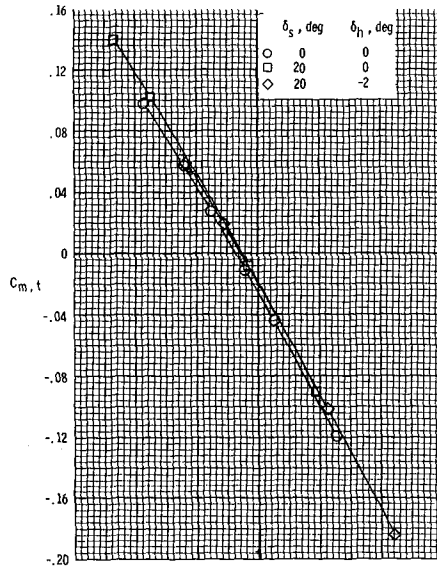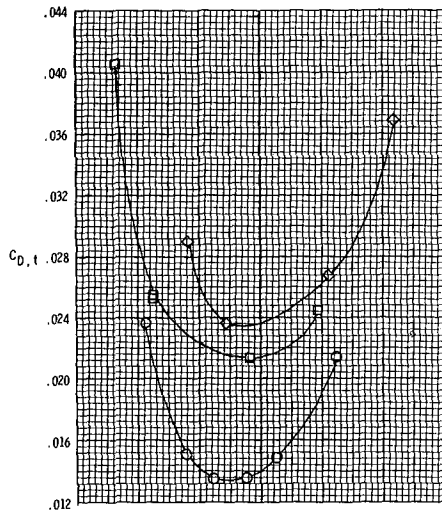
(g) Afterbody-nozzle characteristics.
M = 1.25; NPR, 8.0.

(h) Afterbody characteristics.
M = 1.25; NPR, 8.0.

Figure 13.- Continued.
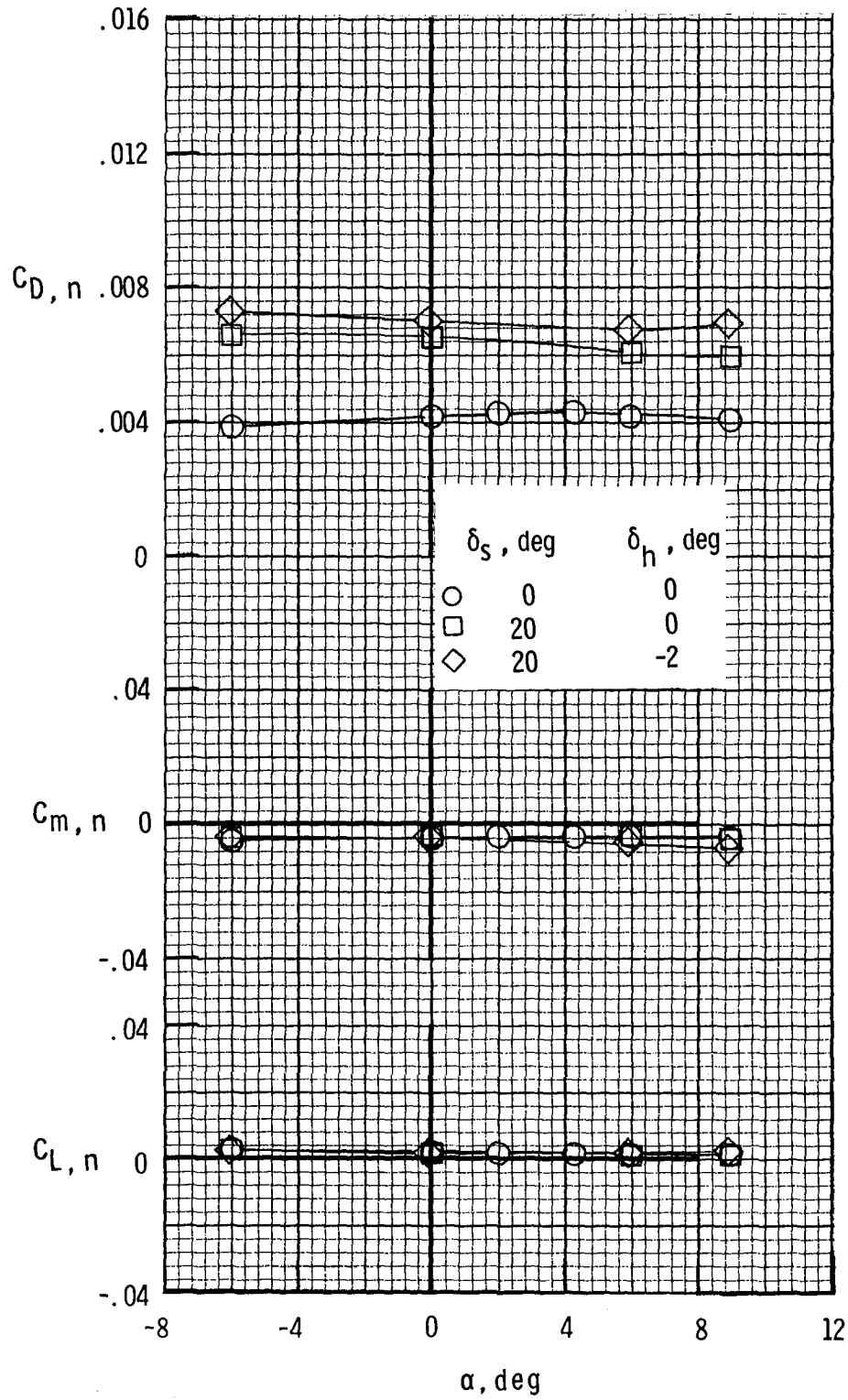
(i) Nozzle characteristics.
M = 1.25; NPR, 8.0.

Figure 13.- Concluded.
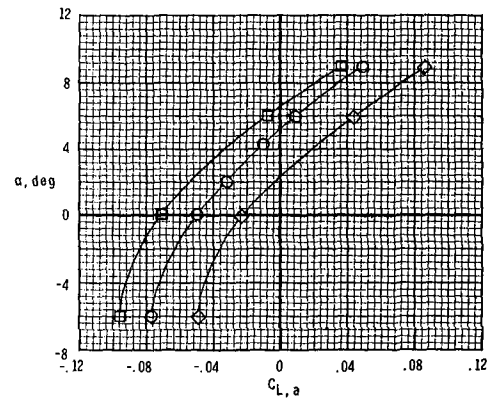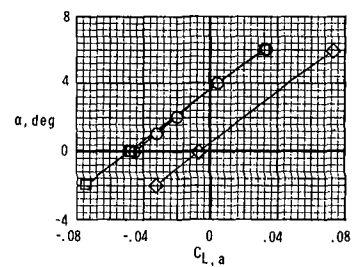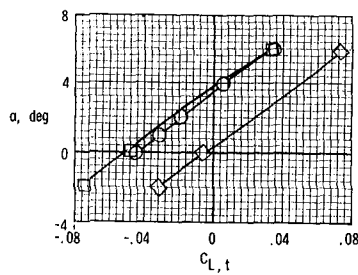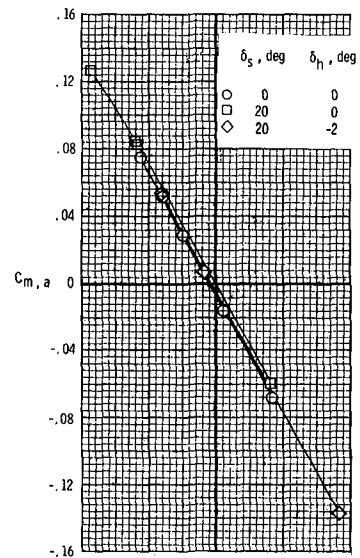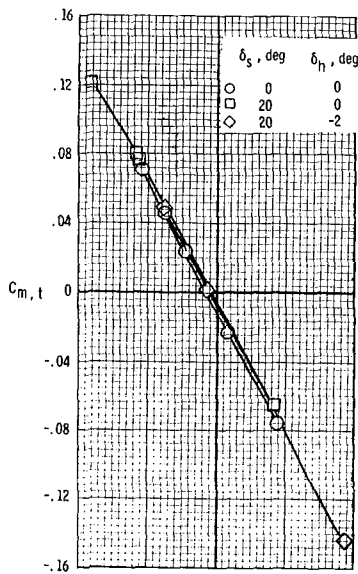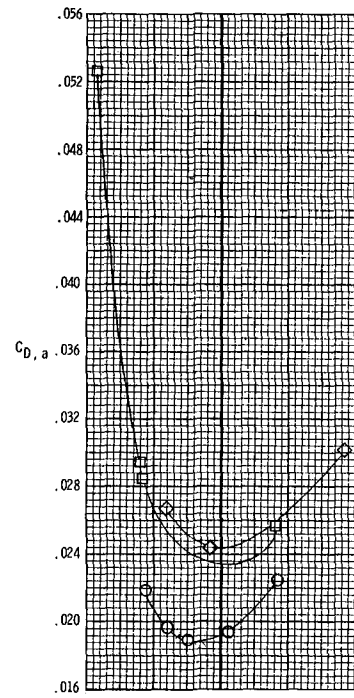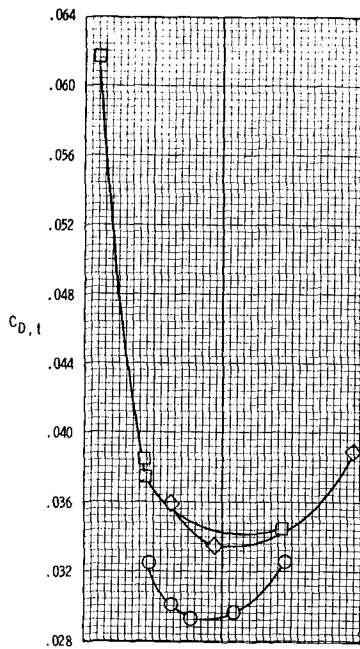
(a) Afterbody-nozzle characteristics.
M = 0.9; NPR, 5.5.

(b) Afterbody characteristics.
M = 0.9; NPR, 5.5.

Figure 14.- Typical effects of 20° speed-brake deployment and in combination
with horizontal-tail deflection on afterbody-nozzle aerodynamic characteristics
for configuration with cruise nozzles in forward position. Λ = 68°.
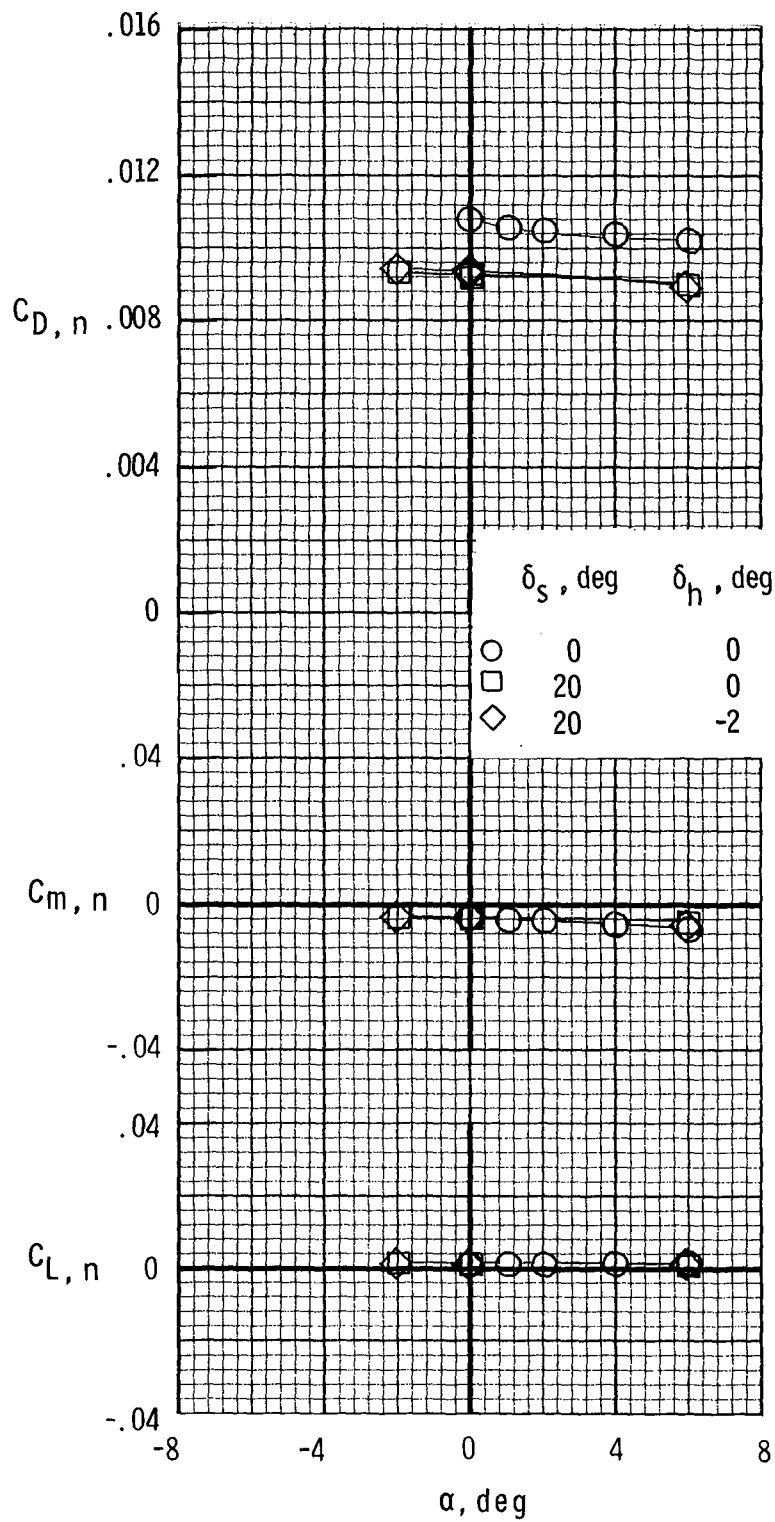
(c) Nozzle characteristics.
M = 0.9; NPR, 5.5.

Figure 14.- Continued.
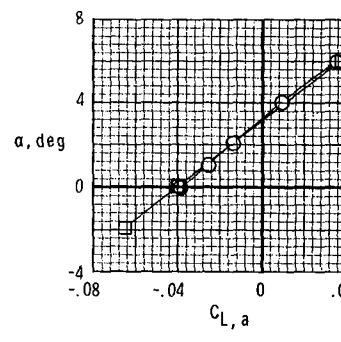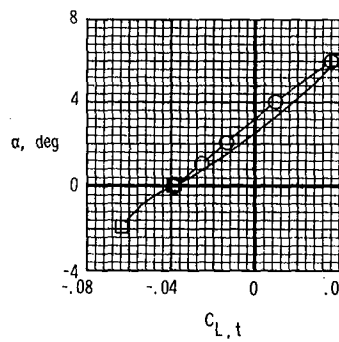
(d) Afterbody-nozzle characteristics.
M = 1.15; NPR, 8.0.

(e) Afterbody characteristics.
M = 1.15 NPR, 8.0.

Figure 14.- Continued.

(f) Nozzle characteristics.
M = 1.15;   NPR, 8.0.

Figure 14.- Continued.
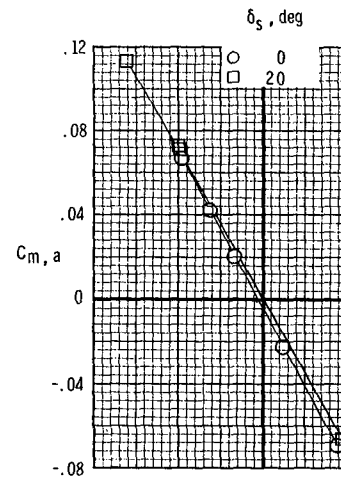
(g) Afterbody-nozzle characteristics.
M = 1.25; NPR, 8.0.

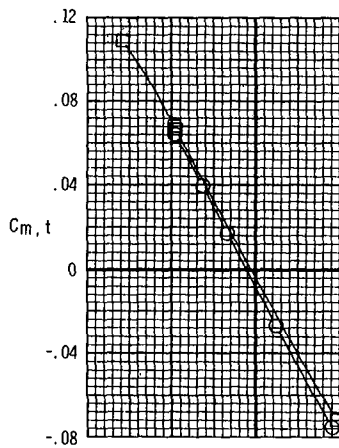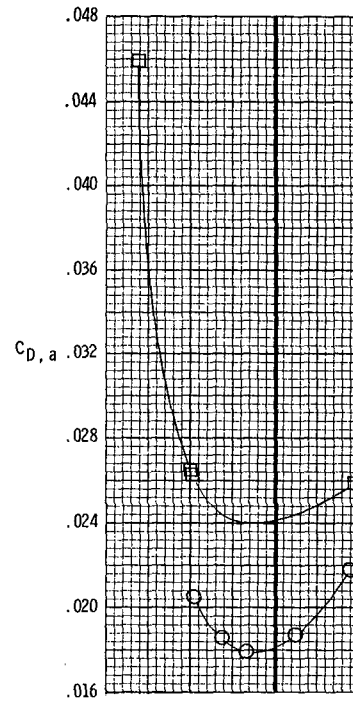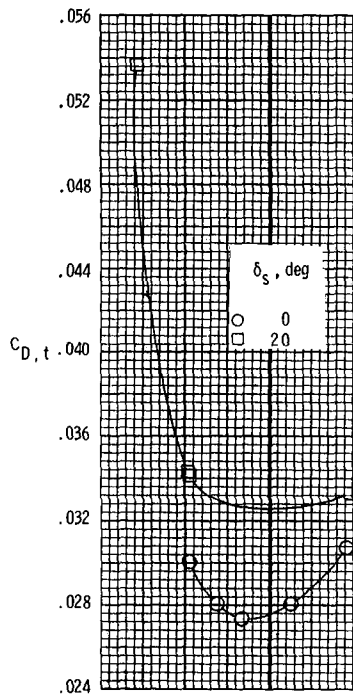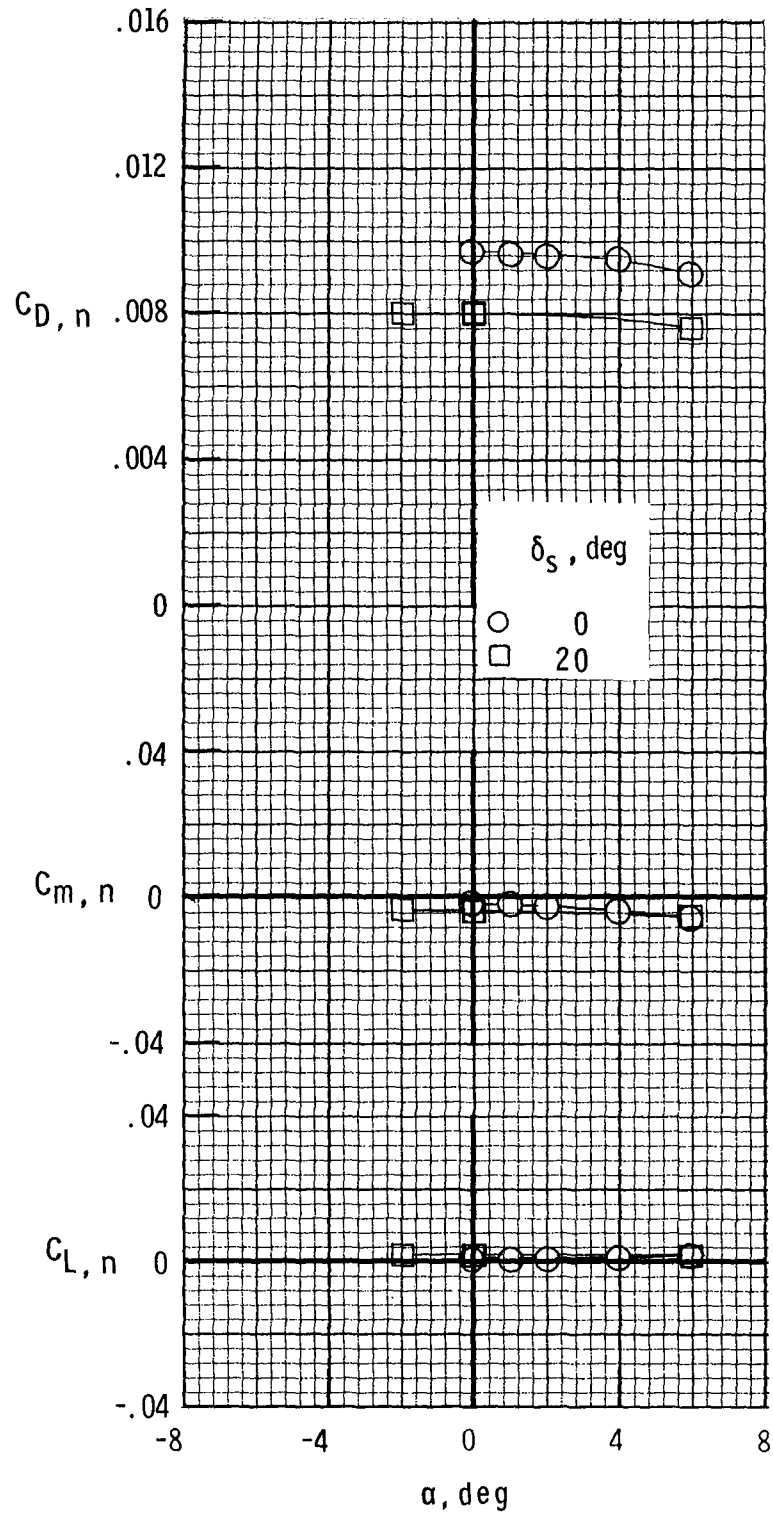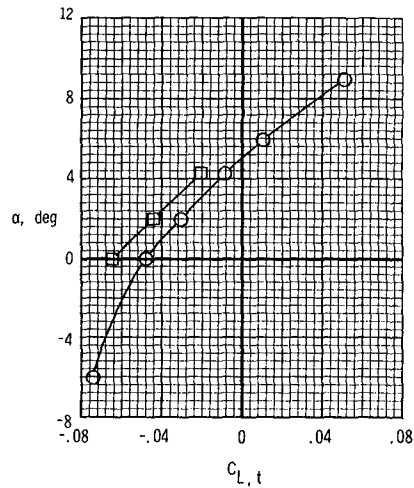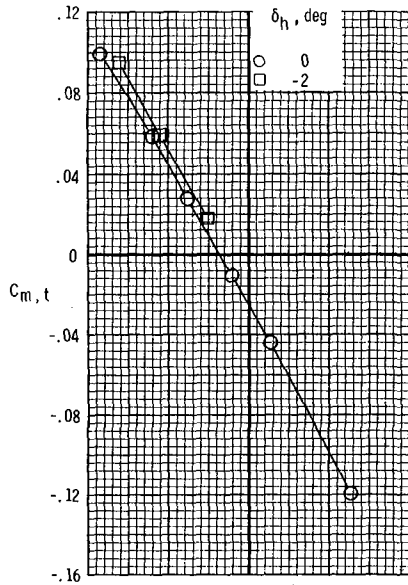(h) Afterbody characteristics.
M = 1.25; NPR, 8.0.

Figure 14.- Continued.

122

(i) Nozzle characteristics.
M = 1.25; NPR, 8.0.

Figure 14.- Concluded.
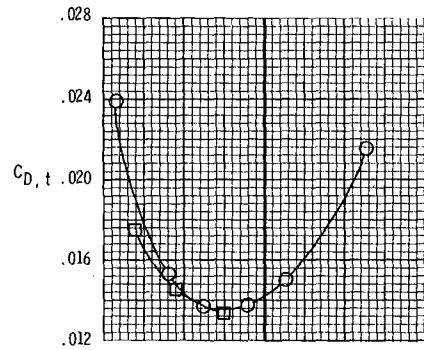
(a) Cruise nozzles. Afterbody-nozzle characteristics.

Figure 15.- Typical effects of horizontal-tail deflection on afterbody-nozzle aerodynamic characteristics for configurations with nozzles in forward position. M = 0.9; NPR, 5.5; Λ = 68°.
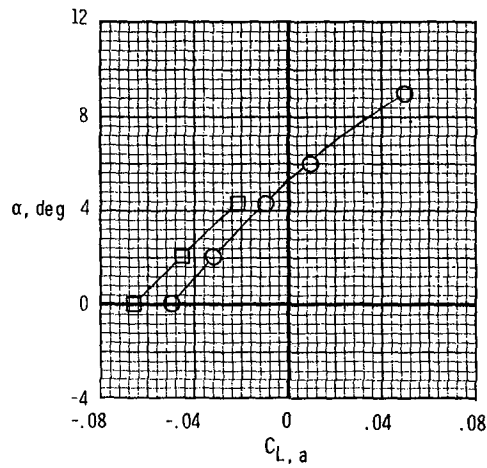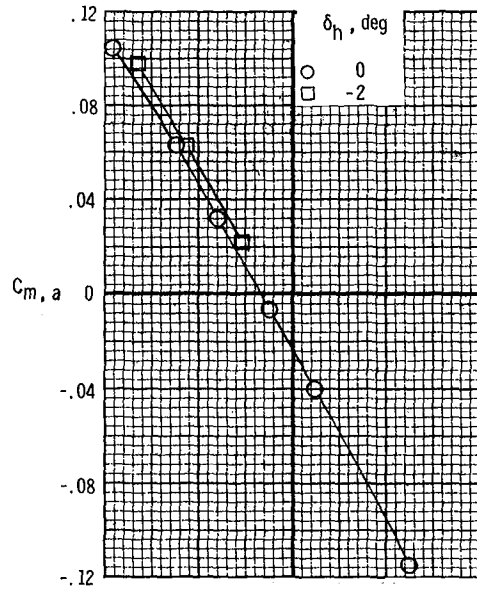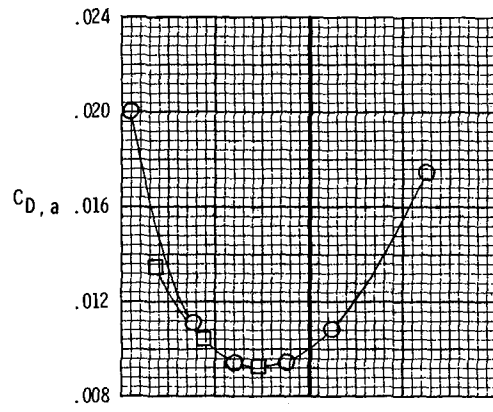
(a) Cruise nozzles - continued.
Afterbody characteristics.

Figure 15.- Continued.
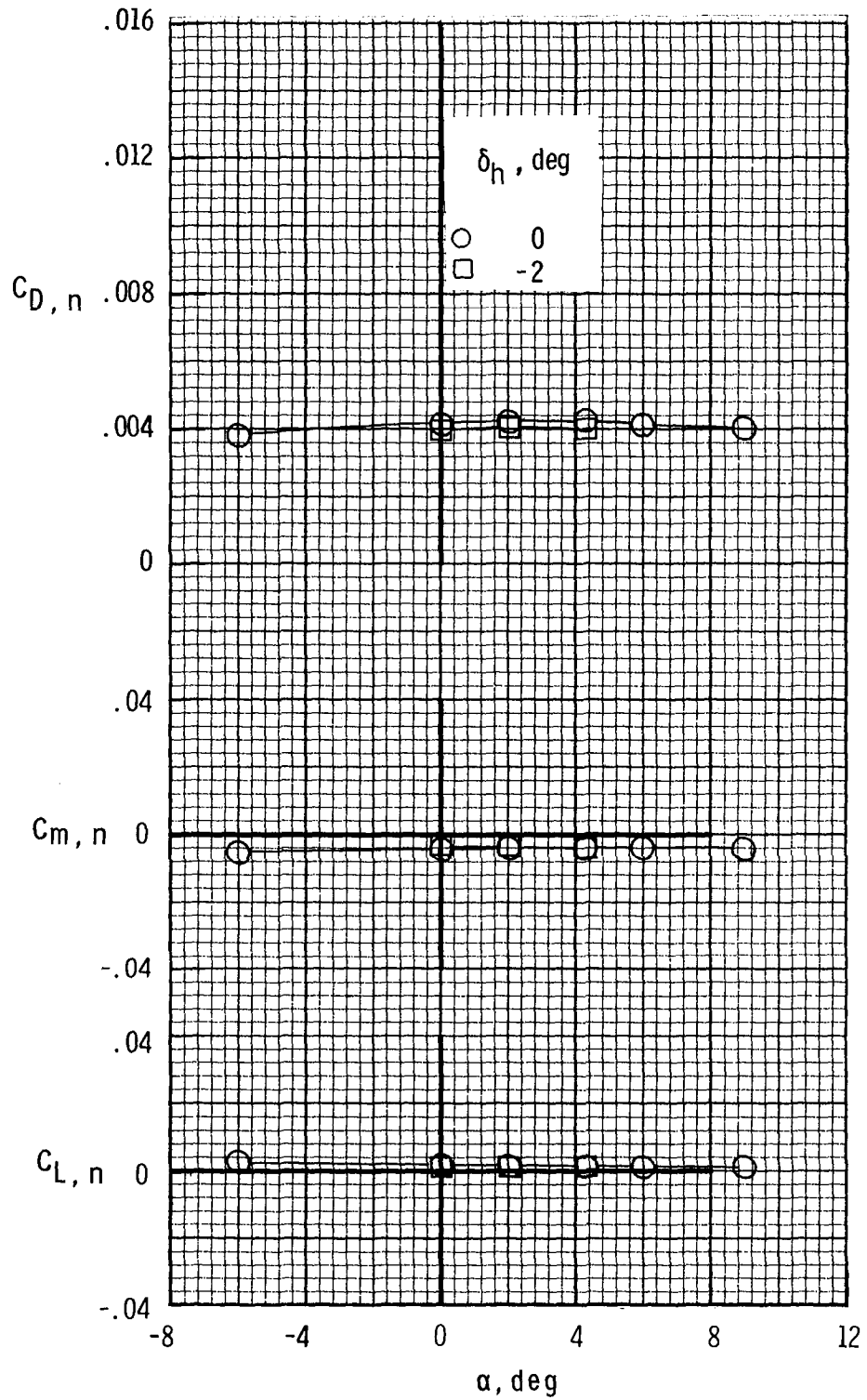
(a) Cruise nozzles - concluded.
Nozzle characteristics.

Figure 15.- Continued.

(b) A/B nozzles. Afterbody-nozzle characteristics.

Figure 15.- Continued.

(b) A/B nozzles - continued. Afterbody characteristics.

Figure 15.- Continued.

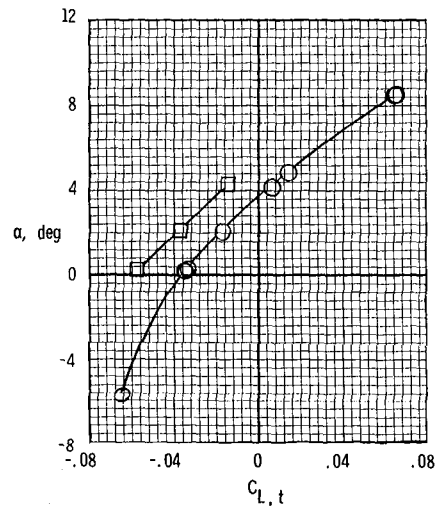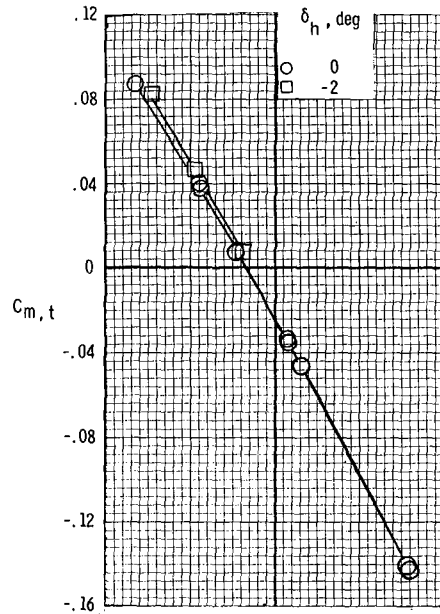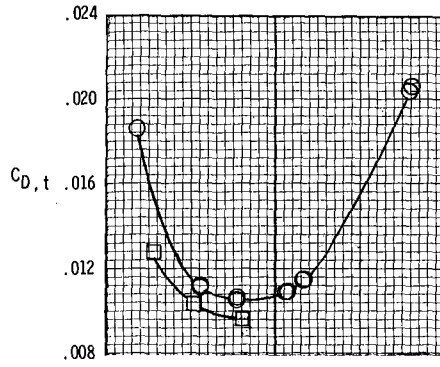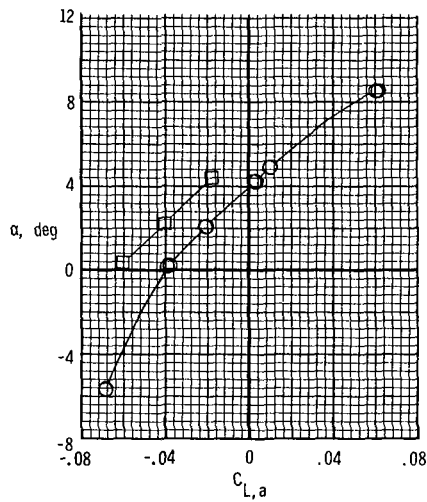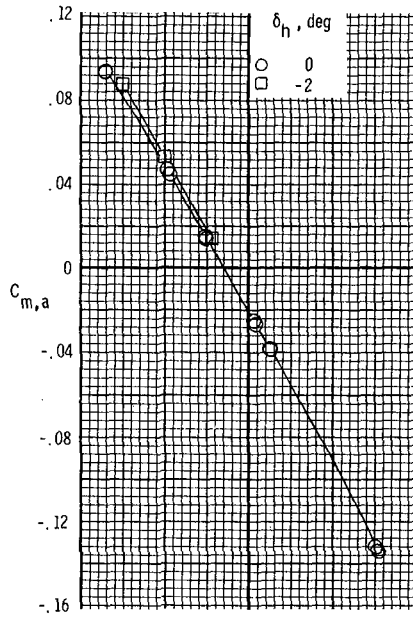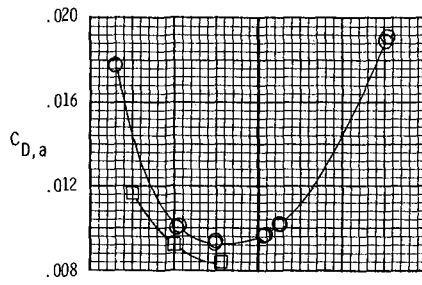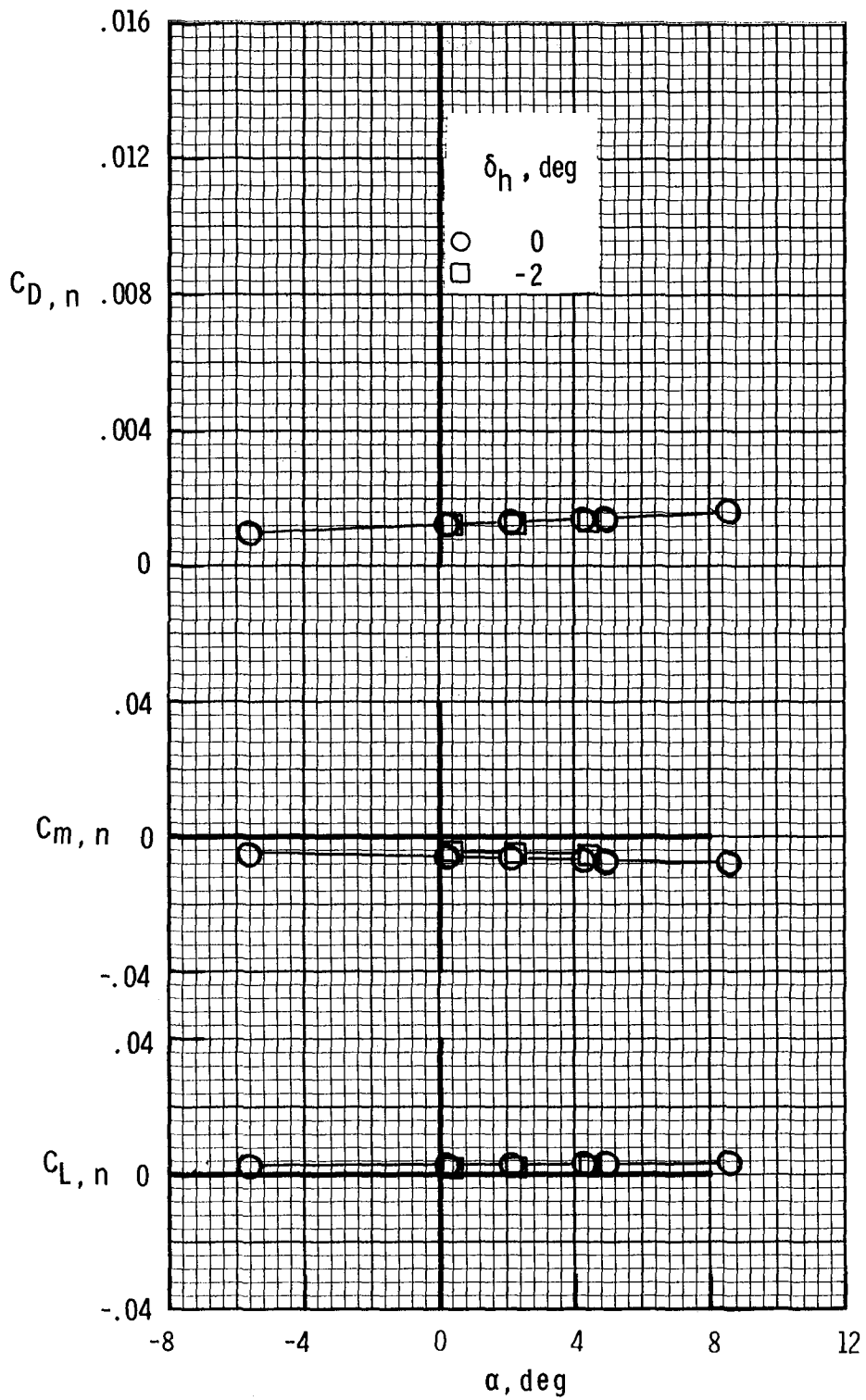(b) A/B nozzles - concluded. Nozzle characteristics.

Figure 15.- Concluded.

1. Report No. NASA TM-83250	2. Government Accession No.	3. Recipient's Catalog No.
4. Title and Subtitle EFFECTS OF INSTALLATION OF F101 DFE EXHAUST NOZZLES ON THE AFTERBODY-NOZZLE CHARACTERISTICS OF THE F-14 AIRPLANE		5. Report Date March 1982
		6. Performing Organization Code 505-31-43-04
7. Author(s) David E. Reubush and John R. Carlson		8. Performing Organization Report No. L-14895
		10. Work Unit No.
9. Performing Organization Name and Address NASA Langley Research Center Hampton, VA 23665		11. Contract or Grant No.
		13. Type of Report and Period Covered Technical Memorandum
12. Sponsoring Agency Name and Address National Aeronautics and Space Administration Washington, DC 20546		14. Sponsoring Agency Code

15. Supplementary Notes

16. Abstract

A wind-tunnel investigation was conducted to determine the effects of F101 DFE (derivative fighter engine) nozzle axial positioning on the afterbody-nozzle longitudinal aerodynamic characteristics of the F-14 airplane. The model was tested in the Langley 16-Foot Transonic Tunnel at Mach numbers from 0.7 to 1.25 and angles of attack from about -2° to 6°. Compressed air was used to simulate nozzle exhaust flow at jet total-pressure ratios from 1 (jet off) to about 8. The results of the investigation show that for subsonic Mach numbers the intermediate cruise nozzle position of the three positions tested resulted in the lowest drag.

17. Key Words (Suggested by Author(s)) Afterbody drag Fighter airplane Boattail drag Jet effects	18. Distribution Statement Unclassified - Unlimited Subject Category 02
19. Security Classif. (of this report) Unclassified	20. Security Classif. (of this page) Unclassified	21. No. of Pages 131	22. Price A07

THIRD-CLASS BULK RATE

NASA